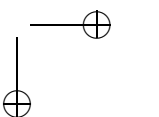
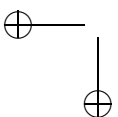
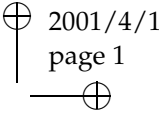
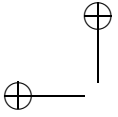
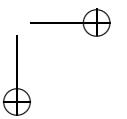
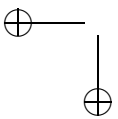
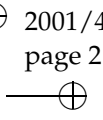
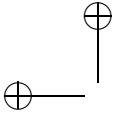
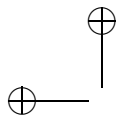


# Discontinuous modelling of strain localisation and failure







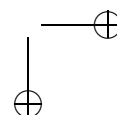
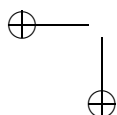
# Discontinuous modelling of strain localisation and failure

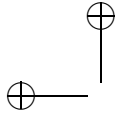
## Proefschrift

ter verkrijging van de graad van doctor  
aan de Technische Universiteit Delft,  
op gezag van de Rector Magnificus prof. ir. K. F. Wakker,  
voorzitter van het College van Promoties,  
in het openbaar te verdedigen

op 12 juni 2001 om 16.00 uur

door Garth Nathan WELLS  
Bachelor of Engineering with First Class Honours, The University of Western  
Australia  
geboren te Perth, Western Australia





Dit proefschrift is goedgekeurd door de promotor:  
prof. dr. ir. R. de Borst

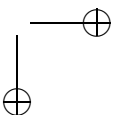
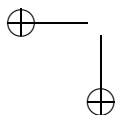
Toegevoegd promotor:  
dr. ir. L. J. Sluys

Samenstelling promotiecommissie:

|                              |  |
|------------------------------|--|
| Rector Magnificus            | Voorzitter   |
| prof. dr. ir. R. de Borst    | Technische Universiteit Delft, promotor              |
| dr. ir. L. J. Sluys          | Technische Universiteit Delft, toegevoegd promotor   |
| prof. dr. ir. M. G. D. Geers | Technische Universiteit Eindhoven                    |
| dr. M. Jirásek               | École Polytechnique Fédéral de Lausanne, Zwitserland |
| prof. dr. ir. A. van Keulen  | Technische Universiteit Delft                        |
| prof. dr. ir. J. G. Rots     | Technische Universiteit Delft                        |
| prof. dr. K. Runesson        | Chalmers University of Technology, Zweden            |

Copyright © 2001 by G. N. Wells

ISBN 90-9014731-4



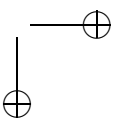
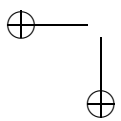
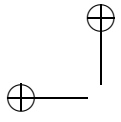
## Foreword

The research presented in this thesis was carried out at the Faculty of Aerospace Engineering and the Faculty of Civil Engineering and Geosciences at Delft University of Technology.

I am most grateful to Bert Sluys and René de Borst, who gave me the opportunity to come to Delft, and whose scientific insight and experience was invaluable. From my colleagues, I did not only learn much but they added a lot of ‘pleasure’. For this I thank past and present colleagues, Harm Askes, Frank Everdij, Miguel Gutiérrez, Frank Hashegen, Otto Heeres, Giovanna Lilliu, Erik-Jan Lingen, Jerzy Pamin, Joris Remmers, Mario de Rooij, Carla Roovers, Ingrid Schipperen, Chunxia Shi, Angelo Simone, Martijn Stroeven, Akke Suiker, Harold Thung, Gideon van Zijl and Wang Weimin.

This research was supported by the Netherlands Technology Foundation STW (under grant DCT.4010, sub-project IIb), applied science division of NWO, the technology program of the Ministry of Economic Affairs and the Ministry of Public Works and Water Management, The Netherlands.

Garth Wells  
Delft, June 2001



## Contents

|  |           |
|--|-----------|
| <b>List of symbols</b>   | <b>ix</b> |
| <b>1 Introduction</b>  | <b>1</b>  |
| 1.1 Objectives . . . . .   | 1         |
| 1.2 Outline . . . . .  | 2         |
| 1.3 Computational modelling of strain localisation and failure . . . . .   | 3         |
| 1.4 Bifurcation, ill-posed equations and discontinuity analysis . . . . .  | 9         |
| <b>2 Kinematics of a displacement discontinuity</b>                        | <b>13</b> |
| 2.1 Displacement jump . . . . .  | 14        |
| 2.2 Local coordinate system at a discontinuity . . . . .                   | 15        |
| 2.3 Role of generalised functions . . . . .                                | 16        |
| <b>3 Discrete constitutive models</b>                                      | <b>17</b> |
| 3.1 Discrete damage-type model for quasi-brittle heterogeneous materials   | 18        |
| 3.2 Discrete plasticity model refined from the continuum case . . . . .    | 20        |
| <b>4 Embedded discontinuity element based on incompatible strain modes</b> | <b>29</b> |
| 4.1 Variational formulation . . . . .                                      | 30        |
| 4.2 Kinematic enhancement . . . . .  | 34        |
| 4.3 Element formulation . . . . .  | 36        |
| 4.4 Comparison of the EAS-based model and smeared crack formulations       | 44        |
| 4.5 Finite element implementation . . . . .                                | 46        |
| 4.6 Numerical examples . . . . .   | 48        |
| 4.7 Summary of embedded discontinuity formulation . . . . .                | 63        |
| <b>5 Cohesive zone model based on partitions of unity</b>                  | <b>65</b> |
| 5.1 Partition of unity concept . . . . .                                   | 66        |
| 5.2 Finite elements as partitions of unity . . . . .                       | 67        |
| 5.3 Enhancement of the standard basis with a discontinuous function . . .  | 68        |
| 5.4 Modelling propagating discontinuities and implementation aspects . .   | 73        |
| 5.5 Numerical examples . . . . .   | 77        |

|          |  |            |
|----------|--|------------|
| 5.6      | Summary of the partition of unity formulation and comparison with the incompatible modes formulation . . . . . | 88         |
| <b>6</b> | <b>Simulation of delamination in laminated composite materials</b>   | <b>91</b>  |
| 6.1      | Non-linear kinematics . . . . .  | 92         |
| 6.2      | Weak equilibrium equations and linearisation . . . . .   | 94         |
| 6.3      | Implementation aspects for laminated materials . . . . .   | 100        |
| 6.4      | Numerical examples of interface delamination . . . . .   | 102        |
| <b>7</b> | <b>Combined continuum–discontinuous model for crack propagation and strain localisation</b>                    | <b>109</b> |
| 7.1      | Continuum theories for cracked media and strain localisation . . . . .   | 110        |
| 7.2      | Perzyna viscoplastic model . . . . .   | 114        |
| 7.3      | Inclusion of discontinuities in a viscoplastic medium . . . . .  | 118        |
| 7.4      | Implementation aspects . . . . .   | 121        |
| 7.5      | Numerical examples . . . . .   | 123        |
| <b>8</b> | <b>Conclusions</b>   | <b>151</b> |
|          | <b>References</b>  | <b>155</b> |
|          | <b>Summary</b>   | <b>163</b> |
|          | <b>Samenvatting</b>  | <b>165</b> |
|          | <b>Stellingen</b>  | <b>167</b> |
|          | <b>Curriculum vitae</b>  | <b>171</b> |

## List of symbols

|                           |  |
|---------------------------|--|
| <b>a</b>                  | regular nodal degrees of freedom                 |
| $A_e$                     | area of a discontinuity plane within an element  |
| <b>b</b>                  | enhanced nodal degrees of freedom                |
| <b>B</b>                  | compatible strain interpolation matrix           |
| $B$                       | vector containing derivatives of shape functions |
| <b>C</b>                  | right Cauchy-Green tensor                        |
| $d$                       | rate of deformation tensor                       |
| <b>D</b>                  | continuum constitutive tangent matrix            |
| $D^e$                     | elastic constitutive tangent matrix              |
| $f$                       | yield function/loading function                  |
| $f_t$                     | tensile strength                                 |
| $E$                       | Young's modulus                                  |
| $\mathbf{f}^{\text{ext}}$ | external nodal force vector                      |
| $\mathbf{f}^{\text{int}}$ | internal nodal force vector                      |
| <b>F</b>                  | deformation gradient                             |
| $\hat{\mathbf{F}}$        | continuous deformation gradient                  |
| $\tilde{\mathbf{F}}$      | enhanced deformation gradient                    |
| $G_f$                     | fracture energy                                  |
| <b>G</b>                  | kinematic enhanced strain matrix                 |
| $\mathbf{G}^*$            | static enhanced strain matrix                    |
| $h$                       | continuum hardening modulus                      |
| $\bar{h}$                 | discrete hardening modulus                       |
| $h_{s,t}$                 | shear (sliding) stiffness                        |
| <b>K</b>                  | stiffness matrix                                 |
| $l_0$                     | initial discontinuity length                     |
| $l$                       | velocity gradient                                |
| <b>m</b>                  | displacement jump direction                      |
| <b>n</b>                  | normal vector to a discontinuity                 |
| $N_i$                     | shape function of node $i$                       |
| <b>N</b>                  | shape function matrix                            |
| <b>P</b>                  | nominal stress tensor                            |
| <b>Q</b>                  | acoustic tensor                                  |

x

LIST OF SYMBOLS

|                           |  |
|---------------------------|--|
| $r_\lambda$               | plastic multiplier residual                      |
| $\mathbf{r}_\sigma$       | stress residual                                  |
| $\mathbf{S}$              | deviatoric stress tensor                         |
| $t$                       | time   |
| $\mathbf{t}$              | unit vector, traction vector                     |
| $\bar{\mathbf{t}}$        | boundary traction                                |
| $\mathbf{T}$              | discrete constitutive tangent matrix             |
| $\mathbf{u}$              | displacement field                               |
| $\hat{\mathbf{u}}$        | regular displacement                             |
| $\tilde{\mathbf{u}}$      | displacement jump function                       |
| $[[\mu]]^{\text{eq}}$     | equivalent displacement jump measure             |
| $[[\mathbf{u}]]$          | discrete displacement jump                       |
| $\mathbf{x}$              | spatial coordinate vector                        |
| $\mathbf{X}$              | material coordinate vector                       |
| $V_e$                     | volume of an element                             |
| $\alpha$                  | internal element degrees of freedom              |
| $\gamma$                  | compatible strain variation, enhanced basis      |
| $\tilde{\gamma}$          | enhanced strain variation                        |
| $\Gamma_d$                | discontinuity surface                            |
| $\Gamma$                  | boundary surface                                 |
| $\delta_{\Gamma_d}$       | Dirac-delta distribution centred on $\Gamma_d$   |
| $\varepsilon$             | strain tensor/vector                             |
| $\bar{\varepsilon}$       | non-local strain tensor                          |
| $[[\varepsilon]]$         | strain jump                                      |
| $\zeta$                   | magnitude of a strain/displacement jump          |
| $\eta$                    | viscosity parameter                              |
| $\eta$                    | displacement variation                           |
| $\hat{\eta}$              | enhanced displacement variation                  |
| $\tilde{\eta}$            | discontinuous displacement variation             |
| $\kappa$                  | history parameter, inelastic deformation measure |
| $\lambda$                 | plastic multiplier, stretch, Lamé coefficient    |
| $\bar{\lambda}$           | bounded plastic multiplier                       |
| $\mu$                     | Lamé coefficient                                 |
| $\nu$                     | Poisson’s ratio                                  |
| $\mathbf{v}$              | displacement jump across a surface               |
| $\rho$                    | density  |
| $\bar{\sigma}$            | yield stress                                     |
| $\sigma$                  | stress tensor/vector                             |
| $\overset{\circ}{\sigma}$ | Truesdell rate of the Cauchy stress              |
| $\Sigma$                  | second Piola-Kirchhoff stress tensor             |
| $\tau^{\text{res}}$       | resolved stress                                  |

LIST OF SYMBOLS

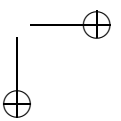
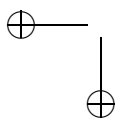
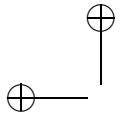
xi

|                           |   |
|---------------------------|---|
| $\tau$                    | stress variation  |
| $\langle \phi \rangle$    | overstress function   |
| $\Phi$                    | deformation map   |
| $\varphi_i$               | partition of unity function                                     |
| $\varphi_e$               | kinematic enhancement function                                  |
| $\omega$                  | damage  |
| $\Omega$                  | volume  |
| $c$                       | spatial constitutive tensor                                     |
| $\mathcal{C}$             | elastic constitutive tangent tensor/constitutive tangent tensor |
| $\mathcal{C}^{\text{ep}}$ | elasto-plastic constitutive tangent tensor                      |
| $\mathcal{H}$             | Heaviside function  |

**Vector and tensor operations**

(summation convention is applied over repeated indices)

|                                     |                                  |
|-------------------------------------|----------------------------------|
| $\mathbf{a}$                        | $a_i$                            |
| $\mathbf{A}$                        | $A_{ij}$                         |
| $\mathbf{A}^T$                      | $A_{ji}$                         |
| $\mathbf{A}^s$                      | $\frac{1}{2}(A_{ij} + A_{ji})$   |
| $\mathbf{a} \cdot \mathbf{b}$       | $a_i b_i$                        |
| $\mathbf{a} \otimes \mathbf{b}$     | $a_i b_j$                        |
| $(\mathbf{a} \otimes \mathbf{b})^s$ | $\frac{1}{2}(a_i b_j + a_j b_i)$ |
| $\mathbf{A}:\mathbf{B}$             | $A_{ij} B_{ij}$                  |
| $\ \mathbf{a}\ $                    | $(a_i a_i)^{\frac{1}{2}}$        |
| $\ \mathbf{A}\ $                    | $(A_{ij} A_{ij})^{\frac{1}{2}}$  |
| $\mathbf{A}\mathbf{b}$              | $A_{ij} b_j$                     |
| $\mathbf{b}\mathbf{A}$              | $A_{ij} b_i$                     |
| $\mathbf{A}\mathbf{B}$              | $A_{ik} B_{kj}$                  |
| $\mathcal{C}\mathbf{A}$             | $C_{ijkl} A_{kl}$                |
| $\mathbf{A}\mathcal{C}$             | $C_{ijkl} A_{ij}$                |
| $\mathcal{C}\mathbf{a}$             | $C_{ijkl} a_l$                   |
| $\mathbf{a}\mathcal{C}$             | $C_{ijkl} a_i$                   |
| $\text{tr}(\mathbf{A})$             | $A_{ii}$                         |
| $\nabla a$                          | $a_{,i}$                         |
| $\nabla \mathbf{a}$                 | $a_{i,j}$                        |
| $\nabla^s \mathbf{a}$               | $\frac{1}{2}(a_{i,j} + a_{j,i})$ |



## Chapter 1

### Introduction

The use of computers in modern engineering has allowed whole new classes of problems to be tackled. Problems of a scale and complexity never before considered can now be solved. However, the use of computers does not remove a dependence on sound underlying theories. Computational methods are built upon mathematical descriptions of a physical phenomenon. If the underlying mathematical description itself is not sound, the computational result can never be relied upon. The challenge in the development of modern computational techniques is twofold; the development of computational methods and the development of sound mathematical descriptions that are suitable for computer implementation.

The simulation of localised failure in solids is one example where the traditional theory has proved inadequate. The inclusion of strain softening (decreasing load carrying capacity with increasing strain at a material point) in a classical continuum material description leads to an underlying mathematical description which is meaningless. One method of improving the underlying material description is to allow discontinuities in the kinematic fields. This results in a sound underlying theory, although is difficult in implementation. The challenge of incorporating propagating kinematic discontinuities in a computational framework for inelastic solids forms the basis of this thesis.

#### 1.1 Objectives

The objective of this work is to develop numerical models that allow the inclusion of displacement discontinuities. The primary requirement is that the spatial orientation of the surface across which a displacement jump occurs be independent of the spatial discretisation. The spatial orientation of a discontinuity surface should be determined only by the mechanical state in a body. Within the finite element method in the absence of remeshing, this implies that displacement discontinuities must be able to propagate through solid finite elements. It is required of a numerical model that:

- the computed results are insensitive to the spatial discretisation;

- no remeshing is performed; and
- no artificial (non-physical) length scales be used in the constitutive model.

The requirement that computed results be independent of the spatial discretisation precludes the use of interface elements, since this limits potential discontinuities to inter-element boundaries which leads to results which are inherently dependent on the spatial discretisation.

One motivation for allowing displacement discontinuities is that analyses can be performed with relatively coarse finite element meshes compared to continuous models. By capturing a displacement jump, it is not necessary to capture the very high strain gradients which arise in continuous descriptions. It is of course necessary that the discretisation be fine enough to capture accurately the continuum response. The incorporation of displacement jumps is intuitively appealing for fracture problems. However, the same methods can be applied to model strain localisation. Through the ‘cohesive zone’ concept, fracture and strain localisation can be modelled within the same framework. It is the aim of this work to use the inclusion of displacement discontinuities to simulate both fracture and strain localisation.

## 1.2 Outline

The rest of this chapter reviews different numerical approaches for simulating localised failure and examines the relationship between stability at a material point and the development of kinematic discontinuities. The kinematics of a body crossed by a displacement jump are elaborated in chapter 2. The kinematic relationships developed in chapter 2 form a common thread throughout this work. The kinematic relations are presented in a form that is useful for later manipulations. Through the use of generalised functions, even in the presence of a displacement jump, the concept of deformation gradients is maintained. This allows a body crossed by a displacement discontinuity to be considered as a single body, rather than as two.

In chapter 3, discrete constitutive models are developed for different applications. The term ‘discrete’ constitutive models is used to describe constitutive models which relate traction forces acting at a surface and the displacement jump across the surface. One class of models is derived from phenomenological considerations of fracture as a discrete process. A second class is derived as the limiting case of the classical strain softening continuum when all inelastic deformation localises at a surface. The first model developed in chapter 3 is intended for mode-I (tensile) failure and the second for mode-II (shear) dominated failure.

The first method for incorporating displacement discontinuities in finite elements is introduced in chapter 4. The method is based on incompatible strain modes, making it simple to implement in existing finite element codes. The formulation of the model is critically evaluated and its performance is illustrated with three-dimensional examples. A second method for incorporating displacement disconti-

COMPUTATIONAL MODELLING OF STRAIN LOCALISATION AND FAILURE 3

nities is developed in chapter 5. In contrast to the first model, the model in chapter 5 is theoretically sounder, more general and flexible, although is more complex in implementation than the model in chapter 4. Calculations are performed for two-dimensional problems under quasi-static and impact loading. The method developed in chapter 5 is applied in chapter 6 to laminated composite materials. This involves the extension to non-linear kinematics and to materials with a regular structure. The failure of laminated composite materials is simulated by representing the separation of individual layers of a material (delamination) as displacement discontinuities, with the structure of a finite element mesh and of the laminate decoupled. It is shown that the concepts used for modelling unstructured materials can be applied to structured materials, and offer substantial advantages over conventional methods.

In chapter 7, a departure is made from discrete constitutive models. A regularised continuum model (viscoplastic) with strain softening is used to simulate microcracking and plastic flow in a continuum. When the material strength in the continuum is exhausted, a displacement discontinuity is inserted. In the case of tensile failure, a discontinuity represents a macroscopic crack, across which no forces can be transmitted. For compressive failure, a discontinuity represents a plane on which sliding occurs.

### 1.3 Computational modelling of strain localisation and failure

Modelling techniques for the simulation of strain localisation and fracture have traditionally fallen into two distinct categories: continuous and discontinuous. Continuous methods simulate failure assuming a smooth, continuous displacement field throughout a body. Since the displacement field is differentiable, a strain field can also be defined uniquely everywhere in a body. Based on these assumptions, a body can be considered as a continuous medium and continuum theory can be applied. In contrast to continuous methods, discontinuous methods allow for the development of jumps in the displacement field of a body. In physical terms, this translates to the development of failure surfaces within a body. The distinction between continuous and discontinuous methods is not sharp. A case which falls between continuous and discontinuous methods, as defined above, is when the displacement field is continuous, but not differentiable at all positions within the body. This represents a case where displacements are continuous but a jump occurs in the strain field. This type of discontinuity is usually termed a ‘weak discontinuity’.

For some materials, the choice between discontinuous or continuous models is obvious. For very brittle materials, like glass, discrete cracks (displacement jumps) develop at almost the instant the yield strength of the material is reached. In contrast, highly ductile materials exhibit displacement jumps only at the last stages of failure, well past the peak load and just prior to catastrophic collapse. A difficulty arises when considering quasi-brittle materials. The description ‘quasi-brittle’ covers a huge range of traditional and modern engineering materials. Concrete, ma-

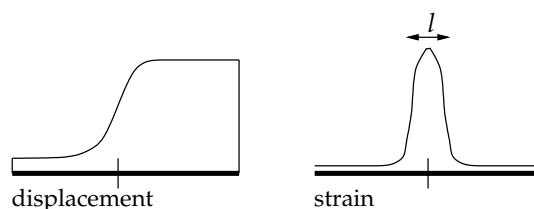


Figure 1.1: Smeared representation of a discontinuity or localised zone. The length scale  $l$  is a measure of the zone in which strains localise.

sonry, rocks, laminates, polymers, some ceramics and some metals can be considered quasi-brittle materials. Also, under particular atmospheric conditions many others materials, which are normally regarded as brittle or ductile, can be considered quasi-brittle. In the failure of quasi-brittle materials, two stages of the failure process can be identified. Close to the peak load, inelastic strains begin to localise in thin bands. At this stage continuum models possess considerable merit as the development of microcracks (damage) or plastic flow can be represented as a degradation of the continuum (strain softening). At some intermediate stage of loading between initial yielding and catastrophic failure, displacement jumps develop across surfaces. At this stage discontinuous formulations are more appropriate.

### 1.3.1 Continuum failure models

Continuum models for failure analysis are generally based on *strain softening*. That is, with accumulated inelastic strain the load carrying capacity of a material decreases. Effectively, the underlying processes driving softening at the level of the material structure are represented in an averaged, smeared sense. The kinematic fields are considered continuous, as illustrated in figure 1.1 for one dimension. The first continuum models applied to failure analysis were based on classical continuum theory. That is, the stress state at a point is a function of the strain state and material history (accumulated plastic strain, damage, dislocation density, etc) at the point. Different models have used the concepts of continuum damage mechanics (Mazars and Pijaudier-Cabot, 1989), fixed, multiple and rotating cracks (Bažant and Oh, 1983; Rots, 1988) (which are effectively anisotropic damage models) and plasticity (Feenstra and De Borst, 1995). Classical continuum models which incorporate strain softening however can become ill-posed. The governing equations of classical continuum theory predict that, upon softening, strains will localise into a band of zero width. The physical implication of this is that complete loss of integrity will occur with zero energy dissipation. The practical implication when using finite elements is that the response is inherently dependent on the spatial discretisation. The energy dissipated in failure is a function of element size and the failure mode is dependent on the structure of the mesh. The seriousness of the ill-posed nature of the classical

COMPUTATIONAL MODELLING OF STRAIN LOCALISATION AND FAILURE 5

continuum governing equations in the presence of strain softening is partly hidden when using the finite element method. The conventional finite element method involves discontinuities in the strain field at element boundaries. It will be shown later in this chapter that when the governing equations become ill-posed, the criterion for the development of a strain discontinuity is simultaneously met. Discontinuities in the strain field at the boundaries of elements allow strains to localise in finite volumes (although the volumes are dependent on the spatial discretisation). When applying classical strain softening models with a numerical method that uses interpolating functions with a high degree of continuity, it is not possible to reach sensible results (Jirásek, 1998a).

To maintain well-posed governing equations in the presence of strain softening, non-classical continuum models have been used. Non-classical models differ from classical models in that the stress at a point is not a function only of the local strain state and local history parameters. Models which include non-local terms can lead to well-posed governing equations in the presence of softening (Pijaudier-Cabot and Bazant, 1987). Also, models which include gradients of internal variables can lead to well-posed problems (De Borst and Mühlhaus, 1992; Peerlings et al., 1998), as can models which include strain rate dependency (Needleman, 1988; Sluys and De Borst, 1992). The preceding non-classical models can be considered enhancements of the classical continuum in that they maintain the continuum concepts of continuous displacements and strains and are based on the same kinematic considerations. It is also possible to consider a polar continuum where rotational degrees of freedom are added to the usual translational degrees of freedom. It has been shown for Cosserat continuum theory (a polar continuum) that the governing equations remain well posed for mode-II loading (De Borst and Sluys, 1991).

A common feature of all the non-classical continuum models outlined is that at least one additional material parameter, absent in the classical theory, is required. All these models possess a length scale, which is either explicitly (as for non-local, gradient and polar models) or implicitly (as for rate-dependent models, where under quasi-static loading the length scale is implied through the viscosity in combination with the strain rate) included. Upon strain localisation, the length scale controls the width of the zone in which strains localise. Setting the length scale to zero, classical continuum theory is recovered. By specifying the width of the failure zone, the spurious case of complete failure with zero energy dissipation is avoided as the localisation zone is of non-zero volume.

### 1.3.2 *Discontinuous failure models*

Discontinuous failure models (models involving kinematic discontinuities) originate from two different considerations. The first is the physical observation of discrete cracks. The clear displacement jumps that occur across surfaces provide a motivation for allowing displacement discontinuities. From a physical stand point, the most

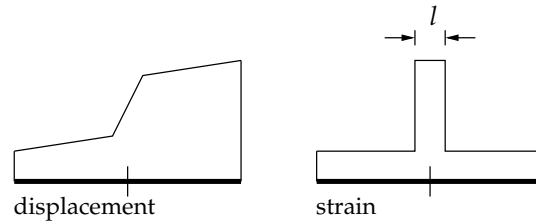


Figure 1.2: One dimensional representation of the displacement and strain fields for a weak discontinuity. The length scale  $l$  specifies the width across which the strain jump occurs.

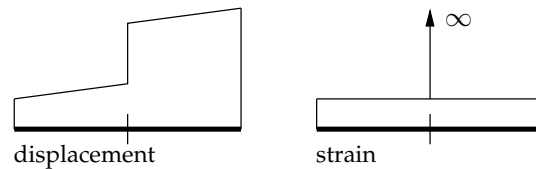


Figure 1.3: One dimensional representation of the displacement and strain fields for a strong discontinuity. The strain at the discontinuity is unbounded.

simple discontinuous models are based on linear-elastic fracture mechanics (LEFM) which considers traction-free cracks in elastic bodies. A second motivation for discontinuous models is the observation of continuous fields which exhibit steep gradients across a small region. This type of problem is commonly seen in metals and granular materials where slip lines develop. While the displacement field is actually continuous, depending on the level of observation, it can be considered to exhibit a weak discontinuity (discontinuity in the strain field) or a strong discontinuity (discontinuity in the displacement field). A weak and a strong discontinuity, in one dimension, are shown in figures 1.2 and 1.3, respectively.

For quasi-brittle materials, LEFM is unable to incorporate the considerable inelastic deformations that occur ahead of a crack tip. In heterogeneous materials, crack faces are not smooth surfaces, but tortuous. Also, significant ‘crack bridging’ can occur in some materials. Figure 1.4 shows a crack bridged by ‘fibres’, as is common in polymers and fibre-reinforced materials and a tortuous crack, as is common in quasi-brittle heterogeneous materials. To model inelastic deformation ahead of a crack tip, Dugdale (1960) and Barenblatt (1962) proposed that inelastic deformations ahead of a crack be modelled as cohesive forces acting on a fictional extension of the crack. This concept is illustrated in figure 1.5. Moving along the fictional crack towards the actual crack tip, the traction forces on the crack faces reduce to zero. An attractive feature of this cohesive crack concept is that it removes the stress singularity at a crack tip that is predicted by LEFM. Also, the cohesive crack concept is attractive for simulating crack bridging and can incorporate the effects of a tortuous crack. For modelling quasi-brittle fracture in concrete, the cohesive crack concept was used by

COMPUTATIONAL MODELLING OF STRAIN LOCALISATION AND FAILURE

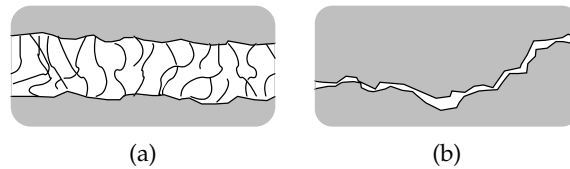


Figure 1.4: Schematic representation of (a) crack bridging and (b) tortuous crack with shear interlock.

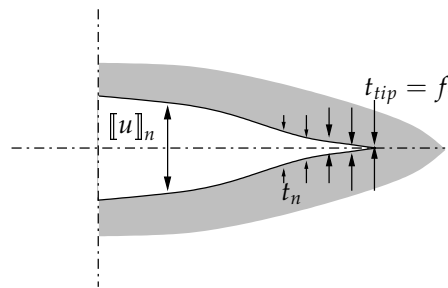


Figure 1.5: Fictitious crack model for mode-I opening.

Hillerborg et al. (1976). The normal traction–separation response was controlled by the tensile strength of the material and the fracture energy, which was considered an additional material parameter. The effects of plastic flow, micro-crack evolution and a tortuous crack path are all compressed onto a surface. The tractions acting on the fictitious crack faces are determined by the relative separation of the surfaces. As a crack opens, the tractions acting on it approach zero. The fracture energy is the energy dissipated in developing a unit area of traction-free crack. The cohesive crack concept is equally applicable to problems such as slip lines, hence the more appropriate term ‘cohesive zone’ which will be used.

The greatest challenge in using discontinuous failure models is incorporating displacement discontinuities in numerical models. Until recently, two techniques were used for incorporating displacement discontinuities within the finite element method. For elastic crack growth, adaptive remeshing schemes have been used (Swenson and Ingraffea, 1988). Crack propagation is modelled by adapting the finite element mesh to explicitly model a discontinuity. However, adaptive remeshing can be computationally expensive and difficult to implement. The second approach is the use of interface elements. By placing elements of zero width between solid finite elements, displacements jumps can be modelled. This approach is simple to implement, although it has two main disadvantages. The first is that a discontinuity path is dependent on the mesh structure. A discontinuity propagating through a structured mesh is shown schematically in figure 1.6. This is not a serious problem for structured materials, such as masonry and laminated composites, where the in-

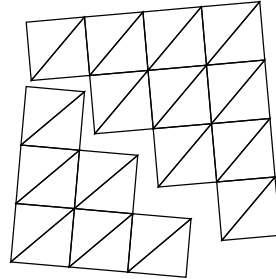


Figure 1.6: Discrete crack modelling with finite elements and interface elements. Discrete separation can occur only at element boundaries.

interface elements represent real interfaces between different materials, at which cracks are expected to propagate. For unstructured materials, the response using interface elements is always mesh dependent. Theoretically, upon infinite mesh refinement an infinite number of discontinuity paths are possible, making the method mesh independent. However, in practical implementation, the influence of the mesh structure cannot be overcome (Tijssens et al., 2000). Another serious difficulty with interface elements is that they require a ‘dummy’ elastic stiffness. To model a perfect bond, the interfaces should have an infinite elastic stiffness. In implementation, an elastic interface stiffness must be chosen that approximates the real (infinite) stiffness while maintaining a well conditioned global stiffness matrix that can be solved accurately. Use of a too low dummy stiffness results in an overly flexible response and an incorrect distribution of stresses while a high dummy stiffness can result in severe stress oscillations and a poorly conditioned system of equations. The interface stiffness must be carefully chosen and special numerical integration schemes used to achieve optimal results (Rots, 1988; Schellekens and De Borst, 1993).

Recent developments in so-called ‘meshless methods’ (Belytschko et al., 1994; Duarte and Oden, 1996) have led to advancements in the modelling of discontinuities. Removing the restrictions imposed by a mesh structure, the modelling of arbitrarily propagating discontinuities becomes much simpler. Displacement jumps can be included by cutting the domain of a body or by adding discontinuous functions to the basis functions approximating the displacement field (Belytschko et al., 1994; Fleming et al., 1997). Unfortunately, at this time meshless methods lack the robustness and computational efficiency of the finite element method. Nevertheless, developments stemming from research into meshless methods have led to a better understanding of finite elements. Some of these developments will be exploited in chapter 5 using finite elements.

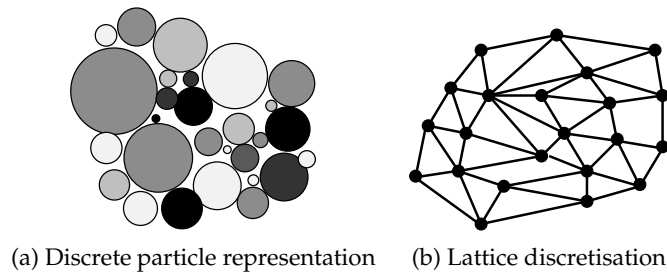


Figure 1.7: Discretised representation of a solid material.

### 1.3.3 Discrete element methods

Somewhat separate from continuum and discontinuous failure models are discrete element models. In both continuum and discontinuous failure models, the bulk of the material is modelled as a continuum with the concepts of stress and strain applied. Discrete element models abandon the concept of stress and strain and are formulated in terms of discrete elements with the interaction between elements defined. Discrete particle models have proved popular for the analysis of granular materials and for granular flow where particles are representative of the actual material. Through defining simple relationships for how individual particles interact, highly complex phenomena can be modelled. The difficulty is that problems of practical interest are usually of a scale where many millions of discrete elements are required to represent the real material structure. For other materials, lattice-type models have been used. Lattices are formed from a collection of connected truss or beam elements. Unlike discrete particle methods which directly represent the material structures, lattice models are in general a discretisation of a continuum. A collection of discrete particles and a lattice-type model are shown in figure 1.7.

## 1.4 Bifurcation, ill-posed equations and discontinuity analysis

The development of kinematic discontinuities is closely related to bifurcation analysis and whether or not the governing differential equations are well-posed. For an incremental constitutive model (rate-independent), the stress and strain rates are related through a constitutive tensor  $\mathcal{C}$ :

$$\dot{\boldsymbol{\sigma}} = \mathcal{C} \dot{\boldsymbol{\varepsilon}} \quad (1.1)$$

where the fourth-order tensor  $\mathcal{C}$  possesses the symmetries:

$$C_{ijkl} = C_{jikl} = C_{ijlk}. \quad (1.2)$$

Motivated by physical observations of strain localisation, it can be assumed that strain jumps occur across surfaces, while the displacement field remains continuous,

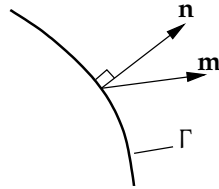


Figure 1.8: Definition of unit vectors  $\mathbf{n}$  and  $\mathbf{m}$  at a surface  $\Gamma$  across which a weak discontinuity develops.

which is a weak discontinuity. Using Maxwell’s kinematic compatibility condition, the strain jump across a surface can be written as:

$$[[\boldsymbol{\varepsilon}]] = \zeta (\mathbf{m} \otimes \mathbf{n})^s \quad (1.3)$$

where  $\zeta$  is the magnitude of the strain jump,  $\mathbf{m}$  is a unit vector describing the direction of the jump and  $\mathbf{n}$  is the unit normal to the discontinuity plane (see figure 1.8). If the vectors  $\mathbf{m}$  and  $\mathbf{n}$  are aligned, the mode of deformation is pure mode-I separation, and if  $\mathbf{m}$  and  $\mathbf{n}$  are perpendicular, the deformation is pure mode-II sliding. Considering a linear comparison solid and substituting the strain jump into equation (1.1), the stress rate jump can be expressed in terms of the strain rate jump as:

$$[[\dot{\boldsymbol{\sigma}}]] = \mathcal{C} [[\dot{\boldsymbol{\varepsilon}}]] \quad (1.4)$$

To satisfy equilibrium, the traction rate jump across a surface must be zero.

$$[[\dot{\mathbf{t}}]] = [[\dot{\boldsymbol{\sigma}}]] \mathbf{n} = \mathbf{0} \quad (1.5)$$

Substituting equation (1.4) into equation (1.5),

$$\mathbf{n} \mathcal{C} [[\dot{\boldsymbol{\varepsilon}}]] = \mathbf{0}. \quad (1.6)$$

Substituting the strain jump from equation (1.3) into the above, and using the symmetry properties of  $\mathcal{C}$ , leads to:

$$(\mathbf{n} \mathcal{C} \mathbf{n}) \mathbf{m} = \mathbf{0} \quad (1.7)$$

for a non-trivial solution ( $\zeta \neq 0$ ). The expression within the brackets in equation (1.7) is known as the *acoustic tensor*,  $\mathbf{Q}$ . Equation (1.7) implies that the acoustic tensor is singular. Therefore the localisation condition is often written as:

$$\det(\mathbf{n} \mathcal{C} \mathbf{n}) = 0 \quad (1.8)$$

which is the classical form of the bifurcation condition. At this point the strain field in a body can change suddenly from a homogeneous state to a localised state, characterised by a strain discontinuity. This condition also coincides with violation of

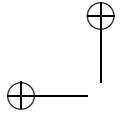
the ellipticity condition for the constitutive operator  $\mathcal{C}$  (Marsden and Hughes, 1983), which in turn translates to a loss of ellipticity of the governing differential equations for static problems and loss of hyperbolicity for dynamic problems. Therefore, it can be considered that the loss of ellipticity for quasi-static problems, or the loss of hyperbolicity for dynamic problems, implies the development of a discontinuity in the strain field. The localisation condition is also intimately related to material stability (Rice, 1976). For an associative elasto-plastic model, the condition  $\det(\mathbf{Q}) < 0$  can be met if and only if strain softening is included.

#### 1.4.1 Wave propagation in a strain softening medium

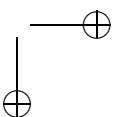
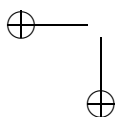
More insight can be gained into material stability and kinematic discontinuities by considering wave propagation in a solid. Strain localisation can be considered as the transformation of a propagating wave into a stationary wave. It was shown by Hill (1962) that the loss of ellipticity condition (at constitutive level, not the governing equations for a symmetric constitutive operator) coincides with a vanishing wave speed for an incremental, rate-independent constitutive model. Further, Bažant and Belytschko (1985) considered the exact solution for a wave propagating in a one-dimensional bar. It was shown that upon strain softening, the Dirac-delta distribution develops in the strain field. If the classical constitutive relationships are maintained (stress–strain relationship), this leads to the physically impossible situation of complete failure with zero energy dissipation since the Dirac-delta distribution occupies zero volume. However, maintaining the continuum constitutive model ignores the physical significance of the Dirac-delta distribution, as it implies the development of a displacement discontinuity (as will be shown in chapter 2) and demands that the nature of the constitutive model at the location of the distribution be changed from a continuum relationship to a discrete traction–separation relationship.

#### 1.4.2 Simulating weak and strong discontinuities

Computationally, attempts have been made to capture weak discontinuities within finite elements (Belytschko et al., 1988; Ortiz et al., 1987; Sluys and Berends, 1998). Similar to enhanced continuum models, weak discontinuity models require a material length scale that specifies the width across which the strain jump takes place. This width cannot be inferred from the classical material properties (Young's modulus, Poisson's ratio, etc.). A strong discontinuity can be considered a special case of a weak discontinuity with the material length scale set to zero. This translates physically to a displacement jump across a surface. A jump in the displacement field leads to an unbounded strain field at the surface across which the jump occurs, as shown in figure 1.3. Several attempts have been made to include displacement jumps within finite elements (Armero and Garikipati, 1996; Dvorkin et al., 1990; Klisinski et al., 1991; Larsson and Runesson, 1996; Lotfi and Shing, 1995; Oliver, 1996b; Simo et al., 1993;



Wells and Sluys, 2001c,f). Unlike weak discontinuities in which continuum constitutive models are still applied, the fundamental nature of the constitutive relationship at a jump can be changed for strong discontinuities. The concepts of stress and strain are no longer applicable, with the response at a discontinuity described by a traction vector and a displacement jump vector.



## Chapter 2

### Kinematics of a displacement discontinuity

To develop numerical methods for solving problems that include displacement discontinuities and to form discrete constitutive models, it is necessary to develop the kinematic relationships that describe a displacement jump across a surface in a three-dimensional body. Mathematically, a displacement jump is described here by a function, with a unit jump at a discontinuity, operating on a smooth, continuous function. It is useful to maintain the idea of a strain field that is defined everywhere in a body that is crossed by a discontinuity, including at the surface across which the jump occurs. This can be done using generalised functions (distributions) and avoids the need to consider a body crossed by a discontinuity as two separate entities, linked by traction forces.

A body  $\Omega$  crossed by a single material discontinuity is shown in figure 2.1. The discontinuity  $\Gamma_d$  divides the body into two sub-domains,  $\Omega^+$  and  $\Omega^-$ , which lie on either side of the discontinuity. The unit normal to the discontinuity,  $\mathbf{n}$ , points to  $\Omega^+$ . The external boundary of the body is denoted  $\Gamma$ . In all chapters, except chapter 6, strains are assumed to be infinitely small so all gradients of displacements relate to the symmetric part only. The necessary extensions for non-linear kinematics are

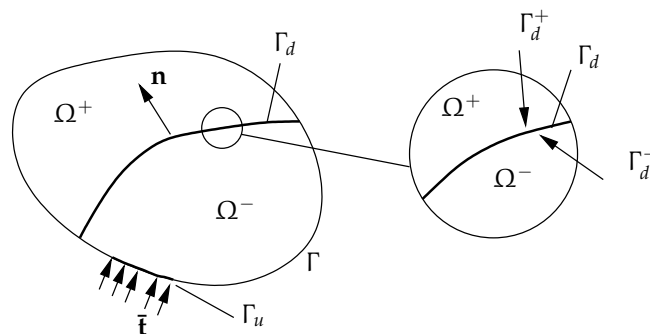


Figure 2.1: Body  $\Omega$  crossed by a displacement discontinuity  $\Gamma_d$ .

developed in chapter 6.

## 2.1 Displacement jump

The displacement field  $\mathbf{u}$  for the body shown in figure 2.1 can be decomposed into a continuous and discontinuous part,

$$\mathbf{u}(\mathbf{x}, t) = \hat{\mathbf{u}}(\mathbf{x}, t) + \mathcal{H}_{\Gamma_d}(\mathbf{x}) \tilde{\mathbf{u}}(\mathbf{x}, t) \quad (2.1)$$

where  $\hat{\mathbf{u}}$  and  $\tilde{\mathbf{u}}$  are smooth, continuous functions on  $\Omega$  and  $\mathcal{H}_{\Gamma_d}$  is the Heaviside function centred at the discontinuity. The Heaviside function is defined as:

$$\mathcal{H}_{\Gamma_d} = \begin{cases} 1 & \mathbf{x} \in \Omega^+ \\ 0 & \mathbf{x} \in \Omega^- \end{cases} \quad (2.2)$$

The displacement jump is provided by the Heaviside jump acting on the continuous function  $\tilde{\mathbf{u}}$ . The magnitude of the displacement jump at a discontinuity  $[[\mathbf{u}]]$  is given by the function  $\tilde{\mathbf{u}}$  at the discontinuity:

$$[[\mathbf{u}(\mathbf{x}, t)]] = \tilde{\mathbf{u}}(\mathbf{x}, t) \quad \mathbf{x} \in \Gamma_d. \quad (2.3)$$

Assuming that the Heaviside function is stationary (that is,  $d\mathcal{H}_{\Gamma_d}/dt = 0$ , which implies that a discontinuity does not translate), the acceleration field is found by differentiating the displacement field in equation (2.1) twice with respect to time.

$$\ddot{\mathbf{u}}(\mathbf{x}, t) = \ddot{\hat{\mathbf{u}}}(\mathbf{x}, t) + \mathcal{H}_{\Gamma_d}(\mathbf{x}) \ddot{\tilde{\mathbf{u}}}(\mathbf{x}, t) \quad (2.4)$$

The strain field for a body crossed by a discontinuity can be found by taking the symmetric gradient of equation (2.1),

$$\nabla^s \mathbf{u} = \boldsymbol{\varepsilon} = \nabla^s \hat{\mathbf{u}} + \mathcal{H}_{\Gamma_d}(\nabla^s \tilde{\mathbf{u}}) + \delta_{\Gamma_d}(\tilde{\mathbf{u}} \otimes \mathbf{n})^s \quad (2.5)$$

where  $\delta_{\Gamma_d}$  is the Dirac-delta distribution centred at the discontinuity. Assuming again that the Heaviside function is stationary, the strain rate field is found by differentiating equation (2.5) with respect to time.

$$\dot{\boldsymbol{\varepsilon}} = \nabla^s \dot{\hat{\mathbf{u}}} + \mathcal{H}_{\Gamma_d}(\nabla^s \dot{\tilde{\mathbf{u}}}) + \delta_{\Gamma_d}(\dot{\tilde{\mathbf{u}}} \otimes \mathbf{n})^s \quad (2.6)$$

The preceding manipulations can be easily extended to the case of multiple, non-intersecting discontinuities. For multiple non-intersecting discontinuities, the displacement field can be expressed as:

$$\mathbf{u}(\mathbf{x}, t) = \hat{\mathbf{u}}(\mathbf{x}, t) + \sum_{i=1}^n \mathcal{H}_{\Gamma_{d,i}} \mathbf{x} \tilde{\mathbf{u}}_i(\mathbf{x}, t) \quad (2.7)$$

where  $n$  is the number of discontinuities and  $\mathcal{H}_{\Gamma_{d,i}}$  and  $\tilde{\mathbf{u}}_i$  correspond to the  $i$ th discontinuity. The displacement decomposition is more complicated for intersecting discontinuities as functions are required that describe the individual discontinuities and the interaction between discontinuities. However, intersecting discontinuities will not be considered.

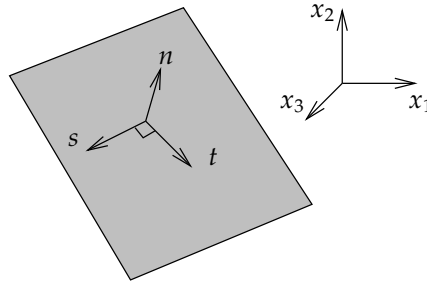


Figure 2.2: Local orthonormal coordinate system at a discontinuity surface. The  $n$  direction is normal to the plane.

## 2.2 Local coordinate system at a discontinuity

In order to examine the kinematics at a discontinuity, it is useful to define a local coordinate system relative to a discontinuity plane. An orthonormal coordinate system  $(n, s, t)$  is defined where the  $n$  component is in the direction of the normal vector to the discontinuity. The local  $(n, s, t)$  system is shown in the global space in figure 2.2. The local coordinate system will be used for the development of discrete constitutive models. Consider the second order symmetric tensor  $\mathbf{A}$  defined by:

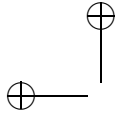
$$\mathbf{A} = ([\mathbf{u}] \otimes \mathbf{n})^s = \frac{1}{2} ([\mathbf{u}] \otimes \mathbf{n} + \mathbf{n} \otimes [\mathbf{u}]). \quad (2.8)$$

For unit vectors  $\mathbf{n}$ ,  $\mathbf{s}$  and  $\mathbf{t}$  in the  $n$ ,  $s$  and  $t$  directions, respectively, it can be shown that:

$$\begin{aligned} A_{nn} &= \mathbf{n} \cdot ([\mathbf{u}] \otimes \mathbf{n})^s \mathbf{n} = [\mathbf{u}] \cdot \mathbf{n} = [u]_n \\ A_{sn} &= \mathbf{s} \cdot ([\mathbf{u}] \otimes \mathbf{n})^s \mathbf{n} = \frac{1}{2} [\mathbf{u}] \cdot \mathbf{s} = \frac{1}{2} [u]_s \\ A_{tn} &= \mathbf{t} \cdot ([\mathbf{u}] \otimes \mathbf{n})^s \mathbf{n} = \frac{1}{2} [\mathbf{u}] \cdot \mathbf{t} = \frac{1}{2} [u]_t \\ A_{ss} &= \mathbf{s} \cdot ([\mathbf{u}] \otimes \mathbf{n})^s \mathbf{s} = 0 \\ A_{ts} &= \mathbf{t} \cdot ([\mathbf{u}] \otimes \mathbf{n})^s \mathbf{s} = 0 \\ A_{tt} &= \mathbf{t} \cdot ([\mathbf{u}] \otimes \mathbf{n})^s \mathbf{t} = 0. \end{aligned} \quad (2.9)$$

In the  $(n, s, t)$  coordinate system, the only non-zero components of the tensor  $\mathbf{A}$  are those which act on the plane of the discontinuity. From the relations in equation (2.9), the tensor  $\mathbf{A}$  in the local  $(n, s, t)$  coordinate system can be written in terms of the components of the displacement jump in the local coordinate system at the discontinuity as:

$$([\mathbf{u}] \otimes \mathbf{n})^s = \begin{bmatrix} [u]_n & \frac{1}{2} [u]_s & \frac{1}{2} [u]_t \\ \frac{1}{2} [u]_s & 0 & 0 \\ \frac{1}{2} [u]_t & 0 & 0 \end{bmatrix}. \quad (2.10)$$



### 2.3 Role of generalised functions

The use of generalised functions provides a mathematical link between discontinuous and continuous analysis. Generalised functions can lack physical meaning, but they provide tools to perform mathematically sound manipulations simply in cases where the traditional theory of smooth functions requires difficult or long derivations. As an example, using Dirac-delta distributions in the strain field for a body crossed by a discontinuity and considering the virtual work principle, the body will be treated as a single body where more traditional theory requires that the body be split into two separate bodies.

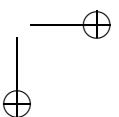
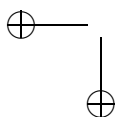
In section 2.1, the Dirac-delta distribution  $\delta$  was introduced as the derivative of the Heaviside function. For later derivations, it is useful to recall some properties of the Dirac-delta distribution in the three-dimensional space. The Dirac-delta distribution possesses an important property when operating on regular functions. In one-dimension,

$$\int_{-\infty}^{\infty} \delta_a(x) \phi(x) dx = \phi(a) \quad (2.11)$$

where  $\delta_a$  is centred at  $x = a$  and  $\phi$  is a continuous function. Equation (2.11) extends to the three-dimensional space,

$$\int_{\Omega} \delta_{\Gamma_a}(\mathbf{x}) \phi(\mathbf{x}) d\Omega = \int_{\Gamma_a} \phi(\mathbf{a}) d\Gamma. \quad (2.12)$$

In equation (2.12), the vector  $\mathbf{a}$  relates to all points on the surface  $\Gamma_a$ .



## Chapter 3

### Discrete constitutive models

Discrete constitutive models, formulated in terms of displacements and tractions at a surface, possess several attractive features for failure analysis. Discrete models do not suffer from the shortcoming of classical continuum models when applied to softening materials. Unlike continuum models, discrete models are formulated in terms of tractions and displacements, which makes them applicable at a surface. The work done at a surface is integrated over the surface, which leads to a non-zero energy dissipation because the surface has a non-zero area. The work done for a continuum model is integrated over a volume, which in the case of a localised surface has a zero volume and hence no energy is dissipated in failure.

Apart from leading to physically meaningful results in the presence of softening, discrete models have several other propitious features. It is relatively simple to develop, linearise and implement discrete constitutive models as tractions and displacements are related through a constitutive operator which is a second-order tensor, rather than a fourth-order tensor which relates stresses and strains in classical continuum theory. Moreover, the individual displacement components have a clear physical meaning; all motions at an interface can be described with one component for the normal separation and two components for sliding motions. An important feature of discrete constitutive models, particularly for the analysis of cracked media, is that anisotropy is naturally introduced. No special considerations are required to reproduce the anisotropy which develops as a natural result of inelastic deformations such as cracking. It will be shown that even isotropic continuum models give an anisotropic response when refined to the special case of a strong discontinuity.

The two models developed in this chapter are those which will be used later for numerical examples. Discontinuities are introduced to the continuum only at the onset of inelastic deformation, so there is no elastic part in the discrete constitutive models. The elastic response prior to and after any inelastic deformation is represented by the continuum. The advantage of this approach is that there is no need to use an artificial elastic interface stiffness (for loading) as is required when using conventional interface elements, thus avoiding the numerical difficulties associated with traditional

interface elements. Two distinct types of models are developed. The first is a damage-type model and is well-suited for the analysis of quasi-brittle materials under tensile loading. The second model is refined from classical rate-independent continuum plasticity. Importantly, all models developed here are displacement driven. That is, the tractions can be calculated explicitly using displacements and history parameters, which is important for efficient and simple implementation in a displacement-based finite element formulation.

### 3.1 Discrete damage-type model for quasi-brittle heterogeneous materials

For modelling materials where mode-I type failure is dominant, a cohesive crack type model is used. Micro-cracking and plastic flow around a macroscopic crack tip are modelled as an equivalent traction force on crack faces. For the model used here, the inelastic response is governed by two key material parameters: the tensile strength  $f_t$  and the fracture energy  $G_f$ . A discontinuity is introduced when the maximum principal stress exceeds the tensile strength of the material. The normal vector to a discontinuity is aligned in the direction of the maximum principal stress. This mode-I criterion is commonly used for quasi-brittle materials. Once a discontinuity is introduced, the tractions transferred at a discontinuity are dependent on the displacement jump across the discontinuity surface. The discrete constitutive model is developed in the local  $(n, s, t)$  coordinate system which was introduced in chapter 2.

Development of a discrete damage-type model requires first the definition of a loading function which describes the loading state at a discontinuity surface (loading or unloading/re-loading). The loading function  $f$  is defined as:

$$f(\llbracket u \rrbracket^{\text{eq}}, \kappa) = \llbracket u \rrbracket^{\text{eq}} - \kappa \quad (3.1)$$

where  $\llbracket u \rrbracket^{\text{eq}}$  is a scalar measure of the displacement jump at a discontinuity and  $\kappa$  is a history parameter, equal to the highest value of  $\llbracket u \rrbracket^{\text{eq}}$  reached. If the loading function is equal to zero, loading is taking place at a discontinuity and if the loading function is less than zero, reloading or unloading is taking place. The equivalent displacement used is equal to:

$$\llbracket u \rrbracket^{\text{eq}} = \llbracket u \rrbracket_n \quad (3.2)$$

where  $\llbracket u \rrbracket_n$  is the normal displacement jump. Therefore, softening behaviour at an interface is driven only by the normal opening. The inclusion of sliding displacements ( $\llbracket u \rrbracket_s, \llbracket u \rrbracket_t$ ) in the equivalent displacement definition has only a minor effect on the response for mode-I dominated problems (Tijssens et al., 2000). The normal tractions  $t_n$  to a discontinuity are made an exponential function of the history parameter, the tensile strength  $f_t$  and the fracture energy  $G_f$ .

$$t_n = f_t \exp\left(-\frac{f_t}{G_f} \kappa\right) \quad (3.3)$$

DISCRETE DAMAGE-TYPE MODEL FOR QUASI-BRITTLE  
HETEROGENEOUS MATERIALS

19

Note that the integral of equation (3.3) approaches  $G_f$  as the history variable  $\kappa$  approaches infinity.

$$\int_{\kappa=0}^{\infty} f_t \exp\left(-\frac{f_t}{G_f}\kappa\right) d\kappa = G_f \quad (3.4)$$

The discontinuity shear (sliding) stiffness in the  $s$  and  $t$  directions is given as an exponential function of the history parameter  $\kappa$ ,

$$\begin{aligned} t_s &= (d_{\text{int}} \exp(h_s \kappa)) \llbracket u \rrbracket_s \\ t_t &= \underbrace{(d_{\text{int}} \exp(h_s \kappa))}_d \llbracket u \rrbracket_t \end{aligned} \quad (3.5)$$

where  $t_{s,t}$  are the tractions in the  $s$  and  $t$  directions,  $d_{\text{int}}$  is the initial shear stiffness ( $\kappa = 0$ ) and  $h_s$  determines how rapidly the shear stiffness decays with normal opening. The parameter  $h_s$  is calculated by:

$$h_s = \ln(d_{\kappa=1}/d_{\text{int}}) \quad (3.6)$$

where  $d_{\kappa=1}$  ( $\leq d_{\text{int}}$ ) is the discontinuity shear stiffness when the opening displacement has reached unity ( $\kappa = 1$  mm). Note that the sign of  $h_s$  is less than or equal to zero.

For implementation with an incremental solution procedure, it is important to cast the relationship between tractions and the displacement jump in a rate form. Differentiating the traction vector with respect to time, the consistently linearised tangent can be formed as:

$$\begin{Bmatrix} \dot{t}_n \\ \dot{t}_s \\ \dot{t}_t \end{Bmatrix} = \underbrace{\begin{bmatrix} -\frac{f_t}{G_f} \exp\left(-\frac{f_t}{G_f}\kappa\right) & 0 & 0 \\ h_s d_{\text{int}} \exp(h_s \kappa) \llbracket u \rrbracket_s & d_{\text{int}} \exp(h_s \kappa) & 0 \\ h_s d_{\text{int}} \exp(h_s \kappa) \llbracket u \rrbracket_t & 0 & d_{\text{int}} \exp(h_s \kappa) \end{bmatrix}}_{\mathbf{T}} \begin{Bmatrix} \llbracket \dot{u} \rrbracket_n \\ \llbracket \dot{u} \rrbracket_s \\ \llbracket \dot{u} \rrbracket_t \end{Bmatrix} \quad (3.7)$$

which in a compact format is expressed as:

$$\dot{\mathbf{t}} = \mathbf{T} \llbracket \dot{\mathbf{u}} \rrbracket \quad (3.8)$$

in the local  $(n, s, t)$  coordinate system. Due to the dependence of the shear stiffness on the normal opening, the tangent  $\mathbf{T}$  is non-symmetric. If shear sliding displacements are small (predominantly mode-I opening failure), or shear forces cannot be transferred across discontinuities, it can be computationally advantageous to make the discontinuity shear stiffness constant ( $h_s = 0$ ) in order to preserve symmetry of the tangent matrix.

For a discontinuity that is unloading ( $f([\mu]^{eq}, \kappa) < 0$ ), the secant stiffness is used for both normal and sliding components. Upon crack closure, full stiffness recovery is assumed, which corresponds to an intact continuum (the material history is however not erased). Considering the definition of a loading function and evolution equations, this discrete constitutive model is analogous to a continuum damage model.

### 3.2 Discrete plasticity model refined from the continuum case

Discrete constitutive models can also be formed by considering the appearance of Dirac-delta distributions in the strain field for classical continuum models. It was shown by Simo et al. (1993) that, under certain conditions, the classical governing equations of a continuum are compatible with the appearance of Dirac-delta distributions. Forming discrete constitutive relationships from continuum models has advantages when considering failure modes other than pure mode-I. For mode-II and mixed-mode failure, the continuum solution yields information over the onset of localisation and the spatial orientation of a discontinuity. To explore the derivation of discrete constitutive models from the continuum case, a model is derived from classical rate-independent associative plasticity. The derivations follow those first set out by Simo et al. (1993) and later elaborated by Armero and Garikipati (1995) and Oliver (1996a).

#### 3.2.1 Associative plasticity

The classical governing equations for rate-independent associative plasticity with isotropic hardening/softening are written as (Simo and Hughes, 1998):

$$\dot{\sigma} = \mathcal{C} (\dot{\epsilon} - \dot{\epsilon}^P) \quad (3.9a)$$

$$\dot{\epsilon}^P = \dot{\lambda} \frac{\partial f}{\partial \sigma} \quad (3.9b)$$

$$h = -\frac{1}{\dot{\lambda}} \frac{\partial f}{\partial \kappa} \dot{\kappa} \quad (3.9c)$$

$$f(\sigma, \kappa) = \phi(\sigma) - \bar{\sigma}(\kappa) \leq 0, \quad \dot{\lambda} \geq 0, \quad \dot{\lambda} f(\sigma, \kappa) = 0 \quad (3.9d)$$

where  $\mathcal{C}$  is the elastic constitutive tensor,  $\dot{\epsilon}^P$  is the plastic strain rate tensor,  $\dot{\lambda}$  is the plastic multiplier rate,  $\kappa$  is a strain-like internal variable,  $h$  is the hardening modulus,  $f$  is a yield function,  $\phi$  is a scalar-valued function and  $\bar{\sigma}$  is the yield strength of the material. The consistency condition,

$$\dot{\lambda} \dot{f}(\sigma, \kappa) = 0 \quad (3.10)$$

is also enforced.

### 3.2.2 Discontinuity development condition

Substituting the strain rate field in equation (2.6) and the plastic strain rate relationship (3.9b) into equation (3.9a) and denoting now  $\partial f / \partial \sigma$  as  $\partial_\sigma f$ , the stress rate tensor can be expressed as:

$$\dot{\sigma} = \mathcal{C} \left( \nabla^s \dot{\mathbf{u}} + \mathcal{H}_{\Gamma_d} (\nabla^s \dot{\mathbf{u}}) + \delta_{\Gamma_d} (\dot{\mathbf{u}} \otimes \mathbf{n})^s - \dot{\lambda} \partial_\sigma f \right). \quad (3.11)$$

The traction rate across a discontinuity can then be expressed as:

$$\dot{\mathbf{t}} = \left( \mathcal{C} \left( \nabla^s \dot{\mathbf{u}} + \mathcal{H}_{\Gamma_d} (\nabla^s \dot{\mathbf{u}}) + \delta_{\Gamma_d} (\dot{\mathbf{u}} \otimes \mathbf{n})^s - \dot{\lambda} \partial_\sigma f \right) \right) \mathbf{n}. \quad (3.12)$$

Physically, the traction rate must be bounded everywhere, and to satisfy equilibrium it must be continuous. The traction continuity requirement is not considered here as it will be shown for the numerical models developed in the following chapters that tractions are continuous across a discontinuity surface. To maintain a bounded traction rate, the unbounded distribution in equation (3.12) must cancel. Since the terms  $\nabla^s \dot{\mathbf{u}}$  and  $\mathcal{H}_{\Gamma_d} (\nabla^s \dot{\mathbf{u}})$  are known to be bounded (the functions  $\dot{\mathbf{u}}$  and  $\dot{\mathbf{u}}$  are continuous), all stresses must be bounded and the yield function is smooth (therefore  $\partial_\sigma f$  is regular), for a non-trivial case ( $\dot{\mathbf{u}} \neq \mathbf{0}$ ), the traction rate can remain bounded only if the Dirac-delta term in equation (3.12) is cancelled by the plastic multiplier rate  $\dot{\lambda}$ . Assuming an elastic response away from the discontinuity ( $\lambda = 0, \mathbf{x} \notin \Gamma_d$ ), the plastic multiplier must be of the form:

$$\lambda = \delta_{\Gamma_d} \bar{\lambda} \quad (3.13)$$

where  $\bar{\lambda}$  is bounded, in order that the unbounded terms cancel. Making  $\lambda$  unbounded implies that the hardening modulus is of the form:

$$h = \frac{\bar{h}}{\delta} \quad (3.14)$$

where  $\bar{h}$  is bounded. Inserting equations (3.14) and (3.13) into equation (3.9c) implies that  $\partial_\kappa f \dot{\kappa}$  (where  $\partial_\kappa f = \partial f / \partial \kappa$ ) is regular. Equating the unbounded parts in equation (3.12), at a discontinuity ( $\delta_{\Gamma_d} \neq 0$ ) it can be written:

$$\begin{aligned} (\mathbf{n} \mathcal{C} \mathbf{n}) \dot{\mathbf{u}} &= \dot{\lambda} \mathbf{n} \mathcal{C} \partial_\sigma f \\ \dot{\lambda} &= \frac{(\mathbf{n} \mathcal{C} \mathbf{n}) \dot{\mathbf{u}}}{\mathbf{n} \mathcal{C} \partial_\sigma f}. \end{aligned} \quad (3.15)$$

Based on the assumption of an elastic response in the bulk away from a discontinuity, from equation (3.9a) the stress rate away from a discontinuity is expressed as:

$$\dot{\sigma} = \mathcal{C} \left( \nabla^s \dot{\mathbf{u}} + \mathcal{H}_{\Gamma_d} (\nabla^s \dot{\mathbf{u}}) \right) \quad (3.16)$$

which implies that the elastic strain rate is equal to  $\dot{\boldsymbol{\varepsilon}}^e = \nabla^s \dot{\mathbf{u}} + \mathcal{H}_{\Gamma_d} (\nabla^s \dot{\mathbf{u}})$ . Considering the stress rate expression in equation (3.9a), this implies that the unbounded part of the strain field constitutes the plastic strain tensor:

$$\dot{\boldsymbol{\varepsilon}}^p = \delta_{\Gamma_d} \dot{\lambda} \partial_{\sigma} f = \delta_{\Gamma_d} (\dot{\mathbf{u}} \otimes \mathbf{n})^s. \quad (3.17)$$

Note that whenever  $\lambda$  operates on a function  $f$ , the result is non-zero only at the discontinuity surface since  $\delta_{\Gamma_d}$  is zero everywhere except at a discontinuity. The following derivations therefore apply at a discontinuity only and the continuous function  $\dot{\mathbf{u}}$  is replaced by the displacement jump rate at a discontinuity,  $[[\dot{\mathbf{u}}]]$ . From the consistency condition in equation (3.10), for loading ( $\dot{\lambda} > 0$ ),

$$\dot{f}(\boldsymbol{\sigma}, \kappa) = \partial_{\sigma} f : \dot{\boldsymbol{\sigma}} + \partial_{\kappa} f \dot{\kappa} = 0 \quad (3.18)$$

and inserting equations (3.11) and (3.13) into equations (3.18) yields:

$$\dot{f}(\boldsymbol{\sigma}, \kappa) = \partial_{\sigma} f : \underbrace{\left[ \mathcal{C} \left( \nabla^s \dot{\mathbf{u}} + \mathcal{H}_{\Gamma_d} (\nabla^s [[\dot{\mathbf{u}}]]) \right) + \delta_{\Gamma_d} ([[ \dot{\mathbf{u}} ]]) \otimes \mathbf{n} \right]^s}_{\dot{\boldsymbol{\sigma}}} - \delta_{\Gamma_d} \dot{\lambda} \partial_{\sigma} f + \partial_{\kappa} f \dot{\kappa} = 0. \quad (3.19)$$

Separating bounded and unbounded parts of equation (3.19),

$$\dot{f}(\boldsymbol{\sigma}, \kappa) = \underbrace{(\partial_{\sigma} f : \mathcal{C} (\nabla^s \dot{\mathbf{u}} + \mathcal{H}_{\Gamma_d} (\nabla^s [[\dot{\mathbf{u}}]])) + \partial_{\kappa} f \dot{\kappa})}_{=0} + \underbrace{\partial_{\sigma} f : (\mathcal{C} ([[ \dot{\mathbf{u}} ]]) \otimes \mathbf{n})^s - \dot{\lambda} \mathcal{C} \partial_{\sigma} f}_{=0} \delta_{\Gamma_d} = 0. \quad (3.20)$$

For equation (3.20) to hold, the unbounded terms must sum to zero. The unbounded part of equation (3.20) can be rearranged to give the bounded form of the plastic multiplier,

$$\dot{\lambda} = \frac{\partial_{\sigma} f : \mathcal{C} ([[ \dot{\mathbf{u}} ]]) \otimes \mathbf{n}^s}{\partial_{\sigma} f : \mathcal{C} \partial_{\sigma} f} \quad (3.21)$$

which is the usual form of the plastic multiplier for elasto-plasticity, with the plastic strain rate replaced by its equivalent in strong discontinuity analysis,  $([[ \dot{\mathbf{u}} ]]) \otimes \mathbf{n}^s$ . At this stage, it is useful to express the displacement jump rate vector in terms of its magnitude  $\dot{\zeta}$  and the unit vector  $\mathbf{m}$  in the direction of the jump.

$$\begin{aligned} [[ \dot{\mathbf{u}} ]]) &= \dot{\zeta} \mathbf{m} \\ ([[ \dot{\mathbf{u}} ]]) \otimes \mathbf{n}^s &= \dot{\zeta} (\mathbf{m} \otimes \mathbf{n})^s \end{aligned} \quad (3.22)$$

DISCRETE PLASTICITY MODEL REFINED FROM THE CONTINUUM CASE 23

Inserting the bounded form of the plastic multiplier in equation (3.15) into equation (3.21) and rearranging, it can be shown that:

$$\mathbf{n} \left( \underbrace{\mathbf{C} - \frac{\mathbf{C} \partial_{\sigma} f \otimes \mathbf{C} \partial_{\sigma} f}{\partial_{\sigma} f : \mathbf{C} \partial_{\sigma} f}}_{\mathbf{C}^{\text{ep}}} \right) \mathbf{nm} = 0 \quad (3.23)$$

where  $\mathbf{C}^{\text{ep}}$  is the perfectly plastic elasto-plastic tangent. Equation (3.23) is the condition for the development of a strong discontinuity given by Simo et al. (1993). The condition is usually written in the form:

$$\underbrace{(\mathbf{n} \mathbf{C}^{\text{ep}} \mathbf{n})}_{\mathbf{Q}(\mathbf{n})} \mathbf{m} = 0 \quad (3.24)$$

where  $\mathbf{Q}(\mathbf{n})$  is the acoustic tensor corresponding to the perfectly plastic tangent.

The condition for the development of a strong discontinuity (equation (3.24)) appears very similar to the more classical condition for the development of a weak (strain) discontinuity (equation (1.7)), for which the acoustic tensor corresponds to the actual elasto-plastic tangent rather than the perfectly plastic elasto-plastic tangent (Hill, 1962; Ottosen and Runesson, 1991; Rudnicki and Rice, 1975; Runesson et al., 1991). The condition for a strong discontinuity in equation (3.24) is reasonable when considered in the context of a weak discontinuity that collapses to a zone of zero width – a strong discontinuity. This idea of a collapsing band has been pursued by Oliver et al. (1999), although the limit case of a strong discontinuity was never reached in implementation. The difficulty is that, in general, the strong discontinuity localisation condition does not allow for the direct transition from a homogeneous, continuous state to a localised state characterised by a displacement discontinuity, as only under certain conditions is the condition in equation (3.24) satisfied at the onset of plastic flow. The existence of a critical hardening modulus  $h_{\text{crit}}$ , above which the determinant of the acoustic tensor is non-zero is well recognised (Ottosen and Runesson, 1991; Rudnicki and Rice, 1975; Runesson et al., 1991). A problem arises if the localisation condition is met for the actual elasto-plastic tangent (at which point the governing equations become ill-posed) and the strong discontinuity condition in equation (3.24) is not met. If at this point no kinematic discontinuities (weak or strong) are introduced, the problem is ill-posed and any results are meaningless. Satisfaction of the strong discontinuity condition in equation (3.24) at the onset of plastic flow requires that the critical hardening modulus be equal to zero. However, the condition for the development of a weak discontinuity does not specify the length across which a strain jump will occur. The length across which the jump occurs is dependent on the material. If the length scale is considered to be zero, then a strain jump is equivalent to a strong discontinuity. Based on this reasoning, if the localisation process is viewed from a scale at which the length scale of a material is zero, it is reasonable to introduce a strong discontinuity when the acoustic tensor corresponding to the actual elasto-plastic tensor becomes singular. Larsson and Runesson (1996)

considered a strong discontinuity as a collapsed weak discontinuity. In this case, the bifurcation condition is identical to the classical condition involving the acoustic tensor relating to the actual elasto-plastic tangent.

In the context of this work, the exact condition for the introduction of a discontinuity is not of key importance since it is the numerical methods for simulating discontinuities being examined. The primary concern is that the governing equations remain well-posed at all times. It is therefore assumed for all numerical examples based on the discrete plasticity formulation that when the continuum yield condition is violated, a displacement discontinuity is introduced (subject to  $\bar{h} < 0$ ).

### 3.2.3 Direction and magnitude of plastic flow

The following developments are concerned with the response at a discontinuity only. Substituting the plastic strain tensor in equation (3.17) into the expression for the plastic strain rate in equation (3.9b), taking into account the distributional form of the plastic multiplier and using equation (3.22), the displacement jump rate can be expressed as:

$$\dot{\zeta} (\mathbf{m} \otimes \mathbf{n})^s = \dot{\lambda} \partial_\sigma f. \quad (3.25)$$

Considering now the components of the basis of  $(\mathbf{m} \otimes \mathbf{n})^s$  from equation (2.9), it follows from equation (3.25) that the direction of plastic flow at a discontinuity can be written as:

$$\partial_\sigma f = \begin{bmatrix} \frac{\partial f}{\partial \sigma_{nn}} & \frac{\partial f}{\partial \sigma_{ns}} & \frac{\partial f}{\partial \sigma_{nt}} \\ \frac{\partial f}{\partial \sigma_{ns}} & 0 & 0 \\ \frac{\partial f}{\partial \sigma_{nt}} & 0 & 0 \end{bmatrix} \quad (3.26)$$

in the  $(n, s, t)$  coordinate system. From the consistency condition it can be computed that,

$$\dot{\lambda} = \frac{\partial_\sigma f : \dot{\boldsymbol{\sigma}}}{\bar{h}}. \quad (3.27)$$

Substituting the above result into equation (3.25), the displacements at the discontinuity can be expressed as:

$$\dot{\zeta} (\mathbf{m} \otimes \mathbf{n})^s = \frac{\partial_\sigma f : \dot{\boldsymbol{\sigma}}}{\bar{h}} \partial_\sigma f. \quad (3.28)$$

From the local basis developed in equation (2.9), the bounded plastic strain term is written as:

$$\dot{\zeta}(\mathbf{m} \otimes \mathbf{n})^s = \begin{bmatrix} \llbracket u \rrbracket_n & \frac{1}{2} \llbracket u \rrbracket_s & \frac{1}{2} \llbracket u \rrbracket_t \\ \frac{1}{2} \llbracket u \rrbracket_s & 0 & 0 \\ \frac{1}{2} \llbracket u \rrbracket_t & 0 & 0 \end{bmatrix}. \quad (3.29)$$

### 3.2.4 Discrete Von Mises model

A discrete plasticity model for the Von Mises yield surface is developed in this section. The more general formulation for the Drucker-Prager yield surface can be found in Wells and Sluys (2001a). The Von Mises yield function reads:

$$f(\boldsymbol{\sigma}, \kappa) = \sqrt{\frac{3}{2}} \|\mathbf{S}\| - \bar{\sigma}(\kappa) \quad (3.30)$$

where  $\mathbf{S}$  is the deviatoric stress tensor. On an interface, only three components of the stress tensor are active; the  $\sigma_{nm}$ ,  $\sigma_{ns}$  and  $\sigma_{nt}$  components. Therefore, the stress invariant  $\|\mathbf{S}\|$  is equal to  $\|\mathbf{S}\| = \sqrt{2\sigma_{ns}^2 + 2\sigma_{nt}^2}$  and the flow direction can be written as:

$$\partial_{\boldsymbol{\sigma}} f = \frac{\sqrt{3}}{2\sqrt{\sigma_{ns}^2 + \sigma_{nt}^2}} \begin{bmatrix} 0 & \sigma_{ns} & \sigma_{nt} \\ \sigma_{ns} & 0 & 0 \\ \sigma_{nt} & 0 & 0 \end{bmatrix} \quad (3.31)$$

Equation (3.31) shows that, due to the volumetric constraint on plastic flow imposed by the Von Mises yield function, no opening displacements are permitted at a discontinuity. Equation (3.31) also shows that the stresses  $\sigma_{ns}$  and  $\sigma_{nt}$  are proportional to the plastic flow rate (the displacement jump rate) in the  $s$  and  $t$  directions, respectively. Inserting now the plastic flow direction in equation (3.31) into equation (3.28) and changing to a vector format,

$$\dot{\zeta} \begin{Bmatrix} m_s \\ m_t \end{Bmatrix} = \begin{Bmatrix} \llbracket \dot{u} \rrbracket_s \\ \llbracket \dot{u} \rrbracket_t \end{Bmatrix} = \frac{3}{\bar{h}} \frac{1}{\sigma_{ns}^2 + \sigma_{nt}^2} \begin{bmatrix} \sigma_{ns}^2 & \sigma_{ns}\sigma_{nt} \\ \sigma_{ns}\sigma_{nt} & \sigma_{nt}^2 \end{bmatrix} \begin{Bmatrix} \dot{\sigma}_{ns} \\ \dot{\sigma}_{nt} \end{Bmatrix} \quad (3.32)$$

(the scalar 2 in equation (3.31) cancels due to the factors 1/2 in equation (3.29)). This is the result presented by Oliver (1996a). Consider a system ( $s'$ ,  $t'$ ) that is orientated in the direction of the displacement jump rate ( $m_{t'} = 0$ ,  $\llbracket \dot{u} \rrbracket_{s'} = \dot{\zeta}$ ,  $\llbracket \dot{u} \rrbracket_{t'} = 0$ ). From the plastic flow direction in equation (3.31), the stress on the plane in the  $t'$  direction must equal zero ( $\sigma_{nt} = 0$ ) since the displacement jump rate is zero in that direction. Equation (3.32) then reduces to a one-dimensional problem,

$$\llbracket \dot{u} \rrbracket_{s'} = \dot{\zeta} = \frac{3}{\bar{h}} \dot{\sigma}_{ns'} = \frac{3}{\bar{h}} \tau^{\text{res}} \quad (3.33)$$

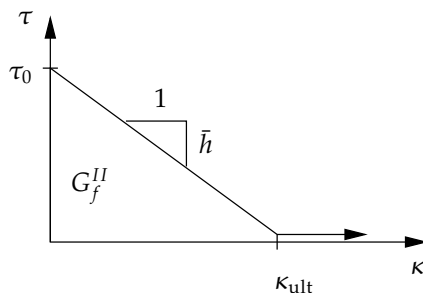


Figure 3.1: Linear softening response for the resolved shear stress on a discontinuity surface.

where  $\tau^{\text{res}}$  is the ‘resolved’ stress rate on the discontinuity plane. This result was presented by Armero and Garikipati (1995). The numerical models developed in later chapters are displacement driven, in that the displacement jump comes from the solution of a boundary value problem. Therefore, it is necessary to express the stress on a discontinuity in terms of the displacement jump rate. Taking the measure of inelastic deformation  $\kappa$  as the greatest absolute value of the displacement slip  $|\zeta|$  reached, for linear softening the resolved stress is given as:

$$\tau^{\text{res}} = |\tau_0^{\text{res}}| + \frac{\bar{h}}{3} \kappa \quad (3.34)$$

where  $\tau_0^{\text{res}}$  is the resolved stress at initiation of a discontinuity. The presence of the scalar  $1/3$  in equation (3.34) is trivial and of no consequence since the value of  $\bar{h}$  reflects the energy dissipated in failure and can be determined by considering the energy dissipated in failure (the mode-II equivalent of the fracture energy  $G_f$ , ‘ $G_f^{II}$ ’) and the initial resolved stress  $\tau_0^{\text{res}}$  (see figure 3.1). Therefore the factor is from this point disregarded and the relationship between  $\tau^{\text{res}}$  and  $\kappa$  is shown in figure 3.1. The stress  $\tau^{\text{res}}$  can be considered as the allowable stress on a discontinuity plane. Since the stress on a discontinuity plane in the  $s$  and  $t$  directions is proportional to the displacement jump rate in the respective directions, the stresses  $\sigma_{ns}$  and  $\sigma_{nt}$  for loading are given by:

$$\begin{aligned} \sigma_{ns} &= \frac{[[\dot{u}]_s]}{\sqrt{[[\dot{u}]_s]^2 + [[\dot{u}]_t]^2}} \tau^{\text{res}} \\ \sigma_{nt} &= \frac{[[\dot{u}]_t]}{\sqrt{[[\dot{u}]_s]^2 + [[\dot{u}]_t]^2}} \tau^{\text{res}} \end{aligned} \quad (3.35)$$

Note that for two-dimensional problems, the relation at a discontinuity reduces to the simple one-dimensional problem,

$$\sigma_{ns} = \frac{[[\dot{u}]]_s}{|[[\dot{u}]]_s|} \tau_{res}. \quad (3.36)$$

To simulate elastic unloading ( $|\zeta| < \kappa$ ), the displacement jump is ‘frozen’ and the stress on the discontinuity comes from the continuum response. Numerically, this can be approximated by making the components of the tangent relating the stress rates on the discontinuity and the displacement jump rates large. An important feature of the discrete Von Mises model is that no return mapping is required. This is due to the displacement jump being wholly inelastic. There is no need to decompose the displacement jump into elastic and plastic components.

### 3.2.5 Determination of the normal to a discontinuity

An important step not yet addressed is the determination of the normal vector to a discontinuity for a plasticity based model. This involves finding roots of the acoustic tensor. There exist two different approaches for determining the normal vector. The first is a numerical search technique with iterative refinement of the solution as proposed by Ortiz et al. (1987). This procedure can be used for any constitutive model. For common constitutive models, analytical solutions are available. For the plasticity-based Von Mises model presented in this chapter, there exist analytical solutions for plane stress, plane strain and three-dimensional cases (Ottosen and Runesson, 1991; Runesson et al., 1991).

From Ottosen and Runesson (1991), in three dimensions, with the coordinate system in the direction of the principal stresses ( $\sigma_1 \geq \sigma_2 \geq \sigma_3$ ), the normal vector is of the form  $(n_1, 0, n_3)$ . That is, the vector in the direction of the second principal stress lies in the plane of the discontinuity surface. The angle  $\theta$  between the  $n_3$  axis and the normal vector to a discontinuity is equal to:

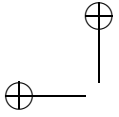
$$\tan^2 \theta = \frac{(1 - \nu) S_1 - \nu S_3}{\nu S_1 - (1 - \nu) S_3} \quad (3.37)$$

where  $\nu$  is Poisson’s ratio and where  $S_i$  are the principal deviatoric stresses ( $S_1 \geq S_2 \geq S_3$ ). In the principal stress coordinate system, the normal vector is therefore equal to  $(\sin \theta, 0, \cos \theta)$ . From Runesson et al. (1991), under plane strain conditions, the angle  $\theta$  is given by:

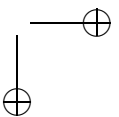
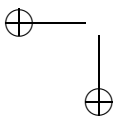
$$\tan^2 \theta = \frac{(1 - \nu) S_1 - \nu S_2}{\nu S_1 - (1 - \nu) S_2}. \quad (3.38)$$

For plane stress conditions,

$$\tan^2 \theta = -\frac{S_1}{S_2}. \quad (3.39)$$



For two-dimensional cases, the normal vector in the principal space is given by  $(\sin \theta, \cos \theta)$ . Note that for all cases there exists two solutions. The selection of the appropriate direction is addressed together with the implementation of the different numerical models.



## Chapter 4

# Embedded discontinuity element based on incompatible strain modes

To introduce a displacement discontinuity that is not aligned with element boundaries, it is necessary to introduce a discontinuity into the kinematic fields of an element. In this chapter, the *effect* of a displacement jump is added to finite elements as an incompatible strain mode. The displacement jump is ‘embedded’ in the element formulation, with the orientation of the discontinuity determined by the local stress or strain field and the constitutive model. By including the effect of a displacement jump only in the strain field of an element as an incompatible mode, the procedure can be easily implemented in existing finite element codes.

Significant work has been carried out into so-called ‘embedded discontinuity’ elements where the effect of a displacement jump is included in the strain field of an element. The approach followed here is based on the work of Simo et al. (1993). The approach developed by Simo et al. (1993) in one dimension was extended into two dimensions by Oliver (1996b) and Armero and Garikipati (1996) and into three dimensions by Wells and Sluys (2001f). The derivations in this chapter are built from the standard three-field variational statements. In this way the required assumptions and differences between formulations, both subtle and significant, can be clearly identified.

The exact form of the incompatible strain modes is determined by equilibrium and kinematic considerations. Through careful consideration of the variational statements, a finite element with incompatible modes is developed. Following from the kinematic relationships developed in chapter 2, the Dirac-delta distribution is included in the incompatible part of the strain field. Through the use of the Dirac-delta distribution, the amplitude of the incompatible mode can be interpreted as a displacement jump. Considering the variational formulation only results in a finite element that is kinematically identical to the standard finite element formulation. Element deformations do not properly reflect the presence of a displacement jump, leading to results which are sensitive to mesh alignment. In attempting to overcome mesh alignment sensitivity, the kinematics of an element crossed by a discontinuity

are considered and a Petrov-Galerkin type approach is used to kinematically enhance the underlying element. It is shown that, despite any kinematic enhancements, the model is closely related to classical smeared continuum models.

The element formulation is deliberately kept completely independent of the constitutive model applied. It will be shown that it is possible to solve for the displacement jump at integration point level, although this requires the introduction of element information to the constitutive model. It is desirable to separate the constitutive update and the element formulations. This allows the same constitutive models to be applied with different numerical models for simulating discontinuities. Further, considering the finite element formulation independently of the constitutive model preserves transparency of the method. Analyses are performed using the discrete constitutive models developed in chapter 3 for both two- and three-dimensional problems and some salient features of the model are highlighted. The performance of the model is carefully examined for objectivity with respect to spatial discretisation. As outlined in the Introduction, the goal in using elements with incompatible modes is the efficient analysis of three-dimensional problems. Therefore the numerical examples at the end of this chapter focus on three-dimensional applications.

#### 4.1 Variational formulation

From the Hu-Washizu functional (Washizu, 1982), taking variations of displacements, strains and stresses yields the so-called three-field variational statements,

$$\int_{\Omega} \nabla^s \boldsymbol{\eta} : \boldsymbol{\sigma} \, d\Omega - \int_{\Omega} \boldsymbol{\eta} \cdot \rho \mathbf{b} \, d\Omega - \int_{\Gamma_u} \boldsymbol{\eta} \cdot \bar{\mathbf{t}} \, d\Gamma = 0 \quad (4.1a)$$

$$\int_{\Omega} \boldsymbol{\tau} : (\nabla^s \mathbf{u} - \boldsymbol{\varepsilon}) \, d\Omega = 0 \quad (4.1b)$$

$$\int_{\Omega} \boldsymbol{\gamma} : (-\boldsymbol{\sigma} + \boldsymbol{\sigma}(\boldsymbol{\varepsilon})) \, d\Omega = 0 \quad (4.1c)$$

where  $(\boldsymbol{\eta}, \boldsymbol{\gamma}, \boldsymbol{\tau}) \in V \times E \times S$  are variations of displacements, strains and stresses, respectively and  $V, E$  and  $S$  are the spaces of admissible variations of displacements, strains and stresses, respectively,  $\rho \mathbf{b}$  are body forces and  $\bar{\mathbf{t}}$  are traction forces acting on  $\Gamma_u$  (see figure 2.1). The actual displacements, strains and stresses are denoted  $(\mathbf{u}, \boldsymbol{\varepsilon}, \boldsymbol{\sigma})$ . The stresses coming from the constitutive model are denoted  $\boldsymbol{\sigma}(\boldsymbol{\varepsilon})$ . The variational statements in equation (4.1) are the starting point for the embedded discontinuity formulation.

The variational statements in equation (4.1) contain three independent variables; the displacement field  $\mathbf{u}$ , the strain field  $\boldsymbol{\varepsilon}$  and the stress field  $\boldsymbol{\sigma}$ . Standard finite element procedures are based on an irreducible formulation where the displacement field  $\mathbf{u}$  is the only independent variable. The strain field is calculated as the gradient of the displacement field ( $\boldsymbol{\varepsilon} = \nabla^s \mathbf{u}$ ), automatically satisfying equation (4.1b).

Further, the stress field is calculated from the strain field ( $\boldsymbol{\sigma} = \boldsymbol{\sigma}(\boldsymbol{\varepsilon})$ ), satisfying equation (4.1c). This leaves only equation (4.1a), which is the usual virtual work expression. Therefore, if the displacement field is the only independent unknown, equations (4.1b) and (4.1c) are redundant and only the virtual work equation is needed. However, for some problems it may be necessary to resort to mixed formulations where the stress or strain field (or both) are interpolated independently of the displacement field. For the method followed here, it is necessary to consider the three-field statements since only part of the strain field will come from the gradient of the displacement field.

#### 4.1.1 Enhanced assumed strains

To add the effect of a displacement discontinuity as an incompatible strain mode, the method of *enhanced assumed strains* (EAS), developed by Simo and Rifai (1990), is utilised. EAS provides a method for enhancing the strain field of an element with incompatible strain modes, while still satisfying the conditions of stability and convergence. Following the EAS approach, the strain field is decomposed into two parts,

$$\boldsymbol{\varepsilon} = \nabla^s \mathbf{u} + \tilde{\boldsymbol{\varepsilon}} \quad (4.2)$$

where  $\nabla^s \mathbf{u}$  is the compatible part and  $\tilde{\boldsymbol{\varepsilon}}$  is the incompatible (or *enhanced*) part of the strain field. Similarly, a variation of the strain field is also decomposed into two parts,

$$\boldsymbol{\gamma} = \nabla^s \boldsymbol{\eta} + \tilde{\boldsymbol{\gamma}} \quad (4.3)$$

where  $\nabla^s \boldsymbol{\eta}$  is the compatible part and  $\tilde{\boldsymbol{\gamma}} \in \tilde{E}$  is the *enhanced* part of the variation of the strain field and  $\tilde{E}$  is the space of admissible enhanced strain variations.

Substitution of equations (4.2) and (4.3) into the three-field variational statements in equation (4.1) leads to three modified variational statements (Simo and Rifai, 1990):

$$\int_{\Omega} \nabla^s \boldsymbol{\eta} : \boldsymbol{\sigma}(\boldsymbol{\varepsilon}) \, d\Omega - \int_{\Omega} \boldsymbol{\eta} \cdot \boldsymbol{\rho} \mathbf{b} \, d\Omega - \int_{\Gamma_u} \bar{\mathbf{t}} \cdot \boldsymbol{\eta} \, d\Gamma = 0 \quad (4.4a)$$

$$\int_{\Omega} \boldsymbol{\tau} : \tilde{\boldsymbol{\varepsilon}} \, d\Omega = 0 \quad (4.4b)$$

$$\int_{\Omega} \tilde{\boldsymbol{\gamma}} : (-\boldsymbol{\sigma} + \boldsymbol{\sigma}(\boldsymbol{\varepsilon})) \, d\Omega = 0. \quad (4.4c)$$

Note that the variational statements in equation (4.4) no longer involve a variation  $\boldsymbol{\gamma}$ , but a variation of the enhanced part,  $\tilde{\boldsymbol{\gamma}}$ .

#### 4.1.2 Inclusion of the effect of displacement jump in the modified three-field statements

In order to include the effect of a displacement jump in the enhanced strain field, the enhanced strain itself is decomposed into two parts; a bounded part  $\tilde{\boldsymbol{\varepsilon}}_b$  and an

unbounded part  $\tilde{\varepsilon}_u$ ,

$$\tilde{\varepsilon} = \tilde{\varepsilon}_b + \tilde{\varepsilon}_u. \quad (4.5)$$

From the strain field in equation (2.5) and assuming that the function  $\tilde{\mathbf{u}}$  is spatially constant (therefore the Heaviside function does not appear in the strain field), the unbounded part of the enhanced strain field  $\tilde{\varepsilon}_u$  should be expressed in terms of a displacement jump, the Dirac-delta distribution and the normal to a discontinuity plane. The enhanced strain field is therefore cast as:

$$\tilde{\varepsilon} = \tilde{\varepsilon}_b + \delta_{\Gamma_d} (\mathbf{v} \otimes \mathbf{n})^s \quad (4.6)$$

where  $\mathbf{v}$  is the actual displacement jump at the surface  $\Gamma_d$  and  $\mathbf{n}$  is the normal to surface. The displacement jump at a surface is denoted  $\mathbf{v}$  rather than  $[[\mathbf{u}]]$  since it relates to the displacement jump within an element on the surface  $\Gamma_d$  and is not continuous across element boundaries (it is however continuous within an element). Variations of enhanced strains are also expressed in the same manner,

$$\tilde{\gamma} = \tilde{\gamma}_b + \delta_{\Gamma_d} (\vartheta \otimes \mathbf{n})^s \quad (4.7)$$

where  $\vartheta \in W$  is an admissible variation of the displacement jump at the discontinuity and  $W$  is the space of admissible variations of the displacement jump at a discontinuity. The decomposed forms of the enhanced strain (equation (4.6)) and variations of enhanced strains (equation (4.7)) can be inserted into equations (4.4b) and (4.4c), yielding:

$$\int_{\Omega} \boldsymbol{\tau} : \tilde{\varepsilon}_b \, d\Omega + \int_{\Omega} \delta_{\Gamma_d} \boldsymbol{\tau} : (\mathbf{v} \otimes \mathbf{n})^s \, d\Omega = 0 \quad (4.8a)$$

$$\int_{\Omega} \tilde{\gamma}_b : (-\boldsymbol{\sigma} + \boldsymbol{\sigma}(\boldsymbol{\varepsilon})) \, d\Omega + \int_{\Omega} \delta_{\Gamma_d} (\vartheta \otimes \mathbf{n})^s : (-\boldsymbol{\sigma} + \boldsymbol{\sigma}(\boldsymbol{\varepsilon})) \, d\Omega = 0. \quad (4.8b)$$

Using the property of the Dirac-delta distribution in equation (2.12), the integrals in equation (4.8) whose integrand contains the Dirac-delta distribution can be changed from volume to surface integrals, eliminating the unbounded terms.

$$\int_{\Omega} \boldsymbol{\tau} : \tilde{\varepsilon}_b \, d\Omega + \int_{\Gamma_d} (\boldsymbol{\tau} \mathbf{n}) \cdot \mathbf{v} \, d\Gamma = 0 \quad (4.9a)$$

$$\int_{\Omega} \tilde{\gamma}_b : (-\boldsymbol{\sigma} + \boldsymbol{\sigma}(\boldsymbol{\varepsilon})) \, d\Omega + \int_{\Gamma_d} [(-\boldsymbol{\sigma} + \boldsymbol{\sigma}(\boldsymbol{\varepsilon})) \mathbf{n}] \cdot \vartheta \, d\Gamma = 0 \quad (4.9b)$$

At this point, an important choice is made regarding the form of the enhanced strain field. The key step in the enhanced assumed strain approach is making the spaces of enhanced strains  $\tilde{E}$  and stresses  $S$  orthogonal in an  $L_2$  sense. Assuming a Galerkin procedure, enhanced strain variations come from the space of actual enhanced strains

and stress variations come from the space of actual stresses. Therefore the orthogonality condition can be expressed as:

$$\int_{\Omega_e} \tilde{\boldsymbol{\varepsilon}} : \boldsymbol{\tau} \, d\Omega = \int_{\Omega_e} \tilde{\boldsymbol{\gamma}} : \boldsymbol{\sigma} \, d\Omega = 0. \quad (4.10)$$

Note that the superscript ‘e’ has been added to the integral limits in equation (4.10) to denote that the orthogonality condition is enforced on a per element basis. It is stressed that the assumption of a Galerkin procedure allows the interchange of actual enhanced strains and variations of enhanced strains since any enhanced strain is an admissible variation of enhanced strain. The same argument applies for the actual stress field and variations of stresses. This is an essential assumption in the work of Simo and Rifai (1990).

A direct consequence of the orthogonality condition in equation (4.10) is that equation (4.4b) is satisfied (and therefore equation (4.9a) also). Substitution of the relationships in equation (4.10) into equation (4.9b) allows the stress field  $\boldsymbol{\sigma}$  to be eliminated from the unknown fields. Equation (4.9b) can then be rephrased as:

$$\int_{\Omega_e} \tilde{\boldsymbol{\gamma}}_b : \boldsymbol{\sigma}(\boldsymbol{\varepsilon}) \, d\Omega + \int_{\Gamma_{d,e}} (\boldsymbol{\sigma}(\boldsymbol{\varepsilon}) \mathbf{n}) \cdot \boldsymbol{\vartheta} \, d\Gamma = 0. \quad (4.11)$$

The orthogonality condition has enabled the stress field to be eliminated from the unknown fields, leaving the enhanced strain field and the displacement field as the only unknowns. Equation (4.11), together with the usual virtual work expression in equation (4.4a), provide two weak equilibrium equations:

$$\int_{\Omega} \nabla^s \boldsymbol{\eta} : \boldsymbol{\sigma}(\boldsymbol{\varepsilon}) \, d\Omega - \int_{\Omega} \boldsymbol{\eta} \cdot \rho \mathbf{b} \, d\Omega - \int_{\Gamma_u} \bar{\mathbf{t}} \cdot \boldsymbol{\eta} \, d\Gamma = 0 \quad (4.12a)$$

$$\int_{\Omega_e} \tilde{\boldsymbol{\gamma}}_b : \boldsymbol{\sigma}(\boldsymbol{\varepsilon}) \, d\Omega + \int_{\Gamma_{d,e}} \mathbf{t} \cdot \boldsymbol{\vartheta} \, d\Gamma = 0 \quad (4.12b)$$

where  $\mathbf{t} (= \boldsymbol{\sigma}(\boldsymbol{\varepsilon}) \mathbf{n})$  is the traction force acting at a discontinuity  $\Gamma_d$ . Equation (4.12b) can be interpreted as enforcing traction continuity at a discontinuity in a weak sense, with the force in the continuum part of an element equal and opposite to the traction forces acting on the discontinuity. It supplements the usual virtual work equation, enforcing traction continuity within an element.

The final step is to determine the form of the enhanced strain field, ensuring that it fulfils the orthogonality condition in equation (4.10). Rearranging equation (4.9a) yields:

$$\int_{\Omega_e} \boldsymbol{\tau} : \tilde{\boldsymbol{\varepsilon}}_b \, d\Omega = - \int_{\Gamma_{d,e}} (\boldsymbol{\tau} \mathbf{n}) \cdot \boldsymbol{\nu} \, d\Gamma. \quad (4.13)$$

It is assumed at this stage that a discontinuity through an element is a flat plane (that is,  $\mathbf{n}$  is constant through an element). Assuming also a constant stress and strain

field within an element (which is exact for three-noded triangular and four-noded tetrahedral elements), equation (4.13) can be integrated explicitly leading to:

$$\tilde{\boldsymbol{\varepsilon}}_b = -\frac{A_e}{V_e} (\boldsymbol{\nu} \otimes \mathbf{n})^s \quad (4.14)$$

where  $A_e$  is the area of the plane through an element and  $V_e$  is the volume of the element. The orthogonality condition, which is equivalent to the enforcement of traction continuity, has dictated the form of the bounded part of the enhanced strain field.

#### 4.1.3 Kinematic equivalence with the standard formulation

In the preceding sections, a formulation has been developed that allows the inclusion of the Dirac-delta distribution in the incompatible part of the strain field of a finite element. Because the imposition of the orthogonality condition in equation (4.13) can be interpreted as the enforcement of traction continuity, the enhanced strain field has been formulated from static considerations. However, it is well recognised that finite element calculations that involve strain softening are sensitive to mesh alignment. In attempting to overcome mesh alignment sensitivity, an element must be enhanced kinematically. When an element is crossed by a discontinuity, it is essential that nodes on opposite sides of the discontinuity move relative to each other. For this to happen, the enhanced strain field must be a function of the position of the discontinuity within an element relative to the element nodes. The enhanced strain in equation (4.14) will fail since it is a function of the normal vector to the discontinuity and the ratio between the area of the discontinuity and the volume of the element only. A detailed discussion relating to the need for kinematic enhancement can be found in Jirásek (2000).

The advantages of the formulation over standard finite elements with continuum strain softening models are that discrete constitutive models can be applied and there is no need for the direct inclusion of an artificial length scale in the constitutive model coming from the element size. It must be realised however that an element length scale is introduced in the enhanced strain interpolation through the scalar ratio  $A_e/V_e$  in equation (4.14).

## 4.2 Kinematic enhancement

A possible solution to overcome mesh sensitivity is to construct a kinematically motivated enhanced strain field. A displacement at a discontinuity within an element should be ‘mapped’ to the element nodes. A displacement  $\boldsymbol{\nu}$  at a discontinuity should be equivalent to a displacement  $\boldsymbol{\nu}$  at the nodes on one side of the discontinuity. Figure 4.1 shows a three-noded triangular element crossed by a discontinuity such that node one ‘separates’ from nodes two and three. Any displacement at the discontinuity should give that same displacement at node one (assuming a rigid continuum

KINEMATIC ENHANCEMENT

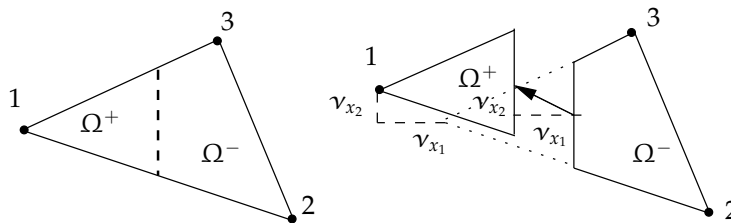


Figure 4.1: Three-noded triangular element crossed by a discontinuity. The discontinuity is shown by the dashed line.

and a constant jump within an element). A displacement jump should induce strains in the continuum that are equal and opposite to the strains that would be induced by the same displacement at the nodes on one side of a discontinuity. To do this, a function  $\varphi_e$  is required that has a value of unity at nodes on one side of a discontinuity and is zero at nodes on the other side. When this function is multiplied by the displacement jump at a discontinuity, the effect of the jump is ‘transferred’ to the element nodes,

$$\mathbf{u}^*(\mathbf{x}) = -\varphi_e(\mathbf{x})\mathbf{v} \quad (4.15)$$

where  $\mathbf{u}^*$  is incompatible. The negative sign in front of  $\varphi_e$  is necessary since the strain field must be opposite to that induced by a nodal displacement. Equation 4.15 is only used for developing the kinematic (incompatible) strain field. The term  $\mathbf{u}^*$  does not appear anywhere in the formulation. The function  $\varphi_e$  can be constructed using the shape functions of a finite element. For nodes which belong to the domain  $\Omega_e^+$  ( $\mathbf{x}_i \in \Omega_e^+$ , where  $\mathbf{x}_i$  is the position of node  $i$ ), their shape functions are denoted  $N_i^+$ . The function  $\varphi_e$  is formed by:

$$\varphi_e = \sum_{i=1}^{n^+} N_i^+ \quad (4.16)$$

where  $n^+$  denotes the number of nodes belonging to the domain  $\Omega^+$ . For the case shown in figure 4.1, the function  $\varphi_e$  is equal to the shape function of node one. Taking the gradient of equation (4.15), the ‘enhanced’ part of the strain field is written as:

$$\tilde{\boldsymbol{\varepsilon}}^k = -(\mathbf{v} \otimes \nabla \varphi_e)^s. \quad (4.17)$$

The superscript  $k$  has been added to distinguish the kinematically formulated enhanced strain field from the enhanced strain in equation (4.14). The kinematic enhanced strain field in equation (4.17) differs from the enhanced strain strain field in equation (4.14), with the term  $(A_e/V_e)\mathbf{n}$  in equation (4.14) replaced by  $\nabla \varphi_e$ .

The problem in using the enhanced strain field in equation (4.17) is that it does not, in general, satisfy the orthogonality requirement of EAS since  $\int_{\Omega_e} \tilde{\boldsymbol{\varepsilon}}^k d\Omega \neq 0$ ,

which was shown in equation (4.12b) to be equivalent to enforcing traction continuity for constant stress elements. A possibility, first proposed by Simo et al. (1993), is to distinguish the test functions (variations) from the trial functions (actual fields). Departing from a Galerkin procedure, the kinematically formulated strain enhanced field is used as the trial function in calculating the actual strain field (used for the stress update), while the EAS (statically derived) strain field is used as the test function. This is the key difference between the approach of Armero and Garikipati (1996), Oliver (1996b) and Wells and Sluys (2001f), where the kinematic enhancement is used, and the approach of Larsson and Runesson (1996) where only the statically derived enhanced strain field is used.

While the Petrov-Galerkin formulation possesses kinematic enhancements to assist in overcoming mesh alignment sensitivity, it is variationally inconsistent. A key assumption in the EAS methodology is that the spaces of the enhanced test and trial functions are identical. This assumption is necessary for the relationships in equation (4.10) to hold which allows the stress field to be eliminated as an unknown from equation (4.9b).

### 4.3 Element formulation

For finite element calculations, the preceding developments must be cast in a discretised and a linearised form, suitable for implementation. The enhanced strain fields from the previous sections will be cast in a matrix format. Since the enhanced modes are incompatible, the displacement jump is represented by degrees of freedom at an internal element node. Therefore no extra global degrees of freedom are created when a discontinuity is initiated. Considering the assumption of a constant strain field in the previous section, three-noded triangular and four-noded tetrahedral elements are developed. A four-noded tetrahedral element, crossed by a discontinuity plane is shown in figure 4.2. Higher-order elements should be approached with caution since  $\int_{\Omega_e} \tilde{\epsilon} d\Omega = 0$  does not guarantee  $\int_{\Omega_e} \tilde{\epsilon} : \sigma d\Omega = 0$  if  $\sigma$  is not constant. Due to the assumptions in the variational formulation, the extension to elements with non-constant strain fields is highly questionable.

#### 4.3.1 Influence of the function $\varphi_e$

Under certain conditions, it can be shown that the statically and kinematically formed strain fields are equivalent. For the element shown in figure 4.3,  $\varphi_e$  is equal to the shape function  $N_1$  of node one (from equation (4.16)) and the discontinuity through the element is aligned with one edge of the element. Through some simple calcula-

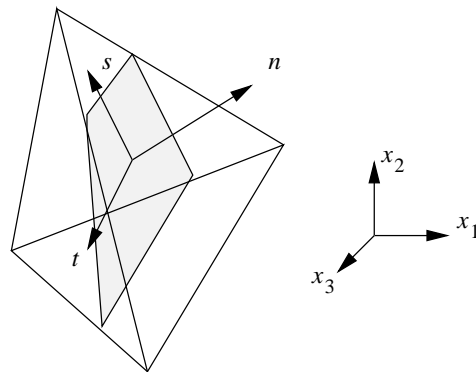


Figure 4.2: Tetrahedral element crossed by a discontinuity plane.

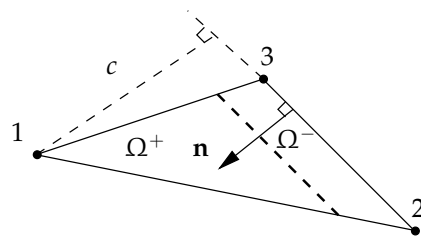


Figure 4.3: Triangular element crossed by a discontinuity (represented by the dashed line) with the discontinuity aligned with an element edge.

tions it can be shown that:

$$\nabla \varphi_e = \begin{Bmatrix} \frac{\partial N_1}{\partial x_1} \\ \frac{\partial N_1}{\partial x_2} \end{Bmatrix} = \frac{1}{c} \begin{Bmatrix} n_1 \\ n_2 \end{Bmatrix} \quad (4.18)$$

where  $c$  is a scalar (shown in figure 4.3) and  $n_1$  and  $n_2$  are components of the normal vector in the  $x_1$  and  $x_2$  directions, respectively. Using the result in equation (4.18) and comparing the enhanced strain fields in equations (4.14) and (4.17), the qualitative difference between the enhanced strain fields  $\tilde{\epsilon}_b$  and  $\tilde{\epsilon}^k$  disappears, with  $\tilde{\epsilon}^k$  being a scalar multiple of  $\tilde{\epsilon}_b$ . Therefore, for the case when a discontinuity is aligned with an element edge,  $\tilde{\epsilon}^k = (V_e c / A_e) \tilde{\epsilon}_b$ . This result is not surprising when considering that conventional smeared models perform well when an element edge is aligned in the direction of the crack or shear band. From figure 4.3 and equation (4.18), the kinematic enhancement can be considered as projecting a discontinuity such that it is parallel to an element side, a case in which conventional finite elements are known to perform well. The scalar  $c$  provides a measure of the element size and the ‘normal vector’ is not dependent on the discontinuity orientation, rather the spatial orientation of the element edge. The motivation for the enhanced strain field given by Oliver (1996b) that the ‘incompatible displacement’ equals  $\mathcal{H}_{\Gamma_d} - \varphi_e$  which is chosen since it is equal to zero at element nodes thus seems improper and gives an incorrect justification to the kinematic enhanced strain field. The kinematic enhancement simply makes the strain enhancement element-dependent. The enhancement is dependent not only on element size, but also element orientation.

It must be emphasised that the use of the function  $\varphi_e$  introduces numerical length scales to the formulation. Taking the gradient of  $\varphi_e$  can be considered as a sophisticated measure of the width of an element. From equation (4.18), the gradient  $\nabla \varphi_e$  implies a length scale and an element-dependent normal vector. Alternatively (and equivalently), it can be considered to imply two element length scales. Consider the element shown in figure 4.4. The element is crossed by a discontinuity such that  $\varphi_e$  is equal to the shape function of node one,  $N_1$ . Through algebraic manipulations, it can be shown that  $\partial \varphi_e / \partial x_1 = 1/l_{x_1}$  and  $\partial \varphi_e / \partial x_2 = 1/l_{x_2}$ , where  $l_{x_1}$  and  $l_{x_2}$  are shown graphically in figure 4.4. The kinematic enhanced continuum strains in terms of a displacement jump are expressed as:

$$\tilde{\epsilon}_{11}^k = -\frac{\nu_{x_1}}{l_{x_1}} \quad (4.19a)$$

$$\tilde{\epsilon}_{22}^k = -\frac{\nu_{x_2}}{l_{x_2}} \quad (4.19b)$$

$$2\tilde{\epsilon}_{12}^k = -\frac{\nu_{x_1}}{l_{x_2}} - \frac{\nu_{x_2}}{l_{x_1}}. \quad (4.19c)$$

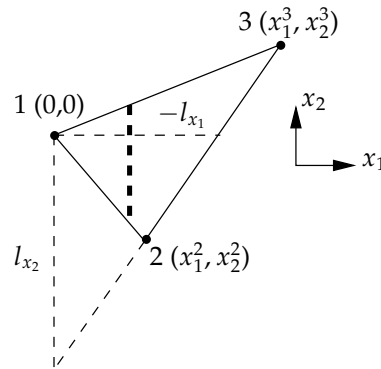


Figure 4.4: Element length scales implied by the kinematic enhancement.

Equation (4.19) shows that use of the kinematic enhancement implies a different numerical length scale in each spatial direction in the global coordinate system. This can be compared to the EAS enhancement where only one length scale,  $l = A_e/V_e$ , is implied. The kinematic enhancement is intimately related to element size and shape.

Experience from three-dimensional calculations for mode-I dominated problems with a low sliding stiffness at discontinuities has shown that modifications of the function  $\varphi_e$  are required for robust implementation with the four-noded tetrahedral element. The difficulty arises particularly when two nodes lie on each side of a discontinuity. Use of  $\varphi_e$ , as defined in equation (4.16), leads to excessive tangential sliding at interfaces for a patch of elements in pure tension. This has severe consequences for the robustness of the procedure. A solution is to modify the derivatives of the function  $\varphi_e$  such that a normal displacement  $v_n$  does not induce any shear strains in the continuum. To do this, the function  $\varphi_e$  is calculated according to equation (4.16) and its derivatives are computed. Then the vector containing the derivatives of  $\varphi_e$ , is rotated into the local  $n, s, t$  coordinate system and any terms orthogonal to the  $n$ -direction are removed and the vector is rotated back to the global coordinate system. Numerical tests indicate that the removal of the orthogonal terms has a negligible impact on the response of patches of elements but is crucial for the convergence behaviour. For large problems, it is not possible to calculate a converged solution without modifying  $\varphi_e$ .

The use of the kinematic enhancement in equation (4.16) raises some serious questions over the stability of the method when a discontinuity is located close to an element node. For a discontinuity located close to a node, a very small change in the position of the discontinuity or the normal vector to the discontinuity can result in a sudden and large change in equation (4.16). This is illustrated in figure 4.5 where a small change in the normal vector results in a sudden change in the function  $\varphi_e$  for an element. Comparing the cases in figure 4.5, the normal vectors are near identical ( $\mathbf{n}_1 \approx \mathbf{n}_2$ ) while the kinematic enhancement functions differ signifi-

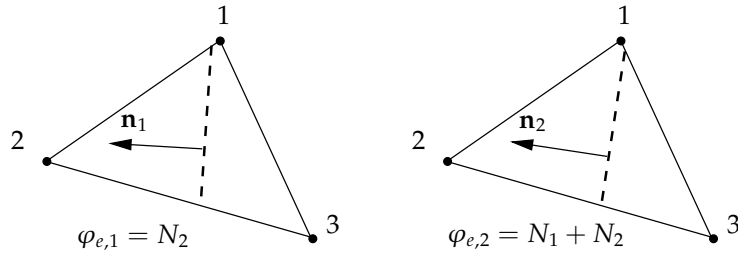


Figure 4.5: Elements crossed by a discontinuity (dashed line) which passes close to an element node. This results in a sudden change in the function  $\varphi_e$ .

cantly ( $\varphi_{e,1} \not\approx \varphi_{e,2}$ ).

#### 4.3.2 Discretised weak equilibrium equations

The two weak governing equations in (4.12), ignoring body forces, can be expressed in a discretised form as:

$$\int_{\Omega} \mathbf{B}^T \boldsymbol{\sigma} d\Omega - \int_{\Gamma_u} \mathbf{N}^T \bar{\mathbf{t}} d\Gamma = \mathbf{0} \quad (4.20a)$$

$$\int_{\Omega_e} \mathbf{G}^{*T} \boldsymbol{\sigma} d\Omega + \int_{\Gamma_{de}} \mathbf{t} d\Gamma = \mathbf{0}. \quad (4.20b)$$

where  $\mathbf{N}$  and  $\mathbf{B}$  are matrices containing the usual displacement and strain interpolations (from the compatible part of the displacement field), respectively (Zienkiewicz and Taylor, 1994),  $\boldsymbol{\sigma}$  is a vector containing components of the stress tensor and  $\mathbf{G}^*$  is a matrix containing interpolations of the variations of the bounded part of the enhanced strain  $\tilde{\boldsymbol{\varepsilon}}_b$ . Equation (4.20b) applies to all elements crossed by a discontinuity. From equation (4.14), the matrix  $\mathbf{G}^*$  is expressed as:

$$\mathbf{G}_e^* = -\frac{A_e}{V_e} \mathbf{n}_e \quad (4.21)$$

where the matrix  $\mathbf{n}_e$  is of the form:

$$\mathbf{n}_e = \begin{bmatrix} n_1 & 0 & 0 \\ 0 & n_2 & 0 \\ 0 & 0 & n_3 \\ n_2 & n_1 & 0 \\ 0 & n_3 & n_2 \\ n_3 & 0 & n_1 \end{bmatrix} \quad (4.22)$$

where  $n_1$ ,  $n_2$  and  $n_3$  are the components of the unit vector  $\mathbf{n}$  for an element. To determine the strain field in the continuum, the kinematically derived enhanced strain  $\tilde{\boldsymbol{\varepsilon}}^k$

is used. The strain rate at a point in an element is calculated using:

$$\boldsymbol{\varepsilon}(\mathbf{x}) = \mathbf{B}(\mathbf{x})\mathbf{a} + \mathbf{G}(\mathbf{x})\boldsymbol{\alpha} \quad (4.23)$$

where  $\mathbf{a}$  are the regular nodal displacements and  $\boldsymbol{\alpha}$  are the enhanced nodal displacements at a discontinuity (representing the displacement jump components). The displacement jump components are internal degrees of freedom of an element. From the strain field in equation (4.17), the matrix  $\mathbf{G}_e$  for an element is written as:

$$\mathbf{G}_e = - \begin{bmatrix} \frac{\partial \varphi_e}{\partial x_1} & 0 & 0 \\ 0 & \frac{\partial \varphi_e}{\partial x_2} & 0 \\ 0 & 0 & \frac{\partial \varphi_e}{\partial x_3} \\ \frac{\partial \varphi_e}{\partial x_2} & \frac{\partial \varphi_e}{\partial x_1} & 0 \\ 0 & \frac{\partial \varphi_e}{\partial x_3} & \frac{\partial \varphi_e}{\partial x_2} \\ \frac{\partial \varphi_e}{\partial x_3} & 0 & \frac{\partial \varphi_e}{\partial x_1} \end{bmatrix}. \quad (4.24)$$

A curious feature of the Petrov-Galerkin type approach is that the formulation is independent of the area of the discontinuity  $A_e$ . Integrating the last term on the left-hand side of equation (4.20b) over the area of the discontinuity, and inserting equation (4.21), (4.20b) can be written as:

$$A_e \int_{\Omega_e} -\frac{1}{V_e} \mathbf{n}_e^T \boldsymbol{\sigma} d\Omega + A_e \mathbf{t} = \mathbf{0}. \quad (4.25)$$

Since the stress field is calculated using  $\mathbf{G}$ , in which  $A_e$  does not appear (see equation (4.24)), rather than  $\mathbf{G}^*$ , the area of the discontinuity plane acts as an integration weight which cancels since the right-hand side of equation (4.25) is zero. Therefore an element response is dependent on the normal vector to the discontinuity and the position of the discontinuity relative to the element nodes, and independent of the discontinuity area.

#### 4.3.3 Linearised system of equations

The stress rate in terms of nodal displacement velocities is given by:

$$\dot{\boldsymbol{\sigma}} = \mathbf{D}(\mathbf{B}\dot{\mathbf{a}} + \mathbf{G}\dot{\boldsymbol{\alpha}}) \quad (4.26)$$

where  $\mathbf{D}$  is a material tangent matrix relating the stress and strain rates. The traction rate at a discontinuity is given by:

$$\dot{\mathbf{t}} = \mathbf{T}\dot{\boldsymbol{\alpha}} \quad (4.27)$$

where  $\mathbf{T}$  is the tangent relating the traction rate and the displacement jump rate. Note that equation (4.27) is in the global coordinate system and not the local  $(n, s, t)$  coordinate system. To form the element stiffness matrix, the stress and traction rate expressions are inserted into the weak governing equations in (4.20). This yields for an element:

$$\begin{bmatrix} \mathbf{K}_{bb,e} & \mathbf{K}_{bg,e} \\ \mathbf{K}_{g^*b,e} & \mathbf{K}_{g^*g,e} + \mathbf{K}_{t,e} \end{bmatrix} \begin{Bmatrix} d\mathbf{a}_e \\ d\boldsymbol{\alpha}_e \end{Bmatrix} = \begin{Bmatrix} \mathbf{f}_{u,e}^{\text{ext}} \\ \mathbf{0} \end{Bmatrix} - \begin{Bmatrix} \mathbf{f}_{u,e}^{\text{int}} \\ \mathbf{f}_{\alpha,e}^{\text{int}} \end{Bmatrix} \quad (4.28)$$

where

$$\mathbf{K}_{bb,e} = \int_{\Omega_e} \mathbf{B}_e^T \mathbf{D} \mathbf{B}_e d\Omega \quad (4.29a)$$

$$\mathbf{K}_{bg,e} = \int_{\Omega_e} \mathbf{B}_e^T \mathbf{D} \mathbf{G}_e d\Omega \quad (4.29b)$$

$$\mathbf{K}_{g^*b,e} = \int_{\Omega_e} \mathbf{G}_e^{*T} \mathbf{D} \mathbf{B}_e d\Omega \quad (4.29c)$$

$$\mathbf{K}_{g^*g,e} = \int_{\Omega_e} \mathbf{G}_e^{*T} \mathbf{D} \mathbf{G}_e d\Omega \quad (4.29d)$$

$$\mathbf{K}_{t,e} = \int_{\Gamma_{d,e}} \mathbf{T}_e d\Gamma \quad (4.29e)$$

$$\mathbf{f}_{u,e}^{\text{ext}} = \int_{\Gamma_{u,e}} \mathbf{N}_e^T \bar{\mathbf{t}} d\Gamma \quad (4.29f)$$

$$\mathbf{f}_{u,e}^{\text{int}} = \int_{\Omega_e} \mathbf{B}_e^T \boldsymbol{\sigma} d\Omega \quad (4.29g)$$

$$\mathbf{f}_{\alpha,e}^{\text{int}} = \int_{\Omega_e} \mathbf{G}_e^{*T} \boldsymbol{\sigma} d\Omega + \int_{\Gamma_{d,e}} \mathbf{t}_e d\Gamma \quad (4.29h)$$

and  $d\mathbf{a}_e$  and  $d\boldsymbol{\alpha}_e$  are the iterative-incremental displacements. The subscript ‘ $e$ ’ has been added to denote that the stiffness matrix is for a single element. Note that irrespective of the material model used, the element stiffness matrix is non-symmetric. This is a direct result of Petrov-Galerkin type formulation. Based on this, the terminology ‘symmetric formulation’ is used from this point for the EAS-Galerkin approach ( $\mathbf{G} = \mathbf{G}^*$ ) and ‘non-symmetric formulation’ for the Petrov-Galerkin type approach ( $\mathbf{G} \neq \mathbf{G}^*$ ).

#### 4.3.4 Static condensation

Since the enhanced displacement modes are incompatible, they can be solved at element level. First, the element stiffness matrix and internal force vector in equation (4.28) are condensed.

$$\mathbf{K}_{\text{con},e} = \mathbf{K}_{bb,e} - \mathbf{K}_{bg,e} [\mathbf{K}_{g^*g,e} + \mathbf{K}_{t,e}]^{-1} \mathbf{K}_{g^*b,e} \quad (4.30)$$

$$\mathbf{f}_{\text{con},e}^{\text{int}} = \mathbf{f}_{u,e}^{\text{int}} - \mathbf{K}_{bg,e} [\mathbf{K}_{g^*g,e} + \mathbf{K}_{t,e}]^{-1} \mathbf{f}_{\alpha,e}^{\text{int}} \quad (4.31)$$

The condensed element stiffness matrices and internal force vectors are used in assembly of the global system of equations. After solving the global system of equations for the iterative-incremental displacements  $d\mathbf{a}$ , the iterative-incremental displacements at the discontinuity within an element can be found.

$$d\alpha_e = - [\mathbf{K}_{g^*g,e} + \mathbf{K}_{t,e}]^{-1} [\mathbf{K}_{g^*b,e} d\mathbf{a}_e + \mathbf{f}_{\alpha,i}^{\text{int}}] \quad (4.32)$$

The advantage of using incompatible modes is that the extra degrees of freedom representing the enhanced modes never enter the global system of equations. For fracture and strain localisation problems where discontinuities are added to relatively few elements compared to the total number of elements, the computational cost of solving the extra degrees of freedom is minimal. Also, since the extra degrees of freedom are solved at element level, the method can be easily implemented in existing finite element codes.

#### 4.3.5 Discrete versus regularised discontinuity

Several versions of the embedded discontinuity model that have been developed do not use discrete constitutive models, but rather approximate the Dirac-delta distribution with a bounded function, allowing the application of continuum constitutive models (Larsson and Runesson, 1996; Oliver, 1996b; Simo et al., 1993). In these approaches, the Dirac-delta distributions are smeared over a small finite width  $k$ . The Dirac-delta distribution is approximated by:

$$\delta \approx \frac{1}{k}. \quad (4.33)$$

It has been shown in a rigorous manner that this ‘regularised strong discontinuity’ is identical to a weak discontinuity (De Borst et al., 2001). Further, the approach has some fundamental flaws. Firstly, it requires a numerical parameter  $k$  which is not related to the material, but must be used in the continuum constitutive model. The hardening modulus used in the constitutive model  $\bar{h}$  is a function of  $k$  and the ‘actual’ hardening modulus  $h$ .

$$\bar{h} = \frac{h}{k} \quad (4.34)$$

Equation (4.34) is reminiscent of smeared crack approaches with crack band width regularisation, in which the finite element size is included in the constitutive model. A second problem with the regularised version is in implementation. The direct use of continuum constitutive models in combination with a regularised discontinuity can lead to a response which is dependent on  $k$ . With the direct application of a Rankine plasticity model in the regularised embedded discontinuity framework,

stress locking as a function of the regularisation parameter can be observed (Wells and Sluys, 2000). Stress locking in that case becomes more severe as  $k$  approaches zero, closer to a true discontinuity. In other cases, as  $k$  approaches zero, the robustness of the procedure is reduced (Wells and Sluys, 1999). For practical application, it is not possible to use very small values of  $k$  relative to the element size.

#### 4.4 Comparison of the EAS-based model and smeared crack formulations

At this point, it is useful to reflect on aspects of the embedded discontinuity formulation and appraise their significance critically. To begin, the condensed element stiffness matrix is examined. Assuming an elastic response in the continuum, from equation (4.30), the condensed element stiffness matrix is expressed as:

$$\begin{aligned} \mathbf{K}_{\text{con},e} = & \int_{\Omega_e} \mathbf{B}^T \mathbf{D}^e \mathbf{B} \, d\Omega \\ & - \int_{\Omega_e} \mathbf{B}^T \mathbf{D}^e \mathbf{G} \, d\Omega \left( \int_{\Omega_e} \mathbf{G}^{*T} \mathbf{D}^e \mathbf{G} + \int_{\Gamma_{d,e}} \mathbf{T}_e \, d\Gamma \right)^{-1} \int_{\Omega_e} \mathbf{G}^{*T} \mathbf{D}^e \mathbf{B} \, d\Omega \end{aligned} \quad (4.35)$$

where  $\mathbf{D}^e$  is the elastic material tangent. For constant strain elements, the integrals in equation (4.35) can be eliminated,

$$\mathbf{K}_{\text{con},e} = V_e \mathbf{B}^T \mathbf{D}^e \mathbf{B} - V_e \mathbf{B}^T \mathbf{D}^e \mathbf{G} \left( V_e \mathbf{G}^{*T} \mathbf{D}^e \mathbf{G} + A_e \mathbf{T}_e \right)^{-1} V_e \mathbf{G}^{*T} \mathbf{D}^e \mathbf{B}. \quad (4.36)$$

Defining a matrix  $\tilde{\mathbf{D}}$  as:

$$\tilde{\mathbf{D}} = V_e \mathbf{D}^e \mathbf{G} \left( V_e \mathbf{G}^{*T} \mathbf{D}^e \mathbf{G} + A_e \mathbf{T}_e \right)^{-1} \mathbf{G}^{*T} \mathbf{D}^e \quad (4.37)$$

and then considering the definition of the matrix  $\mathbf{G}^*$  in equation (4.21),

$$\tilde{\mathbf{D}} = \mathbf{D}^e (-\mathbf{G}) \left( \mathbf{n}_e^T \mathbf{D}^e (-\mathbf{G}) + \mathbf{T}_e \right)^{-1} \mathbf{n}_e^T \mathbf{D}^e. \quad (4.38)$$

Note that  $\mathbf{n}_e$  is not the normal vector to a discontinuity, rather it is a matrix that contains components of the normal vector (see equation (4.22)). Using the result in equation (4.38), equation (4.36) can be rearranged to yield:

$$\mathbf{K}_{\text{con},e} = V_e \mathbf{B}^T \underbrace{(\mathbf{D}^e - \tilde{\mathbf{D}})}_{\mathbf{D}} \mathbf{B} \quad (4.39)$$

where  $\mathbf{D}$  is the equivalent continuum tangent, showing that the EAS-based model can be cast in an equivalent continuum format and solved using a conventional Galerkin procedure. This applies for both the symmetric and non-symmetric (Petrov-Galerkin) models. The tangent  $\mathbf{D}$  in equation (4.39) is almost identical in form to the more traditional smeared crack formulation (De Borst and Nauta, 1985; Rots, 1988).

COMPARISON OF THE EAS-BASED MODEL AND SMEARED CRACK FORMULATIONS 45

The only difference to the smeared crack formulation for a single crack is the matrix  $\mathbf{G}$ , which is a measure of the element size and reflects the element geometry. For the symmetric approach ( $\mathbf{G} = \mathbf{G}^*$ , leading to a symmetric  $\tilde{\mathbf{D}}$  matrix), the only difference with smeared crack formulations is the inclusion of the scalar  $A_e/V_e$  in the tangent, which is a measure of element size. This avoids the need to adjust the hardening modulus element-wise, since the element length scale is already included in the formulation. In light of this equivalence of the embedded discontinuity formulation and classical smeared crack models, it must be concluded that many of the difficulties which dog classical smeared crack models will persist. The embedded discontinuity model has not been implemented in a continuum format since this involves the direct introduction of element length scales into the constitutive model, which is in conflict with the requirements set out in chapter 1.

The material tangent can be further refined for the Von Mises model developed in chapter 3, for which the direction of the displacement jump is fixed and can be described by a scalar in two-dimensions. In two dimensions, the displacement jump vector  $\boldsymbol{\alpha}$  is described by:

$$\boldsymbol{\alpha} = \zeta \mathbf{m} \quad (4.40)$$

where  $\mathbf{m}$  is the direction of the displacement jump (orthogonal to the discontinuity normal) and  $\zeta$  is the magnitude of the displacement jump. This allows the displacement jump at a discontinuity to be described by a scalar quantity. The enhanced degrees of freedom  $\boldsymbol{\alpha}$  can be reduced to a scalar by substituting  $\mathbf{G}$  with  $\mathbf{G}\mathbf{m}$  and  $\mathbf{G}^*$  with  $\mathbf{G}^*\mathbf{m}$  in the weak governing equations and the linearised equations. Following the same procedures as for equations (4.35) to (4.38), equation (4.38) reduces to:

$$\tilde{\mathbf{D}} = \frac{\mathbf{D}^e (-\mathbf{G}\mathbf{m}) (\mathbf{n}_e\mathbf{m})^T \mathbf{D}^e}{(\mathbf{n}_e\mathbf{m})^T \mathbf{D}^e (-\mathbf{G}\mathbf{m}) + T_e} \quad (4.41)$$

Note the similarity of the expression in equation (4.41) to the plastic tangent for non-associative plasticity. The term  $\mathbf{n}_e\mathbf{m}$  that contains the normal components to the discontinuity and the jump direction is analogous to the gradient of the yield surface, the term  $-\mathbf{G}\mathbf{m}$  is analogous to the gradient of the plastic potential and the scalar  $T_e$  can be considered as the hardening modulus (it is a scalar since it is assumed that the direction of the displacement jump  $\mathbf{m}$  is fixed, reducing the discrete constitutive model at a discontinuity to one-dimensional relationship). Defining the ‘elasto-plastic’ tangent as:

$$\mathbf{D}^{\text{ep}} = \mathbf{D}^e - \tilde{\mathbf{D}} = \mathbf{D}^e - \frac{\mathbf{D}^e (-\mathbf{G}\mathbf{m}) (\mathbf{n}_e\mathbf{m})^T \mathbf{D}^e}{(\mathbf{n}_e\mathbf{m})^T \mathbf{D}^e (-\mathbf{G}\mathbf{m}) + T_e} \quad (4.42)$$

shows that the embedded discontinuity model based on incompatible strain modes for Von Mises plasticity could be implemented in an equivalent form as a continuum

plasticity model with a standard Galerkin finite element procedure. The tangent matrix shown in equation (4.42) was derived by Borja (2000) without following the EAS formulation. This can be done by considering the gradient of the yield surface  $f$  as being equal to:

$$\frac{\partial f}{\partial \boldsymbol{\sigma}} = \mathbf{n}_e \mathbf{m} \quad (4.43)$$

and the gradient of the plastic potential  $g$  as:

$$\frac{\partial g}{\partial \boldsymbol{\sigma}} = -\mathbf{G} \mathbf{m}. \quad (4.44)$$

Equation (4.44) implies that the plastic strain field is equal to:

$$\boldsymbol{\varepsilon}^p = -\zeta (\mathbf{G} \mathbf{m}) = -\mathbf{G} \boldsymbol{\alpha} \quad (4.45)$$

and therefore the elastic strain field is equal to:

$$\boldsymbol{\varepsilon}^e = \mathbf{B} \mathbf{a} + \zeta (\mathbf{G} \mathbf{m}) = \mathbf{B} \mathbf{a} + \mathbf{G} \boldsymbol{\alpha}. \quad (4.46)$$

It is clear then that the plastic strain field is made a function of the element size and position of the discontinuity through the formation of the matrix  $\mathbf{G}$ . Therefore, rather than adjusting the hardening modulus per element (as is done for smeared crack models), the plastic strain field is dependent on the element size and discontinuity position.

#### 4.5 Finite element implementation

The use of incompatible strain modes leads to a formulation which can be easily implemented in a conventional finite element framework. The static condensation procedure means that the structure of the global system of equations is identical to that for standard  $C^0$  compatible finite elements. There are however some important implementation aspects not yet addressed. These include whether or not discontinuity paths should be continuous, integration schemes, how the normal vector is determined and when exactly in the solution procedure discontinuities should be introduced. These issues are addressed in this section. Following from assumptions in the variational formulation, only constant strain elements are considered.

##### 4.5.1 Introduction of a discontinuity and numerical integration

Incompatible modes are added to an element at the end of a loading step if the criterion for the development of a discontinuity is met. The criteria for different models were presented in chapter 3. Discontinuities are introduced only at the end of a loading step for two reasons. Firstly, it is undesirable to introduce a discontinuity

into a non-equilibrium state (as would be the case if discontinuities were allowed to develop during the iterative procedure). Secondly, introducing discontinuities at the end of a loading step preserves the quadratic convergence behaviour of the full Newton-Raphson solution scheme.

Three-noded triangular and four-noded tetrahedral elements which are crossed by a discontinuity are numerically integrated with a one-point integration scheme. Since the strain field is constant, the location of the integration point is of no consequence. At the integration point, the stress in the continuum is calculated from the continuum strain and the tractions at a discontinuity are calculated from the displacement jump. History variables need to be stored for both the continuum (if an inelastic continuum model is used) and discontinuity interface parts.

#### 4.5.2 Path continuity

The question of whether or not continuity of discontinuities in a geometric sense should be enforced is not trivial when the discontinuities are included as incompatible modes. Since the displacement jump is not continuous across element boundaries, there is no theoretical reason why path continuity must be enforced. There are however practical considerations which influence whether or not path continuity should be enforced. The undesirable aspect of path continuity is that the element-local nature of the calculation is lost, since the placement of a discontinuity within an element is affected by the position of discontinuities in neighbouring elements.

For the symmetric formulation, enforcement of discontinuity-path continuity is necessary to reasonably calculate the energy dissipated in failure since the formulation is dependent on the area of a discontinuity. For the non-symmetric formulation however, in many cases enforcement of path continuity is not essential since the formulation is independent of the area of a discontinuity. This is an important advantage for three-dimensional calculations where it is not possible to enforce geometric continuity of flat planes in the three-dimensional space. In implementation, complex kinematic interactions between elements in three dimensions often mean that more than one discontinuity must develop at one time, making enforcement of continuity impossible. For two dimensions, a lack of geometric continuity leads to a significantly simpler algorithm since it is not necessary to ‘trace’ discontinuity tips during a calculation. In cases where path continuity is not enforced, discontinuities pass through the centroid of an element. It will be shown through numerical examples that enforcement of path continuity can lead to improved performance with respect to mesh objectivity, although it is not always robust. Enforcement of path continuity with the non-symmetric approach has an effect on the function  $\varphi_e$  which attempts to ensure that the appropriate nodes of an element separate, as discussed in section 4.3.1.

#### 4.5.3 *Choosing the appropriate solution of the normal vector*

The choice of the normal vector for the mode-I constitutive model is straightforward since it comes from the major tensile principal stress direction. The only difficulty arises in the case of a hydrostatic stress state. However, this is rare in practical calculations and was never encountered. For plasticity-based models, the normal vector to a discontinuity comes from an analysis of the acoustic tensor. It was mentioned in section 3.2.5 that analysis of the acoustic tensor leads to multiple solutions for the normal vector to a discontinuity. The difficulty in implementation is to choose the appropriate normal. One option is to restrict the range of possible orientations a priori by visual observation of a problem. When path continuity is enforced, the appropriate normal comes from the continuity requirement, although an initial direction must be specified for the first discontinuity. The situation is more difficult in three dimensions when path continuity cannot be enforced and elements tend to localise in ‘blocks’ due to the kinematic interaction. The numerical examples in this chapter use a simplified version of the method used by Wells and Sluys (2001a) for choosing the appropriate normal direction. The method fits well within finite element procedures since it is carried out entirely at element level.

The derivatives of the yield function with respect to stresses prescribe the direction of the displacement jump relative to a discontinuity plane for the plasticity-based constitutive model in section 3.2. This information is used in choosing the appropriate normal vector. If, at the end of load step, the criterion for the introduction of a discontinuity is met, each possible solution for the normal vector  $\mathbf{n}$  is calculated. For each possible normal  $\mathbf{n}$ , a discontinuity plane that passes through the centroid of the element is constructed and the incremental nodal displacements for the next load step (or from the previous step) are averaged for the nodes on each side of the discontinuity. The incremental displacements provide an indication of the deformation mode of the element. The normal direction which results in the greatest relative difference in incremental displacements on each side of the discontinuity in the direction of the displacement jump (specified by the constitutive model) is chosen as the appropriate normal vector. This method provides an estimate of which normal direction will result in the largest displacement jump in the following step. The numerical example this chapter using the Von Mises model use this procedure for determining the normal direction. For the Von Mises model, the displacement jump is tangential to the discontinuity plane, so the relative difference in incremental displacements, parallel to the discontinuity, on each side of the discontinuity are compared.

#### 4.6 Numerical examples

The numerical examples in this section focus primarily on three-dimensional problems. Examples are tested for objectivity with respect to spatial discretisation. Several issues regarding the performance of the model are addressed as they arise in

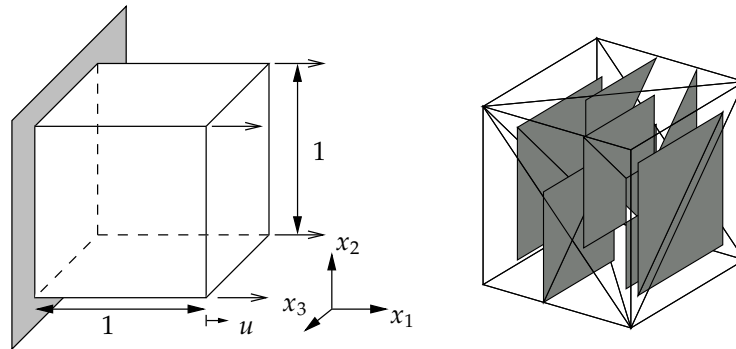


Figure 4.6: Cube of twelve tetrahedral elements pulled in tension. Embedded discontinuities are shown as shaded planes within each element.

the course of analysis. For all numerical examples, an elastic response is assumed in the continuum part of the element, concentrating all inelastic deformations at discontinuities. All problems in this section are solved using a full Newton-Raphson iterative procedure. Unless stated otherwise, all calculations in this section use the non-symmetric formulation.

#### 4.6.1 Comparison of symmetric and non-symmetric implementations

To compare the symmetric and non-symmetric implementations, a unit cube constructed with twelve tetrahedral elements (figure 4.6) is analysed. A node is located at the centre of the cube. The cube is pulled in tension, as shown in figure 4.6, and the discrete constitutive model for mode-I failure developed in chapter 3 is used. A fracture energy of  $G_f = 0.02 \text{ Nmm}^{-1}$  is used. The load–displacement responses and the strain energy, integrated with time, are shown in figure 4.7 for the symmetric and non-symmetric formulations. The input fracture energy is also shown. It would be expected that the strain energy approaches the input fracture energy. It can be seen in figure 4.7 that the symmetric formulation grossly overestimates the energy dissipated in failure, while the non-symmetric approach yields a response closer to the expected response, although the error is still approximately 25%. In this case, the poor performance of the symmetric formulation could be attributed to the calculation of the discontinuity plane area. However, as mentioned previously, it is not possible to enforce path continuity exactly in three dimensions.

#### 4.6.2 Tension bar

To begin examining the objectivity of the model, two simple examples are analysed. Two bars are analysed in tension using three-noded triangular elements. The bars are shown in figure 4.8. The analysis is performed using the mode-I failure mode. To ex-

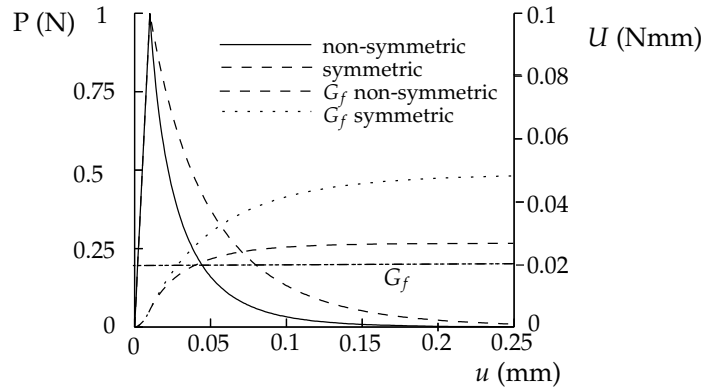


Figure 4.7: Load–displacement response and energy dissipated ( $U$ ) of a unit patch for symmetric and non-symmetric implementations.

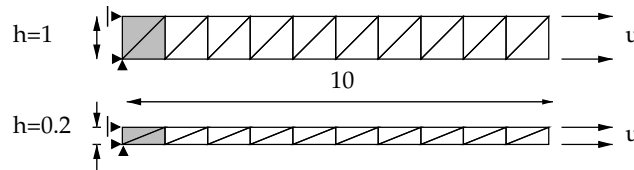


Figure 4.8: Tension bar of height=1 and height=0.2. The shaded elements are slightly weakened. All dimensions in millimetres

amine mesh objectivity, the load–displacement responses of the two bars in figure 4.8 have been normalised by the cross-sectional area of each bar and the tensile strength of the weakened elements. This particular example has been chosen since crack band width models which use simple methods for calculating the characteristic element size often fail for this example. The normalised load–displacement responses for the two bars are shown in figure 4.9. It can be seen that for the embedded discontinuity model that the two bars give an identical response. The response is compared to a smeared crack model based on a Rankine plasticity model. The smeared crack model is adjusted using a length scale  $w$  from the element area  $A_{el}$ , calculated as  $w = \sqrt{2A_{el}}$ . The smeared fracture energy model yields a response identical to that of the embedded discontinuity model for the case of  $h=1$  mm, but overestimates the energy dissipated for the case of  $h=0.2$  mm. This is due to the ambiguity in the calculation of the ‘crack band width’,  $w$ . For the  $h=1$  mm case, the calculated crack band width  $w$  is exact but when  $h=0.2$  mm, the crack bandwidth is mis-calculated. This ambiguity in calculating a crack bandwidth is removed in the embedded model. Also, this is an example where the enforcement of path continuity has no effect on the response since path continuity does not result in a difference in the  $\mathbf{G}$  matrix.

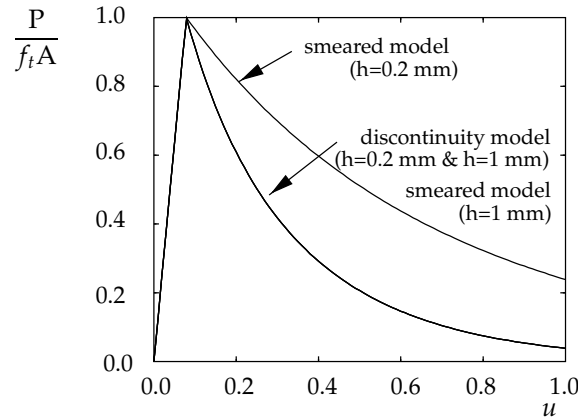


Figure 4.9: Normalised load–displacement response for a tension bar.

#### 4.6.3 Double-notched tension test

The embedded discontinuity model is now used for the analysis of more complex problems. The first example is a double-notched specimen pulled in tension (figure 4.10). The following material properties are adopted: Young’s modulus  $E = 1 \times 10^4$  MPa, tensile strength  $f_t = 1$  MPa, Poisson ratio  $\nu = 0.1$ , fracture energy  $G_f = 0.02$  Nmm<sup>-1</sup> and shear stiffnesses  $d_{\text{int}} = 1 \times 10^2$  Nmm<sup>-3</sup> and  $d_{\kappa=1} = 1 \times 10^{-6}$  Nmm<sup>-3</sup>. To avoid the development of discontinuities where loads are applied or where the specimen is restrained, the specimen is placed between two loading plates. Analyses are performed under load control, with an arclength scheme used to calculate the response past the peak load. The double-notched specimen is analysed using two different, unstructured meshes. The load–displacement responses (displacement is taken as the average displacement of the top loading plate) for two meshes, one with 1534 elements and the other with 3741 elements, are shown in figure 4.11. The load–displacement responses for both the symmetric and non-symmetric formulations are shown. It can be seen that the load-displacement response of the two meshes for the non-symmetric approach are almost identical, indicating objectivity of the load–displacement response with respect to spatial discretisation. Similar to the patch of elements tested in section 4.6.1, the symmetric formulations exhibits an overly ductile response. The deformed meshes for the non-symmetric analyses are shown in figure 4.12. For a finer mesh, with approximately 6000 elements, it was not possible to calculate a converged solution past the peak load. This can be explained by examining the discontinuity patterns through the mesh. Figure 4.13 shows a plane view through the double-notched specimen for the two different meshes. The discontinuity planes have been drawn as planes within elements. Only the finite element mesh on the boundary is visible, although all embedded discontinuities are visible through the depth of the specimen. As the mesh is refined, the number of layers of

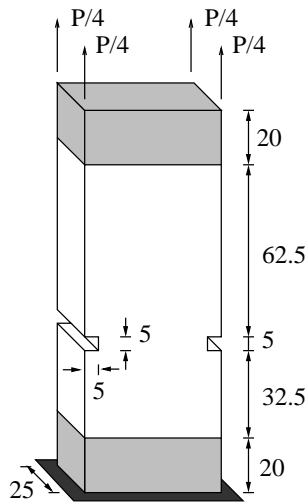


Figure 4.10: Double-notched specimen. The loading plates are shaded. All dimensions in millimetres.

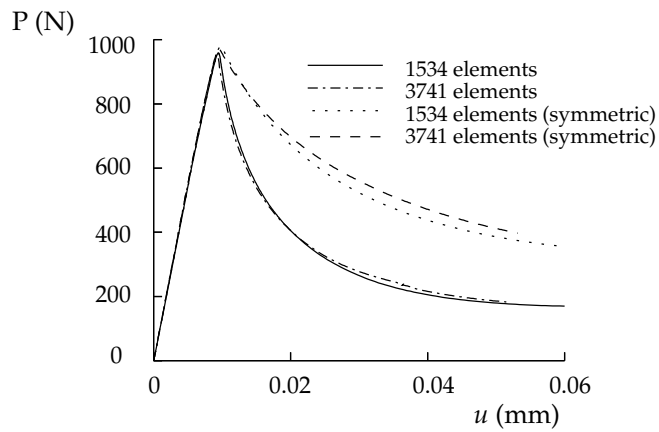


Figure 4.11: Load–displacement response of the double-notched specimen.

NUMERICAL EXAMPLES

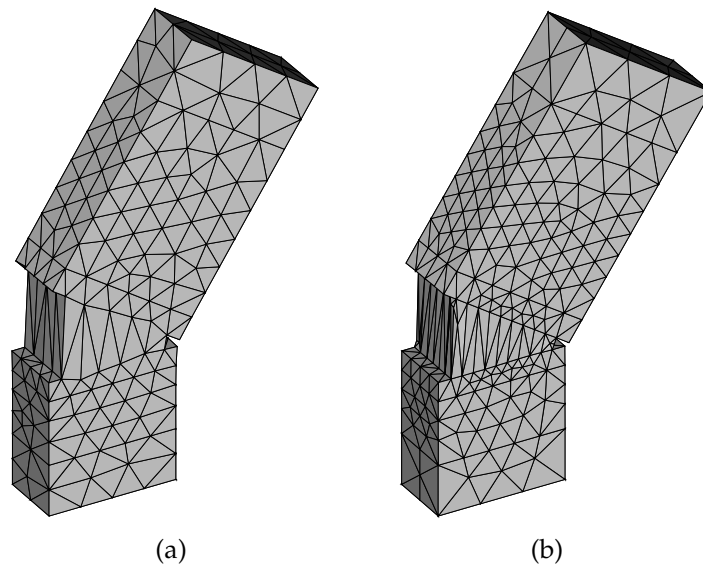
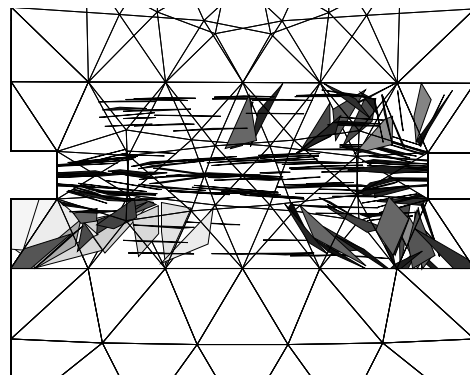
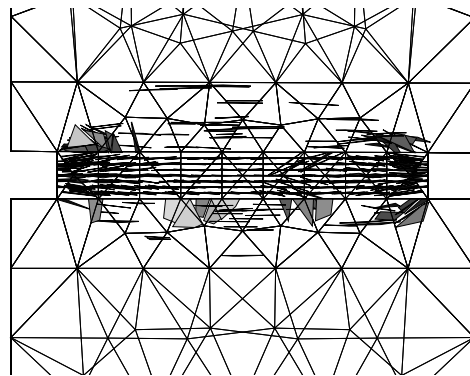


Figure 4.12: Deformed meshes (magnified) with (a) 1534 elements and (b) 3741 elements for the double-notched problem.



(a)



(b)

Figure 4.13: Plane view of embedded discontinuities through the double-notch specimen with (a) 1534 elements and (b) 3741 elements. For clarity, only the mesh of the boundary of the specimen is shown.

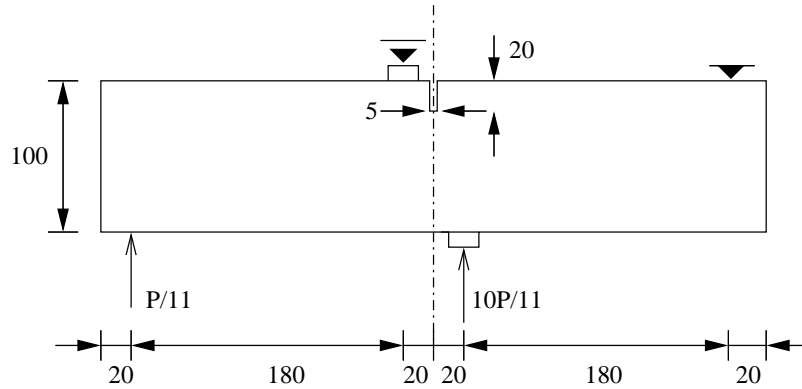


Figure 4.14: SEN beam. Depth = 100. All dimensions in millimetres.

discontinuities increases. As the number of layers increases, it becomes difficult to find a stable equilibrium path. Upon loading, the loading function of parallel discontinuities oscillates within the iterative procedure between loading and unloading. At elements where this occurs, the iterative displacement jump increment at a discontinuity does not approach zero (converged state), but rather changes sign with each iteration. This is similar to problems that are experienced with smeared crack models and stems from the similarity of the formulation with classical smeared models.

#### 4.6.4 Single-edge notched (SEN) beam

A more complex problem is the single-edged notched (SEN) beam, shown in figure 4.14. A series of tests on the SEN beam for concrete were carried out by Schlagen (1993). It was observed experimentally that a crack propagates from the right-hand side of the notch, curving downwards towards the right-hand side of the bottom right support. Previously, smeared crack models in two dimensions have been able to reasonably reproduce the global load–displacement response of the SEN beam, but have failed to capture the correct (curved) failure pattern (Rots, 1988). To capture the correct failure mode with a continuum model, Peerlings et al. (1998) used a strain based version of the isotropic Hoffman criterion. In the stress space, the isotropic Hoffman yield criterion is written as:

$$\frac{3}{2} \|\mathbf{S}\|^2 + (f_c - f_t) \text{tr}(\boldsymbol{\sigma}) - f_c f_t \leq 0 \quad (4.47)$$

where  $f_c$  is the compressive strength of a material. To study the behaviour of the embedded discontinuity model, the SEN beam is analysed in three dimensions. Of special interest is whether the embedded discontinuity model can simulate a curved crack. For analysis of the SEN beam, the mode-I failure model from chapter 3 is used. The materials properties adopted for the analyses are: Young’s modulus  $E =$

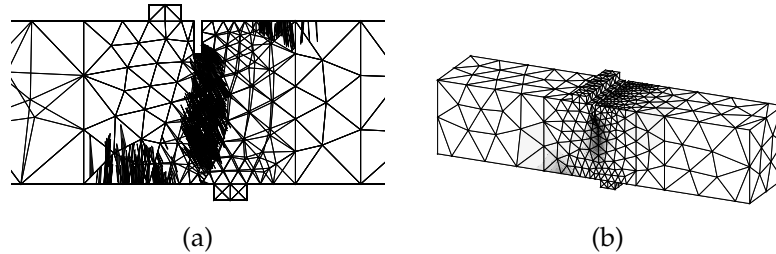


Figure 4.15: Plane view of embedded discontinuities through the SEN beam and the discontinuity normal opening displacement, averaged at element nodes using the principal stress initiation criterion.

$3.5 \times 10^4$  MPa, tensile strength  $f_t = 2.8$  MPa, Poisson’s ratio  $\nu = 0.15$ , fracture energy  $G_f = 0.1$  Nmm $^{-1}$  and the crack shear stiffnesses  $d_{\text{int}} = 1 \times 10^2$  Nmm $^{-3}$  and  $d_{\kappa=1} = 1 \times 10^{-6}$  Nmm $^{-3}$ . Calculations are performed under load control using an arclength procedure to calculate past the peak load. The relative vertical displacement between the two sides of the notch, the crack mouth sliding displacement (CMSD), is used to control the calculation.

Figure 4.15a shows the discontinuities embedded in elements, viewed through the side of the SEN beam. All discontinuity planes through the depth of the SEN beam are shown. Figure 4.15b shows a contour plot on the boundary of the mesh of the opening displacement at the discontinuities, averaged to the element nodes. The contour plot of normal opening displacements shows where discontinuities are open and the dominant crack direction. Examining figure 4.15a, it can be seen that the embedded discontinuity planes around the notch are orientated in a direction which is consistent with experimental observations. However, it can also be seen that a crack does not propagate in the direction of the discontinuities, rather discontinuities develop in parallel layers, propagating directly downwards. This result is very similar to results obtained using smeared crack models (Rots, 1988).

In an ad hoc attempt to simulate a curved crack, the principal stress criterion for discontinuity initiation has been supplemented by the isotropic Hoffman yield function (equation (4.47)), with the compressive strength chosen to be 10 times greater than the tensile strength. If the major tensile principal stress exceeds the tensile strength *and* the Hoffman criterion is violated, a discontinuity is introduced. The discontinuity pattern (at peak load) using the modified criterion is shown in figure 4.16a. The additional criterion avoids the development of discontinuities moving directly downwards from the notch. The resulting crack pattern is consistent with experimental observations (Schlangen, 1993). The combined initiation criterion is however inconsistent with the applied discrete constitutive model and the spatial orientation of a discontinuity. The load–displacement responses for the SEN beam are shown in

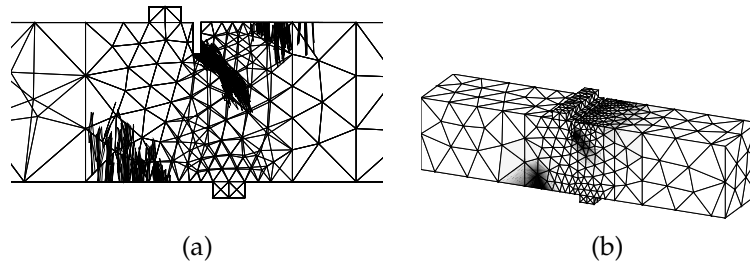


Figure 4.16: Plane view of embedded discontinuities through the SEN beam and the discontinuity normal opening displacement, averaged at element nodes using the modified initiation criterion.

figure 4.17. The predicted peak load for both the principal stress criterion and the modified criterion are in reasonable agreement with the experimental results. Due to a lack of robustness, it was not possible to calculate far past the peak load. Despite the rough load–displacement response for the modified criterion, the solution had converged at the end of all load increments. The cause of the rough load–displacement response is the inconsistency between the constitutive model and the discontinuity introduction criterion. It is possible that when both criteria are met (principal stress and isotropic Hoffman) that the principal stress is considerably greater than the tensile strength of the material (since the extra Hoffman criterion has delayed the introduction of a discontinuity). When a discontinuity is introduced, the normal traction at the discontinuity is made equal to the tensile strength of the material, which can result in a sudden change of the stress state in an element.

The crack patterns in figure 4.15 suggest that a principal stress initiation criterion with enforcement of path continuity could lead to a correct failure mode, since the individual discontinuities are orientated in a direction consistent with experimental observations. To investigate this, the SEN beam is simulated in two dimensions, under plane stress conditions, with path continuity enforced. Figure 4.18 shows the central area of the SEN beam with the discontinuities indicated by the heavy line. Clearly the enforcement of path continuity leads to a curved crack path which is in good agreement with experimental observations. Path continuity places the restriction that only the element ahead of the current ‘crack tip’ may develop a discontinuity, therefore avoiding the development of parallel layers of discontinuities. A consequence of this is that the tensile strength of the material may be exceeded in elements away from the discontinuity (Alfaiate et al., 2001). In some cases, the enforcement of crack path continuity can lead to a loss of robustness of the procedure, such as when a discontinuity must cross an element side to which it is almost parallel. Consider the situation shown in figure 4.19 for an opening crack. The ‘crack tip’ is located in element 1, and if path continuity is enforced can only propagate into

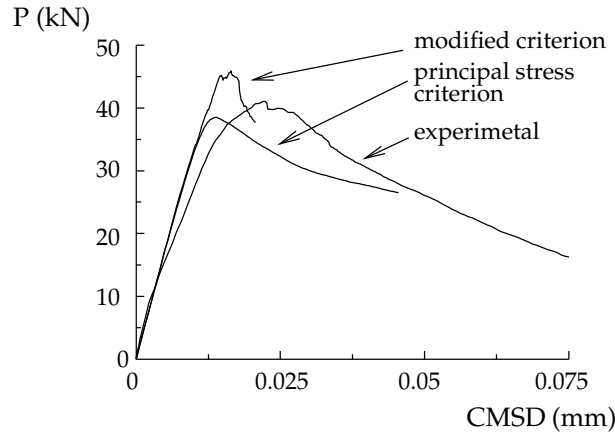


Figure 4.17: Load–displacement response of the SEN beam for the principal stress initiation criterion the modified initiation criterion and experimental results (Schlangen, 1993). The displacement measured is the crack mouth sliding displacement (CMSD).

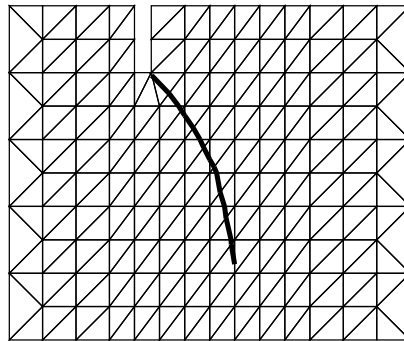


Figure 4.18: Crack path for a two-dimensional SEN beam analysis with path continuity enforced.

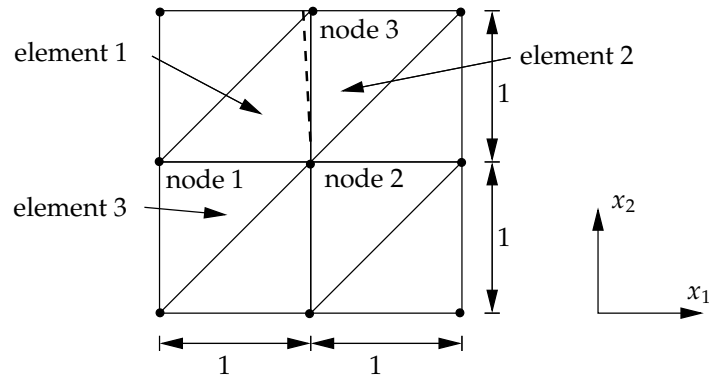


Figure 4.19: Crack pattern for two-dimensional SEN beam analysis with path continuity enforced. The discontinuity is shown as a dashed line.

element 2. The discontinuity is almost vertical ( $\mathbf{n} \approx (1, 0)$ ), and divides node 3 from nodes 1 and 2. The function  $\varphi_e$  for element 1 is equal to the shape function associated with node 3 ( $\nabla \varphi_e = \nabla N_3 = (0, 1)$ ). Important is how tensile stresses in the  $x_1$  direction can develop in element 2 in order to initiate a discontinuity allowing the further propagation of the crack. Ideally, a normal opening displacement  $v_n$  at the discontinuity in element 1 will result in a relative displacement between nodes 2 and 3 in the  $x_1$ -direction equal to  $v_n$ . The derivatives of the shape functions associated with nodes 2 and 3 for element 2 in the  $x_1$  direction are equal to zero and -1, respectively. Therefore a positive displacement at node 2 induces no stress in the  $x_1$  direction and a positive displacement at node 3 in the  $x_1$  will induce compressive stresses in element 2 in the  $x_1$  direction. Any positive displacement in the  $x_1$  direction of node 3 (which reflects correctly the effect of the discontinuity) leads to compressive stresses in element 2. This makes it difficult to develop a tensile stress in element 2, despite the presence of a discontinuity on the boundary of the element. The consequence is that the crack is 'blocked' by an element and the tensile stress in surrounding elements exceeds the tensile strength of the material. For this reason, the method performs poorly when the mesh bias is slightly different to the actual discontinuity path as this requires that discontinuities cross element boundaries to which they are almost parallel. The elements are kinematically unable to transfer the effect of a discontinuity to neighbouring elements. A calculation cannot be performed past the point shown in figure 4.19 since the crack path is blocked. In contrast, if the discontinuity was moved slightly such that it separated node 1 from nodes 2 and 3 and therefore must propagate into element 3, any opening displacement at the discontinuity would induce tensile stresses in element 3, allowing crack propagation into element 3.

It was noted by Borja (2000) that the model performs poorly when the matrices

$\mathbf{G}^*$  and  $\mathbf{G}$  differ significantly. For element 1 in figure 4.19, the matrix  $\mathbf{G}^*$  approaches:

$$\mathbf{G}^* \approx -\frac{1}{1/2} \begin{bmatrix} 1 & 0 \\ 0 & 0 \\ 0 & 1 \end{bmatrix} \quad (4.48)$$

and the matrix  $\mathbf{G}$  is equal to:

$$\mathbf{G} = - \begin{bmatrix} 0 & 1 \\ 0 & 0 \\ 1 & 0 \end{bmatrix} \quad (4.49)$$

For the case shown in figure 4.19, the  $\mathbf{G}^*$  and  $\mathbf{G}$  matrices differ substantially, therefore the performance is very poor. If the discontinuity was moved slightly as to separate node 1 from nodes 2 and 3, the matrices  $\mathbf{G}^*$  and  $\mathbf{G}$  would be qualitatively identical. This problem was illustrated in figure 4.5 where it was shown how a small change in the normal vector results in a sudden change in the kinematic enhancement. For robust implementation and objective results, it is necessary to modify the mesh to avoid a large difference between the matrices  $\mathbf{G}$  and  $\mathbf{G}^*$ . This however is against the intentions of the method, and if mesh modifications are required it may be better to use a conventional smeared model with the element boundaries aligned with the crack or shear band path. The influence of the  $\mathbf{G}$  matrix for the examples in figure 4.19 also highlights the question over the stability of the procedure when an infinitely small difference in the position of a discontinuity can lead to a sudden and discontinuous change of the  $\mathbf{G}$  matrix.

#### 4.6.5 Biaxial test and locking in three dimensions

To examine the embedded discontinuity model in three dimensions for mode-II failure, the biaxial test is analysed (figure 4.20). The biaxial test is analysed using the discrete Von Mises constitutive model. Analysis of the biaxial specimen tests the ability of the method outlined in section 4.5.3 for determining automatically the correct orientation of the discontinuity planes. A uniform downward displacement is imposed on the top edge of the biaxial specimen. Poisson’s ratio is chosen as 0.49 and the front and back sides have been restrained in the  $x_3$  direction to simulate plane strain conditions. For plane strain conditions with Poisson’s ratio  $\nu \rightarrow 0.5$ , it is known that discontinuities should develop at  $\pm 45$  degrees to the  $x_1$  axis according to equation (3.38). Elements in the shaded zone in figure 4.20 have been weakened to induce a shear band. Due to the symmetry of the problem, the range of possible normal directions must be prescribed for the weakened elements.

Figure 4.21 shows the embedded discontinuity planes in the three-dimensional biaxial problem. The automatic procedure has captured the correct orientations of the planes and has been able to capture two orthogonal shear bands without using any global information. Careful observation of the pattern of discontinuities shows

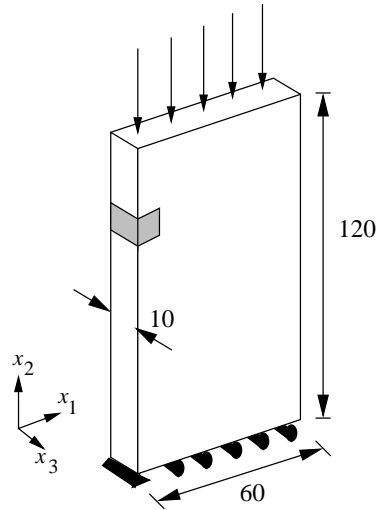


Figure 4.20: Biaxial specimen. All dimensions in millimetres.

that the example is not objective with respect to spatial discretisation. The individual discontinuities are orientated correctly, but the shear band follows the mesh lines. At first consideration, in two dimensions this could be overcome by the enforcement of path continuity, although, for the reasons discussed in the previous section, this would lead to a very poor response since the discontinuities are almost parallel to the element boundaries.

It was not possible to calculate the load–displacement response past the peak load for the three-dimensional biaxial test due to a locking response. The complex interaction between elements in three dimensions, in combination with a kinematic constraint (zero normal opening displacement), make it difficult to avoid locking. Neighbouring elements effectively ‘block’ sliding displacements in elements. The reasons for this can be explained by examining a single element. Consider the three different configurations shown in figure 4.22. Each of the three configurations is analysed using the Von Mises model. The load–displacement responses for the three configurations are shown in figure 4.23 and the deformed modes for configurations (b) and (c) are shown in figure 4.24. When loaded, the first configuration exhibits a locking response and is unable to soften. This case is similar to what occurs in three dimensions when neighbouring elements restrain deformations in an element crossed by a discontinuity, as in the biaxial test. The second case exhibits a softening response, although the elongating failure mode, shown in figure 4.24, is incorrect. For the third case (c), the discontinuity is relocated as to separate node one from nodes two and three. This of course has an impact of the form of the  $\mathbf{G}$  matrix. The element then exhibits a softening response and the expected shearing deformation mode. Again,

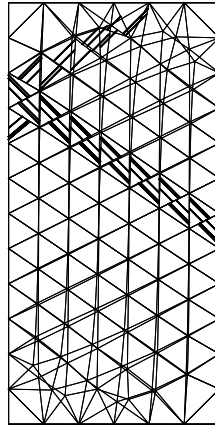


Figure 4.21: Plane view through the mesh for the biaxial specimen. The embedded discontinuities through the specimen are shown as heavy lines. For clarity, only the mesh on the boundary is shown.

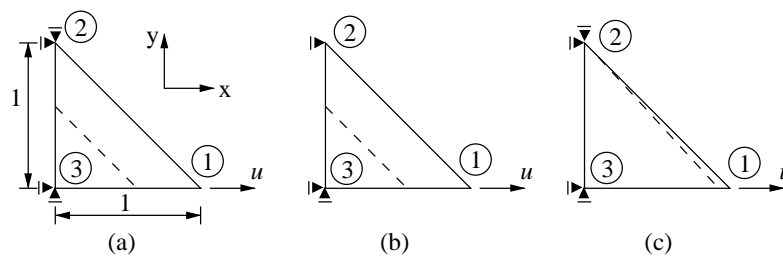


Figure 4.22: Plane view of a tetrahedral element loaded in tension and crossed by a discontinuity (dashed line). The fourth node is fully restrained and lies out of the page directly above node three.

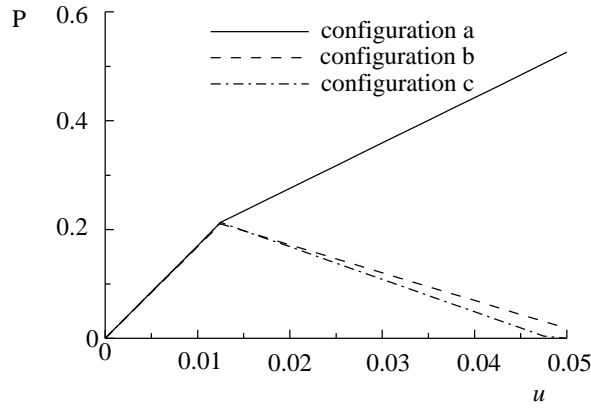


Figure 4.23: Load displacement responses for the three single element configurations shown in figure 4.22.

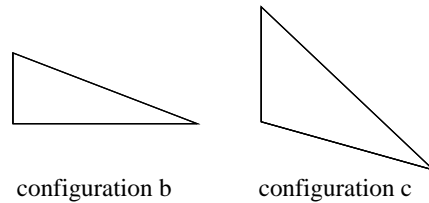


Figure 4.24: Deformation modes for single element tests.

very small changes in the discontinuity position lead to drastic changes in the element response raising serious question regarding the stability of the method.

#### 4.7 Summary of embedded discontinuity formulation

The embedded discontinuity model has been developed and investigated for the simulation of localised failure in three dimensions. It is explored as a more effective and technically sounder method for practical analysis than classical smeared failure models. The model is developed from the three-field variational statements to highlight features of the model and the assumptions required for finite element implementation. Practical considerations in the implementation of the model are addressed, such as when a discontinuity should be introduced, how its orientation can be determined and path continuity. Three-dimensional numerical examples are used to illustrate applications of the model, while small calculations are used to elucidate special features.

The embedded discontinuity model cannot be considered as a discontinuous failure model. The effect of a discontinuity is incorporated in the strain field of an ele-

ment, and through some manipulations the amplitude of the enhanced strain mode can be interpreted as a displacement jump. It is notable that the Heaviside function does not appear anywhere in the formulation. It was shown that both the symmetric and non-symmetric formulations introduce numerical length scales that are related to the element size. It was also shown that the formulations can be cast in a conventional continuum Galerkin format, with the effects of a discontinuity included in the material continuum tangent. The improved kinematic description for the non-symmetric formulation makes it possible to analyse three-dimensional problems with unstructured meshes, although the model is still discretisation-dependent and cannot be considered technically sounder than smeared crack models. From an implementation standpoint, the embedded discontinuity model can be considered as a moderate improvement upon classical smeared models. The improvements can be summarised as:

- discrete constitutive models can be applied;
- no artificial numerical parameters appear in the constitutive model;
- improved objectivity with respect to mesh structure; and
- path continuity can be applied in two dimensions to model curved cracks, although this must be done with caution.

Since the enhanced modes are incompatible, the usual structure of a finite element calculation is preserved. This means that implementation is simple, fast and efficient.

There exists several limitations of the embedded model. The assumptions required in the variational formulations mean that the method should be limited to constant strain elements. Also, assumptions are required in the displacement decomposition which forces the strain field to be equal on opposite sides of a discontinuity. Particularly for geometrically non-linear cases, this is a serious and unjustifiable restriction, as will be shown in chapter 6. Numerical examples have illustrated that the model cannot fully overcome mesh alignment sensitivity in three dimensions. Even for two-dimensional problems, adjustments of the mesh may be necessary for robust implementation. These problems are inevitable when the incorporation of a discontinuity is so closely related to the finite element itself and the problem is ill-posed. Upon mesh refinement in three dimensions, the method lacks robustness. In addition, questions have been raised as to the stability of the method when the element enhancements can change suddenly when the position of a discontinuity is moved slightly. The method developed in the following chapter will be shown to overcome the weakness of the embedded discontinuity model by including discontinuities in the displacement field in a mathematically sound manner, at the expense of increased complexity in implementation.

## Chapter 5

### Cohesive zone model based on partitions of unity

In this chapter, a genuine displacement discontinuity is introduced to the displacement field of finite elements. This is done by adding a discontinuous function to the underlying basis functions used for interpolating the displacement field. By representing a displacement discontinuity in the basis of the displacement field interpolation, a discontinuity can propagate arbitrarily through a body, completely independent of the finite element mesh. Discontinuities can propagate through elements, between elements and the ‘tip’ of a discontinuity does not have to coincide with an element boundary. In stark contrast to the embedded discontinuity formulation in chapter 4, the displacement jump at a discontinuity is continuous along the length of the discontinuity. Since the displacement jump is compatible, there are no restrictions on the type of underlying finite elements used and the interpolation of the displacement jump along a discontinuity is of the same polynomial order as the underlying finite element.

Discontinuous functions are added locally to the underlying displacement basis using partitions of unity. A collection of functions forms a partition of unity if the sum of all the functions at a spatial point is equal to unity. This is a property that has been exploited in the context of meshless methods where moving least-squares shape functions form a partition of unity (Duarte and Oden, 1996). Finite element shape functions also form partitions of unity. Using this property, Babuška and Melnik (1997) used the partition of unity concept to add terms from the span of the analytical solution to the underlying basis of standard polynomial finite elements for problems where standard finite elements were known to perform poorly. To simulate cracks in elastic bodies, Fleming et al. (1997) added the functions spanning the crack near-tip displacement solution to the interpolation basis using the element-free Galerkin method and the partition of unity concept. Using the partition of unity property of finite element shape functions, Belytschko and Black (1999) and Moës et al. (1999) added the span of the near-tip solution to finite elements, simulating cracks in elastic bodies independently of the mesh and without the use of special elements for capturing the stress singularity at a sharp crack tip. To simulate cohe-

sive cracks and slip planes, here the partition of unity property is used to model a propagating discontinuity under both quasi-static and dynamic loading conditions.

To begin the formulation, features of the partition of unity method (PUM) are reviewed and the link with conventional finite elements is elaborated. The formulation is cast in a form that is general for any type of local enrichment of the underlying basis. To simulate a cohesive zone, the Heaviside jump is added to the enhanced basis. Then, similar to chapter 4, kinematic relationships are inserted into the weak equilibrium equation. This leads naturally to the form of the element mass and stiffness matrices and the internal force vector for a finite element formulation which includes displacement discontinuities in the interpolation basis. Unlike the embedded discontinuity model based on incompatible strain modes in chapter 4, a discontinuity is genuinely added to the formulation with a discontinuity appearing in the displacement field. Key aspects of the implementation are addressed before the performance of the method is illustrated with numerical examples.

### 5.1 Partition of unity concept

It was shown by Duarte and Oden (1996) that a field can be interpolated over a body  $\Omega$  using partitions of unity. A collection of functions  $\varphi_i$ , each associated with a discrete point  $i$ , constitutes a partition of unity if:

$$\sum_{i=1}^n \varphi_i(\mathbf{x}) = 1 \quad \forall \mathbf{x} \in \Omega \quad (5.1)$$

where  $n$  is the number of discrete points (nodes). For the partition unity property to hold, the functions  $\varphi_i$  must be uniquely defined on  $\Omega$ . This implies that the functions  $\varphi_i$  must be at least  $C^0$  continuous. If  $\varphi$  is a partition of unity, a field  $u$  over a volume  $\Omega$  can be interpolated in terms of discrete nodal values by:

$$u = \sum_{i=1}^n \varphi_i \left( a_i + \sum_{j=1}^m b_{ij} \gamma_j \right) \quad (5.2)$$

where  $\varphi_i$  is a partition of unity,  $a_i$  and  $b_{ij}$  are discrete nodal values,  $\gamma_j$  is an ‘enhanced’ basis and  $m$  is the number of terms in the enhanced basis for a particular node. To avoid linear dependency, the terms in the enhanced basis  $\gamma$  should not come from the span of the partition unity functions  $\varphi$ . Importantly,  $m$  is not necessarily the same for all nodes, and it can vary during a calculation.

It is equation (5.2) that provides the link between meshless methods and the finite element method. The differences between the methods lies in the choice of the functions  $\varphi$ . The element-free Galerkin method (Belytschko et al., 1994) uses a weighted moving least squares function as the partition of unity with, in general, an empty enhanced basis. More generally, hp clouds (Duarte and Oden, 1996) use a weighted

moving least-squares function as the partition of unity with a non-empty enhanced basis. Importantly, finite element shape functions are also partitions of unity since:

$$\sum_{i=1}^n N_i(\mathbf{x}) = 1. \quad (5.3)$$

The difference between the finite element method and meshless methods lies in the choice of the partition of unity functions. In the standard finite element method, the partition of unity functions are the polynomial shape functions and the enhanced basis is empty. There is however no reason why the enhanced basis cannot be exploited. In this chapter it is shown how the enhanced basis can be used to model propagating discontinuities by adding a discontinuous function to the underlying interpolation basis of the displacement field.

## 5.2 Finite elements as partitions of unity

From equation (5.2) and considering finite element shape functions as partitions of unity, the displacement field over a body can be written in finite element notation as:

$$\mathbf{u} = \mathbf{N}\mathbf{a} + \mathbf{N}_\gamma \mathbf{b} \quad (5.4)$$

where  $\mathbf{N}$  is a matrix containing the usual (polynomial) shape functions,  $\mathbf{a}$  contains the regular nodal degrees of freedom,  $\mathbf{N}_\gamma$  is a matrix containing the enhanced basis terms from  $\gamma$  and  $\mathbf{b}$  is a vector containing the enhanced nodal degrees of freedom. Note that the enhanced basis  $\gamma_j$  is now cast in a matrix format  $\mathbf{N}_\gamma$  and the enhanced degrees of freedom  $b_{ij}$  are now cast as a vector  $\mathbf{b}$ . The number of enhanced degrees of freedom per node is equal to the number of terms in the enhanced basis multiplied by the spatial dimension. The vector form of the strain field in terms of nodal displacements is expressed as:

$$\boldsymbol{\varepsilon} = \mathbf{B}\mathbf{a} + \mathbf{B}_\gamma \mathbf{b} \quad (5.5)$$

where  $\mathbf{B} = \mathbf{L}\mathbf{N}$  and  $\mathbf{B}_\gamma = \mathbf{L}(\mathbf{N}\mathbf{N}_\gamma)$ . The matrix  $\mathbf{L}$  contains differential operators.

$$\mathbf{L} = \begin{bmatrix} \frac{\partial}{\partial x} & 0 & 0 \\ 0 & \frac{\partial}{\partial y} & 0 \\ 0 & 0 & \frac{\partial}{\partial z} \\ \frac{\partial}{\partial y} & \frac{\partial}{\partial x} & 0 \\ 0 & \frac{\partial}{\partial z} & \frac{\partial}{\partial y} \\ \frac{\partial}{\partial z} & 0 & \frac{\partial}{\partial x} \end{bmatrix} \quad (5.6)$$

The general forms of the matrices  $\mathbf{N}_\gamma$  and  $\mathbf{B}_\gamma$  are not elaborated since for the purposes of this chapter they reduce to a particularly simple format, as will be shown in the

following section. The general form of the matrices  $\mathbf{N}_\gamma$  and  $\mathbf{B}_\gamma$  for a single node can be found in Wells and Sluys (2001d).

The critical feature of the interpolation in equation (5.4) is that the interpolation is constructed on a per-node basis. It is possible to enhance the region around individual nodes to improve a solution during a calculation by adding terms to the matrix  $\mathbf{N}_\gamma$ , without modifying the original finite element mesh. The addition of terms to the enhanced basis results in extra degrees of freedom at *existing* nodes. This makes it ideal in situations where the regions in which enhancements are required are not known a priori and are small when compared to the total domain. This feature has been exploited successfully to overcome volumetric locking during plastic flow with low-order elements by locally enhancing the basis with higher-order polynomial terms in regions where plastic flow is detected (Wells and Sluys, 2001d).

### 5.3 Enhancement of the standard basis with a discontinuous function

In order to model discontinuities in the displacement field, it is possible to add discontinuous functions to the enhanced basis. Examining the displacement decomposition in equation (2.1), it can be seen that it is similar in form to the displacement interpolation in equation (5.4). The matrix  $\mathbf{N}$  together with the regular degrees of freedom  $\mathbf{a}$  can be considered to represent the continuous part of the displacement field  $\hat{\mathbf{u}}$  and the matrix product  $\mathbf{N}\mathbf{N}_\gamma$  together with the enhanced degrees of freedom  $\mathbf{b}$  represent the discontinuous part of the displacement field  $\mathcal{H}_{\Gamma_d}\hat{\mathbf{u}}$ . Further, for the discontinuous part, the continuous function  $\hat{\mathbf{u}}$  is interpolated by  $\mathbf{N}$  and the matrix  $\mathbf{N}_\gamma$  reduces simply to the scalar Heaviside function  $\mathcal{H}_{\Gamma_d}$ . Note that no assumptions have been made as to the form of the function  $\hat{\mathbf{u}}$ , as was necessary for the incompatible mode formulation where it was assumed to be a spatially constant function. The function  $\hat{\mathbf{u}}$  is dependent on the chosen order of the shape functions. Inserting the Heaviside function into the enhanced basis in equation (5.4), the displacement and acceleration fields can be written as:

$$\mathbf{u} = \underbrace{\mathbf{N}\mathbf{a}}_{\hat{\mathbf{u}}} + \mathcal{H}_{\Gamma_d} \underbrace{\mathbf{N}\mathbf{b}}_{\hat{\mathbf{u}}} \quad (5.7a)$$

$$\ddot{\mathbf{u}} = \underbrace{\mathbf{N}\ddot{\mathbf{a}}}_{\hat{\ddot{\mathbf{u}}}} + \mathcal{H}_{\Gamma_d} \underbrace{\mathbf{N}\ddot{\mathbf{b}}}_{\hat{\ddot{\mathbf{u}}}}. \quad (5.7b)$$

Taking the gradient of equation (5.7a), the vector form of the strain field is expressed as:

$$\boldsymbol{\varepsilon} = \mathbf{B}\mathbf{a} + \mathcal{H}_{\Gamma_d}\mathbf{B}\mathbf{b} + (\delta_{\Gamma_d}\mathbf{n}_e)\mathbf{N}\mathbf{b} \quad (5.8)$$

where  $\mathbf{n}_e$  is a matrix containing the normal components to a discontinuity, as defined in equation (4.22). Effectively, the regular degrees of freedom  $\mathbf{a}$  represent the continuous part of the displacement field, while the enhanced degrees of freedom  $\mathbf{b}$

represent the displacement jump across a discontinuity. Adding the Heaviside function to the enhanced basis for finite elements results in a displacement jump along a discontinuity of the same order as the interpolating polynomial shape functions. Also, the magnitude of the displacement jump is continuous across element boundaries. Unlike the embedded discontinuity formulation in chapter 4, the degrees of freedom describing the displacement jump are global and cannot be solved for at a local level. The shape functions associated with the degrees of freedom describing the displacement jump overlap and extend beyond the element crossed by a discontinuity. Rather than enhancing an element, the *support* of a node is enhanced.

### 5.3.1 Variational formulation

To develop the finite element formulation, the displacement field which includes a discontinuity must be inserted into the weak equation of motion. Since in this case the displacement jump is compatible, only the standard weak equation of motion need be considered, with the displacement field being the only independent unknown. The weak equation of motion is written as:

$$\int_{\Omega} \nabla^s \boldsymbol{\eta} : \boldsymbol{\sigma} \, d\Omega + \int_{\Omega} \boldsymbol{\eta} \cdot \rho \ddot{\mathbf{u}} \, d\Omega - \int_{\Omega} \boldsymbol{\eta} \cdot \rho \mathbf{b} \, d\Omega - \int_{\Gamma_u} \boldsymbol{\eta} \cdot \bar{\mathbf{t}} \, d\Gamma = 0 \quad (5.9)$$

which must hold for all admissible variations of displacement,  $\boldsymbol{\eta}$ . Taking the space of admissible displacement variations as the same as actual displacements (a Galerkin approach), from the displacement decomposition in equation (2.1), variations of displacement  $\boldsymbol{\eta}$  are decomposed as:

$$\boldsymbol{\eta} = \hat{\boldsymbol{\eta}} + \mathcal{H}_{\Gamma_d} \tilde{\boldsymbol{\eta}}. \quad (5.10)$$

Inserting the variations of the displacement field in equation (5.10) and the actual acceleration field from equation (2.4) into the weak equation of motion and ignoring body forces yields:

$$\begin{aligned} \int_{\Omega} \nabla^s (\hat{\boldsymbol{\eta}} + \mathcal{H}_{\Gamma_d} \tilde{\boldsymbol{\eta}}) : \boldsymbol{\sigma} \, d\Omega + \int_{\Omega} (\hat{\boldsymbol{\eta}} + \mathcal{H}_{\Gamma_d} \tilde{\boldsymbol{\eta}}) \cdot \rho (\ddot{\mathbf{u}} + \mathcal{H}_{\Gamma_d} \ddot{\tilde{\mathbf{u}}}) \, d\Omega \\ = \int_{\Gamma_u} (\hat{\boldsymbol{\eta}} + \mathcal{H}_{\Gamma_d} \tilde{\boldsymbol{\eta}}) \cdot \bar{\mathbf{t}} \, d\Gamma \end{aligned} \quad (5.11)$$

which must hold for all admissible variations  $\hat{\boldsymbol{\eta}}$  and  $\tilde{\boldsymbol{\eta}}$ . From equation (2.5), the gradient of the variation of displacements in equation (5.10) is expressed as:

$$\nabla^s \boldsymbol{\eta} = \nabla^s \hat{\boldsymbol{\eta}} + \mathcal{H}_{\Gamma_d} (\nabla^s \tilde{\boldsymbol{\eta}}) + \delta_{\Gamma_d} (\tilde{\boldsymbol{\eta}} \otimes \mathbf{n})^s. \quad (5.12)$$

Inserting equation (5.12) into the weak equation of motion in equation (5.11) and rearranging yields:

$$\begin{aligned} & \int_{\Omega} \nabla^s \hat{\boldsymbol{\eta}} : \boldsymbol{\sigma} \, d\Omega + \int_{\Omega} \mathcal{H}_{\Gamma_d} (\nabla^s \tilde{\boldsymbol{\eta}}) : \boldsymbol{\sigma} \, d\Omega + \int_{\Omega} \delta_{\Gamma_d} (\tilde{\boldsymbol{\eta}} \otimes \mathbf{n})^s : \boldsymbol{\sigma} \, d\Omega \\ & + \int_{\Omega} \hat{\boldsymbol{\eta}} \cdot \rho \ddot{\mathbf{u}} \, d\Omega + \int_{\Omega} \mathcal{H}_{\Gamma_d} \hat{\boldsymbol{\eta}} \cdot \rho \ddot{\mathbf{u}} \, d\Omega + \int_{\Omega} \mathcal{H}_{\Gamma_d} \tilde{\boldsymbol{\eta}} \cdot \rho \ddot{\mathbf{u}} \, d\Omega + \int_{\Omega} \mathcal{H}_{\Gamma_d} \tilde{\boldsymbol{\eta}} \cdot \rho \ddot{\mathbf{u}} \, d\Omega \\ & = \int_{\Gamma_u} (\hat{\boldsymbol{\eta}} + \mathcal{H}_{\Gamma_d} \tilde{\boldsymbol{\eta}}) \cdot \bar{\mathbf{t}} \, d\Gamma. \end{aligned} \quad (5.13)$$

Integrating the integral whose integrand contains the Dirac-delta distribution over the volume  $\Omega$  (using equation (2.12)) and eliminating the Heaviside functions by changing the integration domain of integrals whose integrand contains the Heaviside function from  $\Omega$  to  $\Omega^+$  (based on equation (2.2)),

$$\begin{aligned} & \int_{\Omega} \nabla^s \hat{\boldsymbol{\eta}} : \boldsymbol{\sigma} \, d\Omega + \int_{\Omega^+} (\nabla^s \tilde{\boldsymbol{\eta}}) : \boldsymbol{\sigma} \, d\Omega + \int_{\Gamma_d} \tilde{\boldsymbol{\eta}} \cdot \mathbf{t} \, d\Gamma + \int_{\Omega} \hat{\boldsymbol{\eta}} \cdot \rho \ddot{\mathbf{u}} \, d\Omega \\ & + \int_{\Omega^+} \hat{\boldsymbol{\eta}} \cdot \rho \ddot{\mathbf{u}} \, d\Omega + \int_{\Omega^+} \tilde{\boldsymbol{\eta}} \cdot \rho \ddot{\mathbf{u}} \, d\Omega + \int_{\Omega^+} \tilde{\boldsymbol{\eta}} \cdot \rho \ddot{\mathbf{u}} \, d\Omega = \int_{\Gamma_u} (\hat{\boldsymbol{\eta}} + \mathcal{H}_{\Gamma_d} \tilde{\boldsymbol{\eta}}) \cdot \bar{\mathbf{t}} \, d\Gamma \end{aligned} \quad (5.14)$$

where  $\mathbf{t}$  ( $= \boldsymbol{\sigma} \mathbf{n}$ ) are traction forces acting at the surface  $\Gamma_d$ . Taking first variations  $\hat{\boldsymbol{\eta}}$  ( $\tilde{\boldsymbol{\eta}} = \mathbf{0}$ ) and then variations  $\tilde{\boldsymbol{\eta}}$  ( $\hat{\boldsymbol{\eta}} = \mathbf{0}$ ), two separate variational statements can be written as:

$$\int_{\Omega} \nabla^s \hat{\boldsymbol{\eta}} : \boldsymbol{\sigma} \, d\Omega + \int_{\Omega} \hat{\boldsymbol{\eta}} \cdot \rho \ddot{\mathbf{u}} \, d\Omega + \int_{\Omega^+} \hat{\boldsymbol{\eta}} \cdot \rho \ddot{\mathbf{u}} \, d\Omega = \int_{\Gamma_u} \hat{\boldsymbol{\eta}} \cdot \bar{\mathbf{t}} \, d\Gamma \quad (5.15a)$$

$$\begin{aligned} & \int_{\Omega^+} \nabla^s \tilde{\boldsymbol{\eta}} : \boldsymbol{\sigma} \, d\Omega + \int_{\Gamma_d} \tilde{\boldsymbol{\eta}} \cdot \mathbf{t} \, d\Gamma + \int_{\Omega^+} \tilde{\boldsymbol{\eta}} \cdot \rho \ddot{\mathbf{u}} \, d\Omega \\ & + \int_{\Omega^+} \tilde{\boldsymbol{\eta}} \cdot \rho \ddot{\mathbf{u}} \, d\Omega = \int_{\Gamma_u} \mathcal{H}_{\Gamma_d} \tilde{\boldsymbol{\eta}} \cdot \bar{\mathbf{t}} \, d\Gamma. \end{aligned} \quad (5.15b)$$

The above equations are reminiscent of a coupled problem. The formulation effectively describes the continuous and discontinuous fields through separate equations which are coupled through the continuum. Consider now a small volume crossed by a discontinuity inside a body (where  $\bar{\mathbf{t}} = \mathbf{0}$ ). Examining equation (5.15b) and rearranging (recalling that  $\ddot{\mathbf{u}} = \ddot{\mathbf{u}} + \ddot{\mathbf{u}}$  on  $\Omega^+$ ):

$$\int_{\Gamma_d} \tilde{\boldsymbol{\eta}} \cdot \mathbf{t} \, d\Gamma = - \left( \int_{\Omega^+} \nabla^s \tilde{\boldsymbol{\eta}} : \boldsymbol{\sigma} \, d\Omega + \int_{\Omega^+} \tilde{\boldsymbol{\eta}} \cdot \rho \ddot{\mathbf{u}} \, d\Omega \right) \quad (5.16)$$

which shows that dynamic equilibrium is satisfied in a weak sense at a discontinuity. A traction force acting on  $\Omega^+$  at  $\Gamma_d$  is resisted by an equal and opposite force in the continuum  $\Omega^+$ . For the static case where  $\ddot{\mathbf{u}} = \mathbf{0}$ , this is equivalent to traction continuity in a weak sense.

ENHANCEMENT OF THE STANDARD BASIS WITH A  
DISCONTINUOUS FUNCTION

71

At this point, an extra condition on the enhanced displacement field  $\tilde{\mathbf{u}}$  is introduced. Anywhere that essential boundary conditions are imposed,  $\tilde{\mathbf{u}} = \mathbf{0}$ . This condition greatly simplifies the imposition of essential boundary conditions. Essential boundary condition can be imposed in the standard fashion for finite elements, avoiding the need for more complex procedures, as are required for meshless methods (Belytschko et al., 1994).

5.3.2 *Discretised weak equations*

The discretised form of the weak governing equations in equation (5.15) are formed by inserting the discretised expressions for the displacement (equation (5.7a)), acceleration (equation (5.7b)) and strain (equation (5.8)) fields. Discretised displacements, variations of displacements (and the corresponding gradients) and accelerations are expressed as:

$$\begin{aligned} \hat{\mathbf{u}} &= \mathbf{N}\mathbf{a} & \hat{\eta} &= \mathbf{N}\mathbf{a}' \\ \tilde{\mathbf{u}} &= \mathbf{N}\mathbf{b} & \tilde{\eta} &= \mathbf{N}\mathbf{b}' \\ \nabla^s \hat{\mathbf{u}} &= \mathbf{B}\mathbf{a} & \nabla^s \hat{\eta} &= \mathbf{B}\mathbf{a}' \\ \nabla^s \tilde{\mathbf{u}} &= \mathbf{B}\mathbf{b} & \nabla^s \tilde{\eta} &= \mathbf{B}\mathbf{b}' \\ \ddot{\mathbf{u}} &= \mathbf{N}\ddot{\mathbf{a}} \\ \ddot{\tilde{\mathbf{u}}} &= \mathbf{N}\ddot{\mathbf{b}} \end{aligned}$$

in terms of nodal displacements, where the primes have been added to indicate variations. Inserting the above relationships into equation (5.15) yields:

$$\int_{\Omega} \mathbf{B}^T \boldsymbol{\sigma} d\Omega + \int_{\Omega} \mathbf{N}^T \rho \mathbf{N} \ddot{\mathbf{a}} d\Omega + \int_{\Omega^+} \mathbf{N}^T \rho \mathbf{N} \ddot{\mathbf{b}} d\Omega = \int_{\Gamma_u} \mathbf{N}^T \bar{\mathbf{t}} d\Gamma \quad (5.18a)$$

$$\begin{aligned} \int_{\Omega^+} \mathbf{B}^T \boldsymbol{\sigma} d\Omega + \int_{\Gamma_d} \mathbf{N}^T \bar{\mathbf{t}} d\Gamma + \int_{\Omega^+} \mathbf{N}^T \rho \mathbf{N} \ddot{\mathbf{a}} d\Omega + \int_{\Omega^+} \mathbf{N}^T \rho \mathbf{N} \ddot{\mathbf{b}} d\Omega \\ = \int_{\Gamma_u} \mathcal{H}_{\Gamma_d} \mathbf{N}^T \bar{\mathbf{t}} d\Gamma \end{aligned} \quad (5.18b)$$

which are the discrete weak governing equations.

5.3.3 *Linearised weak equations*

The stress rate in the continuum (in the bulk, away from a discontinuity) is expressed in terms of nodal displacement velocities as:

$$\dot{\boldsymbol{\sigma}} = \mathbf{D} \dot{\boldsymbol{\varepsilon}} = \mathbf{D} \left( \mathbf{B}\dot{\mathbf{a}} + \mathcal{H}_{\Gamma_d} \mathbf{B}\dot{\mathbf{b}} \right). \quad (5.19)$$

Similarly, the traction rate at a discontinuity can be expressed in terms of the enhanced nodal velocities as:

$$\dot{\mathbf{t}} = \mathbf{T} \dot{\mathbf{u}}_{\mathbf{x} \in \Gamma_d} = \mathbf{T} [\dot{\mathbf{u}}] = \mathbf{T} \mathbf{N} \dot{\mathbf{b}}. \quad (5.20)$$

The weak governing equations in (5.18) can be linearised by inserting equations (5.19) and (5.20). After some straightforward manipulations, the linearised equations can be written as:

$$\mathbf{M} \begin{Bmatrix} \ddot{\mathbf{a}}^{t+dt} \\ \ddot{\mathbf{b}}^{t+dt} \end{Bmatrix} + \mathbf{K} \begin{Bmatrix} d\mathbf{a} \\ d\mathbf{b} \end{Bmatrix} = \begin{Bmatrix} \mathbf{f}_a^{\text{ext},t+dt} \\ \mathbf{f}_b^{\text{ext},t+dt} \end{Bmatrix} - \begin{Bmatrix} \mathbf{f}_a^{\text{int},t} \\ \mathbf{f}_b^{\text{int},t} \end{Bmatrix} \quad (5.21)$$

where the stiffness matrix  $\mathbf{K}$  is expressed as:

$$\mathbf{K} = \begin{bmatrix} \int_{\Omega} \mathbf{B}^T \mathbf{D} \mathbf{B} d\Omega & \int_{\Omega^+} \mathbf{B}^T \mathbf{D} \mathbf{B} d\Omega \\ \int_{\Omega^+} \mathbf{B}^T \mathbf{D} \mathbf{B} d\Omega & \int_{\Omega^+} \mathbf{B}^T \mathbf{D} \mathbf{B} d\Omega + \int_{\Gamma_d} \mathbf{N}^T \mathbf{T} \mathbf{N} d\Gamma \end{bmatrix}, \quad (5.22)$$

the consistent mass matrix  $\mathbf{M}$  is expressed as:

$$\mathbf{M} = \begin{bmatrix} \int_{\Omega} \rho \mathbf{N}^T \mathbf{N} d\Omega & \int_{\Omega^+} \rho \mathbf{N}^T \mathbf{N} d\Omega \\ \int_{\Omega^+} \rho \mathbf{N}^T \mathbf{N} d\Omega & \int_{\Omega^+} \rho \mathbf{N}^T \mathbf{N} d\Omega \end{bmatrix} \quad (5.23)$$

and the force vectors are equal to:

$$\mathbf{f}_a^{\text{ext}} = \int_{\Gamma_u} \mathbf{N}^T \bar{\mathbf{t}} d\Gamma \quad (5.24a)$$

$$\mathbf{f}_b^{\text{ext}} = \int_{\Gamma_u} \mathcal{H}_{\Gamma_d} \mathbf{N}^T \bar{\mathbf{t}} d\Gamma \quad (5.24b)$$

$$\mathbf{f}_a^{\text{int}} = \int_{\Omega} \mathbf{B}^T \boldsymbol{\sigma} d\Omega \quad (5.24c)$$

$$\mathbf{f}_b^{\text{int}} = \int_{\Omega^+} \mathbf{B}^T \boldsymbol{\sigma} d\Omega + \int_{\Gamma_d} \mathbf{N}^T \mathbf{t} d\Gamma. \quad (5.24d)$$

Note that if the material tangent matrices  $\mathbf{D}$  and  $\mathbf{T}$  are symmetric, symmetry of the global stiffness matrix is preserved, unlike the non-symmetric embedded discontinuity formulation based on incompatible modes. This is a significant computational advantage. Also note the influence of the Heaviside function on the linearised equations, implied by the integration over the domain  $\Omega^+$ . This is in contrast to the incompatible modes formulation where the Heaviside function is absent from the formulation. This is particularly significant for dynamic problems. For the incompatible modes formulation, the displacement field is continuous and therefore the consistent mass matrix is the same as for a conventional continuum model. The effect of a discontinuity on the inertial forces is not included. For the partition of unity-based model, the effect of a displacement discontinuity on the mass matrix can be seen in equation (5.23).

#### 5.4 Modelling propagating discontinuities and implementation aspects

During a calculation, the initiation criterion for a discontinuity extension is monitored at all integration points in the element ahead of a discontinuity tip at the end of a load increment. If the criterion is met at any of the integration points in the element ahead of the discontinuity, a discontinuity is introduced through the entire element. The procedure is repeated until the discontinuity initiation criterion is no longer met. In two dimensions, discontinuities are introduced as straight lines within elements (the normal vector to the discontinuity  $\mathbf{n}$  is constant within an element). Geometric continuity of a discontinuity is enforced. This is important for the partition of unity-based model since the displacement jump is continuous across element boundaries. Making discontinuities straight within an element and requiring that a discontinuity propagate through an entire element in one step are implementation aspects and not limitations of the model. It is possible for a discontinuity to be curved (or made from more than one straight segment) within an element or for a discontinuity tip to lie within an element by using a ramp function which is discontinuous behind a discontinuity tip and continuous in front of the tip. However, the use of ramp functions leads to convergence difficulties when simulating propagating discontinuities using an incremental solution procedure. As a discontinuity extends, it is necessary to modify the ramp function which can lead to spurious unloading and sudden jumps in the solution at points affected by the ramp function. Since within the cohesive zone framework energy is dissipated upon opening or sliding at a discontinuity, rather than upon discontinuity extension (unlike for cracks in an elastic body), the numerical result is not particularly sensitive to exactly when a discontinuity is extended or the length of the discontinuity extension. Moreover, upon mesh refinement, the assumption of a straight discontinuity within an element is of no consequence.

Discontinuities are extended only at the end of a load increment for the same reasons outlined in section 4.5.1, namely to preserve the quadratic convergence rate of the full Newton-Raphson solution procedure and to avoid the introduction of discontinuities to non-equilibrium states. The convergence rate of the model is striking, with quadratic convergence achieved even with very large time steps and the overall procedure is extremely robust. This can be attributed to the ‘concentration’ of the non-linear deformations in a small zone – the interface, and the theoretical soundness of the model.

##### 5.4.1 Enhancement of individual nodes

No mention has been made yet as to which nodes are enhanced with extra degrees of freedom. Since the functions in the enhanced basis  $\gamma$  are multiplied by the shape functions of a particular node, the enhanced basis associated with a particular node has an influence only over the support of that node. Therefore the Heaviside function is added only to the enhanced basis of nodes whose support is crossed by a discon-

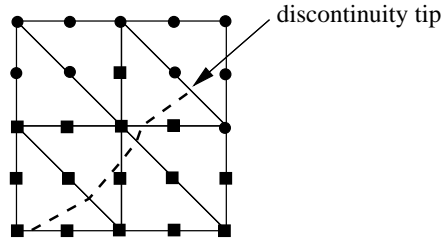


Figure 5.1: Enhanced nodes whose support is crossed by a discontinuity (dashed line). Enhanced nodes are indicated by the squares and regular nodes by the circles.

tinuity. For nodes whose support is not crossed by a discontinuity, the addition of the Heaviside function to the enhanced basis is equivalent to the addition of a constant function. Since a constant function is included in the span of the element shape functions, the resulting system of equation would not be linearly independent. The number of extra degrees of freedom added to an enhanced node is equal to the spatial dimension. When enhancing a node, it is necessary to check what proportions of the support lie on each side of the discontinuity to ensure a well-conditioned global stiffness matrix. If only a very small proportion of the support of a node lies in either  $\Omega^+$  or  $\Omega^-$ , the Heaviside function appears numerically very close to a constant function. Therefore a node is enhanced if its support is crossed by a discontinuity and

$$\frac{\min(\Omega_s^+, \Omega_s^-)}{\Omega_s} > \text{tol} \quad (5.25)$$

where  $\Omega_s$  is the volume of the support of a node,  $\Omega_s^+$  is the volume of the support of a node that belongs to  $\Omega^+$ ,  $\Omega_s^-$  is the volume of the support of a node that belongs to  $\Omega^-$  and 'tol' is a small value that is dependent on the precision of the solver (typically of the order  $10^{-4}$ ).

Another condition that must be satisfied is that the displacement jump at a discontinuity tip is zero. To ensure this, the nodes on an element boundary *touched* by a discontinuity tip are not enhanced. When a discontinuity propagates into the next element, nodes behind the discontinuity tip are enhanced. This is illustrated in figure 5.1 for six-noded triangular elements.

#### 5.4.2 Discontinuity alignment

The most important consideration when extending a discontinuity is that the correct direction is chosen. Since the tip of a discontinuity is not located at a point where the stresses are known accurately (such as conventional Gauss points), the local stress field cannot be relied upon to accurately yield the correct normal vector to a discontinuity (Wells and Sluys, 2001c). To overcome this, non-local stresses at a discontinuity

tip are calculated and used to find the principal directions. Jirásek (1998b) reported that for an incompatible modes type model, using a non-local strain tensor for determining the principal strain directions resulted in a less tortuous crack path. The non-local stress tensor is calculated as a weighted average of stresses using a Gaussian weight function:

$$w = \frac{1}{(2\pi)^{3/2} l^3} \exp\left(-\frac{r^2}{2l^2}\right) \quad (5.26)$$

where  $w$  is the weight,  $l$  determines how quickly the weight function decays away from the discontinuity tip and  $r$  is the distance of a point from the discontinuity tip. It is emphasised that this does not imply any non-locality in the model, but is a method of smoothing stresses in order to accurately determine the principal stress directions. The parameter  $l$  is taken as approximately three times the typical element size. Using a non-local stress tensor for determining the principal stress directions is important when the stress field is not uniform. For problems with a relatively homogeneous stress field, the difference between the directions based on the local and non-local stress tensors is very small.

When dealing with models that predict multiple normal vectors (such as the discrete Von Mises model from chapter 3), the appropriate normal vector must be chosen. The normal vector chosen is that which is closest to the normal vector in the neighbouring element.

#### 5.4.3 Numerical integration of enhanced elements

When using non-standard shape functions, the question arises how the numerical integration should be performed. The most important requirement when using discontinuous functions is that both sides of a discontinuity are adequately integrated. Failure to integrate on both sides of a discontinuity results in a linearly dependent system of equations since the Heaviside function cannot be distinguished from a constant function. Often when a discontinuity crosses an element, the initial Gauss integration scheme is not sufficient to ensure that the global stiffness matrix remains linearly independent.

All numerical examples presented use the six-noded triangular element as the underlying finite element. Elements which are not crossed by a discontinuity are integrated by standard three-point Gauss quadrature. When an element is first crossed by a discontinuity, the domains  $\Omega_e^+$  and  $\Omega_e^-$  on either side of a discontinuity are triangulated into sub-domains. Within each triangular sub-domain, three-point Gauss quadrature is applied. In addition to integration points in the bulk of the element, two integration points are positioned on the discontinuity in order to integrate the traction forces. The integration scheme is illustrated in figure 5.2.

The proposed integration scheme requires 23 integration points per six-noded triangular element which at first seems excessive. However, since only elements

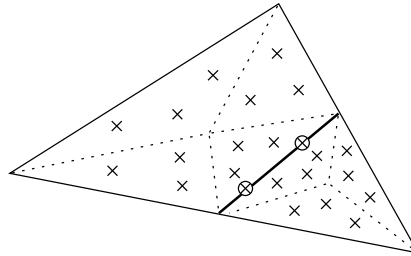


Figure 5.2: Integration scheme for a six-noded triangular element crossed by a discontinuity (heavy line). The crosses are integration points for the continuum and the crosses inside a circle are integration points for the traction forces on the discontinuity.

crossed by a discontinuity require the modified integration scheme, the computational burden is small. In the continuum bulk of the element, the proposed scheme over-integrates the stress field. The scheme is adopted for maximum flexibility since it may be desirable to add enhancement functions other than the Heaviside jump, such as the near-tip fields for linear-elastic fracture mechanics (Belytschko and Black, 1999). The need to change the integration scheme for every different set of enhancement functions is undesirable since the computational cost of over-integrating a small number of elements is negligible. Unlike for interface elements, no special integration schemes are required at the interface since there is no elastic component in the constitutive models.

An alternative to an adaptive integration scheme is to use a scheme with fixed integration points. It is possible to use a Newton-Cotes integration scheme with integration points located on, or close to, element boundaries (Wells and Sluys, 2001e). However, this approach is not as computationally robust as the adaptive integration scheme. The Newton-Cotes integration scheme requires more integration points in elements not crossed by a discontinuity to minimise the number of elements crossed by a discontinuity with all integration points on one side of the discontinuity. Yet, it still does not ensure that elements crossed by a discontinuity are accurately integrated. Also, when traction forces must be integrated at a discontinuity, the integration scheme must be adapted in order to locate integration points on the discontinuity. In this case, avoiding the addition and relocation of continuum integration points is not a significant advantage. Further, when discontinuities must propagate through whole elements, the integration scheme in an element is adjusted no more than once during a calculation. All analyses in this chapter assume an elastic response in the continuum, so no material history is stored at the continuum integration points and the stress can be calculated from the total strain field. The transport of material history for non-linear continuum models with history variables is addressed in chapter 7.

## 5.5 Numerical examples

The numerical examples in this section are intended to show the objectivity, flexibility and robustness of the cohesive zone model based on partitions of unity. All examples are two-dimensional. Mode-I and mode-II failure problems are analysed under both quasi-static and impact loading. Problems are analysed to examine particular features of the model, especially the objectivity with respect to spatial discretisation (element size and orientation) of both the energy dissipated and the failure mode. For two particular problems, one under quasi-static loading and the other under impact loading, numerical results are compared with experimental data.

All analyses are performed using the six-noded triangle as the underlying base element. It is emphasised that this leads to a quadratic interpolation of the displacement jump along a discontinuity and the discontinuity jump is continuous across element boundaries. A full Newton-Raphson solution procedure is used for all examples and an elastic response is assumed in the continuum. For dynamic problems, time integration is performed using the implicit average acceleration version of the Newmark method (Hughes, 1987). A particular feature of this model is that a discontinuity propagates from a point or an existing discontinuity. The ‘imperfect element’ that is used to trigger failure when using continuum models is replaced by an ‘imperfect point’. Also, no branching of discontinuities is permitted. There are no restrictions upon this in the numerical model, rather it is imposed for simplicity and due to the lack of a clear mechanical criterion.

### 5.5.1 Three-point bending test

A simply supported beam is loaded symmetrically by means of an imposed displacement at the centre of the beam on the top edge (figure 5.3). The beam is simulated using the mode-I discrete constitutive model from section 3.1. The following material properties are used: Young’s modulus  $E = 100$  MPa, Poisson’s ratio  $\nu = 0$ , tensile strength  $f_t = 1$  MPa and fracture energy  $G_f = 0.1$  Nmm<sup>-1</sup>. For this example, the crack shear stiffness is set to zero, which leads to a symmetric stiffness matrix. Since the crack shear stiffness is zero, the top row of elements of the beam are prevented from cracking since if a crack propagates through the entire beam, the system of equations becomes singular as the beam has no shear resistance and not all rigid body modes are restrained.

Figure 5.4 shows the crack through the beam for two meshes, one with 523 elements and the other with 850 elements. A crack is initiated at the centre of the beam on the bottom edge. It can be seen that for both meshes a crack propagates directly upwards towards the loading point. The crack is able to propagate independently of mesh alignment. Figure 5.5 shows the mesh with 523 elements with the crack initiated eccentrically. Offsetting the crack slightly ( $x_1 = 5.7$  mm, 0.7 mm offset) tests the ability of the method to model a curved crack. It can be seen in that the crack curves

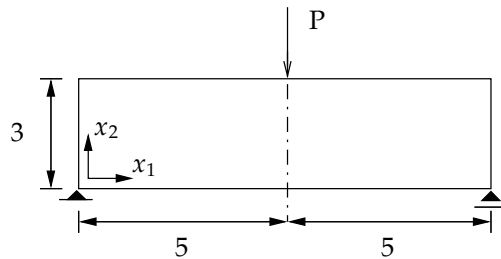


Figure 5.3: Three point bending beam, depth = 1. All dimensions in millimetres.

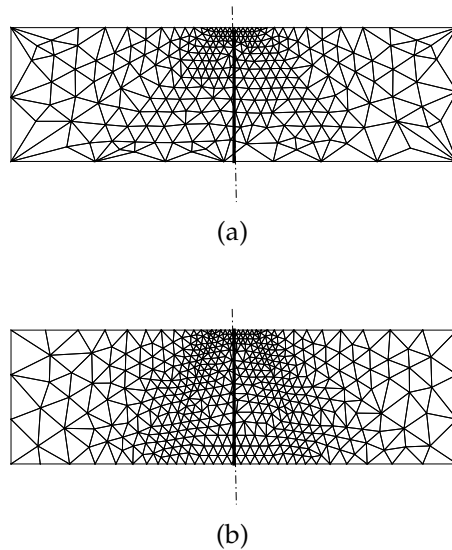


Figure 5.4: Crack paths for the three-point bending test with (a) 523 elements and (b) 850 elements. Cracks are shown by the heavy lines.

towards the centre of the beam, crossing the directional bias of the mesh.

The load–displacement response of the three-point bending test with the concentric crack is shown in figure 5.6. Integrating the load–displacement response for the mesh with 523 elements shows that the energy dissipated is equal to 0.3080 Nmm. This agrees well with the fracture energy multiplied by the depth of the beam which equals 0.3 Nmm, indicating that the energy dissipated is independent of the spatial discretisation. The slight over-estimation of the energy dissipated is due to the top elements being kept elastic to avoid a singular system of equations. Note also that upon mesh refinement, the load–displacement response becomes smoother. As the mesh becomes finer, a discontinuity extends in smaller increments (since discontinu-

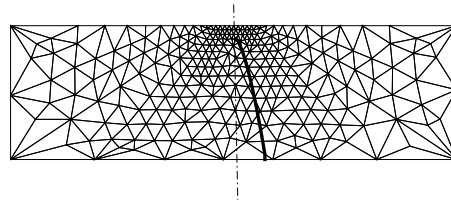


Figure 5.5: Crack path for the three-point bending test with an eccentric crack and 523 element. The crack is shown by the heavy line.

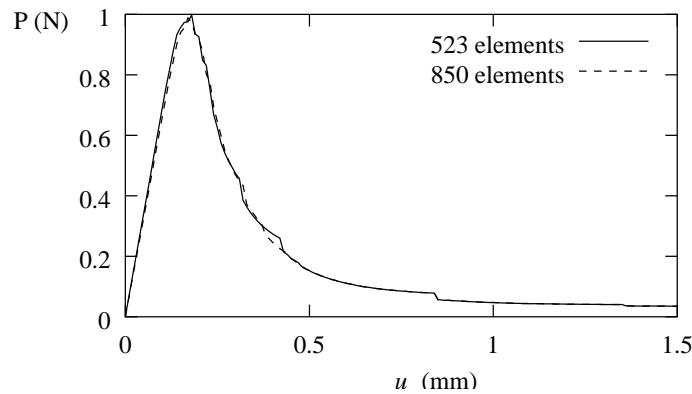


Figure 5.6: Load–displacement response for the three-point bending test.

ities must cross whole elements).

### 5.5.2 Single-edge notched beam

The SEN beam from chapter 4 (figure 4.14) is now analysed using the partition of unity-based model. For the analysis of the SEN beam, the following materials properties are used: Young’s modulus  $E = 3.5 \times 10^4$  MPa, Poisson’s ratio  $\nu = 0.15$ , tensile strength  $f_t = 3$  MPa, fracture energy  $G_f = 0.1$  Nmm<sup>-1</sup> and the shear stiffnesses  $d_{\text{int}} = 1 \times 10^2$  Nmm<sup>-3</sup> and  $d_{\kappa=1} = 1 \times 10^{-4}$  Nmm<sup>-3</sup>. At the loading point and the support near the notch, the loading plates have the material properties of steel. The beam has been analysed under both plane strain and plane stress conditions. Due to the relatively small Poisson’s ratio and since the material response in the third direction is elastic only (stresses in the third direction do not induce any displacements at a discontinuity), the difference between the plane stress and plane strain responses is negligible. The results reported here are for the plane strain case.

It can be seen in figure 5.7 that the predicted crack path is curved. This is in excellent agreement with experimental results (Schlangen, 1993). Examining the crack

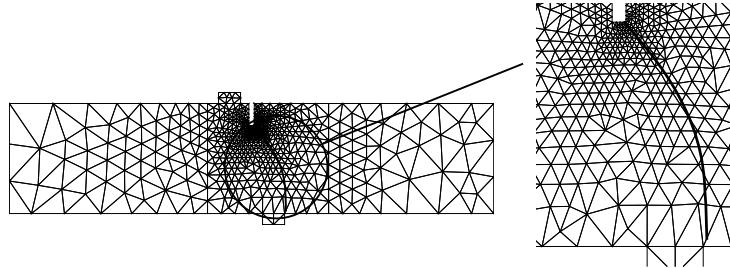


Figure 5.7: SEN beam with 1184 elements. The crack is shown by the heavy line.

path closely, it can be seen that the crack path is independent of the mesh structure. The discontinuity crosses element boundaries with which it is almost parallel. Unlike for the embedded discontinuity model based on incompatible modes, this poses no difficulties since the enhanced degrees of freedom are global and act over the support of a node, rather than over single elements. It is emphasised that the curved crack path is computed using a principal stress initiation criterion only, unlike in section 4.6.4 where a combined criterion was used. In order to capture the correct crack path it is essential that the mesh around the notch is reasonably fine. If the mesh is not fine enough, the high elastic strain gradients around the notch are not adequately captured and the resulting crack path prediction is unreliable.

To further examine the numerical results, the load–displacement response for the simulation is compared to experimental results in figure 5.8. Also shown is a simulation with a constant discontinuity shear stiffness. It can be seen that the calculated peak load is very close to the experimentally measured peak load. The post-peak response is also close to the experimental results. Matching the experimental post-peak response requires some fitting of the material parameters, particularly the shear stiffness. The crack shear stiffness has almost no influence on the peak strength and a negligible influence on the discontinuity path, but has a significant influence on the ductility of the post-peak response. While the response with the constant shear stiffness in figure 5.8 is too brittle, it is computationally advantageous since the tangent relating the traction rate and displacement jump rate is symmetric. The danger is that when crack sliding is significant, a small constant crack shear stiffness may result in an overly brittle response and a high constant crack shear stiffness may result in an overly ductile response (Rots, 1988).

### 5.5.3 Biaxial test – quasi-static and dynamic analysis

To test the model for mode-II failure, the biaxial test is analysed in two-dimensions under plane strain conditions using the discrete Von Mises model from section 3.2.4. The exact geometry and boundary conditions for the analyses are shown in figure 5.9.

NUMERICAL EXAMPLES

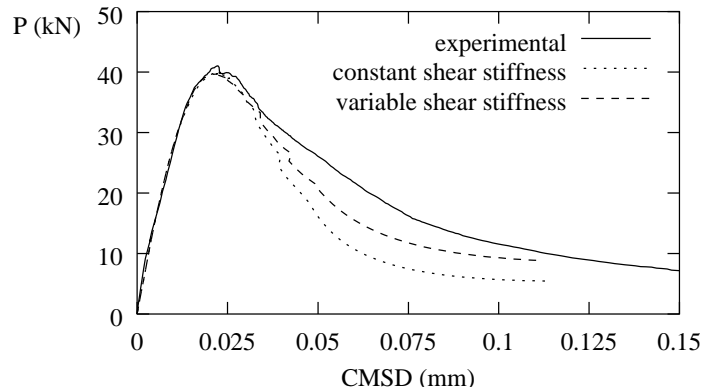


Figure 5.8: Applied load plotted against crack mouth sliding displacement (CMSD) for experimental results (Schlangen, 1993) and simulations with variable shear stiffness ( $d_{init} = 1 \times 10^2 \text{ Nmm}^{-3}$ ,  $d_{\kappa=1} = 1 \times 10^{-4} \text{ Nmm}^{-3}$ ) and constant shear stiffness ( $d_{init} = 1 \text{ Nmm}^{-3}$ ).

In order to trigger a shear band, an imperfection is required. The locations of the imperfections used for the static and dynamic analyses are shown in figure 5.9. The material properties are taken as: Young’s modulus  $E = 11.92 \times 10^3 \text{ MPa}$ , Poisson’s ratio  $\nu = 0.49$  and yield stress  $\bar{\sigma} = 100 \text{ MPa}$ . For the quasi-static analysis the hardening modulus (linear softening)  $\bar{h} = -20 \text{ Nmm}^{-3}$  and for the dynamic analysis  $\bar{h} = -50 \text{ Nmm}^{-3}$  and density  $\rho = 5 \times 10^{-9} \text{ Nsmm}^{-4}$ . A time step of  $\Delta t = 1.5 \times 10^{-6} \text{ s}$  is used for the dynamic examples. When the continuum yield condition is violated, a discontinuity is introduced that bisects the principal stress directions (from equation (3.38)). For the first discontinuity, it is necessary to restrict the range of normal solutions. For the biaxial examples, the normal direction to a discontinuity is calculated based on the local stress field at the integration point ahead of a discontinuity tip where the continuum yield condition is violated. It was not necessary for this problem to use the non-local stress for calculating a reliable discontinuity extension direction.

Quasi-static analysis

For the static analysis, the biaxial test is analysed under displacement control, with a uniform downward displacement imposed on the top edge. A shear band develops from an ‘imperfect point’, which is located on the left-hand side of the specimen, 95 mm from the base (see figure 5.9). The biaxial test is performed using two different meshes, one mesh is constructed with 156 elements and a finer mesh with 656 elements. Figure 5.10 shows the two meshes analysed crossed by a discontinuity. It can be seen for both meshes that the discontinuity follows the same, expected path at  $45^\circ$  to the  $x_1$ -axis. The bias of the mesh structure has been completely overcome in

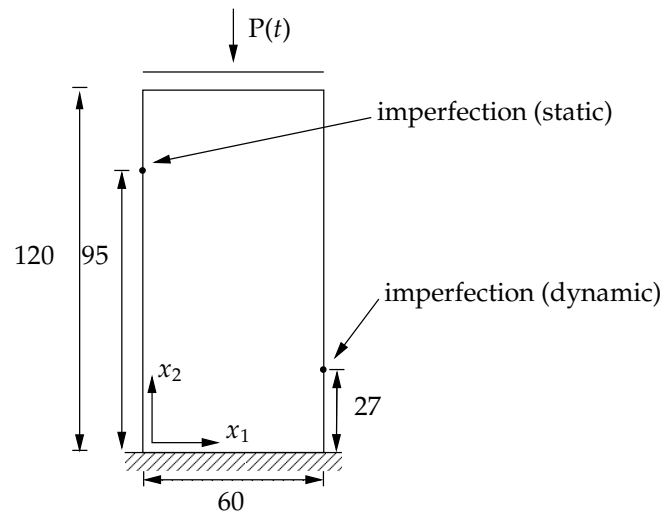


Figure 5.9: Biaxial test specimen (all dimensions in millimetres). Depth = 1 mm. The positions of the imperfections are indicated by the dots.

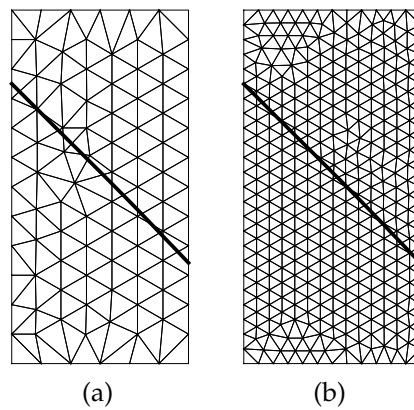


Figure 5.10: Meshes for the quasi-static biaxial test with (a) 156 elements and (b) 656 elements crossed by a discontinuity. The discontinuity (shear band) is shown by the heavy line.

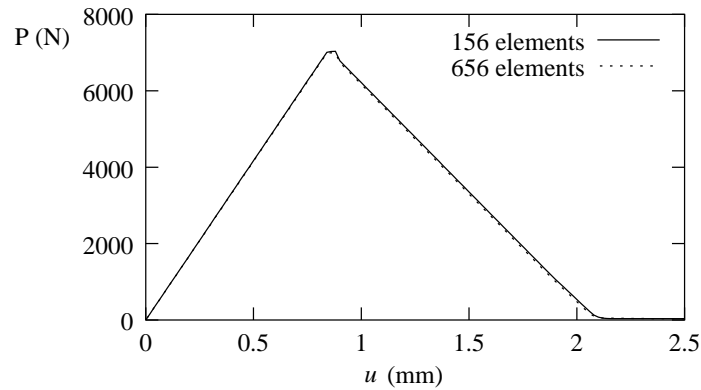


Figure 5.11: Load–displacement response for the quasi-static biaxial test.

both cases, despite the meshes being biased in a direction different to the direction of the shear band. Note again that the discontinuity crosses element boundaries with which it is almost parallel, and this poses no difficulties. The objectivity of the analysis is further confirmed by examining the load–displacement response in figure 5.11. The plotted load is the total applied load and the displacement is the downward displacement of the top edge. The load–displacement responses of the two meshes are indistinguishable.

#### Dynamic analysis

For the analysis of the biaxial test under impact loading, a uniform compressive load which is a function of time, as shown in figure 5.12, is applied on the top edge of the specimen. A shear band initiates when the yield surface is violated at the imperfection, located at the bottom right-hand side of the biaxial specimen, as shown in figure 5.9. The loading is chosen such that a discontinuity is not initiated when the compressive wave first passes the imperfection, but rather when the stress wave reflected from the fixed boundary passes the imperfection. The biaxial specimen is tested for four different meshes with 156, 334, 656 and 2624 elements. To compare the responses of the four meshes, the evolution of the strain energy  $U$  against time is shown in figure 5.13. The strain energy is calculated from:

$$U = \frac{1}{2} \int_{\Omega} \boldsymbol{\sigma} : \boldsymbol{\varepsilon} \, d\Omega + \frac{1}{2} \int_{\Gamma_d} \mathbf{t} \cdot \tilde{\mathbf{u}} \, d\Gamma. \quad (5.27)$$

It can be seen in figure 5.13 that the four meshes yield near identical results. Upon mesh refinement, the difference between the results diminishes. Interestingly, the coarsest mesh (156 elements) exhibits a lower strain energy than the finer meshes, which is in contrast to classical continuum models where the finer the mesh the lesser

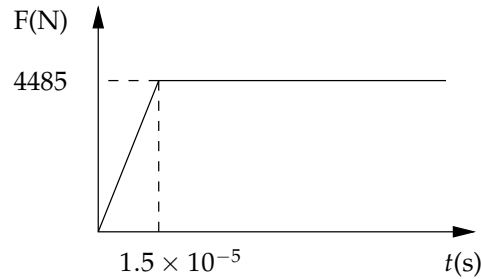


Figure 5.12: Load applied to biaxial specimen as a function of time.

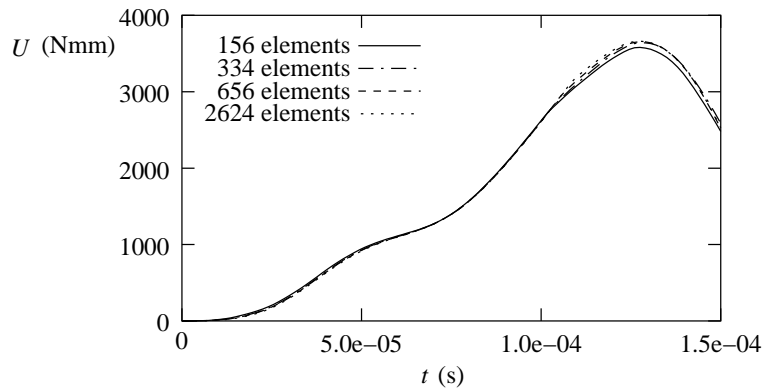


Figure 5.13: Evolution of strain energy  $U$  with time  $t$  for the biaxial test under impact loading.

the strain energy. The slight difference in this case is due to differences in the elastic solution. For the coarse mesh, the elastic stress wave passes the imperfection slightly earlier than for the finer meshes. The result is that development of a shear band is initiated sooner, resulting in an earlier decrease in the strain energy. The four meshes crossed by a discontinuity and in deformed configuration are shown in figure 5.14. The failure mode for all meshes is identical. Clearly, the mesh structure has been completely overcome for all cases. From the results in figure 5.14, it is clear that the model can perform exceptionally with very coarse meshes.

#### 5.5.4 Double-notched specimen under tensile impact loading

A double-notched concrete specimen subjected to impact loading is now analysed. The specimen shown in figure 5.15 has been tested experimentally using a Split-Hopkinson bar apparatus by Weerheijm (1992). A notched specimen is used so that failure is induced as a tensile stress wave passes through the narrowing section. The double-notched specimen is analysed using the mode-I cohesive crack model out-

NUMERICAL EXAMPLES

85

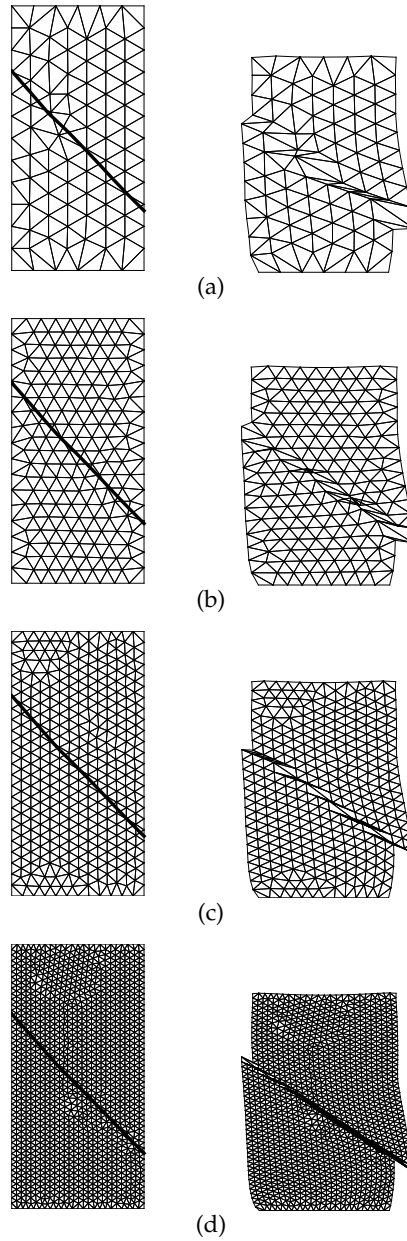


Figure 5.14: Meshes crossed by a discontinuity (heavy line) and in deformed configuration (magnified) for the biaxial test at  $t = 1.5 \times 10^{-4}$  s with (a) 156 elements, (b) 334 elements, (c) 656 elements and (d) 2624 elements.

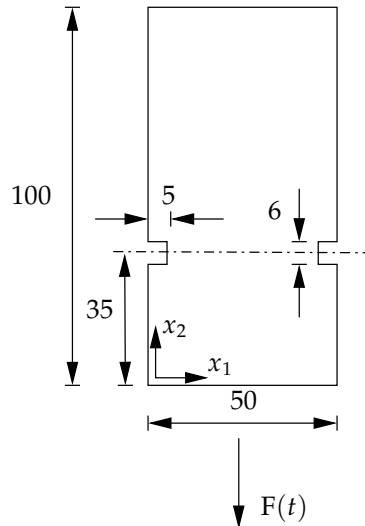


Figure 5.15: Double-notched specimen, depth = 80mm (all dimensions in millimetres).

lined in chapter 3. The material properties, from Sluys and De Borst (1996), are taken as: Young’s modulus  $E = 40.7 \times 10^3$  MPa, Poisson’s ratio  $\nu = 0.2$ , tensile strength  $f_t = 4.9$  MPa, density  $\rho = 2.35 \times 10^{-9}$  Nsmm $^{-4}$ . The fracture energy is taken as  $G_f = 0.25$  Nmm $^{-1}$  and the crack shear stiffness is zero. A time step of  $\Delta t = 2 \times 10^{-6}$  s is used. The applied load as a function of time is shown in figure 5.16. The test is performed assuming plane strain conditions. The Split-Hopkinson bar is approximately 10 metres in length, while the specimen itself is only 100 millimetres, therefore it is not reasonable to simulate the entire bar. As a compromise, the bar is modelled as shown in figure 5.17, as was done by Sluys and De Borst (1996). Further from the specimen, the Young’s modulus is decreased and the density increased to reduce the wave speed, thereby simulating the longer bar and avoiding reflections from ends of the bars. The material properties are chosen such that the acoustic impedance  $Z (= A\sqrt{E\rho})$  is constant, thus avoiding any reflections at the interfaced between regions of the bar with different material parameters.

Numerically, two cases are examined for the double-notched impact test. The first case involves a crack propagating from both notches of the specimen. This corresponds to a symmetric failure mode. The second case is a non-symmetric failure mode where a crack propagates from one notch only. In both cases, it is assumed that a crack propagates from just below the centre of the notch. Figure 5.19 compares the average normal stress transmitted in the  $x_2$ -direction at the top boundary of the specimen ( $x_2 = 100$  mm) as a function of time for two different meshes for the case where a crack propagates from both sides of the specimen with experimental results from

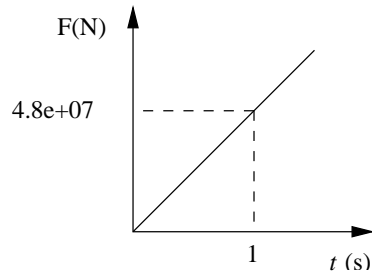


Figure 5.16: Load applied to double-notched specimen specimen as a function of time.

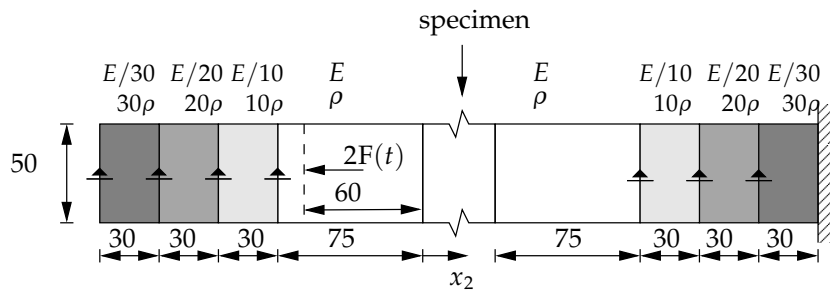


Figure 5.17: Representation of Split-Hopkinson bar apparatus for numerical simulations. The load  $F(t)$  is distributed along the dashed line.

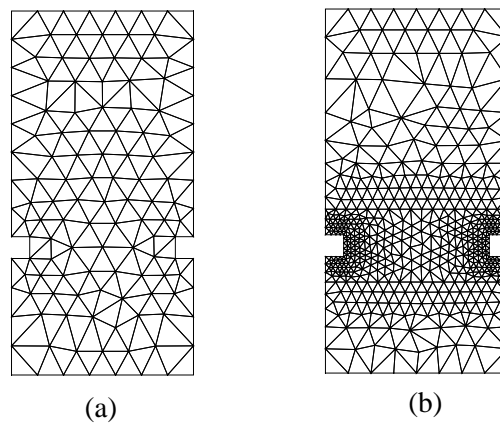


Figure 5.18: Finite element meshes used for the double-notched specimen with (a) 214 elements and (b) 958 elements.

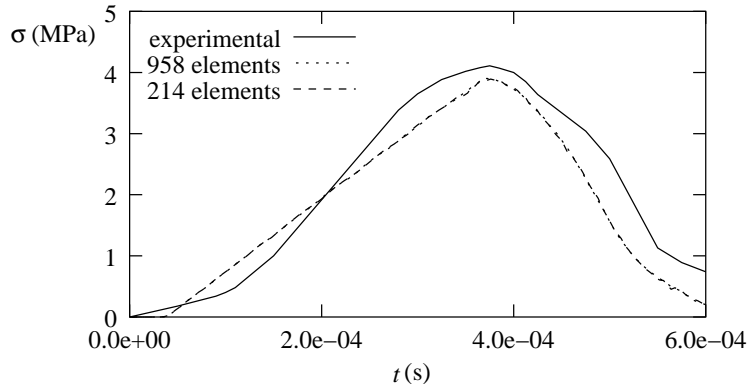


Figure 5.19: Transmitted stress with time for the double-notched specimen for symmetric failure analysis and experimental results.

Weerheijm (1992). It can be seen that the two meshes give an identical response and compare well with the experimental results. Figure 5.20 shows the stress transmitted in the  $x_2$ -direction at the top of the specimen as a function of time for the case of non-symmetric failure and again with experimental results. Interestingly, the difference between the responses for symmetric and non-symmetric failure is very small.

The crack paths for the two meshes for a non-symmetric failure mode are shown in figure 5.21 when the crack has propagated through the entire specimen. The crack paths for the two meshes are almost identical and the paths have been able to overcome the directional bias of the mesh structure in both cases. To further examine the objectivity of the numerical procedure, figure 5.22 shows the strain energy evolution with time for two different meshes. The comparisons between the coarse and fine meshes show how well the model can perform with very coarse meshes. This is particularly the case when a discontinuity path is reasonably straight and the stress field in the continuum is reasonably uniform.

## 5.6 Summary of the partition of unity formulation and comparison with the incompatible modes formulation

It is interesting at this point to draw some comparisons between the partition of unity-based model and the embedded discontinuity model from the previous chapter. The key difference, which has significant consequences, is the continuity of the enhanced functions across element boundaries. The governing equations (compare equations (4.20) and (5.18)) are outwardly similar in appearance, but the differences are fundamental. The difference is that the second equation in (4.20) for the incompatible modes formulation that enforces traction continuity is local to an element as it is enforced per element. In contrast, the second equation in (5.18) is global and can-

SUMMARY OF THE PARTITION OF UNITY FORMULATION AND  
COMPARISON WITH THE INCOMPATIBLE MODES FORMULATION

89

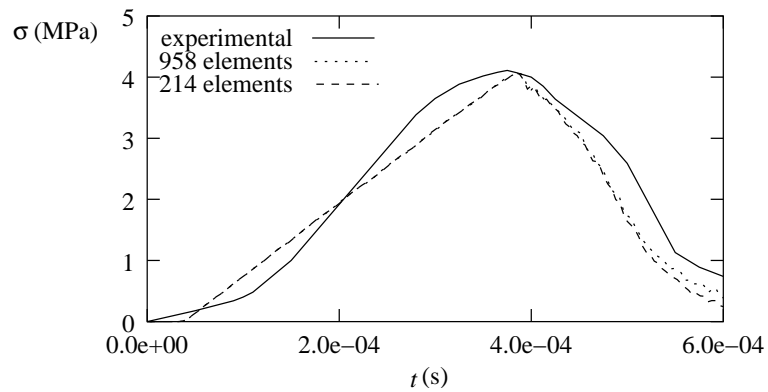


Figure 5.20: Transmitted stress with time for the double-notched specimen for non-symmetric failure analysis and experimental results.

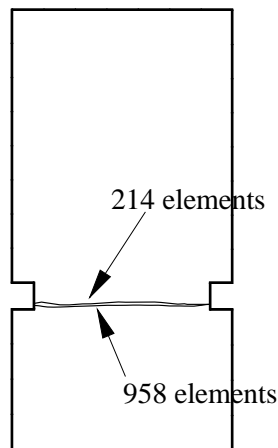


Figure 5.21: Crack paths for two meshes through the double-notched specimen (non-symmetric case).

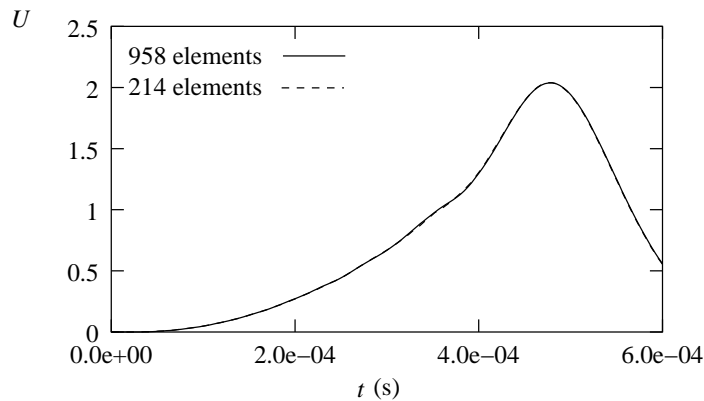


Figure 5.22: Evolution of strain energy  $U$  per unit thickness with time  $t$  for double-notched specimen for symmetric failure.

not be solve at element level. For the partition of unity model, enhanced degrees of freedom influence patches of elements and the influence domains of the enhanced degrees of freedom overlap. This allows sensitivity to mesh alignment to be completely overcome in all cases, irrespective of how a discontinuity crosses an element. Unlike the embedded discontinuity model based on incompatible strain modes, partition of unity formulation is theoretically sound and does not rely upon ad hoc developments to overcome mesh sensitivity. In particular the model is:

- objective with respect to mesh alignment and element size;
- extremely robust in implementation;
- the formulation is Galerkin, which maintains symmetry of the global stiffness matrix if the material tangents are symmetric;
- versatile – no assumptions are made as to the kinematic decomposition or underlying element type; and
- performance is excellent under both static and dynamic loading.

The derivation of the consistent mass matrix highlighted the effect of genuinely adding a displacement jump to the displacement field. It was shown that the consistent mass matrix involves the Heaviside function. This difference is particularly important when considering coarse meshes since the difference between the continuum and discontinuous consistent mass matrices becomes large (Wells and Sluys, 2001b). The cost of the excellent performance is an increased complexity in implementation when compared to standard finite element procedures. However, the extra tasks can be implemented in a highly automated fashion.

## Chapter 6

### Simulation of delamination in laminated composite materials

Composite materials are being used increasingly for a wide variety of applications. The development of composite materials is driven by the wish for light weight, high strength, stiff and durable materials. By combining different materials in layers, it is possible to develop materials with special, customised properties. A simplified schematic representation of a laminate, composed of two different materials, is shown in figure 6.1. The use of laminated composites in the aerospace and automotive industries requires an understanding of how laminated materials fail, their ductility (energy dissipated in failure) and the residual strength of a damaged composite. A key failure mechanism in laminated composites is delamination – the de-bonding of layers – which is considered this chapter.

To analyse laminated composite materials, traditionally two different approaches have been used. The first is to homogenise the laminate structure. An equivalent ‘continuum’ model is formulated and applied using shell or solid-like shell elements. From a computational point of view, this is attractive since laminates are usually very thin compared to their length and width, allowing the use of one element only through the thickness. Homogenised models are ideally suited for modelling large structures and for simulating failure as a consequence of geometric instability. De-

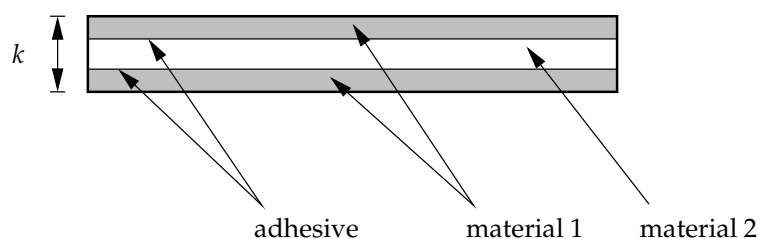


Figure 6.1: Schematic representation of a laminated material composed of three plies and two different material types. The thickness  $k$  is typically 1–3 millimetres.

spite these models having reached a high degree of sophistication (a review of different techniques can be found in Noor and Burton (1990)), they cannot properly simulate the localised de-bonding that occurs between layers of a laminate. Alternatively, a laminate can be viewed from a lower level (commonly referred to as the ‘meso’ level), at which the individual layers are explicitly modelled, with the layers connected by cohesive forces (through an adhesive). It is then possible to explicitly model the de-bonding process between layers using interface elements. De-bonding is simulated by specifying a discrete constitutive model at an interface, similar to that described in section 3.1. Alfano and Crisfield (2001) provide an extensive review of delamination models based on interface elements.

In this chapter, the partition of unity concept is used to simulate inter-laminar de-bonding. It is then possible to simulate a layered composite material with an unstructured finite element mesh, with the structure of the laminated material and the finite element mesh decoupled. The partition of unity-based model avoids the need for an elastic dummy stiffness at an interface, which when using interface elements must be sufficiently high to avoid an overly soft response, while not inducing spurious stress oscillations and poor conditioning of the global stiffness matrix. Also, the need for special, non-standard integration schemes to minimise stress oscillations (Schellekens and De Borst, 1993) is avoided. The key difference from the previous chapter is the extension to non-linear kinematics. In most aspects, the implementation in this chapter is simpler than that in the previous chapter since discontinuities are known to propagate between layers. The formulation in this chapter is intended to illustrate the potential of the partition of unity concept for the analysis of composite materials. It is not the intention to perform rigorous analyses of realistic situations. The formulation is limited to two dimensions (therefore a one-dimensional interface), while it is acknowledged that edge effects and out of plane displacements are important and should be taken into account when simulating realistic problems. In the continuum, inelastic deformations are not considered, with a hyperelastic response assumed. However, the advantages advocated of the partition of unity model still hold, namely the absence of an elastic dummy stiffness, a reduction in the total number of degrees of freedom at the beginning of an analysis and the use of standard Gauss numerical integration.

## 6.1 Non-linear kinematics

The displacement decomposition developed in chapter 2 can be extended in a straightforward manner to the geometrically non-linear case. Considering the displacement decomposition in equation (2.1), the deformation map  $\phi(\mathbf{X}, t)$  for a body crossed by a discontinuity can be written as:

$$\phi(\mathbf{X}, t) = \mathbf{x}(\mathbf{X}, t) = \mathbf{X} + \hat{\mathbf{u}}(\mathbf{X}, t) + \mathcal{H}_{\Gamma_{d,0}}(\mathbf{X}) \tilde{\mathbf{u}}(\mathbf{X}, t) \quad (6.1)$$

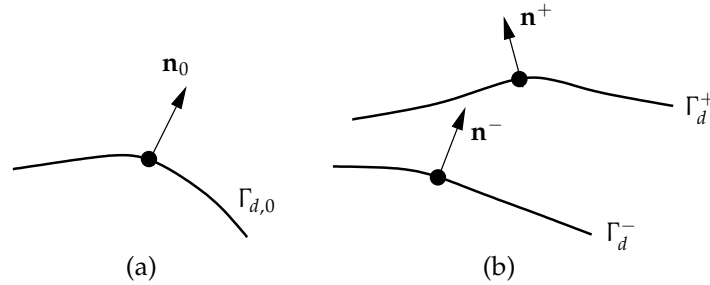


Figure 6.2: A discontinuity in (a) the reference configuration and (b) the current configuration. The normal vector is shown for a point on the discontinuity surface, showing that the normal vector is not unique in the current (deformed) configuration.

where  $\mathbf{X}$  is the position vector of a point in the reference (material) configuration (time  $t = 0$ ) and  $\mathcal{H}_{\Gamma_{d,0}}$  denotes the Heaviside function in the reference configuration. The position vector of a point in the current (spatial) configuration (time  $t > 0$ ) is denoted  $\mathbf{x}$ . The deformation gradient  $\mathbf{F}$  can be calculated from the deformation map in equation (6.1),

$$\mathbf{F} = \nabla_{\mathbf{x}} \boldsymbol{\phi} = \hat{\mathbf{F}} + \mathcal{H}_{\Gamma_{d,0}} \tilde{\mathbf{F}} + \delta_{\Gamma_{d,0}} (\tilde{\mathbf{u}} \otimes \mathbf{n}_0) \quad (6.2)$$

where  $\hat{\mathbf{F}} = \nabla_{\mathbf{X}} (\mathbf{X} + \hat{\mathbf{u}})$ ,  $\tilde{\mathbf{F}} = \nabla_{\mathbf{X}} \tilde{\mathbf{u}}$  and  $\mathbf{n}_0$  is the normal vector to a discontinuity surface  $\Gamma_{d,0}$  in the reference configuration. The displacement decomposition can be extended easily to the case of multiple, non-intersecting discontinuities as done in equation (2.7). For the constitutive update at an interface, the unit normal vector in the current configuration,  $\mathbf{n}$  is required. From Nanson's relation,

$$\mathbf{n} = \det(\mathbf{F}) (\mathbf{F}^T)^{-1} \mathbf{n}_0 \frac{d\Gamma_0}{d\Gamma} \quad (6.3)$$

where  $d\Gamma_0$  is the area of an infinitesimal material surface to which  $\mathbf{n}_0$  is normal in the reference configuration, which in the current configuration has an area  $d\Gamma$ . The vector  $\mathbf{n}$  is normal to the deformed surface. From equation (6.2), it is clear that the deformation gradient is discontinuous across the surface  $\Gamma_d$  due the presence of the Heaviside function. This implies that in the current configuration, the normal vector at a discontinuity is not unique. The normal vector in the current configuration can be defined on *both* the  $\Omega^+$  and the  $\Omega^-$  sides of  $\Gamma_d$  (denoted  $\Gamma_d^+$  and  $\Gamma_d^-$ , respectively). This is illustrated in figure 6.2. The normal vector on each side in terms of the normal vector in the reference configuration is given by:

$$\begin{aligned} \mathbf{n}^- &= \det(\hat{\mathbf{F}}) (\hat{\mathbf{F}}^T)^{-1} \mathbf{n}_0 \frac{d\Gamma_{d,0}}{d\Gamma_d^-} \\ \mathbf{n}^+ &= \det(\hat{\mathbf{F}} + \tilde{\mathbf{F}}) ((\hat{\mathbf{F}} + \tilde{\mathbf{F}})^T)^{-1} \mathbf{n}_0 \frac{d\Gamma_{d,0}}{d\Gamma_d^+} \end{aligned} \quad (6.4)$$

where the surfaces  $\Gamma_d^+$  and  $\Gamma_d^-$  are shown in figure 6.2. This is a fundamental difference to the works of Armero and Garikipati (1996), Steinmann et al. (1997) and Larsson et al. (1998) (which are based on an incompatible modes type formulation), wherein it was assumed that  $\tilde{\mathbf{u}}$  is spatially constant (therefore  $\mathbf{n}^+ = \mathbf{n}^-$ ). Such an assumption is physically unjustifiable and precludes the possibility of geometric instability at an interface since the two surfaces at a discontinuity must remain parallel which does not allow ‘buckling’ at the interface within an element. The kinematic derivations in this section are completely general and do not involve any assumptions as to the form of the functions  $\hat{\mathbf{u}}$  and  $\tilde{\mathbf{u}}$  other than that they be continuous and differentiable over a body  $\Omega$ .

## 6.2 Weak equilibrium equations and linearisation

The variational statements for the geometrically linear case in equation (5.15) are applicable to geometrically non-linear problems if the current configuration is considered. However, the linearisation of the governing weak equations must be extended to include geometrically non-linear effects. The virtual work equation, without body forces, in the reference configuration is written as:

$$\int_{\Omega_0} \nabla_{\mathbf{x}} \boldsymbol{\eta} : \mathbf{P} \, d\Omega_0 - \int_{\Gamma_{u,0}} \boldsymbol{\eta} \cdot \bar{\mathbf{t}}_0 \, d\Gamma_0 = 0 \quad (6.5)$$

where  $\mathbf{P}$  is the nominal stress,  $\bar{\mathbf{t}}_0$  is the nominal traction acting on  $\Gamma_{u,0}$  and the gradient of an admissible variation of displacement  $\boldsymbol{\eta}$  is defined on the reference configuration. Following the same steps as in section 5.3.1, a Galerkin formulation is assumed and the discontinuous displacement field can be inserted into the virtual work equation.

$$\begin{aligned} \int_{\Omega_0} \nabla_{\mathbf{x}} \hat{\boldsymbol{\eta}} : \mathbf{P} \, d\Omega_0 + \int_{\Omega_0} \mathcal{H}_{\Gamma_{d,0}} \nabla_{\mathbf{x}} \tilde{\boldsymbol{\eta}} : \mathbf{P} \, d\Omega_0 + \int_{\Omega_0} \delta_{\Gamma_{d,0}} (\tilde{\boldsymbol{\eta}} \otimes \mathbf{n}_0) : \mathbf{P} \, d\Omega_0 \\ = \int_{\Gamma_{u,0}} \hat{\boldsymbol{\eta}} \cdot \bar{\mathbf{t}}_0 \, d\Gamma_0 + \int_{\Gamma_{u,0}} \mathcal{H}_{\Gamma_{d,0}} \tilde{\boldsymbol{\eta}} \cdot \bar{\mathbf{t}}_0 \, d\Gamma_0 \end{aligned} \quad (6.6)$$

Again, as in section 5.3.1, the Dirac-delta term is eliminated through integration over the domain  $\Omega_0$  and the Heaviside term is eliminated by changing the integration domain from  $\Omega_0$  to  $\Omega_0^+$ .

$$\begin{aligned} \int_{\Omega_0} \nabla_{\mathbf{x}} \hat{\boldsymbol{\eta}} : \mathbf{P} \, d\Omega_0 + \int_{\Omega_0^+} \nabla_{\mathbf{x}} \tilde{\boldsymbol{\eta}} : \mathbf{P} \, d\Omega_0 + \int_{\Gamma_{d,0}} \tilde{\boldsymbol{\eta}} \cdot (\mathbf{P} \mathbf{n}_0) \, d\Gamma_0 \\ = \int_{\Gamma_{u,0}} \hat{\boldsymbol{\eta}} \cdot \bar{\mathbf{t}}_0 \, d\Gamma_0 + \int_{\Gamma_{u,0}} \mathcal{H}_{\Gamma_{d,0}} \tilde{\boldsymbol{\eta}} \cdot \bar{\mathbf{t}}_0 \, d\Gamma_0 \end{aligned} \quad (6.7)$$

Since the weak equilibrium equation in equation (6.7) must hold for all admissible variations  $\hat{\boldsymbol{\eta}}$  ( $\tilde{\boldsymbol{\eta}} = \mathbf{0}$ ) and  $\tilde{\boldsymbol{\eta}}$  ( $\hat{\boldsymbol{\eta}} = \mathbf{0}$ ), it can be split into two equations. Considering also that  $\mathbf{P} = \mathbf{F}\boldsymbol{\Sigma}$ , where  $\boldsymbol{\Sigma}$  is the second Piola-Kirchhoff stress tensor, the weak

governing equations in the reference configuration can be expressed as:

$$\int_{\Omega_0} \nabla_{\mathbf{x}} \hat{\boldsymbol{\eta}} : (\mathbf{F}\boldsymbol{\Sigma}) \, d\Omega_0 = \int_{\Gamma_{u,0}} \hat{\boldsymbol{\eta}} \cdot \bar{\mathbf{t}}_0 \, d\Gamma_0 \quad (6.8a)$$

$$\int_{\Omega_0^+} \nabla_{\mathbf{x}} \tilde{\boldsymbol{\eta}} : (\mathbf{F}\boldsymbol{\Sigma}) \, d\Omega_0 + \int_{\Gamma_{d,0}} \tilde{\boldsymbol{\eta}} \cdot (\mathbf{F}\boldsymbol{\Sigma}\mathbf{n}_0) \, d\Gamma_0 = \int_{\Gamma_{u,0}} \mathcal{H}_{\Gamma_{d,0}} \tilde{\boldsymbol{\eta}} \cdot \bar{\mathbf{t}}_0 \, d\Gamma_0. \quad (6.8b)$$

This form of the weak governing equations in the reference configuration will be used later as the departure point for linearisation of the discretised weak governing equations. To express the weak governing equations in terms of the true stress and true traction, equation (6.8) must be pushed forward to the current configuration. To do this, the following relationships are considered (Bonet and Wood, 1997):

$$\nabla_{\mathbf{x}} \boldsymbol{\eta} = (\nabla_{\mathbf{x}} \boldsymbol{\eta}) \mathbf{F} \quad (6.9a)$$

$$\mathbf{n}_0 = \frac{1}{\det(\mathbf{F})} \mathbf{F}^T \mathbf{n} \frac{d\Gamma}{d\Gamma_0}. \quad (6.9b)$$

$$d\Omega_0 = \frac{1}{\det(\mathbf{F})} d\Omega \quad (6.9c)$$

Note that equation (6.9b) comes from Nanson’s relationship in equation (6.3). Inserting the above relationships into equation (6.8) and considering that:

$$\boldsymbol{\sigma} = \frac{1}{\det(\mathbf{F})} \mathbf{F}\boldsymbol{\Sigma}\mathbf{F}^T \quad (6.10)$$

leads to:

$$\int_{\Omega} \nabla_{\mathbf{x}} \hat{\boldsymbol{\eta}} : \boldsymbol{\sigma} \, d\Omega = \int_{\Gamma_u} \hat{\boldsymbol{\eta}} \cdot \bar{\mathbf{t}} \, d\Gamma \quad (6.11a)$$

$$\int_{\Omega^+} \nabla_{\mathbf{x}} \tilde{\boldsymbol{\eta}} : \boldsymbol{\sigma} \, d\Omega + \int_{\Gamma_d} \tilde{\boldsymbol{\eta}} \cdot \mathbf{t} \, d\Gamma = \int_{\Gamma_u} \mathcal{H}_{\Gamma_d} \tilde{\boldsymbol{\eta}} \cdot \bar{\mathbf{t}} \, d\Gamma \quad (6.11b)$$

where the gradients of  $\hat{\boldsymbol{\eta}}$  and  $\tilde{\boldsymbol{\eta}}$  are now defined on the current configuration and the term  $\boldsymbol{\sigma}\mathbf{n}$  has been replaced by  $\mathbf{t}$ , the true traction acting at a discontinuity. Note that the above equations are identical to the weak governing equations in (5.15) for quasi-static problems. It is useful to express the weak governing equations in the current configuration since the constitutive relationships to be adopted at an interface are in terms of the true tractions.

In equation (6.11), the term  $\boldsymbol{\sigma}\mathbf{n}$  has been replaced by the true traction,  $\mathbf{t}$ . This requires the definition of the normal vector at a discontinuity, which, as shown by equation (6.4), is in general not unique. Conceptually, it is necessary to deviate from classical mechanics when applying a traction force at a discontinuity which is opening. Classically, two bodies can only transmit forces if the bodies are in contact, and being in contact implies that at the point of contact the outward normal vectors to the surfaces of two bodies are identical in direction and opposite in sign. However,

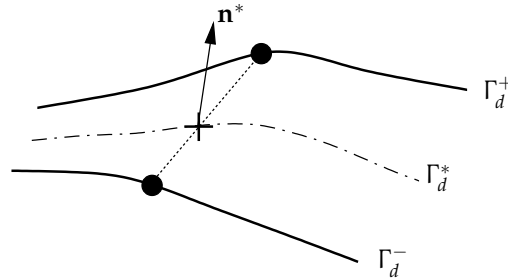


Figure 6.3: Two free surfaces  $\Gamma_d^+$  and  $\Gamma_d^-$  and the mid-surface  $\Gamma_d^*$  which are used for calculating the normal vector to the discontinuity,  $\mathbf{n}^*$ .

here it is possible that forces are transmitted between bodies for which the outward normal vectors are not in the same direction. For implementation, the normal vector at a discontinuity in the current configuration  $\mathbf{n}^*$  is taken as the normal vector to the centre surface (centre line in two dimensions) between the two surfaces  $\Gamma_d^+$  and  $\Gamma_d^-$  (see figure 6.3). The normal vector  $\mathbf{n}^*$  is defined as:

$$\mathbf{n}^* = \det \left( \hat{\mathbf{F}} + \frac{1}{2} \tilde{\mathbf{F}} \right) \left( \left( \hat{\mathbf{F}} + \frac{1}{2} \tilde{\mathbf{F}} \right)^\top \right)^{-1} \mathbf{n}_0 \frac{d\Gamma_{d,0}}{d\Gamma_d^*} \quad (6.12)$$

where  $d\Gamma_{d,0}$  is the area of an infinitesimal discontinuity surface in the reference configuration which has a deformed area  $d\Gamma_d^*$ . The vector  $\mathbf{n}^*$  is used to define the traction vector at a discontinuity and to resolve a displacement jump into normal and tangential components.

### 6.2.1 Linearisation of the weak governing equations

The linearisation of the weak governing equations differs from the geometrically linear case in chapter 5 since geometric effects must now also be included. To this end, the left-hand side of equation (6.8) (the internal ‘virtual work’,  $\delta W_{\text{int}}$ ) is differentiated with respect to time, leading to:

$$\delta \dot{W}_{\text{int}}^a = \int_{\Omega_0} \nabla_x \hat{\boldsymbol{\eta}} : (\dot{\mathbf{F}} \boldsymbol{\Sigma}) \, d\Omega_0 + \int_{\Omega_0} \nabla_x \hat{\boldsymbol{\eta}} : (\mathbf{F} \dot{\boldsymbol{\Sigma}}) \, d\Omega_0 \quad (6.13a)$$

$$\begin{aligned} \delta \dot{W}_{\text{int}}^b = & \int_{\Omega_0^+} \nabla_x \tilde{\boldsymbol{\eta}} : (\dot{\mathbf{F}} \boldsymbol{\Sigma}) \, d\Omega_0 + \int_{\Omega_0^+} \nabla_x \tilde{\boldsymbol{\eta}} : (\mathbf{F} \dot{\boldsymbol{\Sigma}}) \, d\Omega_0 \\ & + \int_{\Gamma_{d,0}} \tilde{\boldsymbol{\eta}} \cdot (\dot{\mathbf{F}} \boldsymbol{\Sigma} \mathbf{n}_0) \, d\Gamma_0 + \int_{\Gamma_{d,0}} \tilde{\boldsymbol{\eta}} \cdot (\mathbf{F} \dot{\boldsymbol{\Sigma}} \mathbf{n}_0) \, d\Gamma_0. \end{aligned} \quad (6.13b)$$

The superscripts ‘a’ and ‘b’ have been added to distinguish between the internal work rate associated with the variation  $\hat{\boldsymbol{\eta}}$  (equation (6.13a)) and the variation  $\tilde{\boldsymbol{\eta}}$  (equation (6.13b)).

tion (6.13b)). It is emphasised that the stress is expressed in a rate form for linearisation purposes only and does not imply that time integration is required to evaluate the constitutive response.

To express the linearised equations in the current (spatial) configuration, equation (6.13) must be pushed forward to the current configuration. To do this, consider that:

$$\dot{\mathbf{F}} = \mathbf{l}\mathbf{F} \quad (6.14)$$

where  $\mathbf{l}$  is the velocity gradient ( $\partial\mathbf{v}/\partial\mathbf{x}$ , with  $\mathbf{v}$  the velocity). Inserting the above relationship and those in equations (6.9a) and (6.9b) into equation (6.13) leads to:

$$\delta\dot{W}_{\text{int}}^a = \int_{\Omega_0} ((\nabla_{\mathbf{x}}\hat{\boldsymbol{\eta}})\mathbf{F}) : (\mathbf{l}\mathbf{F}\boldsymbol{\Sigma}) \, d\Omega_0 + \int_{\Omega_0} ((\nabla_{\mathbf{x}}\hat{\boldsymbol{\eta}})\mathbf{F}) : (\mathbf{F}\dot{\boldsymbol{\Sigma}}) \, d\Omega_0 \quad (6.15a)$$

$$\begin{aligned} \delta\dot{W}_{\text{int}}^b &= \int_{\Omega_0^+} ((\nabla_{\mathbf{x}}\tilde{\boldsymbol{\eta}})\mathbf{F}) : (\mathbf{l}\mathbf{F}\boldsymbol{\Sigma}) \, d\Omega_0 + \int_{\Omega_0^+} ((\nabla_{\mathbf{x}}\tilde{\boldsymbol{\eta}})\mathbf{F}) : (\mathbf{F}\dot{\boldsymbol{\Sigma}}) \, d\Omega_0 \\ &+ \int_{\Gamma_{d0}} \tilde{\boldsymbol{\eta}} \cdot \left( \mathbf{l}\mathbf{F}\boldsymbol{\Sigma} \frac{1}{\det(\mathbf{F})} \mathbf{F}^T \mathbf{n} \frac{d\Gamma}{d\Gamma_0} \right) \, d\Gamma_0 \\ &+ \int_{\Gamma_{d0}} \tilde{\boldsymbol{\eta}} \cdot \left( \mathbf{F}\dot{\boldsymbol{\Sigma}} \frac{1}{\det(\mathbf{F})} \mathbf{F}^T \mathbf{n} \frac{d\Gamma}{d\Gamma_0} \right) \, d\Gamma_0. \end{aligned} \quad (6.15b)$$

Considering the definition of the Truesdell rate of the Cauchy stress  $\overset{\circ}{\boldsymbol{\sigma}}$ ,

$$\overset{\circ}{\boldsymbol{\sigma}} = \frac{1}{\det(\mathbf{F})} \mathbf{F}\dot{\boldsymbol{\Sigma}}\mathbf{F}^T, \quad (6.16)$$

and the definition of the Cauchy stress in equation (6.10) and the relationship in equation (6.9c), after some straightforward manipulations, the linearised equations in equation (6.15) can be expressed in terms of the current configuration as:

$$\delta\dot{W}_{\text{int}}^a = \int_{\Omega} (\nabla_{\mathbf{x}}\hat{\boldsymbol{\eta}}) : (\mathbf{l}\boldsymbol{\sigma}) \, d\Omega + \int_{\Omega_0} (\nabla_{\mathbf{x}}\hat{\boldsymbol{\eta}}) : \overset{\circ}{\boldsymbol{\sigma}} \, d\Omega \quad (6.17a)$$

$$\begin{aligned} \delta\dot{W}_{\text{int}}^b &= \int_{\Omega^+} (\nabla_{\mathbf{x}}\tilde{\boldsymbol{\eta}}) : (\mathbf{l}\boldsymbol{\sigma}) \, d\Omega + \int_{\Omega^+} (\nabla_{\mathbf{x}}\tilde{\boldsymbol{\eta}}) : \overset{\circ}{\boldsymbol{\sigma}} \, d\Omega \\ &+ \int_{\Gamma_d} \tilde{\boldsymbol{\eta}} \cdot (\mathbf{l}\boldsymbol{\sigma}\mathbf{n}) \, d\Gamma + \int_{\Gamma_d} \tilde{\boldsymbol{\eta}} \cdot (\overset{\circ}{\boldsymbol{\sigma}}\mathbf{n}) \, d\Gamma. \end{aligned} \quad (6.17b)$$

Note that at this stage it has not been specified which normal vector at a discontinuity should be used. To complete the linearisation, the Truesdell rate of the Cauchy stress must be expressed in terms of the rate of deformation tensor  $\mathbf{d}$ ,

$$\overset{\circ}{\boldsymbol{\sigma}} = \mathbf{c}\mathbf{d} \quad (6.18)$$

where  $\mathbf{c}$  is the *spatial* constitutive tensor and  $\mathbf{d} = 1/2 (\mathbf{l} + \mathbf{l}^T)$ .

### 6.2.2 Discrete weak governing and linearised governing equations

The discretised internal and external nodal forces are formed by discretising the weak equilibrium statement in equation (6.11). Upon inspection of equation (6.11), it can be seen that it is identical to the geometrically linear case in chapter 5. Therefore, when considering the current configuration, the discretised internal and external force calculation is the same as that in section 5.3.2, with all spatial derivatives defined on the current configuration.

To linearise the internal nodal forces, it is necessary to express equation (6.17) in terms of nodal velocities. To begin, it is clear that the linearisation in equation (6.17) can be split into material and geometric contributions. The material contribution is due to the Truesdell rate of the Cauchy stress ( $\overset{\circ}{\sigma}$ ) and the geometric contribution is due to the velocity gradient ( $l$ ). The stiffness matrix can therefore be decomposed into material ( $\mathbf{K}^{\text{mat}}$ ) and geometric ( $\mathbf{K}^{\text{geo}}$ ) contributions,

$$\mathbf{K} = \mathbf{K}^{\text{mat}} + \mathbf{K}^{\text{geo}}. \quad (6.19)$$

Considering first the material contribution by extracting the terms from equation (6.17) which involve  $\overset{\circ}{\sigma}$ , and using the relationship between the Truesdell rate of the Cauchy stress and the rate of deformation tensor in equation (6.18),

$$\delta \dot{W}_{\text{int}}^{\text{mat}, a} = \int_{\Omega} (\nabla_{\mathbf{x}} \tilde{\eta}) : c d \Omega \quad (6.20a)$$

$$\delta \dot{W}_{\text{int}}^{\text{mat}, b} = \int_{\Omega^+} (\nabla_{\mathbf{x}} \tilde{\eta}) : c d \Omega + \int_{\Gamma_d} \tilde{\eta} \cdot \mathbf{T} \dot{\mathbf{u}} d \Gamma \quad (6.20b)$$

where  $\overset{\circ}{\sigma} \mathbf{n}$  has been replaced by  $\mathbf{T} \dot{\mathbf{u}}$ . Since the tangent  $\mathbf{T}$  is formed in a local coordinate system which rotates with the discontinuity, it is dependent on the chosen normal vector at a discontinuity. For the examples in this chapter, the normal to the mid-surface between the two free surfaces at a discontinuity,  $\mathbf{n}^*$ , is used (see equation (6.12)). Note that the linearisation of the material contribution in the current configuration is identical to that for the geometrically linear case in section 5.3.3. Therefore, the matrix  $\mathbf{K}^{\text{mat}}$  is identical to the stiffness matrix in equation (5.22) when considering the current configuration and using the spatial constitutive tensor, defined in equation (6.18).

Extracting now terms from equation (6.17) which involve  $l$ , the geometric contribution to  $\dot{W}_{\text{int}}$  is expressed as:

$$\delta \dot{W}_{\text{int}}^{\text{geo}, a} = \int_{\Omega} (\nabla_{\mathbf{x}} \tilde{\eta}) : (l \sigma) d \Omega \quad (6.21a)$$

$$\delta \dot{W}_{\text{int}}^{\text{geo}, b} = \int_{\Omega^+} (\nabla_{\mathbf{x}} \tilde{\eta}) : (l \sigma) d \Omega + \int_{\Gamma_d} \tilde{\eta} \cdot (l \mathbf{t}) d \Gamma \quad (6.21b)$$

where the term  $\sigma \mathbf{n}$  has been replaced by the traction  $\mathbf{t}$ , with  $\mathbf{n}$  replaced by  $\mathbf{n}^*$ . In

terms of nodal values,  $l$  is equal to:

$$l_{ij} = \frac{\partial N_J}{\partial x_j} (\dot{a}_{ij} + \mathcal{H}_{\Gamma_d} \dot{b}_{ij}) \quad (6.22)$$

where  $a_{ij}$  denotes the regular degree of freedom in the  $i$  direction at node  $J$  and  $b_{ij}$  denotes the enhanced degree of freedom in the  $i$  direction at node  $J$ . For clarity, index notation has been used. The time derivative of the internal force vector due to geometric changes for the  $I$ th node in the  $i$  direction is therefore expressed as:

$$f_{il}^{a,int, geo} = \int_{\Omega} \frac{\partial N_I}{\partial x_j} \sigma_{kj} \frac{\partial N_J}{\partial x_k} d\Omega \dot{a}_{ij} + \int_{\Omega^+} \frac{\partial N_I}{\partial x_j} \sigma_{kj} \frac{N_J}{\partial x_k} d\Omega \dot{b}_{ij} \quad (6.23a)$$

$$f_{il}^{b,int, geo} = \int_{\Omega^+} \frac{\partial N_I}{\partial x_j} \sigma_{kj} \frac{\partial N_J}{\partial x_k} d\Omega \dot{a}_{ij} + \int_{\Omega^+} \frac{\partial N_I}{\partial x_j} \sigma_{kj} \frac{\partial N_J}{\partial x_k} d\Omega \dot{b}_{ij} \\ + \int_{\Gamma_d} N_I t_k \frac{\partial N_J}{\partial x_k} d\Gamma \dot{a}_{ij} + \mathcal{H}_{\Gamma_d} \int_{\Gamma_d} N_I t_k \frac{\partial N_J}{\partial x_k} d\Gamma \dot{b}_{ij}. \quad (6.23b)$$

Note the appearance of the Heaviside jump in the surface integral in equation (6.23b), which is not uniquely defined on  $\Gamma_d$ . Since the geometric part related to the interface reflects the change in the normal vector to a discontinuity, the linearisation should be consistent with the method used for calculating the normal vector in the constitutive update. From the calculation of the normal vector  $\mathbf{n}^*$  in equation (6.12), the Heaviside function in equation (6.23b) should be replaced by  $1/2$ . From equation (6.23), the geometric part of the stiffness matrix is equal to:

$$\mathbf{K}^{geo} = \begin{bmatrix} \mathbf{K}_{11}^{geo} & \mathbf{K}_{12}^{geo} \\ \mathbf{K}_{21}^{geo} + \mathbf{K}_{21}^{*geo} & \mathbf{K}_{22}^{geo} + \mathbf{K}_{22}^{*geo} \end{bmatrix} \quad (6.24)$$

where  $\mathbf{K}_{11}^{geo}$ ,  $\mathbf{K}_{12}^{geo}$ ,  $\mathbf{K}_{21}^{geo}$  and  $\mathbf{K}_{22}^{geo}$  are attributable to the continuum (volume integrals in equation (6.23)) and  $\mathbf{K}_{21}^{*geo}$  and  $\mathbf{K}_{22}^{*geo}$  are attributable to a discontinuity (surface integrals in equation (6.23)). The continuum contributions are equal to:

$$\mathbf{K}_{11,IJ}^{geo} = \mathbf{I} \int_{\Omega} \mathbf{B}_I^T \bar{\boldsymbol{\sigma}} \mathbf{B}_J d\Omega \quad (6.25a)$$

$$\mathbf{K}_{12,IJ}^{geo} = \mathbf{K}_{21,IJ}^{geo} = \mathbf{I} \int_{\Omega^+} \mathbf{B}_I^T \bar{\boldsymbol{\sigma}} \mathbf{B}_J d\Omega \quad (6.25b)$$

$$\mathbf{K}_{22,IJ}^{geo} = \mathbf{I} \int_{\Omega^+} \mathbf{B}_I^T \bar{\boldsymbol{\sigma}} \mathbf{B}_J d\Omega \quad (6.25c)$$

where  $\mathbf{I}$  is the identity matrix, with dimensions equal to the spatial dimension and  $\bar{\boldsymbol{\sigma}}$  denotes the stress in matrix form,

$$\bar{\boldsymbol{\sigma}} = \begin{bmatrix} \sigma_{11} & \sigma_{12} & \sigma_{13} \\ \sigma_{21} & \sigma_{22} & \sigma_{23} \\ \sigma_{31} & \sigma_{32} & \sigma_{33} \end{bmatrix}. \quad (6.26)$$

The vector  $\mathbf{B}_I^T$  is equal to:

$$\mathbf{B}_I^T = \left\{ \frac{\partial N_I}{\partial x_1} \quad \frac{\partial N_I}{\partial x_2} \quad \frac{\partial N_I}{\partial x_3} \right\}. \quad (6.27)$$

The terms in the geometric stiffness matrix due to the interface, denoted  $\mathbf{K}_{21}^{*\text{geo}}$  and  $\mathbf{K}_{22}^{*\text{geo}}$  in equation (6.24), have not been included in the implementation since they destroy symmetry of the stiffness matrix.

The geometric stiffness of the interface is a linearisation of the changing normal vector at a discontinuity which results in a rotation of the internal forces due to the tractions acting at a discontinuity. The geometric part of the stiffness matrix associated with a discontinuity is significant only when a discontinuity at which significant tractions are acting undergoes large rotations. As the tractions acting at an interface approach zero, so does the contribution of a discontinuity to the geometric part of the stiffness matrix. For many practical problems, the displacement jump across interfaces which are undergoing large rotations is large and therefore the tractions are small, hence the contribution of the interface to the geometric stiffness is small. Traction free surfaces make no geometric contribution to the stiffness matrix. Tests indicate that for problems where the material tangents are symmetric, it is more efficient to ignore the geometric contribution of a discontinuity. The slight increase in the number of iterations required to achieve convergence when the geometric contribution of a discontinuity is ignored is compensated for by the retention of a symmetric stiffness matrix. This however may not be the case when geometric instabilities play an important role in the delamination process. In this case, the inclusion of geometric effects due to a discontinuity may enhance robustness.

### 6.3 Implementation aspects for laminated materials

Implementation of the partition of unity-based model for laminated composite materials is similar to the geometrically linear case in the previous chapter. Since the paths of potential discontinuities are limited to the boundaries between laminate layers, the nodes which may at some stage be enhanced are known before a calculation is commenced and the integration scheme in elements which may be later crossed by a discontinuity can be constructed before a calculation begins. For the six-noded triangular elements used in this chapter, the integration scheme is the same as that described in section 5.4.3. Constructing the integration scheme and identifying nodes which may require enhancement before a calculation begins can simplify implementation in standard finite element codes.

When simulating laminated materials, there are some potential implementation benefits when using a dummy elastic stiffness in the formulation. If a dummy stiffness is used, enhanced degrees of freedom can be activated from the start of a calculation and there is no need to follow where a discontinuity tip is located. This can simplify the implementation greatly when considering a multiple layer material

and when delamination occurs from both ends of a layer. Once a calculation has started, there is no need to monitor exactly where delamination is taking place. It will also be shown that use of an elastic dummy stiffness can lead to a smoother load–displacement response when using a coarse mesh. The disadvantage of using an elastic dummy stiffness is the risk that the response is overly soft or shows a loss of robustness, as will be illustrated by a numerical example.

The position of a discontinuity is described in the undeformed configuration. This is particularly simple for simulating delamination since in the reference configuration, the direction of propagation is known since it follows inter-laminar boundaries. For propagating discontinuities, whose direction is determined during a calculation, the position of a discontinuity is also traced in the reference configuration. Once the direction of propagation is determined in the current configuration, the direction can be ‘pulled-back’ into the reference configuration. In this way the same algorithms can be used for both geometrically linear and non-linear problems.

To integrate the traction forces acting at a discontinuity, it is necessary to calculate the area of the discontinuity in the current configuration. Tractions are integrated over the surface  $\Gamma_d^*$ , which is shown in figure 6.3. For two-dimensional problems, this involves calculating the length of a line in the current configuration. There are two approaches that could be used to calculate the length of a discontinuity in the current configuration. The first is to calculate the position of a number of points on the centre line between the two discontinuity surfaces in the current configuration and interpolate linearly between the points. However, if the geometric contribution of a discontinuity is included in the stiffness matrix, this method is not consistent with the linearisation. A more elegant and consistent approach is in terms of the stretch in the continuum. The updated discontinuity length  $l$  (which is the integration weight for an integration point) is equal to:

$$l = \lambda l_0 \quad (6.28)$$

where  $l_0$  is the discontinuity length in the reference configuration and  $\lambda$  is the stretch, which is given by:

$$\lambda = \sqrt{\mathbf{a}_0 \cdot \mathbf{C} \mathbf{a}_0} \quad (6.29)$$

where  $\mathbf{a}_0$  is the unit vector in the direction of a discontinuity line in the reference configuration (therefore it is orthogonal to the normal vector  $\mathbf{n}_0$ ) and  $\mathbf{C}$  is the right Cauchy-Green tensor ( $\mathbf{C} = \mathbf{F}^T \mathbf{F}$ ). Since the deformation gradient is discontinuous across a discontinuity, the right Cauchy-Green tensor is also discontinuous. The stretch is calculated using  $\mathbf{F} = \hat{\mathbf{F}} + \frac{1}{2} \tilde{\mathbf{F}}$ , which corresponds to the surface midway between the two discontinuity surfaces. This method for calculating  $l$  will be used for the numerical examples in this chapter. It is particularly appealing for interface delamination since the length  $l_0$  and the vector  $\mathbf{a}_0$  are known from the outset of a calculation. For three-dimensional problems, the areas of a surface in the reference and

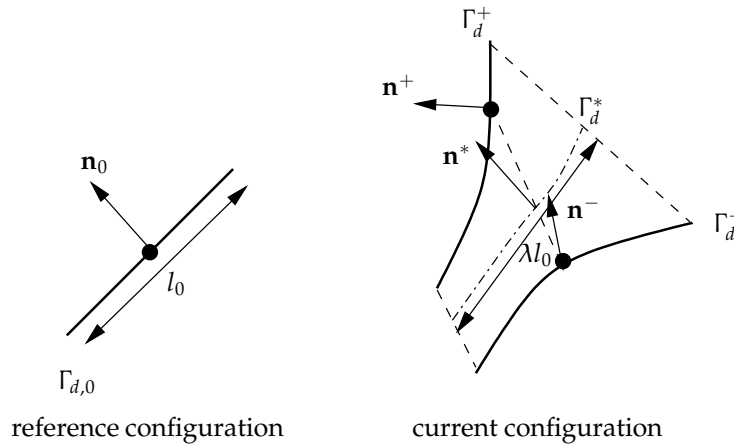


Figure 6.4: An interface length associated with an integration point in the reference and current configurations. The solid dot represents the integration point.

current configurations can be related through Nanson’s formula. Figure 6.4 shows a segment of a straight line in the reference configuration and the integration point associated with the segment and the same segment in the deformed configuration. Note in figure 6.4 that the length  $\lambda l_0$  is shorter than the length of the two free surfaces,  $\Gamma_d^+$  and  $\Gamma_d^-$ . The length  $\lambda l_0$  can be considered the length across which tractions can be transmitted, not the length of the free surfaces in the material.

#### 6.4 Numerical examples of interface delamination

The numerical examples in this section are intended to illustrate the performance and the potential of the geometrically non-linear partition of unity model. All examples are two-dimensional, with the six-noded triangular element used as the underlying element and plane strain conditions are assumed. The continuum is assumed to be elastic, with a compressible neo-Hookean model used. The compressible neo-Hookean model has a stored energy function  $\Psi$  of the form (Bonet and Wood, 1997):

$$\Psi = \frac{\mu}{2} (\text{tr}(\mathbf{C}) - 3) - \mu \ln(\det \mathbf{F}) + \frac{\lambda}{2} (\ln(\det \mathbf{F}))^2 \quad (6.30)$$

where  $\mu$  and  $\lambda$  are Lamé coefficients. Details of the stress calculation and the spatial tangent can be found in Bonet and Wood (1997). For examples with a growing delamination length, a discontinuity is extended when the stress normal to the interlaminar boundary exceeds the tensile strength of the material. Discontinuities are extended in the same direction as the interface between plies. Unless stated otherwise, an elastic dummy stiffness is not used.

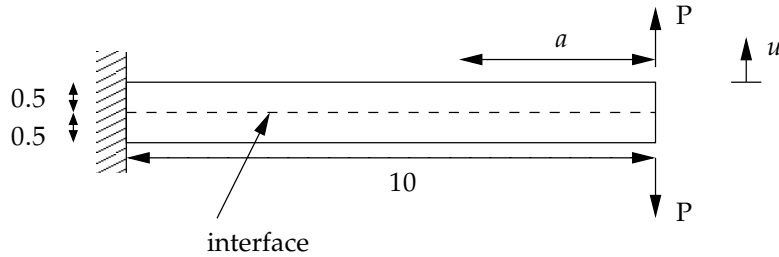


Figure 6.5: Peel test geometry for a two layer laminate. The dashed line is the inter-laminar boundary and the initial delamination length is denoted  $a$ . All dimensions in millimetres.

#### 6.4.1 Peel test with an existing, traction-free discontinuity

To test the geometrically non-linear model, a peel test is performed on a double-cantilever beam (DCB), shown in figure 6.5. The beam is constructed of two layers of the same material. The dashed line in figure 6.5 shows the interface between the two layers and  $a$  is the initial delamination length. The initial delamination length is assumed to be traction-free. The peel test is performed with an initial delamination length of  $a = 8$  mm, and the discontinuity is not allowed to propagate. For the continuum response, Young’s modulus  $E = 100$  MPa and Poisson’s ratio  $\nu = 0.3$  ( $\lambda \approx 57.69$  MPa,  $\mu \approx 38.46$  MPa). The test is performed for two cases. The first involves a structured mesh in which the initial delamination is explicitly modelled by the mesh. The second case involves an unstructured mesh, with the partition of unity model used to simulate the initial delamination length. The intention is to show that the partition of unity model is equivalent to explicitly taking into account a discontinuity in the mesh construction. The two meshes, in the deformed configuration are shown in figure 6.6. Note that the deformations in figure 6.6 are not magnified. The geometrically non-linear load–displacement responses for the two meshes and the geometrically linear response are shown in figure 6.7. The responses of the two meshes for the geometrically non-linear case are near identical, confirming that the partition of unity model leads to a result which is equivalent to explicitly modelling a discontinuity.

#### 6.4.2 Peel test for a growing discontinuity

The peel test is now performed for a growing delamination length with traction forces acting at the discontinuity. An initial delamination length of  $a = 1$  mm is assumed. The discrete constitutive model applied at the discontinuity is that developed in section 3.1. The shear (sliding) stiffness is taken as zero, which, in the absence of the geometric contribution of the discontinuity to the stiffness matrix, leads to a symmetric global stiffness matrix. Prior to delamination, a perfect bond is assumed. Note also that this is an example for which the absence of a geometric contribution

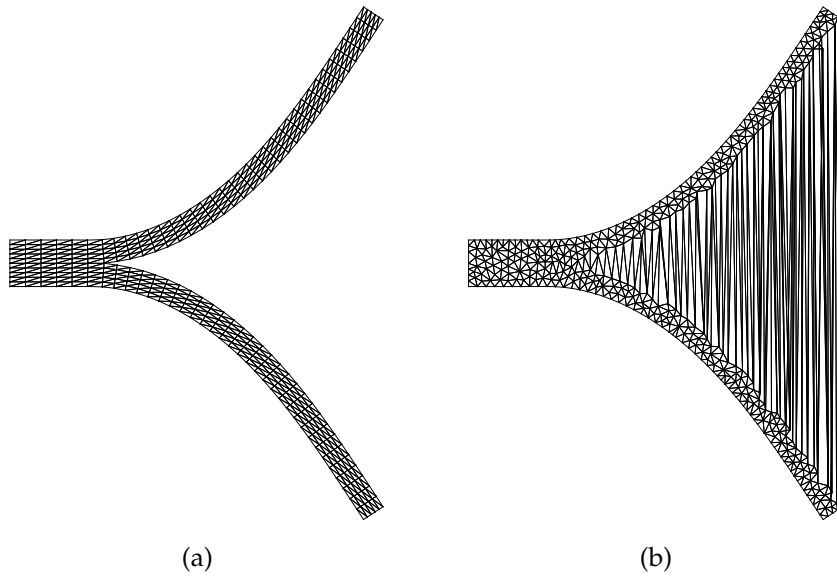


Figure 6.6: Peel test in the deformed configuration for (a) explicitly modelled discontinuity and (b) the enhanced simulation. The deformation is not magnified.

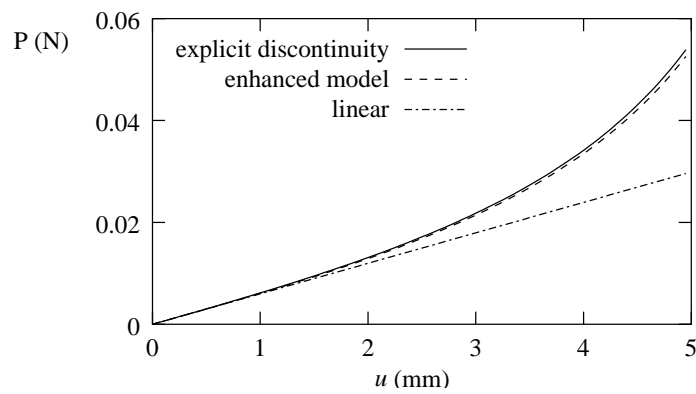


Figure 6.7: Load-displacement response for the traction-free peel test.

to the stiffness matrix due to the tractions acting at the interface is of little consequence since the normal vector used for the discrete constitutive model is constant. The following materials properties are adopted for the analysis: Young’s modulus  $E = 100$  MPa and Poisson’s ratio  $\nu = 0.3$  for the continuum and at the interface the tensile strength  $f_t = 1$  MPa and fracture energy  $G_f = 0.1$  Nmm<sup>-1</sup>.

To test the objectivity of the model with respect to spatial discretisation, the peel test is analysed using two different, unstructured meshes. The first mesh is the same as that shown in figure 6.6b, which consists of 781 elements. The second mesh is composed of 2896 elements. The two meshes, in deformed configuration (not magnified) at displacements of 2 mm and 6 mm, are shown in figure 6.8. For the mesh with 781 elements, the test is also performed using an elastic dummy stiffness (dummy stiffness =  $1 \times 10^3$  Nmm<sup>-3</sup>). For this case, a discontinuity is present from the start of the analysis. The load–displacement responses for the two meshes are shown in figure 6.9. Also shown is the response for the coarser mesh using a dummy elastic stiffness. Note the roughness of the response for the coarser mesh. This is due to extensions of a discontinuity through an entire element and the ‘jumping’ of inelastic deformation from integration point to integration point. Despite this, the solution converged robustly for all load increments. The stress state ahead of the delamination ‘tip’ is complex, and has a very high gradient. As the mesh is refined, the response is smoother. This was also observed for the three-point bending test performed in section 5.5.1. Although the response is very rough for the coarse mesh, the response generally follows the response for the finer mesh, indicating that the computed response is insensitive to spatial discretisation. The response using an elastic dummy stiffness is smoother than for the propagating model, although the numerical convergence was poorer. The calculation using an elastic dummy stiffness diverged at a displacement of  $u = 2.68$  mm. Using a lower dummy stiffness of  $1 \times 10^2$  Nmm<sup>-3</sup> led to a converged result, although the response was overly soft.

#### 6.4.3 Geometric buckling due to existing delamination length

A compression test with a small perturbation is now performed to show the potential for simulating geometric instabilities. This is a very important failure mode for laminated composites since individual layers are generally slender and prone to buckling. It is an application that relies heavily on the inclusion of geometrically non-linear effects to capture the proper failure mode and the mechanism driving delamination. To illustrate buckling of a laminated material, a test similar to the peel test is performed under compressive loading. Rather than two layers being peeled apart, the layers are compressed. A small lateral load triggers the lateral deflection of the layers. The test geometry is shown in figure 6.10. Young’s modulus is taken as  $E = 100$  MPa and calculations are performed for two values of Poisson’s ratio,  $\nu = 0$  and  $\nu = 0.3$ . The mesh used is the same as that in figure 6.6b (781 elements). It is assumed that delamination has occurred along the entire length of the specimen, with tractions only

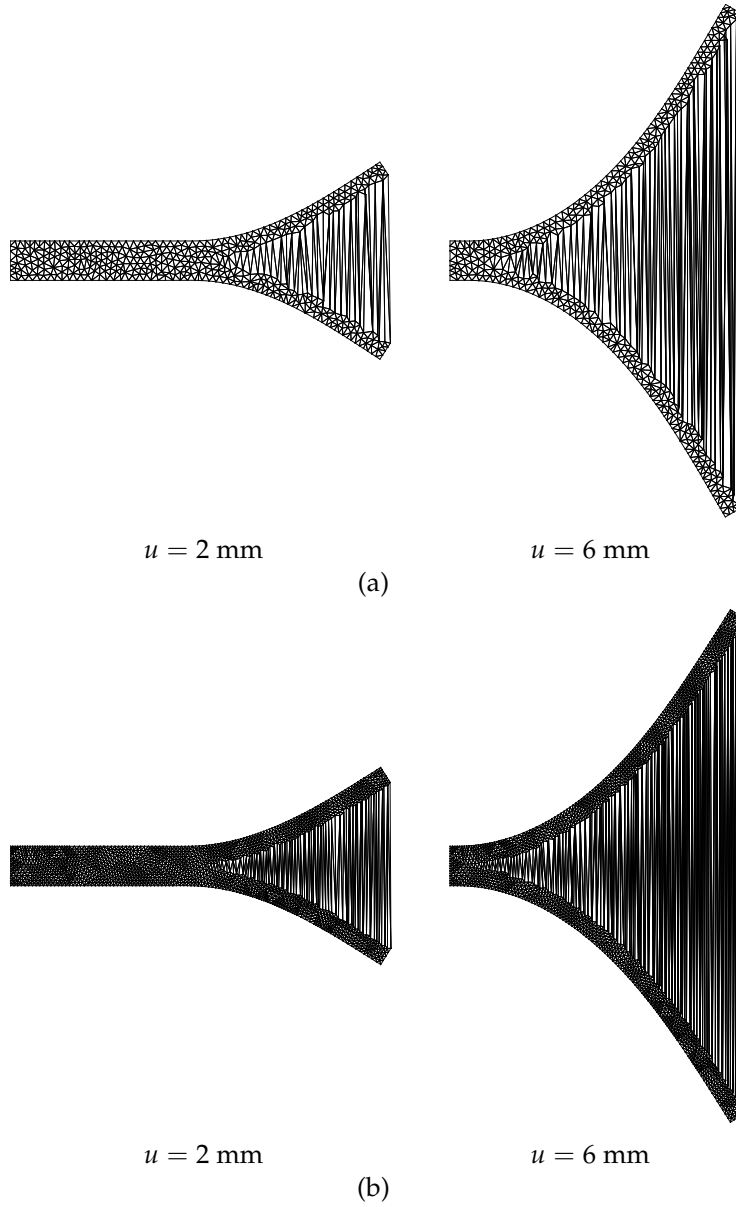


Figure 6.8: Peel test in the deformed configuration at different displacements with (a) 781 elements and (b) 2896 elements. The deformation is not magnified.

NUMERICAL EXAMPLES OF INTERFACE DELAMINATION

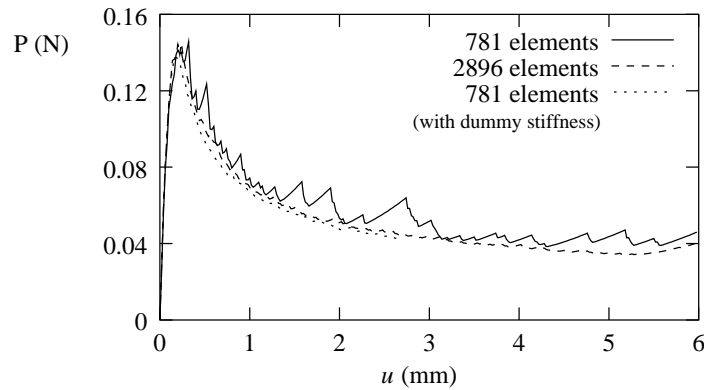


Figure 6.9: Load–displacement response for the peel test with a growing delamination.

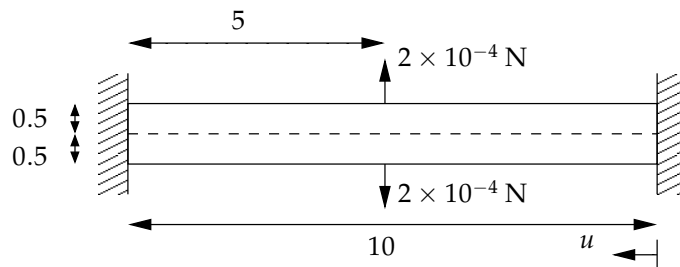


Figure 6.10: Geometry for the compression test. All dimensions in millimetres.

transmitted if the layers come into contact. The test is performed under displacement control, with a horizontal displacement applied at the right-hand side of the specimen.

The load-displacement responses for the two values of Poisson’s ratio are shown in figure 6.11. It can be seen that the response is linear to a critical level, at which point the layers buckle. The critical Euler buckling load  $P_{crit}$  for a column with fully restrained ends is equal to:

$$P_{crit} = \frac{4\pi^2 EI}{L^2} \approx 0.4112 \text{ N} \quad (6.31)$$

where  $I$  is the moment of inertia of the column and  $L$  is the column length. The critical buckling load has been approximated closely in equation (6.31) for the example shown in figure 6.10. This Euler buckling load is in excellent agreement with the critical load calculated numerically for the case with Poisson’s ratio  $\nu = 0$ , which is equal to 0.406 (note that the load in figure 6.11 should be divided by two since it represents two columns). The deformed mesh for the compression test is shown in figure 6.12, showing that the two layers have moved away from each other.

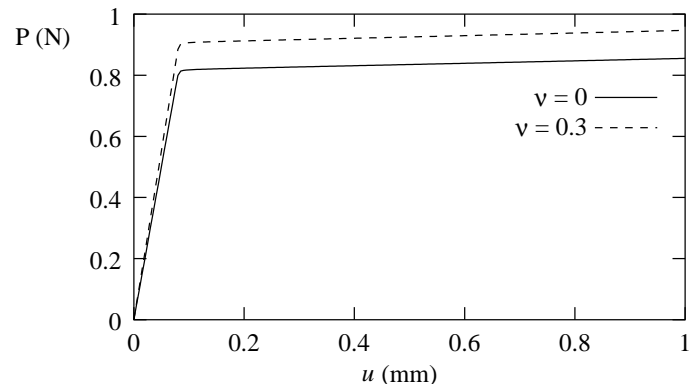


Figure 6.11: Load–displacement response for the compression test.

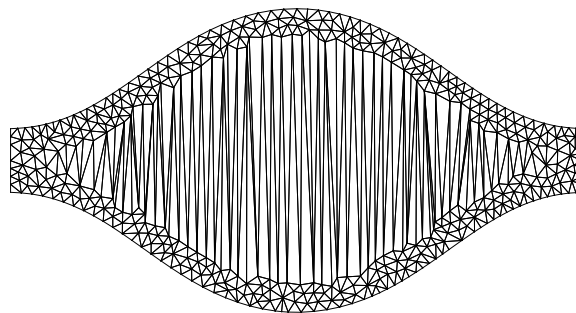


Figure 6.12: Deformed mesh for the compression test at  $u = 1$  mm. The deformation is not magnified.

## Chapter 7

### Combined continuum–discontinuous model for crack propagation and strain localisation

The partition of unity concept is now used to model discontinuities in an inelastic, strain softening medium. When the inelastic deformation at the tip of a discontinuity has reached a critical value, the discontinuity is extended. The material at this critical level of inelastic deformation is considered to lose all coherence, leading to the development of two free surfaces in a body. At this point, the only way forces can be transmitted between the surfaces is through contact. It is intended that this model is better able to represent the entire failure process than a continuum or cohesive zone model alone.

To include strain softening in a continuum description, it is necessary to use a regularised continuum model. There are several different methods of regularisation, as outlined in chapter 1. In this chapter, a rate-dependent continuum model, namely a viscoplastic model, is used. A viscoplastic model is chosen for algorithmic reasons. Unlike several other regularised continuum models, viscoplastic models do not require special element formulations. At the development stage, it is desirable to avoid models which would lead to further complexities at element level. Also, in contrast to non-local models, a consistently linearised (algorithmic) tangent can be formed in a straightforward fashion which results in a robust model that converges rapidly.

Rather than representing inelastic deformations as cohesive forces acting on a discontinuity, inelastic deformations are now modelled in the continuum. A discontinuity is no longer a convenient fictitious concept, but rather a genuine separation in a material. The inclusion of discontinuities into a regularised, strain softening continuum model allows the entire failure process, from the onset of inelastic deformation to complete failure, to be modelled effectively. For fracture problems, it is possible to model the distinct zones observed in a body with a crack under load. The continuum model is able to simulate the plastic flow and micro-cracking around a crack tip, while a traction-free discontinuity represents a macroscopic crack. If the crack tip propagates, the discontinuity can be extended and the continuum part of the model is able to capture the propagating inelastic zone and the inelastic wake. In introduc-

ing discontinuities to a strain softening continuum model, the three main objectives are:

- an improved model for simulating the entire failure process, from initial damage or plastic flow to complete loss of integrity at a material point;
- to avoid the spurious behaviour of some regularised continuum models prior to complete failure; and
- to simulate crack tips – capture the process and inelastic zones around a crack tip.

While the most obvious application of a combined continuum-discrete model is to fracture problems, the approach is also applicable to mode-II failure problems. For mode-II failure under compressive loading, a discontinuity in a strain softening continuum is considered to imply a cohesionless slip plane. An advantage of introducing a discontinuity during failure is that a degree of anisotropy is introduced naturally to a problem. This is a significant advantage when considering that regularised continuum models are inherently complex and the introduction of anisotropy to a regularised continuum model is often highly complex.

## 7.1 Continuum theories for cracked media and strain localisation

Several regularised continuum models which have been used for fracture and strain localisation simulations were discussed in chapter 1. In this section, the responses of several models at the later stages of failure are discussed. The discussion is qualitative in nature and is intended to illustrate the deficiencies of continuum models for simulating the complete failure process. The response of regularised continuum models at the later stages of failure provides a motivation for the introduction of displacement discontinuities.

### 7.1.1 Theories based on non-local strains or strain gradients

Several continuum models have been proposed that are based on non-local fields. Conceptually the most simple is non-local elasticity, where the stress at a point is determined using a non-local strain tensor  $\bar{\epsilon}$ , rather than the usual local strain tensor  $\epsilon$ :

$$\sigma = \mathcal{C}\bar{\epsilon}. \quad (7.1)$$

The non-local strain tensor is calculated as a weighted spatial average of the local strain tensor. A commonly used weighting function is the Gaussian function (equation (5.26)). A special property of non-local elasticity is that while at a sharp crack tip the local strain is singular, the non-local strain is bounded. This, unlike classical elasticity, avoids a stress singularity at a sharp crack tip (Eringen et al., 1977). For strain

softening problems, it was shown by Pijaudier-Cabot and Bažant (1987) that the spurious response of a classical continuum model can be avoided by taking only some fields as non-local. Specifically, for an elasticity based non-local isotropic damage model, the stress at a point is calculated by:

$$\boldsymbol{\sigma} = (1 - \omega) \mathbf{C} \boldsymbol{\varepsilon} \quad (7.2)$$

where  $\omega$  is the damage level ( $\omega = 0$  corresponds to the undamaged state and  $\omega = 1$  corresponds to the fully damaged state). The damage level is calculated as a function of the non-local strain tensor,

$$\omega = \omega(\bar{\boldsymbol{\varepsilon}}). \quad (7.3)$$

The damage is calculated as a regular function of an invariant of the non-local strain tensor. Generally, as the invariant increases, the damage  $\omega$  approaches unity. Since the non-local strain is bounded, at a crack tip the damage level can be less than unity in the presence of a local strain singularity. Therefore, under a constant load a crack tip may remain stationary. This is in contrast to a local damage model where any loading that induces damage at any level will lead to instantaneous crack growth. While for the non-local damage model the damage can remain bounded at a crack tip, the stress is still calculated as a function of the local strain (see equation (7.2)), and therefore if the local strain field is singular, for  $\omega \neq 1$  a stress singularity is predicted and the normal stress along a crack is discontinuous, as for the classical linear-elastic case.

Closely related to non-local models are strain gradient-dependent models (De Borst and Mühlhaus, 1992; Peerlings et al., 1998). Normally for gradient models, the stress at a point is a function of the usual local quantities (strain and history variables) plus the second gradient of a scalar quantity which is a measure of inelastic deformation. In the presence of a sharp crack tip, it was shown by Peerlings (1999) that, for a particular gradient damage model, the same arguments applied for the non-local damage model in the presence of a sharp crack tip hold. The arguments for gradient plasticity models are different since the local stress field is calculated differently. The local stress is calculated by equation (3.9), with the yield stress made a function of gradient terms.

All the enhanced continuum models discussed introduce a length scale directly into the material description. The non-local models require a length scale which determines how quickly the non-local weighting function decays away from a point. Similarly, gradient models require a length scale which controls the sensitivity of the response at a point to the strain gradients.

### 7.1.2 Rate-dependent continuum models

An alternative regularisation technique is the introduction of rate-dependence which requires an extra material parameter – viscosity. The viscosity determines the sensitivity of the material response to the strain rate. It has been shown that the inclusion

of rate-dependency in a continuum constitutive model has a regularising effect in the presence of strain softening, whether this be for viscoplastic (Needleman, 1988; Wang et al., 1997) or smeared crack (Sluys and De Borst, 1992) models. The size of the localisation zone is determined by the viscosity parameter in combination with the loading rate. In the two extreme cases of infinite viscosity and zero viscosity, the elastic and inviscid responses are recovered, respectively. The elastic response of course implies a localisation zone of infinite width and the inviscid response a localisation band of zero width.

One form of rate dependent models are viscoplastic models. Viscoplastic models are similar in form to classical inviscid plasticity models, where the strain field is decomposed into elastic and inelastic (viscoplastic) parts,

$$\dot{\boldsymbol{\varepsilon}} = \dot{\boldsymbol{\varepsilon}}^e + \dot{\boldsymbol{\varepsilon}}^{VP} \quad (7.4)$$

where  $\dot{\boldsymbol{\varepsilon}}^{VP}$  is the viscoplastic strain rate. Similar to classical plasticity models (see equation (3.9)), the stress rate is expressed as:

$$\dot{\boldsymbol{\sigma}} = \mathbf{C} (\dot{\boldsymbol{\varepsilon}} - \dot{\boldsymbol{\varepsilon}}^{VP}). \quad (7.5)$$

Rate-dependency is introduced in the determination of the viscoplastic strain. In the case of zero viscosity (inviscid case), the plastic strain is calculated in the usual fashion, while for infinite viscosity the viscoplastic strain is zero, which according to equation (7.5) leads to an elastic response. It is also clear that if only the inelastic strain is rate-dependent, the elastic response is rate-independent.

### 7.1.3 Limitations of enhanced models near complete failure

The performance of several non-local and gradient enhanced models deteriorates significantly towards the end of the failure process as they are unable to represent the development of internal surfaces (slip lines or cracks). At some stage in the failure process, very thin zones develop where the load carrying capacity of the material is exhausted. Physically, these very thin zones represent the development of internal surfaces. Considering these very thin zone as surfaces, the strain on these surfaces approaches infinity and the stress is equal to, or approaches, zero. However, the response at points near the surface is influenced by the strain at the ‘surface’ and by points on the other side of the surface. For non-local models, the high strain at a ‘surface’ contributes significantly to the non-local strain integral for points close to the surface, and for gradient models the high strains at a ‘surface’ induces very high strain gradients at points near the surface. The numerical implication is that for some models the inelastic zone ‘grows’ spuriously in the directions normal to a discontinuity. At a point next to a crack, the local strain field may be decreasing, while the non-local strain actually increases, driving the development of damage. Eventually, the damaged zone will encompass a whole specimen (Geers, 1997).

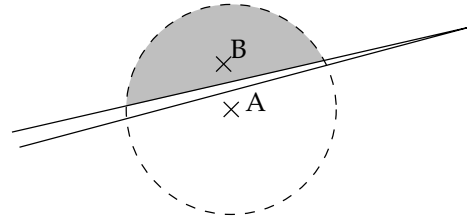


Figure 7.1: Non-local integration domain (dashed line) for point A near a crack. The shaded area should be removed from the integration domain to avoid point B influencing the response at point A.

The solution for non-local models is conceptually straightforward. The integration domain for calculating non-local quantities should be cut at internal interfaces to avoid the interaction of points on opposite sides of a discontinuity and points with zero load carrying capacity should be removed from non-local integrals. This is illustrated in figure 7.1, where points A and B on opposite sides of a crack should not influence each other. For strain gradient models, the solution is more complex. To avoid this problem, Geers et al. (1998) made the length scale that controls the gradient influence variable in order to reduce the influence of the very high strains at a crack. This however does not deal with the underlying problem – the finite element model is unable to represent newly developed surfaces in a continuum. Proper treatment of the problem must allow the development of discontinuity surfaces within a body which are handled in the same manner as external boundaries. Peerlings (1999) dealt with the problem by removing elements which possessed no residual strength. In this case, free surfaces are generated although the procedure requires very fine meshes and the path of a discontinuity is influenced by the mesh structure. Jirásek and Zimmermann (2001) attempted to overcome the limitations of a non-local damage model at the later stages of failure by allowing a transition from continuum, smeared cracking to a cohesive zone. This was however done with an embedded discontinuity model based on incompatible strain modes, as described in chapter 4, which was shown in section 4.4 to be similar to a classical smeared crack model.

Similar arguments can be presented for strain softening viscoplastic models since the strain rate at a discontinuity approaches infinity. As the strain rate increases, the allowable effective stress increases relative to the inviscid yield surface (the ‘overstress’). If the effective stress at a ‘surface’ remains high despite strain softening, material next to the ‘surface’ loads rather than unloads and the localised zone widens. Another consequence of the high strain rates that develop at the centre of a localisation zone is that a specimen often exhibits a residual strength. It can be difficult with rate dependent models to reach a zero load level in the late stages of failure. Often a load plateau is reached which is dependent on the loading rate. The inclusion

of a discontinuity in the formulation results in the material next to a discontinuity unloading, and a zero load level can be reached.

## 7.2 Perzyna viscoplastic model

A commonly used rate-dependent model is the Perzyna viscoplastic model (Perzyna, 1966). This model will be used for calculations in this chapter. The Perzyna model is an overstress type model, where stresses outside the inviscid yield surface are permissible. How severely stress states outside the inviscid yield surface are penalised is determined by the viscosity parameter  $\eta$ . Under stationary loading, the stress state returns to the yield surface with time. For a finite time increment, if  $\eta$  is equal to zero, stress states outside the yield surface are not admissible and the rate independent case is recovered, and if  $\eta$  approaches infinity, stress states outside the inviscid yield surface are not penalised and the elastic case is recovered.

For the Perzyna model, the viscoplastic strain rate for associative flow is given by:

$$\dot{\epsilon}^{\text{VP}} = \frac{1}{\eta} \langle \phi(f) \rangle \partial_{\sigma} f \quad (7.6)$$

where the ‘overstress function’  $\langle \phi(f) \rangle$  is defined as:

$$\langle \phi(f) \rangle = \begin{cases} \left( \frac{f}{\bar{\sigma}_0} \right)^N, & f \geq 0 \\ 0, & f < 0 \end{cases} \quad (7.7)$$

where the scalar  $N$  ( $N \geq 1$ ) in equation (7.7) is a material parameter that is fitted to experimental observations. It is also possible to write equation (7.7) with the ‘current’ yield stress  $\bar{\sigma}$  in the overstress function, rather than the initial yield stress  $\bar{\sigma}_0$ . This is intuitively more appealing, although in implementation for strain softening problems lacks robustness. Considering that for classical plasticity  $\dot{\epsilon}^{\text{P}} = \dot{\lambda} \partial_{\sigma} f$ , from equation (7.6) the plastic multiplier for the Perzyna model can be expressed as:

$$\dot{\lambda} = \frac{\langle \phi(f) \rangle}{\eta}. \quad (7.8)$$

### 7.2.1 Algorithmic formulation for Perzyna viscoplasticity

The rate equations for Perzyna viscoplasticity are integrated with a backward-Euler scheme to calculate the stress and internal variables at the end of a load increment. To do this, two residuals can be formulated, the first for the stresses ( $r_{\sigma}$ ) and a second for the plastic multiplier ( $r_{\lambda}$ ). When cast in this format the computational implementation is very similar to the rate-independent case.

Inserting equation (7.7) into the expression for the stress field in equation (7.5) and rearranging leads to the stress residual  $\mathbf{r}_\sigma$ :

$$\mathbf{r}_\sigma = \boldsymbol{\sigma}_{n+1} - \boldsymbol{\sigma}_{\text{trial}} + \Delta\lambda \mathbf{C} \partial_\sigma f \quad (7.9)$$

where  $\boldsymbol{\sigma}_{n+1}$  is the stress at the end of the load increment and the trial stress  $\boldsymbol{\sigma}_{\text{trial}}$  is equal to:

$$\boldsymbol{\sigma}_{\text{trial}} = \boldsymbol{\sigma}_n + \mathbf{C} \Delta \boldsymbol{\varepsilon}_{n+1} \quad (7.10)$$

where  $\boldsymbol{\sigma}_n$  is the stress at the beginning of the load increment. Consistent with the backward Euler approach, the plastic multiplier increment  $\Delta\lambda_{n+1}$  is assumed to be equal to  $\Delta t \dot{\lambda}_{n+1}$ , where  $\Delta t$  is the time increment. Inserting this into equation (7.8) yields a residual in terms of the plastic multiplier,  $r_\lambda$ .

$$r_\lambda = \Delta\lambda_{n+1} - \frac{\Delta t}{\eta} \langle \phi(f) \rangle \quad (7.11)$$

Differentiating the residuals in equations (7.9) and (7.11) with respect to stresses and the plastic multiplier leads to the linearised equations:

$$\mathbf{0} = (\mathcal{I} + \Delta\lambda \mathbf{C} \partial_{\sigma\sigma} f) d\boldsymbol{\sigma} + \mathbf{C} \partial_\sigma f d\lambda + \mathbf{r}_\sigma \quad (7.12a)$$

$$0 = d\lambda - \frac{\Delta t}{\eta} \phi' \partial_\sigma f : d\boldsymbol{\sigma} + \frac{\Delta t}{\eta} \phi' A d\lambda + r_\lambda \quad (7.12b)$$

where  $\phi' = \partial\phi/\partial f$ ,  $\partial_{\sigma\sigma} f = \partial^2 f / \partial \boldsymbol{\sigma}^2$  and  $\mathcal{I}$  is the fourth-order identity tensor. Note that the scalar  $A$  is equal to:

$$A = -\frac{\partial f}{\partial \kappa} \frac{\partial \kappa}{\partial \lambda} \quad (7.13)$$

The equations in (7.12) can be expressed as:

$$\begin{bmatrix} -\mathcal{P} & -\mathbf{C} \partial_\sigma f \\ \frac{\Delta t}{\eta} \phi' \partial_\sigma f & -\left(1 + \frac{\Delta t}{\eta} \phi' A\right) \end{bmatrix} \begin{Bmatrix} d\boldsymbol{\sigma} \\ d\lambda \end{Bmatrix} = \begin{Bmatrix} \mathbf{r}_\sigma \\ r_\lambda \end{Bmatrix} \quad (7.14)$$

where

$$\mathcal{P} = \mathcal{I} + \Delta\lambda \mathbf{C} \partial_{\sigma\sigma} f. \quad (7.15)$$

The system of equations is solved in an iterative manner. In practice,  $d\lambda$  is first solved by eliminating  $d\boldsymbol{\sigma}$  from equation (7.12b). To do this, equation (7.12a) is multiplied by  $-\partial_\sigma f \mathcal{P}^{-1}$ ,

$$\begin{aligned} \partial_\sigma f : d\boldsymbol{\sigma} + \partial_\sigma f \mathcal{P}^{-1} \mathbf{C} \partial_\sigma f d\lambda &= -\partial_\sigma f \mathcal{P}^{-1} \mathbf{r}_\sigma \\ \partial_\sigma f : d\boldsymbol{\sigma} &= -\partial_\sigma f \mathcal{P}^{-1} \mathbf{C} \partial_\sigma f d\lambda - \partial_\sigma f \mathcal{P}^{-1} \mathbf{r}_\sigma. \end{aligned} \quad (7.16)$$

Inserting this result into equation (7.12b), the iterative increment  $d\lambda$  can be calculated as:

$$d\lambda = -\frac{(\eta/(\Delta t\phi'))r_\lambda + \partial_\sigma f \mathcal{P}^{-1} \mathbf{r}_\sigma}{\partial_\sigma f \mathcal{P}^{-1} \mathcal{C} \partial_\sigma f + A + \eta/(\Delta t\phi')} \quad (7.17)$$

Once  $d\lambda$  is calculated, the iterative stress increment  $d\sigma$  can be calculated by rearranging equation (7.12a).

$$d\sigma = -\mathcal{P}^{-1} (\mathbf{r}_\sigma + \mathcal{C} \partial_\sigma f d\lambda) \quad (7.18)$$

The procedure of updating  $\Delta\lambda$  and  $\sigma$  within a load increment is repeated until the norm of both residuals ( $\mathbf{r}_\sigma$  and  $r_\lambda$ ) is less than a prescribed tolerance. The final step is to form the consistently linearised tangent which is used in forming the global stiffness matrix. The consistent tangent is formed by eliminating  $d\lambda$  from equation (7.14) and expressing the residual  $\mathbf{r}_\sigma$  in terms of the strain increment as  $\mathcal{C}d\epsilon$ . Inserting this and the iterative increment of the plastic multiplier from equation (7.17) (setting  $r_\lambda$  equal to zero) into equation (7.18) yields:

$$d\sigma = \left( \mathcal{R} - \frac{\mathcal{R} \partial_\sigma f \otimes \mathcal{R} \partial_\sigma f}{\partial_\sigma f \mathcal{R} \partial_\sigma f + A + \eta/(\Delta t\phi')} \right) d\epsilon \quad (7.19)$$

where the term in the brackets is the consistently linearised tangent, with  $\mathcal{R} = \mathcal{P}^{-1} \mathcal{C}$ . Note that setting  $\eta = 0$ , the consistent tangent for the rate-independent case is recovered.

### 7.2.2 Yield criteria

The numerical examples at the end of this chapter use two different yield functions. The first is the Von Mises yield function, given in equation (3.30). The second yield function is a modified Rankine yield function, with the classic multi-surface Rankine yield function modified to avoid the vertex since the Perzyna viscoplastic model should not be used for multi-surface yield functions (Simo et al., 1988). Also, the smoothed yield surface simplifies the calculation of the consistently linearised tangent. The modified Rankine yield surface in two dimensions is written as (Pamin, 1994):

$$f(\sigma, \kappa) = \begin{cases} \sigma_1 - f_t(\kappa) & \text{if } \sigma_2 \leq 0 \\ \sqrt{\sigma_{11}^2 + \sigma_{22}^2 + 2\sigma_{12}^2} - f_t(\kappa) & \text{if } \sigma_2 > 0 \end{cases} \quad (7.20)$$

where  $\sigma_1$  and  $\sigma_2$  are the principal stresses ( $\sigma_1 > \sigma_2$ ). Following common convention, the Von Mises yield function is expressed using the yield stress  $\bar{\sigma}$  and the modified Rankine yield function is expressed using the tensile strength  $f_t$ . The modified Rankine yield surface in equation (7.20) is applicable for plane stress conditions. It is also

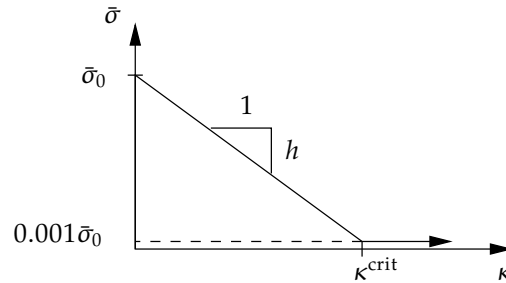


Figure 7.2: Yield stress/tensile strength as a function of the equivalent plastic strain  $\kappa$ .

applicable under plane strain condition if the tensile stress in the third direction ( $\sigma_3$ ) does not exceed the tensile strength  $f_t$ . For all plane strain examples presented in this chapter using the modified Rankine yield surface, the tensile stress in the third direction never exceeded the tensile strength. Outside the apex zone ( $\sigma_2 \leq 0$ ), the yield surface in equation (7.20) is identical to the classic Rankine surface.

The softening response is a function of the plastic deformation. The scalar-valued equivalent plastic strain  $\kappa$  is used as the measure of inelastic deformation. For the Von Mises yield function,

$$\dot{\kappa} = \sqrt{\frac{2}{3}} \|\dot{\epsilon}^{VP}\|. \quad (7.21)$$

and for the Rankine yield function,

$$\dot{\kappa} = \begin{cases} \dot{\epsilon}_1^{VP} & \sigma_2 < 0 \\ \sqrt{(\dot{\epsilon}_1^{VP})^2 + (\dot{\epsilon}_2^{VP})^2} & \sigma_2 \geq 0. \end{cases} \quad (7.22)$$

For all examples in this chapter, a linear softening response as a function of the equivalent plastic strain with a low residual strength is adopted. This is illustrated in figure 7.2.

### 7.2.3 Strain field around a sharp crack tip in a viscoplastic medium

Limited analytical investigations into the near-tip crack fields have been carried out for viscoplastic materials. Of the analytical investigations that have been carried out, many assumptions and simplifications have been required due to the complexity of the problem. Crack propagation in viscoplastic media is usually associated with high strain-rate problems (dynamic fracture) which complicates the problem and key assumptions in all the known analytical investigations concern the form of the viscoplastic model. It was shown by Lo (1983) that for a perfectly plastic material

( $\bar{\sigma} = \bar{\sigma}_0$ ) obeying the Perzyna viscoplastic model, an exponent  $N < 3$  (see equation (7.7)) implies that the singularity in the viscoplastic strain is weaker than the elastic strain singularity, therefore the elastic response dominates. The near-tip form of the asymptotic (singular) fields are the same as for a crack in an elastic body. A similar result was found by Freund and Hutchinson (1985) for a simple viscoplastic model in which the plastic strain rate is linearly proportional to the ‘overstress’. Intuitively, this makes sense since around a growing crack tip with a singular strain field, the strain rate is also singular and for an infinite strain rate a viscoplastic model reduces to an elastic model. However, while the singular strain field in the region very close to a crack tip in a perfectly plastic viscoplastic medium (subject to  $N < 3$ ) is the same as in an elastic solid, this applies only very close to the crack tip. The region in which the elastic strains dominate is generally very small compared to the size of the plastic zone around a crack tip (Freund and Hutchinson, 1985; Lo, 1983). It must be stressed that the outlined results are based on the assumption of perfect plasticity. It is well known that the near-tip fields for rate-independent plasticity are functions of the hardening parameters. The strength of the strain singularity in the HRR fields (Hutchinson (1968) and Rice and Rosengren (1968)), which are the near-tip fields for a crack in a power law hardening material, is dependent on the hardening parameters.

The whole discussion as to the form of the near-tip fields in a viscoplastic medium is somewhat artificial for practical problems. Analytical investigations are based on a sharp crack tip which leads to the strain singularity around the crack tip. This may be a reasonable approximation for an initially machined crack which is very thin, although for propagating cracks, experimental observations have shown that the tip of a propagating crack is often far from sharp. Therefore, the inclusion of near tip fields in a computation for a propagating crack is not necessarily an improvement on the approximation, but rather an assumption as to the shape of the crack tip. Therefore, despite it being possible to include the near-tip elastic singular fields using the partition of unity concept (Belytschko and Black, 1999; Moës et al., 1999; Wells and Sluys, 2001e), no near-tip fields are considered for the examples in this chapter.

### 7.3 Inclusion of discontinuities in a viscoplastic medium

This section focuses on introducing discontinuities when the load carrying capacity at a material point is exhausted. Discontinuities are introduced in manner similar to that in chapter 5. A disadvantage of viscoplastic models, alluded to in the previous section, is that the strain rate at a discontinuity tip is very high and therefore stresses at a discontinuity tip do not approach zero. The introduction of a traction-free discontinuity surface results in stress jumps upon discontinuity extension as the ‘overstress’ is released. The continuum parameters, particularly the softening response, must be reassessed when simulating real problems. Using the same parameters as for a continuum viscoplastic model, the model which allows discontinuities to develop will generally lead to a more brittle response.

7.3.1 *Discontinuity extension criterion and determination of the normal vector*

A discontinuity is considered to propagate when the inviscid yield stress  $\bar{\sigma}(\kappa)$  at the tip of the discontinuity reaches zero. Numerically, it is not possible to reach zero since at this stage the yield surface has collapsed to a point (for the Von Mises yield function), making it no longer possible to calculate the plastic flow direction  $\partial_{\sigma} f$ . Therefore, numerically a discontinuity is considered to extend when the yield stress reaches 0.1% of the initial yield stress,  $\bar{\sigma}_0$ . This corresponds to a critical equivalent plastic strain  $\kappa^{\text{crit}}$ , shown for linear softening in figure 7.2. Once it is determined that a discontinuity will extend, it is necessary to determine the direction of the ‘new’ extension. Unlike for the inviscid case, the rate-dependent model is well-posed so it is not possible to extract a direction of propagation from linear stability analysis. The propagation direction for a new discontinuity extension is taken as the direction in which the effective stress  $\sigma^{\text{eff}}$  is maximum. The direction is calculated using a weighted spatial average for points ahead of a discontinuity tip. For the Von Mises model, the effective stress is equal to:

$$\sigma^{\text{eff}} = \sqrt{\frac{3}{2}} \|\mathbf{S}\| \quad (7.23)$$

and for the modified Rankine model,

$$\sigma^{\text{eff}} = \begin{cases} \sigma_1 & \text{if } \sigma_2 \leq 0 \\ \sqrt{\sigma_{11}^2 + \sigma_{22}^2 + 2\sigma_{12}^2} & \text{if } \sigma_2 > 0 \end{cases} \quad (7.24)$$

At first, it would be intuitively reasonable to use the principal tensile stress direction at a discontinuity tip for the smoothed Rankine model. The effective stress concept is used to maintain consistency with the Von Mises model and generality for other yield surfaces.

The vector in the direction of discontinuity propagation  $\bar{\mathbf{p}}$  is calculated from:

$$\bar{\mathbf{p}} = \sum_{i=1}^n \left( \mathcal{H}_i \mathbf{p}_i \sigma_i^{\text{eff}} w_i V_i / \|\mathbf{p}_i\| \right) \quad (7.25)$$

where the vector  $\mathbf{p}_i$  is in the direction of the  $i$ th integration point (see figure 7.3),  $\mathcal{H}_i$  is the Heaviside jump as a function of the angle between the vector  $\mathbf{p}_i$  and the vector tangential to the discontinuity at the tip,  $\mathbf{p}_t$ ,

$$\mathcal{H}_i = \begin{cases} 1 & \text{if } \mathbf{p}_i \cdot \mathbf{p}_t \geq 0 \\ 0 & \text{if } \mathbf{p}_i \cdot \mathbf{p}_t < 0, \end{cases} \quad (7.26)$$

$\sigma_i^{\text{eff}}$  is the effective stress at integration point  $i$ ,  $w_i$  is a weight (the Gaussian weight function in equation (5.26) is used),  $V_i$  is the volume associated with integration point

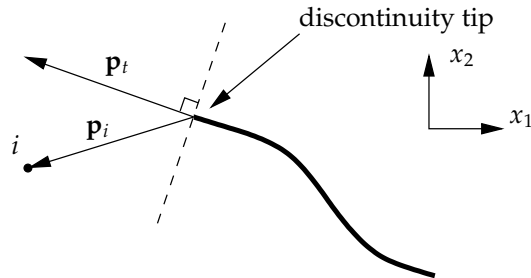


Figure 7.3: Calculating the direction of a discontinuity extension. Only discrete points in front of a line normal normal to the crack tip (dashed line) are sampled.

$i$  and  $n$  is the number of integration points. The length parameter  $l$  in the weighting function is taken as two to three times larger than the typical element size and the distance  $r$  is equal to  $\|\mathbf{p}_i\|$ . After normalising  $\bar{\mathbf{p}}$ , the normal vector to a discontinuity extension can be calculated. The described procedure is effective when a discontinuity tip is a reasonable distance from a boundary or a discontinuity approaches a boundary perpendicular to the boundary with an effective stress field that is approximately symmetric about the discontinuity. If a discontinuity approaches a boundary obliquely, the integration domain for calculating the discontinuity extension direction is no longer symmetric and becomes skewed in one direction. This gives more weight to the effective stress on one side of the discontinuity and causes the discontinuity path to deviate away from a boundary. This problem can be avoided by reducing the length parameter  $l$  in the weighting function as a discontinuity approaches a boundary, and when a discontinuity is very close to a boundary, the propagation direction should be fixed.

The use of an effective stress as the scalar quantity used in a spatial average to determine the direction of discontinuity propagation is somewhat arbitrary. Since there is no mathematical indication in which direction a discontinuity will propagate, an assumption is required. Often in fracture mechanics, it is assumed that the direction of crack growth is normal to the principal tensile stress direction. Here however, it is intended that the propagation direction comes from the continuum response which in turn is dependent on the chosen yield surface. It is also intended that the criterion is general in the sense that it is not specific to a particular failure mode. The effective stress concept is chosen based on observing both mode-I and mode-II failure calculations in which a discontinuity was present but was not allowed to propagate. From these calculations, it was observed that the effective stress was a good predictor of where strains localised, before actual localisation occurred. After localisation in a zone, the effective stress would decrease. This applied for both mode-I and mode-II problems. An intuitive alternative would be the equivalent plastic strain. However, for some problems, the plastic zone extends only a very short distance in front of a

discontinuity tip (as is known in elasto-plastic fracture mechanics and will be shown in section 7.5 by examples) and the equivalent plastic strain can never decrease, so it leaves a significant wake which is behind and to the side of a discontinuity tip. This wake disturbs the averaging process. The equivalent plastic strain is an effective measure for determining the propagation direction only for cases where plastic deformation extends significantly beyond a discontinuity tip.

### 7.3.2 *Tension/compression response at a discontinuity*

In the context of this chapter, the introduction of a discontinuity implies a physical separation of material within a body and the development of two free surfaces. Since a clear break has occurred in a body, if the surfaces are not in contact no tractions can be transferred and therefore no constitutive model is applicable. Irrespective of the model used for the intact continuum, there can exist no kinematic constraints on the opening or sliding displacement jumps across a discontinuity since no material ‘exists’ at the discontinuity. Unlike the cohesive zone model based on Von Mises plasticity, allowing opening at a discontinuity in this context does not violate the isochoric plastic flow requirement since no material ‘exists’ at the discontinuity. This results in a fundamentally different response, particularly under tensile loading since cleavage modes are possible. Under compressive loading, a discontinuity is considered as a frictionless slip plane. Penetration of surfaces is not permitted, with only sliding displacements possible. Any crushing or dilative/contractive deformations should be modelled in the continuum. It is however possible to model a discontinuity under compression as a frictional slip plane, which may be appropriate for some materials.

## 7.4 Implementation aspects

Details of the numerical implementation are largely the same as those described in chapter 5 for cohesive zone models. The key differences are that the deformation history in the continuum part must now be considered and the normal vector to a discontinuity extension can no longer be calculated from bifurcation analysis, nor is it assumed that the spatial orientation of a discontinuity extension is determined by the principal stress direction. The implementation in this chapter is based on geometrically linear kinematics. As in previous chapters, discontinuity tips are restricted to element boundaries to avoid problems with the incremental solution procedure.

### 7.4.1 *Calculating the extension criterion*

A discontinuity in a viscoplastic medium is extended when the equivalent plastic strain reaches the critical value  $\kappa^{\text{crit}}$ , as shown in figure 7.2. In implementation, a discontinuity tip always lies on an element boundary and the inelastic deformation history is stored at integration points inside elements. To estimate the equivalent

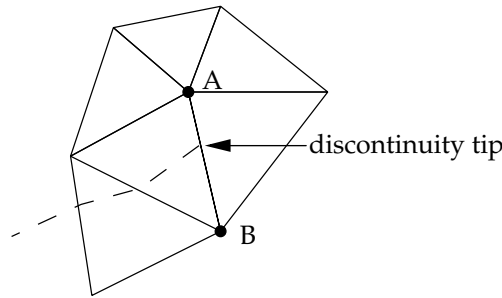


Figure 7.4: Calculation of the equivalent plastic strain at a discontinuity tip for a triangular element. The equivalent plastic strain is extrapolated to nodes A and B and then linearly interpolated along the line  $\overline{AB}$  to calculate the equivalent plastic strain at the discontinuity tip.

plastic strain at a discontinuity tip, the equivalent plastic strain at integration points is extrapolated using the element shape functions to the corner nodes (see figure 7.4). Then, the plastic strain is linearly interpolated between the two nodes between which the discontinuity tip lies.

#### 7.4.2 Numerical integration and transfer of history parameters

The integration of six-noded triangular elements crossed by a discontinuity is performed as described in section 5.4.3 and shown in figure 5.2. The difference in this section is that history terms are stored at continuum integration points and the stress at a point can no longer be calculated using the total strain field. When an element is crossed by a discontinuity and the new integration points are distributed within the element, the deformation history at the original integration points must be transferred to the new integration points. The transfer of history terms differs from conventional remeshing procedures since the history terms need only be transported *within* an element. It is therefore possible to devise a scheme which is performed entirely at element level.

The history at the ‘old’ integration points in an element is mapped to the new integration points based on the distance between the old and the new points. Denoting old integration points  $i$  and new points  $j$ , a history term  $H$  at a new integration point  $j$  is calculated by:

$$H_j^{\text{new}} = \frac{\sum_{i=1}^{n_{\text{old}}} H_i^{\text{old}} (1/r_{ij})}{\sum_{i=1}^{n_{\text{old}}} (1/r_{ij})} \quad (7.27)$$

where  $n_{\text{old}}$  is the number of old integration points in an element (three for the six-noded triangular element) and  $r_{ij}$  is the distance between the ‘old’ integration point  $i$  and the ‘new’ integration point  $j$ . If a new and an old integration point coincide, the new point simply inherits the history of the old point. The distribution of history

using equation (7.27) results in a smoothing since the history variables at the new points can only be less than or equal to largest history variable at the old points. However, since the transfer of history is occurring only within an element the error is small and diminishes upon mesh refinement.

An alternative to the adaptive scheme mentioned in chapter 5 is to use a scheme with fixed integration points, thereby avoiding the need to transport material history. However, even with a fixed continuum integration scheme and discontinuities which are traction-free when opening, integration points must still be placed on a discontinuity to detect any contact during a calculation.

## 7.5 Numerical examples

As in previous chapters, the six-noded triangle is used as the underlying finite element. All examples use the Perzyna viscoplastic model with the overstress function exponent  $N = 1$ . As in previous chapters, a full Newton-Raphson procedure is used for all examples. For dynamic analyses, as in chapter 5, the average acceleration version of the Newmark scheme is used for time integration and the consistent mass matrix from equation (5.23) (which involves discontinuous terms near a discontinuity) is used. The focus in this section is on the failure modes for various problems with different continuum yield functions and different boundary conditions. Viscosity is used for regularising the continuum problem, and for most examples is not representative of real materials. The viscosity parameter is chosen such that strain localisation occurs in zones several elements wide when using reasonably fine meshes.

### 7.5.1 Biaxial test with Von Mises viscoplasticity in tension and compression

To examine the response of a specimen under tension and compression and to investigate the effect of boundary conditions, the biaxial test is again analysed. The geometry of the specimen is shown in figure 5.9. The material properties are taken as: Young’s modulus  $E = 11.92 \times 10^3$  MPa, Poisson’s ratio  $\nu = 0.2$ , initial yield stress  $\bar{\sigma}_0 = 100$  MPa, viscosity  $\eta = 7.5$  s and the hardening modulus  $h = -4000$  MPa. The Von Mises yield function is used. The loading is quasi-static and plane strain conditions are assumed. The test is analysed under both load and displacement control. For the displacement control tests, a uniform displacement is imposed on the top edge of the specimens (fixed top boundary). The loading rate  $\dot{u} = \pm 1$  mms<sup>-1</sup>. For the load control examples, a uniformly distributed load is applied to the top edge of the specimens (flexible top boundary). An arclength procedure is used to pass the peak load under load control. The time increment  $\Delta t$  is back-calculated such that the average loading rate at the top edge is equal to 1 mms<sup>-1</sup>. When examining the load–displacement responses, the load is taken as the total applied load and the displacement as the average displacement of the top edge of the specimen.

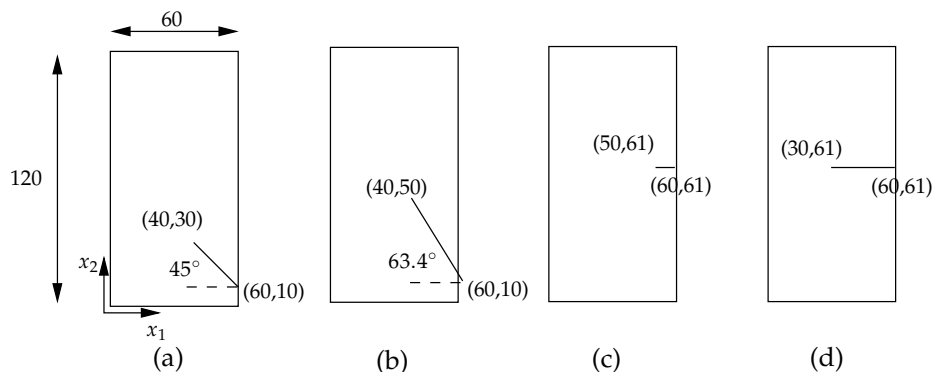


Figure 7.5: Biaxial specimen with different initial discontinuities.

Localised failure is triggered by a cut in the specimen. The influence of the length and orientation of the initial cut on the failure mode is examined by analysing four different cases. The initial discontinuities for the four cases are shown in figure 7.5. The analyses are performed with two different meshes, a structured mesh composed of 2500 elements and an unstructured mesh composed of 2626 elements. For determining the propagation direction, the length scale  $l$  in the weighting function is taken as 5 mm. When a discontinuity tip is less than 10 mm from a side boundary, the propagation direction is kept fixed to avoid spurious deviations due to the lack of symmetry of the deformation with respect to the boundary.

### Compression

The biaxial specimen is first analysed under compressive loading by displacement control with inclined initial discontinuities (figures 7.5a and 7.5b). To begin, the two different cases are analysed, with the initial discontinuity prevented from propagating. The plastic strain contours and deformed meshes for the structured mesh are shown in figure 7.6. As expected, a shear band develops in a zone greater than one element wide and the shear band does not follow the mesh structure. Note that the bias in the structure of the mesh is not in the same direction as the shear band propagation. Now, the same test is performed and a discontinuity is allowed to propagate. Figure 7.7 shows the equivalent plastic strain contours, the discontinuity and the deformed mesh for the case of an initial discontinuity at  $45^\circ$  with the structured and the unstructured meshes. Similarly, shown in figure 7.8 is the case of an initial discontinuity at  $63.4^\circ$  for a structured and unstructured mesh. The discontinuity has propagated through the centre of the plastic zone for both cases in the same direction as the shear band for the stationary discontinuity. The deformed meshes for a stationary and propagating discontinuity are different. When a discontinuity is introduced, the material adjacent the discontinuity unloads and it can be seen that deformations

NUMERICAL EXAMPLES

125

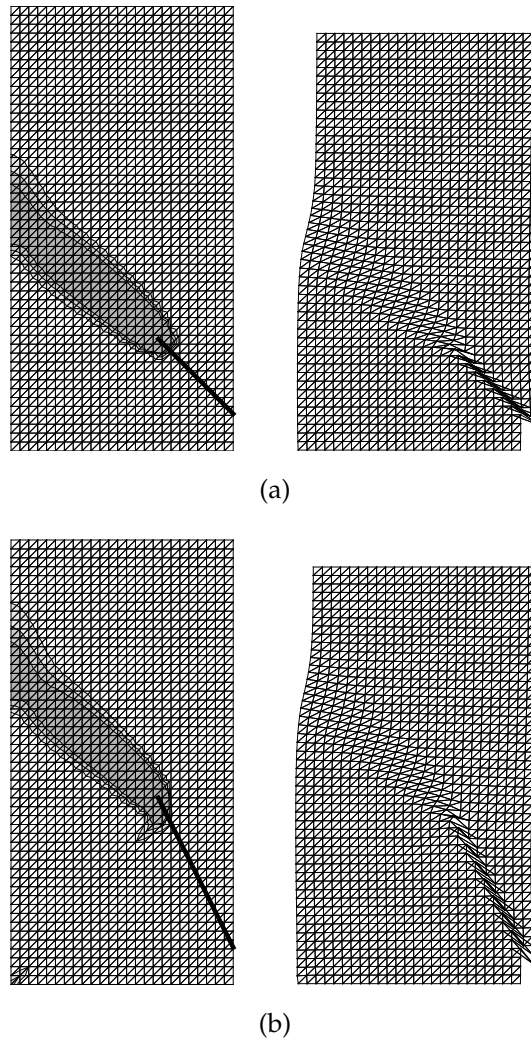


Figure 7.6: Equivalent plastic strain contours at  $u = -1.5$  mm and deformed meshes (magnified 5 times) for the biaxial specimen with a stationary discontinuity (heavy line) at an initial inclination of (a)  $45^\circ$  and (b)  $63.4^\circ$ .

localise at a surface. It is also clear that the effective stress criterion is suitable for predicting the direction of discontinuity propagation for mode-II failure.

Figures 7.7 and 7.8 show that the equivalent plastic strain field and the failure mode are the same for both the structured and unstructured mesh. To compare the global response for the two meshes, the load–displacement response is examined for the case of an initial discontinuity at  $45^\circ$  that can propagate. The load–displacement responses for the structured and unstructured meshes are shown in figure 7.9. The two responses are almost identical, further indicating that the model is insensitive to the spatial discretisation. The examples in figures 7.7 and 7.8 show the deformed configuration near the end of the loading process when a discontinuity has propagated through the entire specimen with deformations concentrated at the discontinuity. To show the deformation state at an intermediate stage of loading, the equivalent plastic strain contours, discontinuity and deformed mesh for the case of an initial discontinuity at  $63.4^\circ$  are shown in figure 7.10 for a displacement of  $u = -1.25$  mm. The unstructured mesh is used. Three regions can be identified; the first is at the initial discontinuity where sliding displacements are large; the second near the discontinuity tip where limited sliding has taken place on the discontinuity plane; and the third is ahead of the discontinuity tip where inelastic deformations start to localise.

Comparing figure 7.6 (stationary discontinuity) with figures 7.7 and 7.8 (propagating discontinuities) shows that the inclusion of a discontinuity under compressive loading has no significant impact on the failure mode. By including a discontinuity when the load carrying capacity is exhausted, deformations localise at the discontinuity, although the direction is the same as for a continuum model. This is not surprising since under compression only sliding is allowed on a discontinuity plane, which does not result in any inelastic volume change. For this reason, the difference between a fixed and flexible upper boundary (load and displacement control) under compressive loading is negligible since if no penetration of discontinuity surfaces is allowed, the upper boundary is unable to rotate significantly under load control. Results obtained under load control are qualitatively identical to the displacement control results.

### Tension

To examine the response of the biaxial specimen under tension, the three cases shown in figure 7.5a, c and d are analysed under both load and displacement control. As discussed in section 7.3.2, the key difference between compressive and tensile loading is the response normal to a discontinuity. For this reason, the response under tension is far more sensitive to the boundary conditions and the initial discontinuity, as will be shown through examples. Unlike for a continuum model, the inclusion of a discontinuity allows a cleavage mode of failure under tension. This mode of failure is not observed with a continuum model due to the isochoric nature of the plastic deformation. In this section analyses are presented for both a fixed and flexible upper

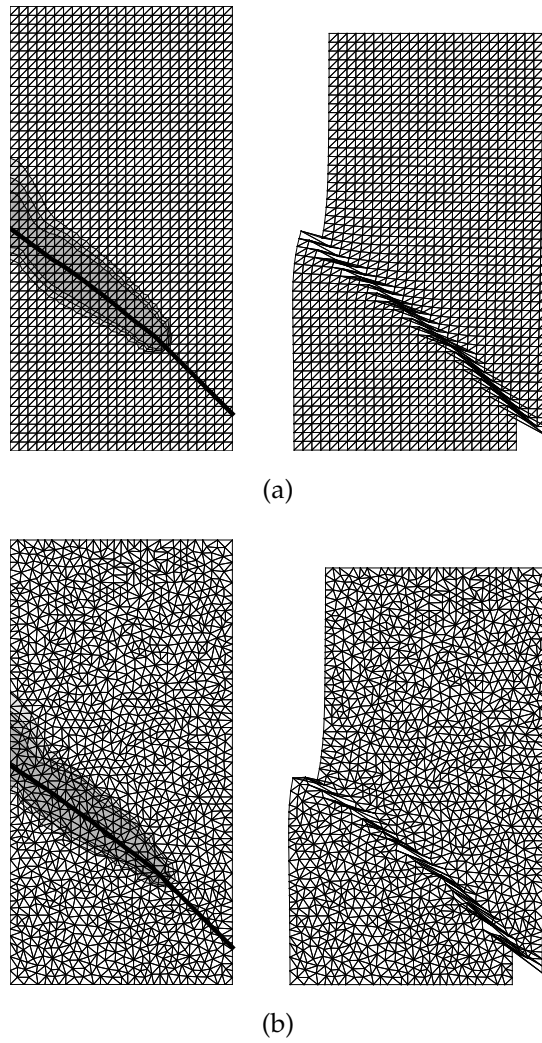


Figure 7.7: Equivalent plastic strain contours and deformed meshes (magnified 5 times) at  $u = -1.5$  mm for the biaxial specimen with a propagating discontinuity (heavy line) at an initial inclination of  $45^\circ$  with (a) structured and (b) unstructured meshes.

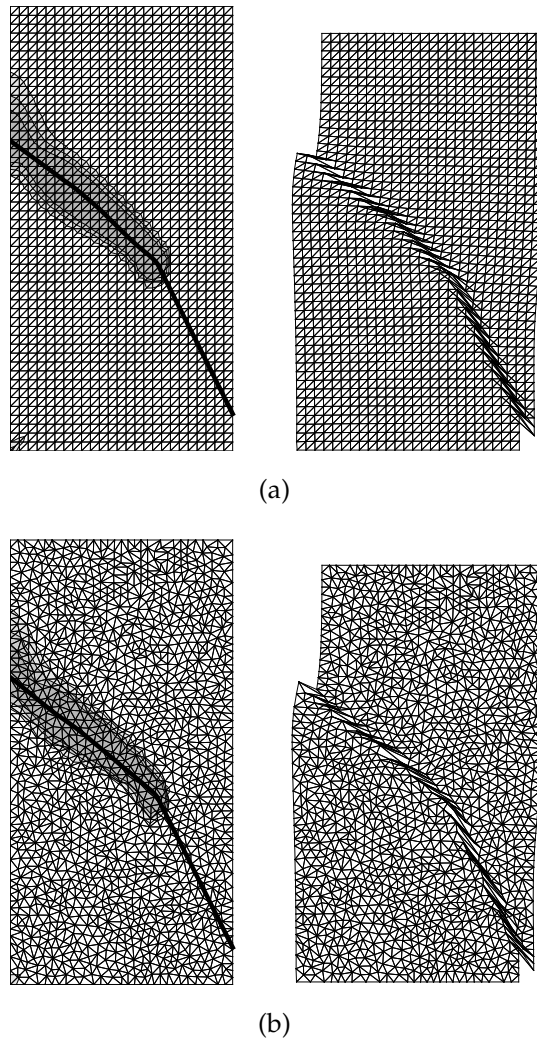


Figure 7.8: Equivalent plastic strain contours and deformed meshes (magnified 5 times) at  $u = -1.5$  mm for the biaxial specimen with a propagating discontinuity (heavy line) at an initial inclination of  $63^\circ$  with (a) structured and (b) unstructured meshes.

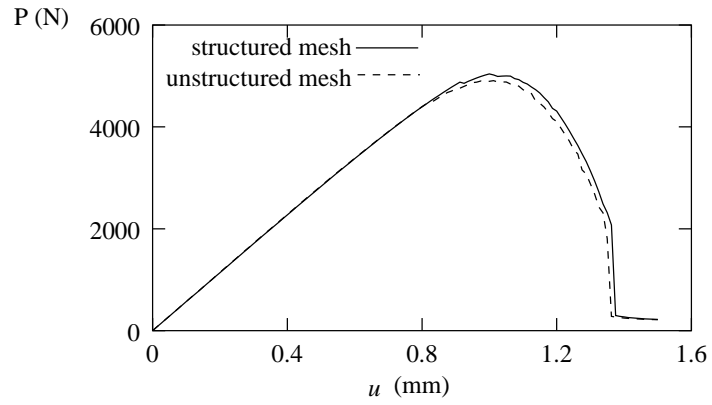


Figure 7.9: Load–displacement response for the biaxial specimen under compressive loading with an initial discontinuity at  $45^\circ$  to the  $x_1$  axis for the structured and unstructured meshes.

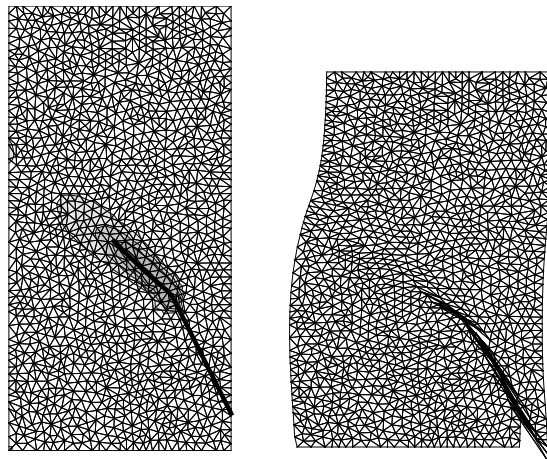


Figure 7.10: Equivalent plastic strain contour and deformed mesh (magnified 10 times) at  $u = -1.25$  mm for the biaxial specimen with a propagating discontinuity (heavy line) at an initial inclination  $63.4^\circ$ .

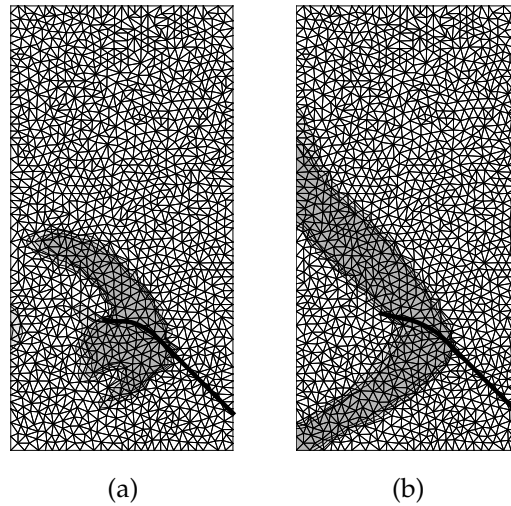


Figure 7.11: Plastic strain contours and discontinuity for the biaxial test under tension with an initial discontinuity at  $45^\circ$  to the horizontal loading for (a) flexible and (b) fixed top boundaries.

boundary. Since it was shown for compression examples, and previously for cohesive zone models, that the numerical model is insensitive to spatial discretisation, only the unstructured mesh is used for the tension examples.

To highlight the differences between compressive and tensile loading, the biaxial test is analysed with an initial discontinuity inclined at  $45^\circ$  to the horizontal (figure 7.5a), which was tested previously under compressive loading. The equivalent plastic strain contours and the discontinuity path are shown in figure 7.11 for load and displacement control. The discontinuity path has extended in a direction approximately normal to the principal tensile stress direction with a smooth transition from the initial inclination. This is in contrast to the compression tests where the discontinuity propagated at approximately  $45^\circ$  to the principal stress directions. For a fixed boundary (figure 7.11b), two shear bands have developed (only one formed under compressive loading) and under load control a plastic hinge has begun to develop. The absence of a branching criterion means that discontinuities cannot develop following the two shear bands.

The biaxial test under tensile loading is now analysed with the horizontal initial discontinuities, shown in figures 7.5c and 7.5d, with a fixed upper boundary (displacement control). Figure 7.12 shows the equivalent plastic strain contours, the discontinuity path and the deformed mesh for an initial discontinuity that is 10 mm long at a late stage of failure. It can be seen that the discontinuity has propagated only a short distance, approximately equal to the width of the shear bands that em-

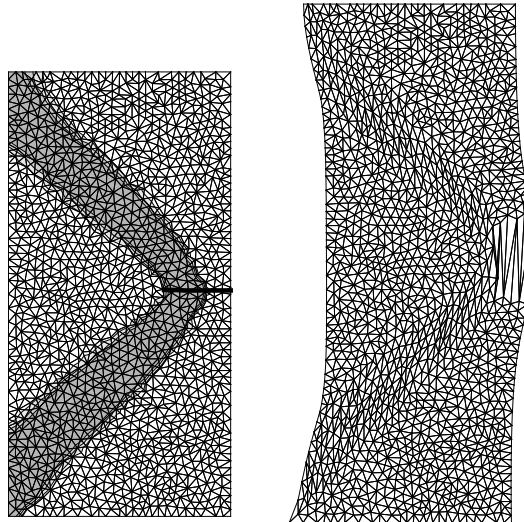


Figure 7.12: Equivalent plastic strain contours and deformed mesh (magnified 10 times) at  $u = 2$  mm for the biaxial specimen with a fixed top boundary. The initial discontinuity has a length of 10 mm.

anate from the discontinuity tip. The straight shear bands that develop from the initial discontinuity are typical of what is seen when using a continuum model. The results of the analysis with an initial discontinuity length of 30 mm are shown in figure 7.13. Similar to the case with a 10 mm long initial discontinuity, straight shear bands develop from the discontinuity tip and the discontinuity propagates only a short distance. For both initial discontinuities, the failure mode is typical continuum mode-II (shear banding). Again, due to the absence of a criterion for branching of a discontinuity, it is not possible to have a discontinuity propagate through the centre of the two shear bands that develop from the initial discontinuity.

The two cases of a 10 and a 30 mm initial discontinuity are now analysed under load control. The equivalent plastic strain contours, the discontinuity path and deformed mesh for the 10 mm long initial discontinuity are shown in figure 7.14. As for the fixed boundary case, the discontinuity propagates only over a short distance. However, the shear bands that develop from the discontinuity tip are curved, and from the deformed mesh it is clear that a plastic hinge has developed. The results with a 30 mm long initial discontinuity are shown in figure 7.15. From the shape of the plastic zone and the deformed mesh, it is clear that the failure mode for this case is fundamentally different from the other cases. The specimen has failed in mode-I, with the discontinuity having propagated through the entire specimen. Rather than shear bands extending from the discontinuity tip, a plastic zone develops, and when

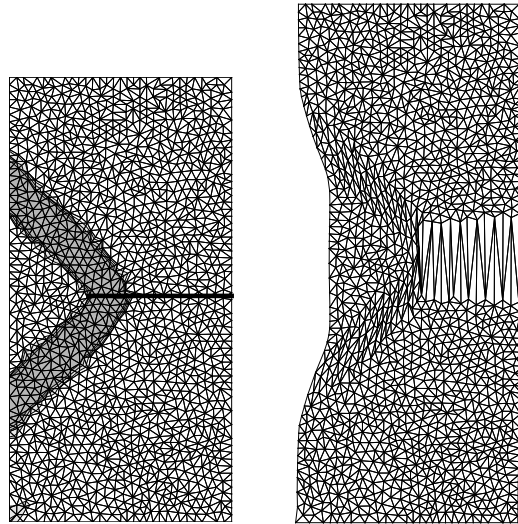


Figure 7.13: Equivalent plastic strain contours and deformed mesh (magnified 10 times) at  $u = 2$  mm for the biaxial specimen with a fixed top boundary. The initial discontinuity has a length of 30 mm.

the discontinuity begins to propagate the plastic zone grows with the discontinuity. To illustrate this, the evolution of the equivalent plastic strain and the discontinuity during the loading process are shown in figure 7.16. Note in figure 7.16 that the plastic zone does not extend far in front of the discontinuity tip. For cases such as in figure 7.16, use of the equivalent plastic strain to determine propagation direction is unreliable. The load–displacement response is shown in figure 7.17 for both the structured and unstructured meshes. The responses are nearly identical, again confirming the objectivity with respect to spatial discretisation. Despite the roughness of the load–displacement response, a strict convergence criterion was met for every load increment. The roughness is due to the sudden energy dissipation upon discontinuity extension.

Under displacement control, significant opening displacement at a discontinuity is not possible and the failure mode is similar to the continuum case. However, under load control, the upper boundary of the specimen is able to rotate which allows significant opening at a discontinuity and possible mode-I type failure. The degree to which mode-I failure is possible under load control is dependent on the length of the initial discontinuity. The numerical examples with a flexible top boundary show the importance of including displacement discontinuities to model failure in materials that obey a Von Mises flow rule but also exhibit mode-I type failure under certain

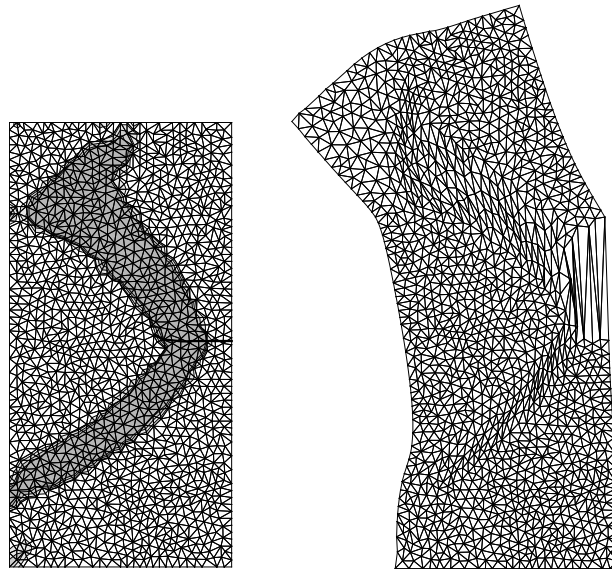


Figure 7.14: Equivalent plastic strain contours and deformed mesh (magnified 10 times) at an average top boundary displacement  $u = 2.5$  mm for the biaxial specimen with a flexible top boundary. The initial discontinuity has a length of 10 mm.

conditions. Depending on the boundary conditions and the initial discontinuity, it is possible to simulate shear bands, plastic hinges and mode-I failure. This is important for the analysis of metals, which have been observed to fail in the three different modes under different conditions.

#### 7.5.2 *Influence of viscosity, Poisson's ratio and the plane stress/strain condition on the failure zone*

It is well known in elasto-plastic fracture mechanics that the size of the plastic zone around of a crack tip differs under plane stress and plane strain conditions, and therefore is also dependent on Poisson's ratio. Also, for strain softening problems, the viscosity parameter, in combination with the loading rate, controls the width of the localisation zone. To examine the effect of these parameters on the failure process, the biaxial test is analysed with a fixed and flexible top boundary and with an initial discontinuity of 30 mm (see figure 7.5d). The influence of the different parameters and constraints is compared by examining the plastic strain field at or near complete failure. Unless stated otherwise, the material parameters are the same as those in the previous section.

To begin, analyses are performed for the fixed boundary case under plane stress

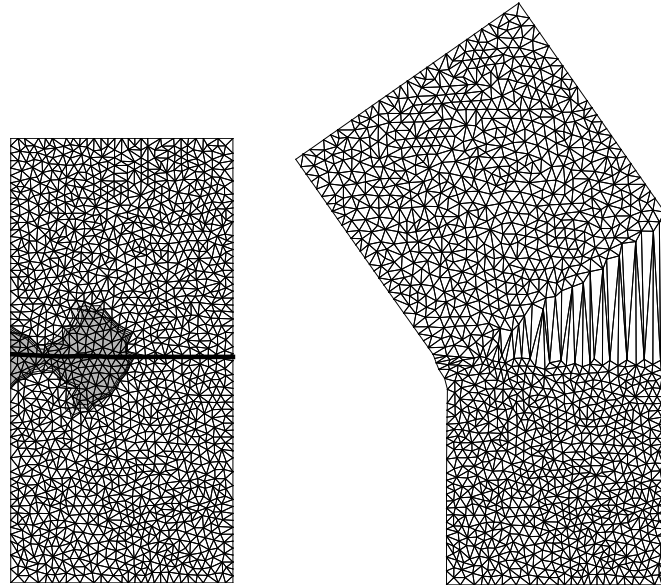


Figure 7.15: Equivalent plastic strain contours and deformed mesh (magnified 5 times) at an average top boundary displacement  $u = 3$  mm for the biaxial specimen with a flexible top boundary. The initial discontinuity has a length of 30 mm.

and plane strain conditions. To accentuate the differences between the plane stress and plane strain analyses, Poisson's ratio is set to 0.49. Comparing the equivalent plastic strain field and deformed meshes in figure 7.18, the failure mode of the plane stress and plane strain problems are qualitatively the same under displacement control, with a thicker shear band developing for the plane stress case, and for that reason the discontinuity extends further. The same problem is shown in figure 7.19 for a flexible top boundary at the stage when the discontinuity has propagated entirely through the specimen. The failure is in mode-I for the plane stress case, with a small plastic zone. There is no indication of short shear bands emanating from the discontinuity tip that were observed in previous examples. For the plane strain case, the discontinuity has propagated through the specimen, although a small plastic hinge has developed below the discontinuity at a late stage of failure. Comparing this result to the plane strain example in figure 7.15, where Poisson's ratio was equal to 0.2, the shear band-like extensions from the discontinuity tip are larger for higher values of Poisson's ratio. This is a result of competing mode-I and mode-II failure mechanisms. For a longer initial discontinuity, the mode-I effects increase and for higher values of Poisson's ratio under plane strain conditions, the mode-II effects increase. The exact failure mode is determined by a combination of boundary conditions, ini-

NUMERICAL EXAMPLES

135

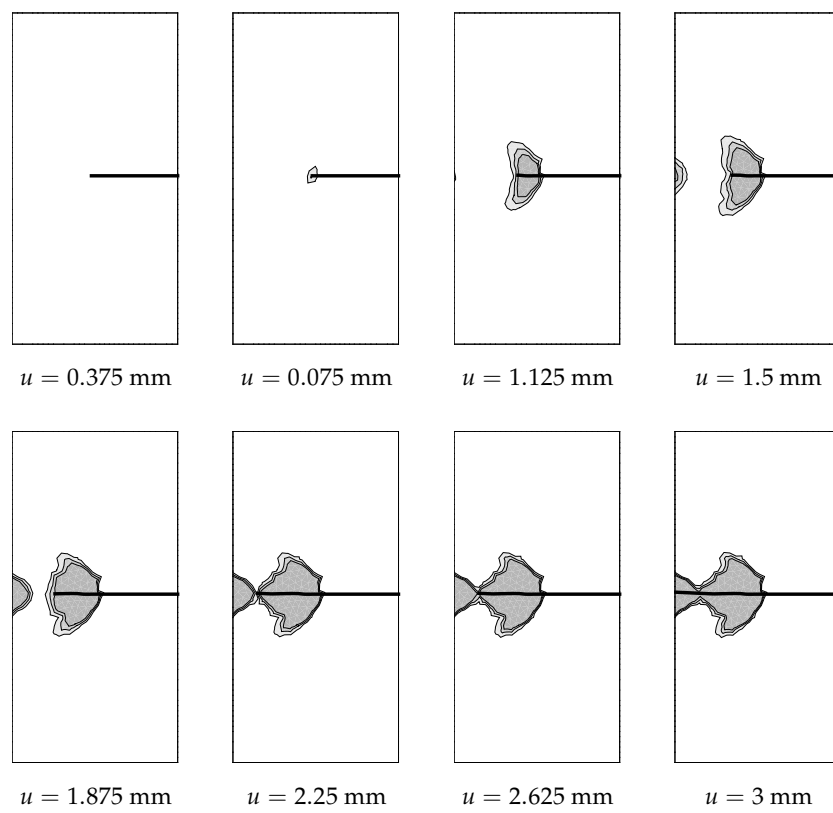


Figure 7.16: Evolution of equivalent plastic strain contours and discontinuity for the biaxial test under tension with a flexible top boundary. The initial discontinuity has a length of 30 mm.

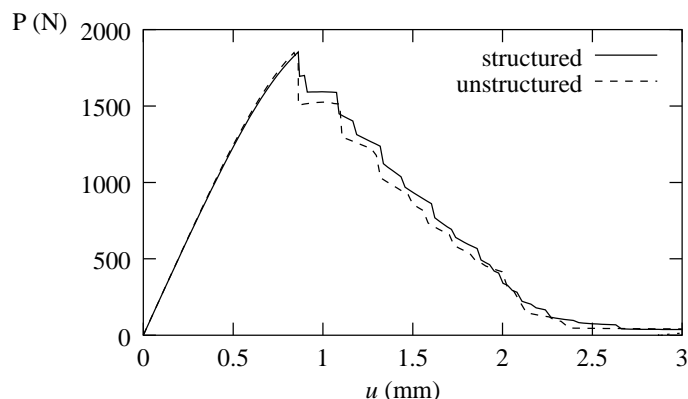


Figure 7.17: Load–displacement response for biaxial specimen under tensile loading with a flexible top boundary for structured and unstructured meshes. The initial discontinuity for the structured mesh is 30 mm long and 30.47 mm for the unstructured mesh.

tial conditions and material parameters.

To examine the influence of viscosity on the response, the biaxial test is analysed with different viscosities. The original material parameters are adopted except that the original viscosity parameter of 7.5 s is halved to 3.75 s, doubled to 15 s and quadrupled to 30 s. For a continuum model, increasing the viscosity leads to a response which is closer to the elastic response than the inviscid response so the size of the localisation zone increases. The equivalent plastic strain field is shown in figure 7.20 for three different viscosities at an intermediate stage of failure. The results in figure 7.20 show that, as expected, the viscosity has an influence on the size of the plastic zone. Also, the viscosity has a significant influence on the shape of the plastic zone and it delays the extension of a discontinuity.

### 7.5.3 Three-point bending test

The three-point bending test performed in section 5.5.1 is again simulated. This test is mechanically very similar to the biaxial test with a flexible top boundary. The geometry of the test is shown in figure 5.3. The materials properties are initially taken as: Young's modulus  $E = 1 \times 10^2$  MPa, Poisson's ratio  $\nu = 0.2$ , yield stress (tensile strength)  $\bar{\sigma} = f_t = 1$  MPa, viscosity  $\eta = 2$  s and the hardening modulus  $h = -200$  MPa. The length  $l$  used in the spatial averaging for determining the propagation direction is taken as 0.2 mm. The beam is loaded via an imposed downward velocity at the centre of the beam on the top edge of  $-1 \text{ mms}^{-1}$ . The reported displacements are the downward displacement of the point where the displacement is imposed. In this section, the beam is analysed using both the Von Mises and the smoothed Rankine yield criteria. Of particular interest is the shape of the inelastic

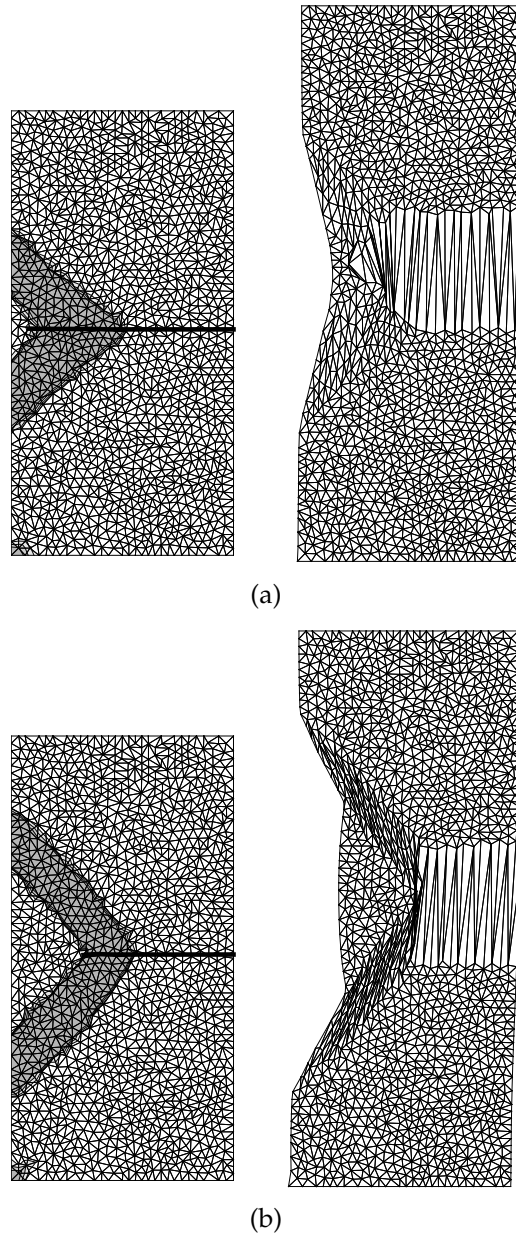


Figure 7.18: Equivalent plastic strain contours and deformed meshes (magnified 10 times) at  $u = 3$  mm for the biaxial specimen with a fixed top boundary under (a) plane stress and (b) plane strain conditions.

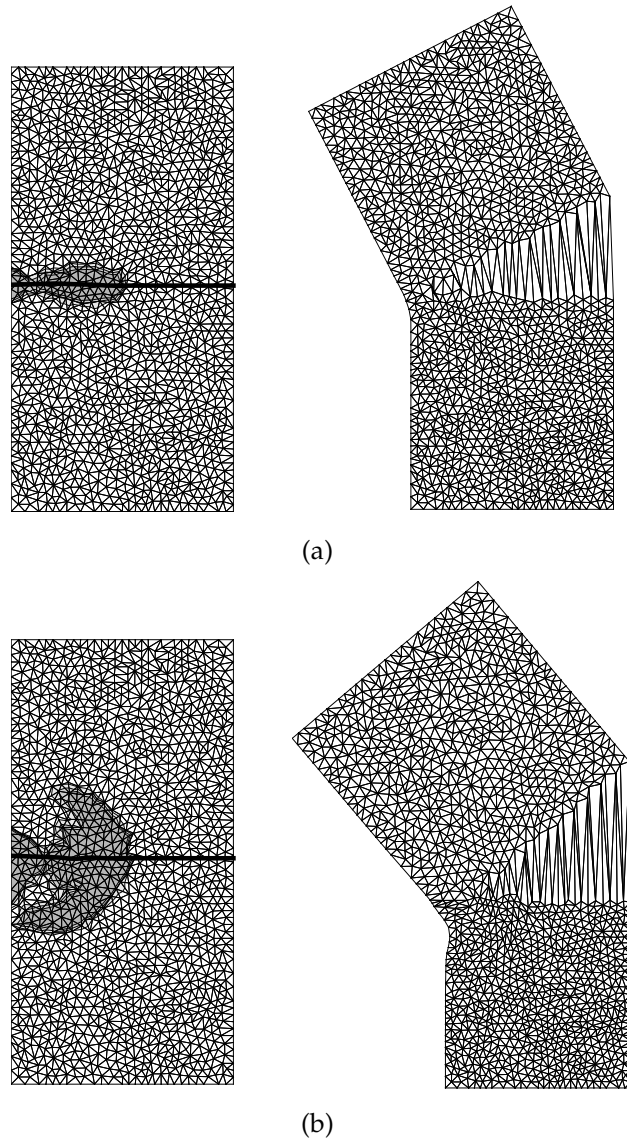


Figure 7.19: Equivalent plastic strain contours and deformed meshes (magnified 5 times) for the biaxial specimen with a flexible top boundary under (a) plane stress and (b) plane strain conditions.

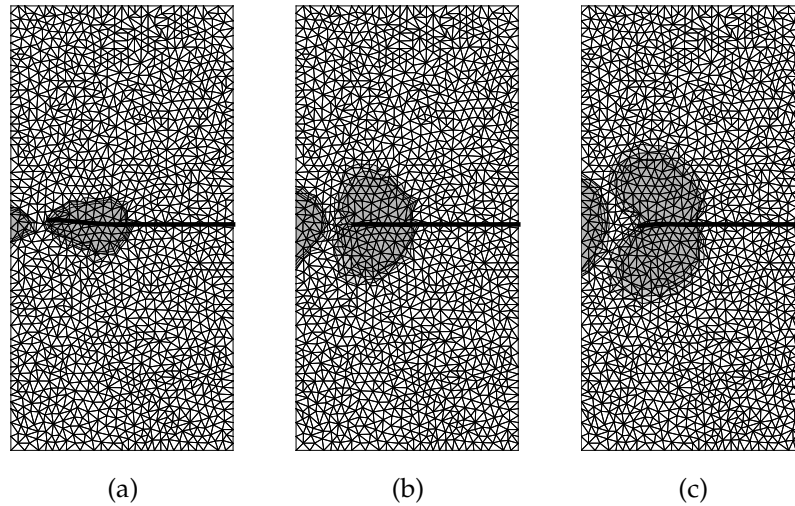


Figure 7.20: Influence of viscosity on the plastic zone. The equivalent plastic strain field is shown for (a)  $\eta = 3.75$  s, (b)  $\eta = 15$  s and (c)  $\eta = 30$  s.

zone and the failure mode for the different yield functions. In addition, for the three-point bending test, the influence of the hardening modulus on the shape and size of the inelastic zone and the influence on the failure mode is investigated.

Analyses are performed using both a structured and unstructured mesh. The meshes for this analysis must be particularly fine in order to capture the inelastic continuum deformations and to determine the propagation direction reliably. Meshes such as those used in section 5.5.1 are too coarse for this analysis and yield unreliable predictions of the discontinuity path. Therefore the meshes used in this section are considerably finer than those used for the cohesive zone simulations. The structured mesh is composed of 4750 elements and the unstructured mesh 3631 elements. A discontinuity propagates from a 0.5 mm long initial discontinuity which is vertical and begins from the centre of the bottom edge of the beam.

#### Note on the post-processing of results

In this section the influence of the hardening modulus is examined. Contour plots showing the equivalent plastic strain field are used to indicate the size and shape of the plastic zone, with contours based on four equal divisions from zero to the ultimate equivalent strain,  $\bar{\sigma}_0/h$ . Therefore, when comparing contour plots for the same specimen but for different values of the hardening modulus, consider that the contour values are dependent on the hardening modulus and cannot be compared quantitatively.

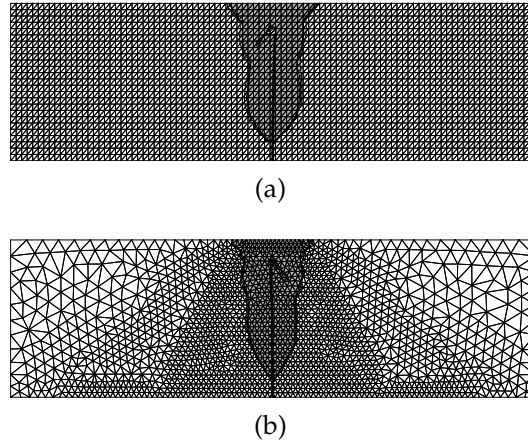


Figure 7.21: Equivalent plastic strain contours and discontinuity path for the three-point bending test with the Von Mises yield criterion under plane strain conditions at  $u = -0.4$  mm with (a) structured and (b) unstructured meshes.

#### Von Mises yield function

The three-point bending test is first analysed using the Von Mises yield criterion under plane strain conditions. As observed for the biaxial test under tension with a flexible boundary, it is possible to simulate mode-I failure using the Von Mises yield criterion if displacement discontinuities are allowed. Figure 7.21 shows the discontinuity and equivalent plastic strain field for a structured and unstructured mesh. It can be seen in figure 7.21 that a plastic zone has developed and a discontinuity has propagated through the middle of the plastic zone. The load-displacement responses for the two meshes are shown in figure 7.22. Again, despite the roughness of the load-displacement response, a strict convergence criterion was met for every increment. The inclusion of discontinuities in the solution can actually enhance the robustness of the overall numerical procedure since it limits the plastic strains that develop and induces unloading next to a discontinuity. All further analyses are performed using the unstructured mesh.

The evolution of the equivalent plastic strain field and displacement discontinuity are shown in figure 7.23. The load level at the various stages can be inferred from figure 7.22. Plastic zones have developed at the top and bottom of the beam. Note that the plastic zone that develops in the compressive region exhibits short shear band-like extensions. Around the displacement discontinuity tip, there is no extension of the plastic zone beyond the tip. At a late stage in loading when the plastic zones meet, a plastic hinge forms near the top of the beam. At this stage the discontinuity does not propagate significantly further. At this stage of failure, the load carrying

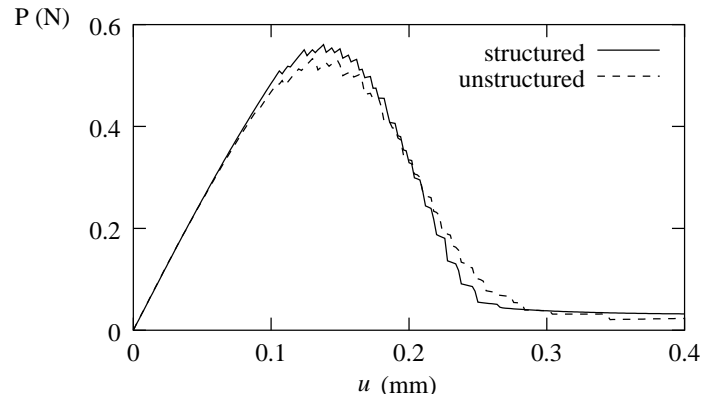


Figure 7.22: Load–displacement response for the three-point bending test using the Von Mises yield surface for the structured and unstructured meshes.

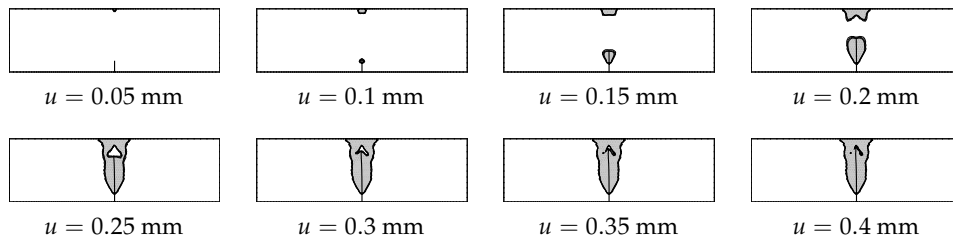


Figure 7.23: Evolution of equivalent plastic strain contours and discontinuity for the three-point bending test under plane strain conditions with the Von Mises yield function and Poisson’s ratio  $\nu = 0.2$ .

capacity of the beam has been almost exhausted. The stage at which the plastic hinge develops can be seen from the load–displacement response (figure 7.22). The plateau in the load–displacement response towards the end of the loading corresponds to the development of the hinge, at which stage propagation of the discontinuity is arrested. The beam has failed primarily in mode-I, with a plastic hinge forming only at the last stages of failure.

To show the influence of the displacement discontinuity on the failure mode, the three-point bending test is again analysed, although the initial discontinuity is not allowed to propagate. The equivalent plastic strain field and the initial discontinuity are shown in figure 7.24. Comparing the plastic zones for a stationary discontinuity in figure 7.24 and a propagating discontinuity in figure 7.21, the failure mode is different. For the stationary discontinuity, a plastic hinge has formed with the centre of the beam remaining elastic, while for the propagating discontinuity the centre of the beam is plastic. The reason for the different failure mode is that propagation of

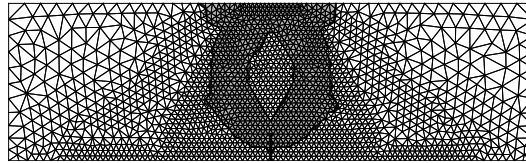


Figure 7.24: Equivalent plastic strain contours for a stationary discontinuity at  $u = 1$  mm for the Von Mises yield surface.

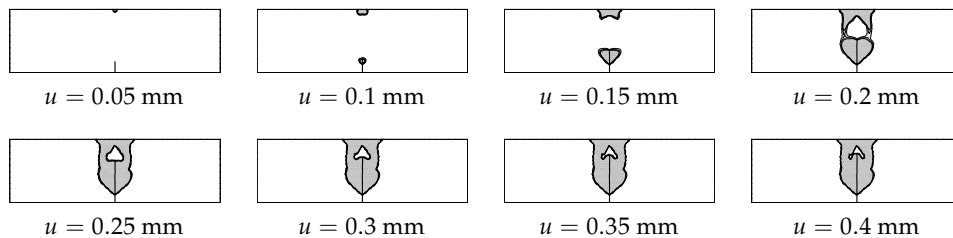


Figure 7.25: Evolution of equivalent plastic strain contours and discontinuity for the three-point bending test under plane strain conditions with the Von Mises yield function and Poisson’s ratio  $\nu = 0.49$ .

a discontinuity releases the plastic incompressibility constraint and allows mode-I cleavage opening. If mode-I opening is prevented, the only plastic volume preserving failure mode is a plastic hinge.

To investigate the influence of material parameters, the three-point bending problem with a propagating discontinuity is analysed for an increased value of Poisson’s ratio of  $\nu = 0.49$ . The evolution of the equivalent plastic strain field and the discontinuity path are shown in figure 7.25. The results are qualitatively the same the case with Poisson’s ratio equal to 0.2, with the plastic zone larger for the larger value of Poisson’s ratio. The failure mode however is still mode-I dominated. The plastic zones at the top and bottom meet sooner and the elastic zone inside the plastic hinge is larger. When a plastic hinge develops, the discontinuity has not propagated as far as it did for the case with a smaller value of Poisson’s ratio. As mentioned previously, a higher value of Poisson’s ratio increases the mode-II effects, leading to a larger plastic hinge and the earlier development of the hinge.

Until now, the influence of the hardening modulus on the response has not been examined. The hardening modulus controls the ductility of the response (in combination with the loading rate and viscosity), and as such could be expected to influence the response. Intuitively, it would be expected that a brittle response would lead to more mode-I dominated failure with the plastic zone not extending far in front of a discontinuity tip and a rapidly propagating discontinuity. Conversely, a more ductile

NUMERICAL EXAMPLES

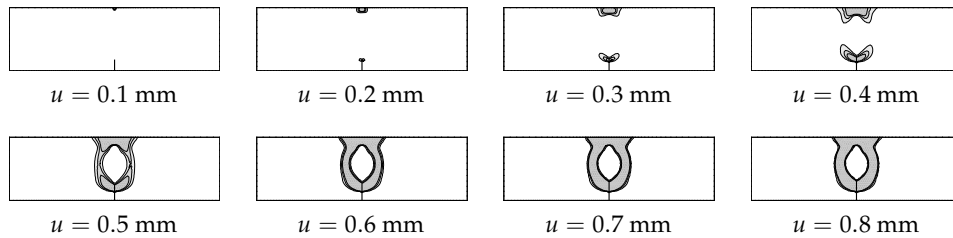


Figure 7.26: Evolution of equivalent plastic strain contours and discontinuity for the three-point bending test under plane strain conditions with the Von Mises yield function for a ductile beam. The hardening modulus  $h$  is equal to  $-20$  MPa.

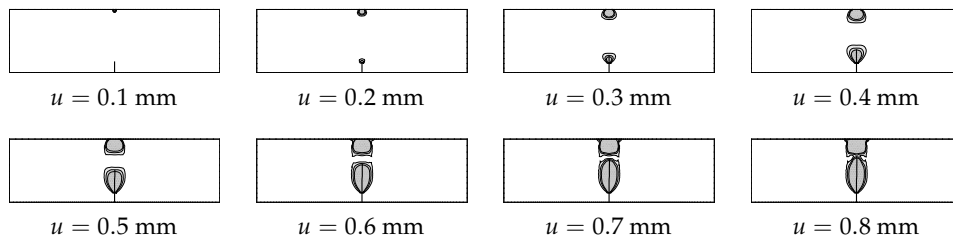


Figure 7.27: Evolution of equivalent plastic strain contours and discontinuity for the ductile ( $h = -20$  MPa) three-point bending test under plane stress conditions with the Von Mises yield function and Poisson’s ratio  $\nu = 0.2$ .

response would involve a slower propagating discontinuity with a larger plastic zone extending further in front of a discontinuity tip. To examine the response of a more ductile beam, the three-point bending test is analysed with a hardening modulus of  $h = -20$  MPa, a factor ten different from the hardening modulus used for previous examples. The evolution of the equivalent plastic strain and the discontinuity path are shown in figure 7.26. The analysis is performed under plane strain conditions with Poisson’s ratio equal to 0.2. Comparing the results for the ductile beam in figure 7.26 with those in figure 7.23 for the more brittle beam, it can be seen that the failure mode is different, with the plastic zone extending further from the discontinuity tip and the discontinuity not propagating as far for the more ductile beam. The plastic zones from the top and bottom of the beam meet, forming a hinge, before the discontinuity has extended significantly. As the material is made more ductile, the dominant failure mode becomes a plastic hinge. The ductile beam is now analysed under plane stress conditions. The evolution of the equivalent plastic strain field and the discontinuity are shown in figure 7.27. The failure mode is different from the plane strain case. The failure mode for the ductile beam under plane stress con-

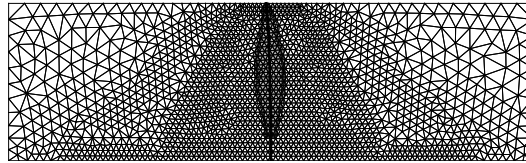


Figure 7.28: Equivalent plastic strain contours and discontinuity path for three-point bending test with the smoothed Rankine model under plane strain conditions at  $u = 0.25$  mm.

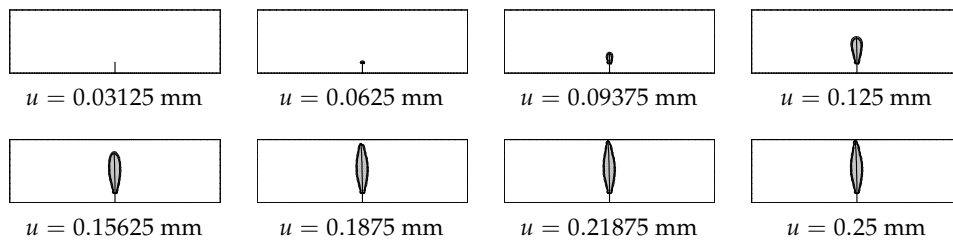


Figure 7.29: Evolution of equivalent plastic strain contours and discontinuity for the three-point bending test under plane stress conditions with the smoothed Rankine yield function.

ditions resembles the failure mode of the brittle beam under plane strain conditions. The plastic zone does not extend ahead of the discontinuity tip. There is no indication of a plastic hinge forming, rather the beam fails entirely in mode-I. Analysis of the three-point bending test shows that the hardening modulus has also an effect on the failure mode when using the Von Mises yield criterion under plane strain conditions. A ductile beam tends to fail in mode-II, while a brittle beam in mode-I.

#### Smoothed Rankine yield function

The three-point bending test is now analysed using the smoothed Rankine yield function, which was discussed in section 7.2.2. The equivalent plastic strain contours and the discontinuity path under plane strain conditions are shown in figure 7.28. It can be seen that plastic strains localise in a narrow zone in the centre of the beam. The plastic zone is very narrow around the initial discontinuity tip, widens in the centre of the beam and tapers again towards the top of the beam. The evolution of the equivalent plastic strain field and the discontinuity are shown in figure 7.29. The plastic zone develops at the initial discontinuity tip and moves with the discontinuity tip. Note that the plastic zone is much narrower than for the Von Mises yield function. As would be expected for the Rankine criterion, the failure mechanism is pure mode-I.

The load-displacement responses for the two meshes is shown in figure 7.30. The two meshes show a very similar response, with the unstructured mesh exhibiting

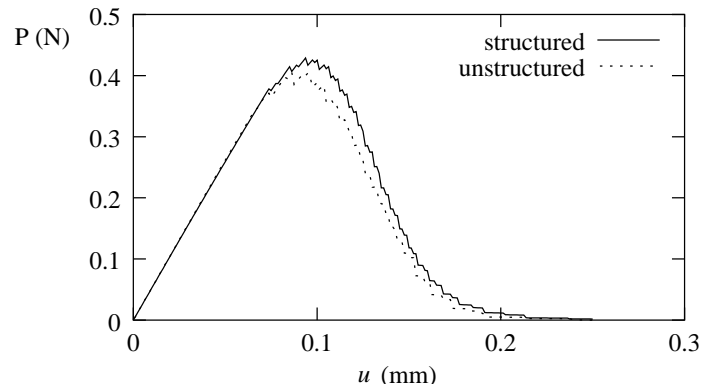


Figure 7.30: Load–displacement responses for the three-point bending test with the smoothed Rankine yield surface with a structured and an unstructured mesh.

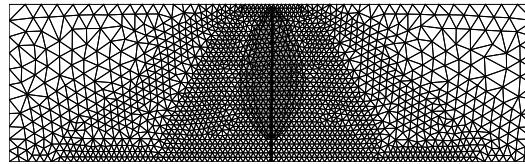


Figure 7.31: Equivalent plastic strain contours and discontinuity path at  $u = 0.8$  mm with hardening modulus  $h = -20$  MPa.

a slightly lower peak load than the structured mesh. This is explained by the finer mesh around the initial discontinuity tip for the unstructured mesh which leads to a higher stress at the initial tip and therefore the discontinuity begins to propagate slightly earlier.

To examine the influence of the hardening modulus on the response, the unstructured mesh is analysed with a hardening modulus of  $h = -20$  MPa. From the equivalent plastic strain field in figure 7.31, it can be seen that the failure mode is identical to the more brittle case (shown in figure 7.28), although size of the plastic zone is considerably greater. As is intuitively reasonable, the more ductile the response, the larger the plastic zone, although unlike for the Von Mises model, the hardening modulus has no influence on the failure mode.

As mentioned previously, the material parameters must be reassessed when a displacement discontinuity is introduced to account for the extra dissipative mechanism and the influence on the mechanical response. To show the differences, the three-point bending test is analysed (using a hardening modulus of  $h = -200$  MPa) with a discontinuity that does not propagate. It is expected that the plastic zone will be larger since the introduction of a discontinuity results in unloading in the continuum

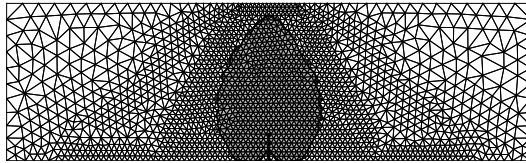


Figure 7.32: Equivalent plastic strain contours for a stationary discontinuity at  $u = 1$  mm for the smoothed Rankine yield surface.

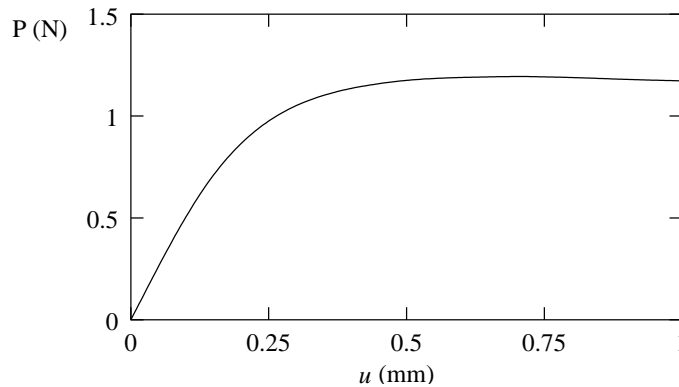


Figure 7.33: Load–displacement response for the three-point bending test with a stationary discontinuity and the smoothed Rankine yield surface.

next to a discontinuity and limits extension of the plastic zone in directions perpendicular to the discontinuity. The equivalent plastic strain zone shown in figure 7.32 (stationary discontinuity) is larger than that which develops when a discontinuity is allowed to extend (figure 7.28). However, for the Rankine yield surface, the failure mode is the same. Due to the larger plastic zone, the continuum-only model yields a more ductile response. This is evident in the load–displacement response for the case of a stationary discontinuity, shown in figure 7.33.

The response of the three-point bending test using the smoothed Rankine yield surface under plane stress conditions is very similar to the plane strain case. The plane stress/strain condition has little influence on the results beyond what is seen for an elastic analysis. This can be easily explained since if the stress in the third direction does not exceed the yield stress, there is no plastic flow in the third direction. Therefore, under plane stress and plane strain conditions the failure mode is qualitatively the same. Due to the absence of a kinematic constraint on plastic flow for the smoothed Rankine yield surface, the inclusion of a displacement discontinuity does not lead to results that are significantly different to a continuum model, in a qualitative sense. For the smoothed Rankine yield surface, the inclusion of a displacement

discontinuity has an influence on the load–displacement response. The response can be calculated through to a zero load level (as shown in figure 7.30), at which stage a discontinuity has propagated entirely through a specimen.

#### 7.5.4 Double-notched specimen under tensile dynamic loading

The concrete double-notched specimen analysed under impact loading in section 5.5.4 with a cohesive crack model is now re-analysed using the combined continuum-discontinuous model. The main intention is to show that the model is suitable for dynamic analyses. The geometry of the specimen is shown in figure 5.15. The use of a rate-dependent model is particularly appropriate for analysing concrete under impact loading since concrete is known to exhibit a significantly higher strength under impact loading than under quasi-static loading.

The double notched specimen is analysed using the smoothed Rankine yield surface. The adopted material parameters are the same as those in chapter 5, except the tensile strength  $f_t = 4.5$  MPa, the viscosity is chosen as  $\eta = 3 \times 10^{-2}$  s and the continuum hardening modulus  $h = -2000$  MPa. The mesh shown in figure 5.18b is used for the analysis. The coarse mesh shown in figure 5.18a, which performed well for the cohesive zone model, is too coarse for use with the continuum-discontinuous model. It is necessary to use a relatively large length  $l$  of 10 mm for the weighting function used in determining the propagating direction due to the large elements in the central area between the notches. The modelling of the split-Hopkinson bar and the loading is the same as described in section 5.5.4. The double-notched specimen is analysed for the case of a single crack propagating from one notch (non-symmetric failure) and the case of a crack propagating from each notch (symmetric failure). Also, the problem is analysed with a continuum-only model.

The equivalent plastic strain field and the discontinuity path for symmetric and non-symmetric failure and the continuum model are shown in figure 7.34. From the equivalent plastic strain field, it can be seen that cracking occurs in a zone between the notches. The most severe cracking has taken place along an axis between the notches and through this zone a discontinuity has propagated. The plastic zone for the two cases with a discontinuity is almost identical. For the continuum-only model, the plastic zone is slightly larger.

The average normal stress transmitted in the vertical direction at the top boundary for the two failure modes and the continuum-only is compared to the experimental results from Weerheijm (1992) in figure 7.35. For the calculations with a discontinuity, the response is shown up to the point at which a crack has propagated through the entire specimen. At this stage the stress transmitted at the top boundary has not yet reduced to zero since a tensile wave is still travelling in the top half of the specimen. The results for the discontinuity model compare reasonably with the experimental results, although not as well as for the cohesive zone model in chapter 5. This could be partly attributed to exponential softening being more appropriate than

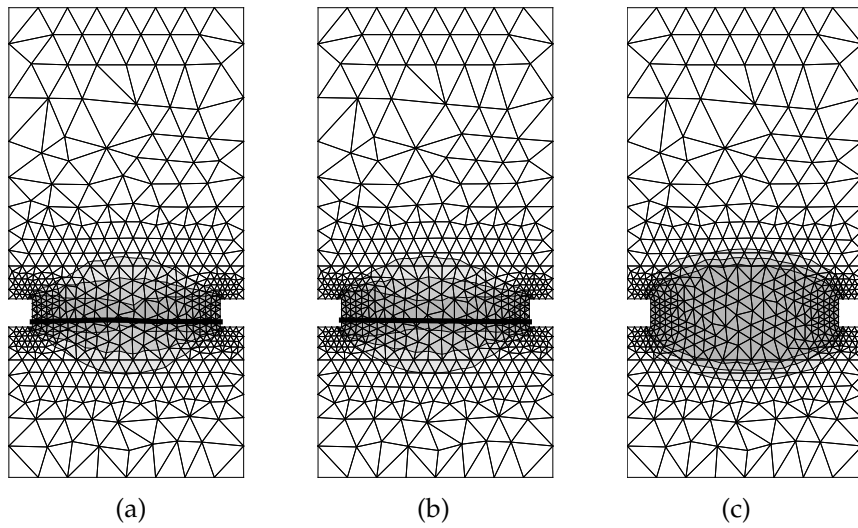


Figure 7.34: Equivalent plastic strain contours and discontinuity path for the double-notched specimen for (a) symmetric ( $t = 5.18 \times 10^{-4}$  s) and (b) non-symmetric ( $t = 5.22 \times 10^{-4}$  s) failure and the (c) continuum-only model ( $t = 6 \times 10^{-4}$  s).

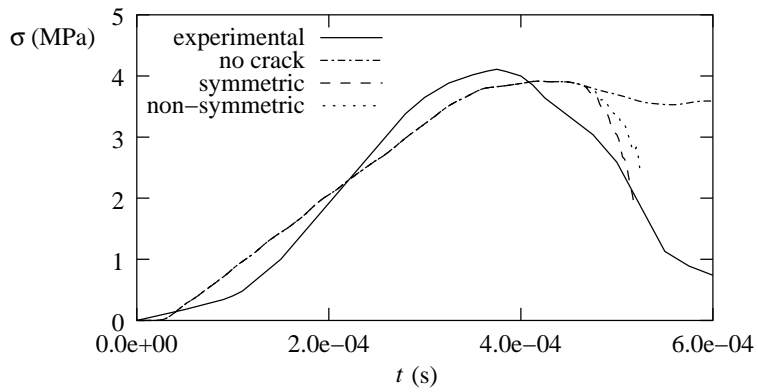
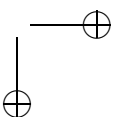
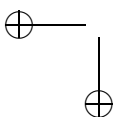
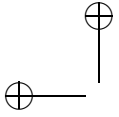
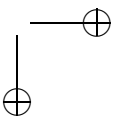
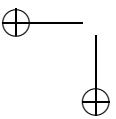
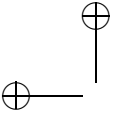


Figure 7.35: Average normal stress transmitted at the top boundary in the  $x_2$  direction for the double-notched specimen.

linear softening. As for the cohesive zone model, the responses for symmetric and non-symmetric failure are remarkably similar. The inclusion of a displacement discontinuity when using a viscoplastic model is important for simulating the entire response of the double-notched specimen. When a discontinuity is not included, the response cannot be traced effectively far past the peak, as shown in figure 7.35 where the stress transmitted for the continuum-only model does not decrease significantly. Soon after the peak, the inviscid yield function reduces to zero (numerically the tensile strength is equal to  $0.001f_t$ ). At this stage, the strain rate is very high and the transmitted stress begins to increase. Figure 7.35 shows clearly when a discontinuity begins to propagate from the notches of the specimen. A discontinuity begins to propagate at the point where the response for the discontinuity models and the continuum-only model diverge. Discontinuities develop at a relatively late stage in the analysis. This is an example of where the continuum model represents the early deformations in the continuum and at a late stage of failure discontinuities develop, representing complete failure. The introduction of discontinuities allows the response just before complete failure to be better simulated, as shown by the steeply decreasing response of the discontinuity models in figure 7.35.





## Chapter 8

### Conclusions

Discontinuities arise in all fields of mechanics. Some examples, such as cracks in elastic bodies, are obvious, while others, such as the interface between different materials or a block stress wave travelling in a one-dimensional elastic bar, are less obvious. A more abstract example of a discontinuity is the edge of a structure where there is a discontinuity in the material from ‘air’ to a solid. Many other problems can be considered to exhibit discontinuities, depending on the level of observation. Continuous fields with a steep gradient across a small zone appear discontinuous when viewed from a distance. For practical engineering problems this means that many continuous problems appear discontinuous when viewed from the level of practical interest. Also, fields which appear continuous may be discontinuous when viewed at a much lower scale. Solids are usually described assuming a continuous displacement field, while at the microlevel separation occurs between discrete particles.

The inclusion of arbitrary displacement discontinuities within the finite element method poses many challenges. Using finite elements, discontinuities have traditionally been modelled explicitly through the construction of the mesh. Such a procedure suffers several limitations. When using a fixed mesh, potential discontinuity paths are restricted to inter-element boundaries. Adaption of the mesh can be difficult and computationally expensive. A translating discontinuity, such as a shock wave or Lüders bands (translating shear bands) cannot be captured with a fixed mesh or easily through remeshing. The most flexible and efficient method to simulate discontinuities is to model them in a mathematical sense, rather than geometrically through mesh adaption or inter-element interfaces. The geometric structure of a mesh and the geometric representation of a discontinuity surface can then be decoupled, which allows new problems to be tackled. This concept has been investigated for simulating failure in solids.

Two different methods were investigated to model arbitrary discontinuities that can pass through solid finite elements. The goal was to develop robust methods that are independent of the spatial discretisation. The spatial orientation of discontinuities should come only from the mechanical fields. The first approach investigated

added the *effect* of a displacement discontinuity to solid finite elements. This was done by adding incompatible strain modes which attempted to reflect the presence of a displacement discontinuity, although a displacement discontinuity was not explicitly included in the formulation. Through careful consideration of the variational formulation, it is possible to apply a discrete constitutive model that is formulated in terms of tractions and displacements. The advantage of this approach is that it can be implemented easily in existing finite element codes. However, in order to minimise the sensitivity of the model to mesh alignment, it was necessary to follow an approach that is not variationally consistent and leads to a loss of symmetry of the global stiffness matrix, irrespective of the material model used.

It was shown in chapter 4 that the embedded discontinuity model that is based on incompatible strain modes can be cast in an equivalent, standard continuum format. Since the formulation can be cast in a continuum format, it will exhibit the same basic features of conventional continuum models. Namely, element-based length scales are involved and sensitivity to mesh alignment cannot be fully overcome. Despite the application of discrete constitutive models, the model still involves length scales that are derived from the size and geometry of individual elements. For cases where a discontinuity crosses an element boundary to which it is almost parallel, the model is unable to properly resolve the kinematics and fails. In light of the equivalence between the incompatible modes formulation and classical smeared models, it should be used with caution and not regarded as a discontinuous failure model.

The second approach was based on partitions of unity, the special property that requires that a collection of functions sum to unity at all points in a body. Using partitions of unity, a field can be interpolated in terms of discrete nodal points at which degrees of freedom describe the amplitude of the partition of unity functions and any additional functions added to the interpolation basis. Since standard finite element shape functions form a partition of unity, they are used to add to the underlying interpolation basis a discontinuous function. This approach is more general and far more flexible than the incompatible modes formulations as it addresses the problem at a different level. The partition of unity concept relates to how a field can be interpolated in terms of a collection of discrete points (nodes) and does not directly involve any finite element concepts. Due the generality of the partition of unity based model, there are no restrictions on the underlying base element. The polynomial order of the displacement jump interpolation is the same as the underlying element and the magnitude of the displacement jump is continuous across element boundaries. Since the interpolated fields are compatible, standard variational concepts can be used for the formulation which are consistent and preserve symmetry of the global stiffness matrix if the material tangent matrices are also symmetric. This is an important feature for efficient numerical implementation.

The partition of unity model was first used to simulate cohesive zones for both mode-I and mode-II problems under quasi-static and impact loading. Various problems were analysed, illustrating objectivity with respect to spatial discretisation. The

model proved extremely robust for both dynamic and quasi-static loadings and in the presence of strong non-linearities. It was shown that the model can perform excellently with coarse meshes. To simulate delamination in laminated composite materials, the kinematic fields were extended to the geometrically non-linear case. In this way, the structure of the laminate and the finite element mesh are decoupled. The partition of unity concept offers several advantages over traditional interface elements for analysing laminated composites. A dummy elastic stiffness is not required at interfaces which improves the robustness of calculations. Efficiency can be improved since the enhanced degrees of freedom are needed only when separation begins at an interface.

In chapter 7, a departure was made from the cohesive zone concept. Rather than simulating all inelastic deformations at a surface, inelastic deformations were modelled in the continuum with traction-free discontinuities introduced using the partition of unity model. To simulate strain softening in the continuum, a viscoplastic model was used to provide regularisation. Discontinuities were introduced when the inelastic deformation reached a critical level at a discontinuity tip, representing complete failure of the material. It was shown that the introduction of a discontinuity into a viscoplastic continuum could lead to failure modes that cannot be modelled with a continuum model only. It was also shown that material parameters, boundary conditions and initial discontinuities all have an influence on the failure mode. The model holds great potential for simulating industrial processes such as metal cutting, stamping and forming, as well as for simulating modern materials such as fibre-reinforced concrete. It is a particularly attractive model for ductile failure problems, as they usually exhibit significant plastic deformations before displacement discontinuities develop.

#### Future directions

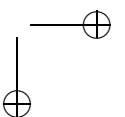
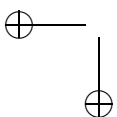
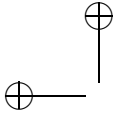
The generality and flexibility of the partition of unity concept makes it applicable for a wide range of problems. A straightforward extension to the work presented here is to more complex discrete constitutive models and initiation criteria. Also, the model could be extended for the simulation of propagating discontinuities that intersect. An important extension for simulating failure is to three dimensions. The most difficult problem in three dimensions is the simulation of the evolving failure surface.

An important area for further research is into translating discontinuities such as block stress waves in an elastic body, shock waves in compressible fluids, propagating discontinuous chemical fronts in solids and phase transformations. In many respects, these problems in two dimensions are similar to cohesive zone modelling in three dimensions, where a front translates in the three-dimensional space. For all these problems the most important aspect is modelling the position of a discontinuity.

More generally, the partition of unity concept holds great potential for continu-

ous and combined continuous-discontinuous problems. It can be used to represent the geometry of a structure or material independently of the mesh structure. It is not necessary that the boundary of a structure coincide with the boundary of a mesh to perform a simulation. For complex geometries, a 'background' mesh could be formed and the actual geometry of the problem laid over the mesh. The boundary of problems could be represented mathematically using discontinuous functions. This avoids the need for generating meshes for complex geometries. This concept is similar to what was used to simulate laminated composites in chapter 6.

The partition of unity idea is also ideal for implementing 'multiscale' models (Hughes, 1995) with finite elements. The coarse scale representation can be modelled by the standard displacement field and the fine, resolved scale by enhanced degrees of freedom. In the same vein, 'moving' p-adaptivity can be performed by adding polynomial terms to the underlying basis locally and removing the enhanced polynomials when no longer required. This is ideal for wave propagation problems where high gradients exist near the wave front. Yet another application to coupled problems. For problems with multiple fields which require different interpolation orders, a simple base element could be used (linear for example), with the higher-order polynomial terms added through the addition of extra degrees of freedom at the nodes of the base element. This avoids the difficulty of dealing with two different sets of shape function for one element and avoids the need for element edge nodes.



## References

- Alfaiate, J., Wells, G. N. and Sluys, L. J. (2001). Strong embedded discontinuities for simulating fracture in quasi-brittle materials. In *Fourth International Conference on Fracture Mechanics of Concrete and Concrete Structures*, R. de Borst, J. Mazars, G. Pijaudier-Cabot and J. G. M. van Mier, editors. Balkema, Rotterdam.
- Alfano, G. and Crisfield, M. A. (2001). Finite element interface models for the delamination analysis of laminated composites: mechanical and computational issues. *International Journal for Numerical Methods in Engineering* **50** (7), pp. 1701–1736.
- Armero, F. and Garikipati, K. (1995). Recent advances in the analysis and numerical simulation of strain localization in inelastic solids. In *Computational Plasticity, Fundamentals and Applications*, D. R. J. Owen, E. Oñate and E. Hinton, editors, pp. 547–561. Pineridge Press, Swansea.
- Armero, F. and Garikipati, K. (1996). An analysis of strong discontinuities in multiplicative finite strain plasticity and their relation with the numerical simulation of strain localization. *International Journal of Solids and Structures* **33** (20–22), pp. 2863–2885.
- Babuška, I. and Melenk, J. M. (1997). The Partition of Unity Method. *International Journal for Numerical Methods in Engineering* **40** (4), pp. 727–758.
- Barenblatt, G. I. (1962). The mathematical theory of equilibrium cracks in brittle fracture. *Advances in Applied Mechanics* **7**, pp. 55–129.
- Bažant, Z. P. and Belytschko, T. B. (1985). Wave propagation in a strain-softening bar: Exact solution. *ASCE Journal of Engineering Mechanics* **111** (3), pp. 381–389.
- Bažant, Z. P. and Oh, B. (1983). Crack band theory for fracture of concrete. *RILEM Materials and Structures* **16** (93), pp. 155–177.
- Belytschko, T. and Black, T. (1999). Elastic crack growth in finite elements with minimal remeshing. *International Journal for Numerical Methods in Engineering* **45** (5), pp. 601–620.

- Belytschko, T., Fish, J. and Engelmann, B. E. (1988). A finite element with embedded localization zones. *Computer Methods in Applied Mechanics and Engineering* **70** (1), pp. 59–89.
- Belytschko, T., Lu, Y. Y. and Gu, L. (1994). Element-free Galerkin methods. *International Journal for Numerical Methods in Engineering* **37** (2), pp. 229–256.
- Bonet, J. and Wood, R. D. (1997). *Nonlinear continuum mechanics for finite element analysis*. Cambridge University Press, Cambridge.
- Borja, R. I. (2000). A finite element model for strain localization of strongly discontinuous fields based on standard Galerkin approximation. *Computer Methods in Applied Mechanics and Engineering* **190** (11–12), pp. 1529–1549.
- De Borst, R. and Mühlhaus, H.-B. (1992). Gradient-dependent plasticity – formulation and algorithmic aspects. *International Journal for Numerical Methods in Engineering* **35** (3), pp. 521–539.
- De Borst, R. and Nauta, P. (1985). Non-orthogonal cracks in a smeared finite element model. *Engineering Computations* **2** (1), pp. 35–46.
- De Borst, R. and Sluys, L. J. (1991). Localization in a Cosserat continuum under static and dynamic loading conditions. *Computer Methods in Applied Mechanics and Engineering* **90** (1–3), pp. 805–827.
- De Borst, R., Wells, G. N. and Sluys, L. J. (2001). Some observations on embedded discontinuity models. *Engineering Computations* **18** (1–2), pp. 241–254.
- Duarte, C. A. and Oden, J. T. (1996). H-p clouds – an h-p meshless method. *Numerical Methods for Partial Differential Equations* **12** (6), pp. 673–705.
- Dugdale, D. S. (1960). Yielding of steel sheets containing slits. *Journal of the Mechanics and Physics of Solids* **8**, pp. 100–108.
- Dvorkin, E. N., Cuitiño, A. M. and Gioia, G. (1990). Finite-elements with displacement interpolated embedded localization lines insensitive to mesh size and distortions. *International Journal for Numerical Methods in Engineering* **30** (3), pp. 541–564.
- Eringen, A. C., Speziale, C. G. and Kim, B. S. (1977). Crack-tip problem in non-local elasticity. *Journal of the Mechanics and Physics of Solids* **25** (5), pp. 339–355.
- Feenstra, P. H. and De Borst, R. (1995). A plasticity model and algorithm for mode-I cracking in concrete. *International Journal for Numerical Methods in Engineering* **38** (15), pp. 2509–2529.
- Fleming, M., Chu, Y. A., Moran, B. and Belytschko, T. (1997). Enriched element-free Galerkin methods for crack tip fields. *International Journal for Numerical Methods in Engineering* **40** (8), pp. 1483–1504.

REFERENCES

157

- Freund, L. B. and Hutchinson, J. W. (1985). High strain-rate crack growth in rate-dependent plastic solids. *Journal of the Mechanics and Physics of Solids* **33** (2), pp. 169–191.
- Geers, M. G. D. (1997). *Experimental Analysis and Computational Modelling of Damage and Fracture*. PhD thesis, Eindhoven University of Technology.
- Geers, M. G. D., De Borst, R., Brekelmans, W. A. M. and Peerlings, R. H. J. (1998). Strain-based transient-gradient damage model for failure analyses. *Computer Methods in Applied Mechanics and Engineering* **160** (1–2), pp. 133–153.
- Hill, R. (1962). Acceleration waves in solids. *Journal of the Mechanics and Physics of Solids* **10**, pp. 1–16.
- Hillerborg, A., Modeer, M. and Petersson, P. E. (1976). Analysis of crack formation and crack growth in concrete by means of fracture mechanics and finite elements. *Cement and Concrete Research* **6** (6), pp. 773–782.
- Hughes, T. J. R. (1987). *The Finite Element Method*. Prentice-Hall International, New Jersey.
- Hughes, T. J. R. (1995). Multiscale phenomena: Green’s functions, the Dirichlet-to-Neumann formulation, subgrid scale models, bubbles and the origins of stabilized methods. *Computer Methods in Applied Mechanics and Engineering* **127** (1–4), pp. 387–401.
- Hutchinson, J. W. (1968). Singular behaviour at the end of a tensile crack in a hardening material. *Journal of the Mechanics and Physics of Solids* **16**, pp. 13–31.
- Jirásek, M. (1998a). Element-free Galerkin method applied to strain-softening materials. In *EURO-C 1998 Computer Modelling of Concrete Structures*, R. de Borst, N. Bićanić, H. Mang and G. Meschke, editors, pp. 311–319. Balkema, Rotterdam.
- Jirásek, M. (1998b). Embedded crack models for concrete fracture. In *EURO-C 1998 Computer Modelling of Concrete Structures*, R. de Borst, N. Bićanić, H. Mang and G. Meschke, editors, pp. 291–300. Balkema, Rotterdam.
- Jirásek, M. (2000). Comparative study on finite elements with embedded discontinuities. *Computer Methods in Applied Mechanics and Engineering* **188** (1–3), pp. 307–330.
- Jirásek, M. and Zimmermann, T. (2001). Embedded crack model. Part II: Combination with smeared cracks. *International Journal for Numerical Methods in Engineering* **50** (6), pp. 1291–1305.
- Klisinski, M., Runesson, K. and Sture, S. (1991). Finite element with inner softening band. *ASCE Journal of Engineering Mechanics* **117** (3), pp. 575–587.

- Larsson, R. and Runesson, K. (1996). Element-embedded localization band based on regularized displacement discontinuity. *ASCE Journal of Engineering Mechanics* **122** (5), pp. 402–411.
- Larsson, R., Steinmann, P. and Runesson, K. (1998). Finite element embedded localization band for finite strain plasticity based on a regularized strong discontinuity. *Mechanics of Cohesive-Frictional Materials* **4** (2), pp. 171–194.
- Lo, K. K. (1983). Dynamic crack-tip fields in rate-sensitive solids. *Journal of the Mechanics and Physics of Solids* **31** (4), pp. 287–305.
- Lotfi, H. R. and Shing, P. B. (1995). Embedded representation of fracture in concrete with mixed finite elements. *International Journal for Numerical Methods in Engineering* **38** (8), pp. 1307–1325.
- Marsden, J. E. and Hughes, T. J. R. (1983). *Mathematical Foundations of Elasticity*. Prentice-Hall, New Jersey.
- Mazars, J. and Pijaudier-Cabot, G. (1989). Continuum damage theory – application to concrete. *ASCE Journal of Engineering Mechanics* **115** (2), pp. 345–365.
- Moës, N., Dolbow, J. and Belytschko, T. (1999). A finite element method for crack growth without remeshing. *International Journal for Numerical Methods in Engineering* **46** (1), pp. 131–150.
- Needleman, A. (1988). Material rate dependence and mesh sensitivity in localization problems. *Computer Methods in Applied Mechanics and Engineering* **67** (1), pp. 69–85.
- Noor, A. K. and Burton, W. S. (1990). Assessment of computational model for multi-layered composite shells. *Applied Mechanics Review* **43** (4), pp. 67–97.
- Oliver, J. (1996a). Modelling strong discontinuities in solid mechanics via strain softening constitutive equations. Part 1: Fundamentals. *International Journal for Numerical Methods in Engineering* **39** (21), pp. 3575–3600.
- Oliver, J. (1996b). Modelling strong discontinuities in solid mechanics via strain softening constitutive equations. Part 2: Numerical simulation. *International Journal for Numerical Methods in Engineering* **39** (21), pp. 3601–3623.
- Oliver, J., Cervera, M. and Manzoli, O. (1999). Strong discontinuities and continuum plasticity models: the strong discontinuity approach. *International Journal of Plasticity* **15** (3), pp. 319–351.
- Ortiz, M., Leroy, Y. and Needleman, A. (1987). A finite element method for localized failure analysis. *Computer Methods in Applied Mechanics and Engineering* **61** (2), pp. 189–214.

## REFERENCES

159

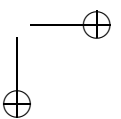
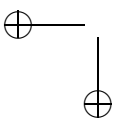
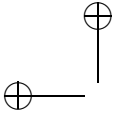
- Ottosen, N. S. and Runesson, K. (1991). Properties of discontinuous bifurcation solutions in elasto-plasticity. *International Journal of Solids and Structures* **27** (4), pp. 401–421.
- Pamin, J. K. (1994). *Gradient-dependent plasticity in numerical simulation of localization phenomena*. PhD thesis, Delft University of Technology.
- Peerlings, R. H. J. (1999). *Enhanced damage modelling for fracture and fatigue*. PhD thesis, Eindhoven University of Technology.
- Peerlings, R. H. J., De Borst, R., Brekelmans, W. A. M. and Geers, M. G. D. (1998). Gradient-enhanced damage modelling of concrete fracture. *Mechanics of Cohesive-Frictional Materials* **3** (4), pp. 323–342.
- Perzyna, P. (1966). Fundamental problems in viscoplasticity. In *Recent Advances in Applied Mechanics*, vol. 9, pp. 243–377. Academic Press, New York.
- Pijaudier-Cabot, G. and Bažant, Z. (1987). Nonlocal damage theory. *ASCE Journal of Engineering Mechanics* **113** (10), pp. 1512–1533.
- Rice, J. R. (1976). The localization of plastic deformation. In *Theoretical and Applied Mechanics*, W. T. Koiter, editor, pp. 207–220. North-Holland Publishing Company, Amsterdam.
- Rice, J. R. and Rosengren, G. F. (1968). Plane strain deformation near a crack tip in a power law hardening material. *Journal of the Mechanics and Physics of Solids* **16**, pp. 1–12.
- Rots, J. G. (1988). *Computational modeling of concrete fracture*. PhD thesis, Delft University of Technology.
- Rudnicki, J. W. and Rice, J. R. (1975). Conditions for the localization of deformation in pressure-sensitive dilatant solids. *Journal of the Mechanics and Physics of Solids* **23**, pp. 371–394.
- Runesson, K., Ottosen, N. S. and Peric, D. (1991). Discontinuous bifurcations of elastic-plastic solutions at plane-stress and plane-strain. *International Journal of Plasticity* **7** (1–2), pp. 99–121.
- Schellekens, J. C. J. and De Borst, R. (1993). On the numerical integration of interface elements. *International Journal for Numerical Methods in Engineering* **26** (1), pp. 43–66.
- Schlangen, E. (1993). *Experimental and numerical analysis of fracture processes in concrete*. PhD thesis, Delft University of Technology.
- Simo, J. C. and Hughes, T. J. R. (1998). *Computational Inelasticity*. Springer, London.

- Simo, J. C., Kennedy, J. G. and Govindjee, S. (1988). Non-smooth multisurface plasticity and viscoplasticity. Loading/unloading conditions and numerical algorithms. *International Journal for Numerical Methods in Engineering* **26** (10), pp. 2161–2185.
- Simo, J. C., Oliver, J. and Armero, F. (1993). An analysis of strong discontinuities induced by strain-softening in rate-independent inelastic solids. *Computational Mechanics* **12**, pp. 277–296.
- Simo, J. C. and Rifai, M. S. (1990). A class of mixed assumed strain methods and the method of incompatible modes. *International Journal for Numerical Methods in Engineering* **29** (8), pp. 1595–1638.
- Sluys, L. J. and Berends, A. H. (1998). Discontinuous failure analysis for mode-I and mode-II localization problems. *International Journal of Solids and Structures* **35** (31–32), pp. 4257–4274.
- Sluys, L. J. and De Borst, R. (1992). Wave-propagation and localization in a rate-dependent cracked medium: Model formulation and one-dimensional examples. *International Journal of Solids and Structures* **29** (23), pp. 2945–2958.
- Sluys, L. J. and De Borst, R. (1996). Failure in plain and reinforced concrete – an analysis of crack width and crack spacing. *International Journal of Solids and Structures* **33** (20–22), pp. 3257–3276.
- Steinmann, P., Larsson, R. and Runesson, K. (1997). On the localization properties of multiplicative hyperelasto-plastic continua with strong discontinuities. *International Journal of Solids and Structures* **34** (8), pp. 969–990.
- Swenson, D. V. and Ingraffea, A. R. (1988). Modeling mixed-mode dynamic crack propagation using finite elements: Theory and applications. *Computational Mechanics* **3** (5), pp. 381–397.
- Tijssens, M. G. A., Sluys, L. J. and Van der Giessen, E. (2000). Numerical simulation of quasi-brittle fracture using damaging cohesive surfaces. *European Journal of Mechanics A/Solids* **19** (5), pp. 761–779.
- Wang, W. M., Sluys, L. J. and De Borst, R. (1997). Viscoplasticity for instabilities due to strain softening and strain-rate softening. *International Journal for Numerical Methods in Engineering* **40** (20), pp. 3839–3864.
- Washizu, K. (1982). *Variational Methods in Elasticity and Plasticity*. Third edn. Pergamon Press Ltd, Oxford.
- Weerheijm, J. (1992). *Concrete under impact tensile loading and lateral compression*. PhD thesis, Delft University of Technology.

REFERENCES

161

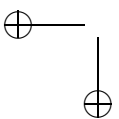
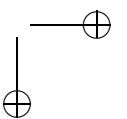
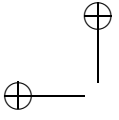
- Wells, G. N. and Sluys, L. J. (1999). Application of continuum laws in discontinuity analysis based on a regularised displacement jump. In *Proceedings of the European Conference on Computational Mechanics (CDROM)*, W. Wunderlich, editor.
- Wells, G. N. and Sluys, L. J. (2000). Application of embedded discontinuities for softening solids. *Engineering Fracture Mechanics* **65** (2–3), pp. 263–281.
- Wells, G. N. and Sluys, L. J. (2001a). Analysis of slip planes in three-dimensional solids. *Computer Methods in Applied Mechanics and Engineering* **190** (28), pp. 3591–3606.
- Wells, G. N. and Sluys, L. J. (2001b). Discontinuous analysis of softening solids under impact loading. *International Journal for Numerical and Analytical Methods in Geomechanics* **25** (7), pp. 691–710.
- Wells, G. N. and Sluys, L. J. (2001c). A new method for modelling cohesive cracks using finite elements. *International Journal for Numerical Methods in Engineering* **50** (12), pp. 2667–2682.
- Wells, G. N. and Sluys, L. J. (2001d). A p-adaptive scheme for overcoming volumetric locking during plastic flow. *Computer Methods in Applied Mechanics and Engineering* (submitted).
- Wells, G. N. and Sluys, L. J. (2001e). Partition-of-unity for brittle fracture. In *Bifurcation and Localisation in Soils and Rocks 99*, H.-B. Müllhaus, A. V. Dyskin and A. Pasternak, editors. Balkema, Rotterdam. (in press).
- Wells, G. N. and Sluys, L. J. (2001f). Three-dimensional embedded discontinuity model for brittle fracture. *International Journal of Solids and Structures* **38** (5), pp. 897–913.
- Zienkiewicz, O. C. and Taylor, R. L. (1994). *The Finite Element Method. Volume 1: Basic Formulations and Linear Problems*. Fourth edn. McGraw-Hill Book Company.



## Summary

The computational simulation of failure in solids poses many challenges. A proper understanding of how structures respond under loading, both before and past the peak load, is important for safe and economical constructions. This requires numerical models for failure which are both faithful to the physical reality and mathematically well founded. A serious computational issue is that of objectivity with respect to the spatial discretisation of a problem. This requires that upon refinement of the spatial discretisation of a problem, a unique, physically meaningful result is approached. One approach to ensure objectivity with respect to spatial discretisation when simulating failure in solids is to allow displacement discontinuities in the solution. In this work, different techniques, of varying complexity, are developed to simulate displacement discontinuities which are independent of the spatial discretisation using finite elements. The different techniques are then critically evaluated.

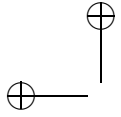
The first model examined involves adding only the effect of a displacement discontinuity to a finite element as an incompatible strain mode. This allows a traction-separation relationship to be applied at an interface and can be implemented simply in a standard finite element code. It is however shown that this type of model can be cast in an equivalent continuum format, a form which is known to be sensitive to the spatial discretisation. The second approach developed involves the addition of the Heaviside function to the underlying finite element interpolation basis. This method is based on the partition of unity concept, and allows the Heaviside function to be added locally to a finite element mesh to simulate a propagating displacement discontinuity. The approach is formulated for geometrically linear, geometrically non-linear, quasi-static and dynamic problems. It is shown to be completely independent of the spatial discretisation. The partition of unity-based model is used also to simulate failure using a regularised strain softening model. When a critical level of inelastic deformation is reached, a displacement discontinuity is inserted. This model is better suited to modelling the entire failure process than a continuum or discontinuous model alone. Through numerical examples, it is shown that the inclusion of a displacement discontinuity during the failure process can lead to a different failure mode than for a continuum-only model.



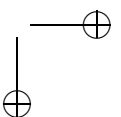
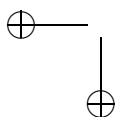
## Samenvatting

Het numeriek simuleren van bezwijkprocessen in vaste stoffen stelt vele uitdagingen. Een goed begrip van het gedrag van constructies ten gevolge van belastingen, zowel voor als na de piekbelasting, is van belang voor een veilige en economische manier van construeren. Dit vraagt om numerieke bezwijkmodellen die zowel recht doen aan de fysische realiteit als wiskundig goed gefundeerd zijn. Een belangrijk numeriek aspect is de objectiviteit met betrekking tot de ruimtelijke discretisatie. Dit vereist dat bij het verfijnen van de ruimtelijke discretisatie van een probleem een uniek, fysisch betekenisvol resultaat wordt bereikt. Eén methode om objectiviteit met betrekking tot de ruimtelijke discretisatie te garanderen bij het simuleren van bezwijken in vaste stoffen is het toestaan van verplaatsingsdiscontinuïteiten in de oplossing. In deze studie worden verscheidene technieken, variërend in complexiteit, ontwikkeld om verplaatsingsdiscontinuïteiten te simuleren die onafhankelijk zijn van de ruimtelijke discretisatie bij gebruik van de eindige-elementenmethode. De verschillende technieken worden vervolgens kritisch geëvalueerd.

Het eerste model omvat het toevoegen van het effect een verplaatsingsdiscontinuïteit aan een eindig element als een niet-compatibele rekvelde. Op deze wijze kan een relatie tussen tractie en relatieve verplaatsing opgesteld worden in een grenslaag die eenvoudig geïmplementeerd kan worden in een standaard eindige-elementenprogramma. Het wordt echter aangetoond dat dit type model kan worden gevat in een equivalent continuümformaat, waarvan bekend is dat deze gevoelig is voor ruimtelijke-discretisatieaspecten. De tweede methode die is ontwikkeld behelst het toevoegen van de Heaviside functie aan de onderliggende interpolatiebasis van de eindige elementen. Deze methode is gebaseerd op het partition-of-unity concept, waarbij de Heaviside functie lokaal aan een eindige-elementennet kan worden toegevoegd om een voortplantende verplaatsingsdiscontinuïteit te simuleren. De techniek is geformuleerd voor geometrisch lineaire en niet-lineaire, quasi-statische en dynamische problemen. Aangetoond wordt dat deze volledig onafhankelijk is van de ruimtelijke discretisatie. Het model, gebaseerd op het partition-of-unity principe, is ook gebruikt om bezwijken te simuleren met behulp van een geregulariseerd softeningmodel. Zodra een kritisch niveau van inelastische vervorming is bereikt, wordt een verplaatsingsdiscontinuïteit aangebracht. Dit model is beter geschikt om het gehele bezwijkproces te modelleren dan een continu of discontinu model afzonder-



lijk. Met numerieke voorbeelden wordt aangetoond dat het toevoegen van een verplaatsingsdiscontinuïteit tijdens het bezwijkproces tot een andere bezwijkvorm kan leiden dan een zuiver continuümmodel.



## Stellingen

1. Through the introduction of the Dirac-delta distribution, the mathematical differences between discontinuous and continuum descriptions disappear.

*Door het gebruik van de Dirac-delta functie verdwijnen de wiskundige verschillen tussen discontinue en continue beschrijvingen.*

2. Objective results with discrete models can only be achieved if discontinuities are modelled independently of the mesh structure. This does not exclude using features of the mesh but the discrete enhancements and the underlying finite element should not intrinsically be one entity.

*Alleen als discontinuïteiten onafhankelijk van de eindige-elementendiscretisatie worden gemodelleerd, kunnen objectieve resultaten worden gekregen met discontinue modellen. Dit sluit niet uit dat de eigenschappen van de eindige-elementendiscretisatie gebruikt worden, maar de discrete uitbreidingen en het onderliggend eindige element mogen intrinsiek niet één entiteit zijn.*

3. Even in the light of new numerical techniques, the power and versatility of the finite element method should not be underestimated.

*Zelfs in het licht van nieuwe numerieke technieken moeten de kracht en de veelzijdigheid van de eindige-elementenmethode niet worden onderschat.*

4. While the simplicity of Duvaut-Lions viscoplasticity and its close relationship with inviscid plasticity are appealing, it is poorly suited for strain-softening problems. This is particularly the case in the presence of sharp crack tips.

This proposition was statically condensed from four subroutines and approximately 400 lines of code.

*Hoewel de eenvoud van Duvaut-Lions viscoplasticiteit en de nauwe relatie ervan met tijdonafhankelijke plasticiteit aantrekkelijk zijn, is de theorie ongeschikt voor ‘strain-softening’ problemen. Dit is met name het geval bij het optreden van een scherpe scheurtip.*

*Deze stelling is statisch gecondenseerd uit vier subroutines en ongeveer 400 regels code.*

5. Computational plasticity cannot be studied and evaluated solely for the Von Mises yield function, although unfortunately in the literature this is often the case.

*Numerieke plasticiteit kan niet alleen met de Von Misesvloei functie worden bestudeerd en geëvalueerd, hoewel dit in de literatuur helaas te vaak het geval is.*

6. Blurring the distinction between constitutive model and numerical method is dangerous. Special care is needed when a numerical method possesses its own length scale.

*Het is gevaarlijk om constitutief model en numerieke methode te vermengen. Met name het geval dat de numerieke methode zelf een lengteschaal bevat, verdient speciale aandacht.*

7. Clarity is an unheralded virtue in the academic world.

*Duidelijk is een niet-erkende deugd in de academische wereld.*

8. Unspoken knowledge is of no common value. Therefore language is a researcher's most valuable and important tool.

*Onuitgesproken kennis dient het algemeen belang niet. Daarom is taal het waardevolste en belangrijkste instrument van een onderzoeker.*

9. Intuition is a researcher's second most valuable tool.

*Intuïtie is het op-één-na waardevolste instrument van een onderzoeker.*

10. Compulsory voting is undemocratic, but good for a democracy.

*Verplicht stemmen is ondemocratisch, maar goed voor een democratie.*

11. Preferential voting is the fairest method of voting.

*De eerlijkste manier van stemmen is door middel van een ranglijst van voorkeuren.*

12. The ease with which industrialised nations criticise developing nations for exploiting their natural resources is hypocritical when considering that industrialised nations have already profited from and decimated their own natural environments.

*Het gemak waarmee geïndustrialiseerde landen het exploiteren van natuurlijke hulpbronnen door ontwikkelingslanden bekritisieren, is hypocriet gezien het feit dat de geïndustrialiseerde landen hun natuurlijke omgeving al hebben uitgebuit.*

13. The recent refusal of the United States government to ratify the 1997 Kyoto global warming treaty is inward-looking and a sign of self-centredness. Placing economic concerns far above environmental ones prompts the question: 'what is the economy without an environment?'

STELLINGEN

169

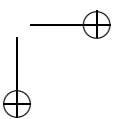
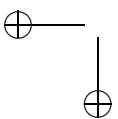
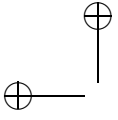
*De recente weigering van de regering van de Verenigde Staten om het '1997 Kyoto global warming treaty' te ratificeren is kortzichtig en een teken van egocentrisme. Economische belangen veel zwaarder laten tellen dan milieubelangen roept de vraag op: 'wat is een economie zonder milieu?'*

14. Stellingen are often the most interesting part of a thesis.

*Vaak zijn de stellingen het interessantste deel van een proefschrift.*

15. A true test of intellect is the appreciation of test cricket.

*Een echte 'test' van het intellect is het waarderen van test cricket.*



## Curriculum vitae

|                     |   |
|---------------------|---|
| 21 March 1976       | Born in Perth, Western Australia.   |
| Jan. 1989–Dec. 1993 | Como Senior High School, Perth, Western Australia.  |
| Feb. 1994–Nov. 1997 | Civil engineering studies, The University of Western Australia.                                   |
| April 1998          | Bachelor of Engineering (civil) with First Class Honours.   |
| Jan. 1998–Dec. 1998 | Research assistant, Faculty of Civil Engineering and Geosciences, Delft University of Technology. |
| Jan. 1999–present   | Research assistant, Faculty of Aerospace Engineering, Delft University of Technology.             |